Characterization of hydraulic behavior of orifices in conduits

THÈSE N^{O} 8090 (2017)

PRÉSENTÉE LE 1 DÉCEMBRE 2017
À LA FACULTÉ DE L'ENVIRONNEMENT NATUREL, ARCHITECTURAL ET CONSTRUIT
LABORATOIRE DE CONSTRUCTIONS HYDRAULIQUES
PROGRAMME DOCTORAL EN GÉNIE CIVIL ET ENVIRONNEMENT

ÉCOLE POLYTECHNIQUE FÉDÉRALE DE LAUSANNE

POUR L'OBTENTION DU GRADE DE DOCTEUR ÈS SCIENCES

PAR

Nicolas Jean François Pascal Ghislain ADAM

acceptée sur proposition du jury:

Prof. D. Lignos, président du jury
Prof. A. Schleiss, Dr G. De Cesare, directeurs de thèse
Prof. L. Lia, rapporteur
Dr R. Gabl, rapporteur
Dr M. Farhat, rapporteur

ÉCOLE POLYTECHNIQUE
FÉDÉRALE DE LAUSANNE

Suisse
2017

"*It's hard to observe without imposing a theory to explain what we're seeing, but the trouble with theories, as Einstein said, is that they explain not only what is observed but what CAN BE observed. We start to build expectations based on our theories. And often those expectations get in the way.*"

— Michael Crichton, Travels

Abstract

High-head power plants are the main pillar of Swiss peak electricity production. With the 2050 Energy Strategy approved by Swiss voters, the annual production of hydroelectricity should increase by 4%, while about 90% of the technically feasible potential is already used. The flexibility of high-head storage power plants may be improved by increasing the installed capacity or heightening existing dams in order to concentrate the electricity production on periods of peak demand and on the critical winter half-year. These upgrades of existing hydropower plants can lead to more critical mass oscillations between the upstream reservoir and the surge tank, which is a hydraulic device allowing dampening of the fast change of discharge and reducing the consequences of water hammer in the pressure tunnel of high-head power plants. A simple way to reduce the amplitudes of the mass oscillations is to place an orifice at the entrance of the surge tank.

Three different orifice geometries, chamfered, rounded orifices with a sharp side or two chamfered orifices, were systematically studied in conduits with laboratory experiments and numerical simulations in order to gain deeper knowledge of the behavior of orifices such as the steady and transient head losses, influence and reattachment length and the incipient cavitation number.

Steady head losses were evaluated with both approaches. A catalog summarizes the produced head loss coefficients in the two different flow directions as a function of all the geometries. Furthermore, three different empirical relationships were developed in order to predict the head loss coefficient for a sharp, chamfer or rounded approach flows and to design orifices as throttle.

On the one hand, the length of the zone disturbed by the orifice has been experimentally evaluated and increases with the orifice opening area. On the other hand, reattachment length has been numerically estimated and does not depend on the presence of a chamfer. Empirical formulas were derived to predict the two characterizing lengths.

Transient experiments were performed on chamfered orifices and revealed a clear transient behavior that could account for up to 20% of the steady head losses. The global head losses were higher for accelerate flow and less for decelerate flow than the corresponding steady head losses.

The incipient cavitation number was evaluated for chamfered orifices with single-phase computational fluid dynamics (CFD) simulations in order to develop predictive empirical relationships. This allowed for the assessment of the risk of cavitation. A cavitation number predicting the cavitation of the vena-contracta was also determined. A graphical view of the cavitation risk is suggested to evaluate the cavitation risk for surge throttles during mass oscillations.

Finally, one-dimensional (1-D) numerical simulations were conducted with the numerical software Hydraulic System on an existing high-head power plant to determine the throttling effects on the whole waterway.

KEYWORDS: *High-head and storage power plant, surge tank, mass oscillations, throttle, orifice, steady head loss, influence length, reattachment length, transient head loss, incipient cavitation*

Zusammenfassung

Hochdruckspeicherwasserkraftwerke sind das wichtigste Standbein der Schweizer Stromproduktion. Die vom Stimmvolk angenommen Energiestrategie 2050 sieht vor die jährliche Stromproduktion von Wasserkraft um 4% zu steigern, wobei etwa 90% des technisch möglichen Potenzials bereits ausgeschöpft ist. Um die Stromproduktion auf die Spitzenstunden des Verbrauchs sowie das für die Versorgung kritische Winterhalbjahr konzentrieren zu können, muss die Flexibilität der Speicherkraftwerke mit dem Zubau der installierten Leistung oder mit Erhöhungen von bestehenden Staumauern erhöht werden. Diese Leistungssteigerungen können zu verstärkten kritischen Massenschwingungen zwischen dem höhergelegenen Stausee und dem Wasserschloss führen. Das Wasserschloss ist ein hydraulisches Bauwerk, welches eine abrupte Änderung des Durchflusses dämpft und somit die Belastung des Druckstosses im Triebwassersystem verringert. Ein einfacher Ausatz die Amplituden der Massenschwingungen zu reduzieren ist die Anordnung einer Drosselblende beim Einlass in das Wasserschloss.

Drei verschiedene Drosselgeometrien, nämlich einseitig scharfkantige oder gerundete Blenden sowie zweiseitig scharfkantige Blenden, wurden systematisch mit Laborexperimenten und mittels numerischen Simulationen in einer Leitung untersucht. Damit konnten bessere Kenntnisse über das Verhalten von Blenden wie stationäre Druckverluste, instationäre Druckverluste, den Einfluss und die Länge der Ablösezone und der Grenzkavitationszahl gewonnen werden.

Die stationären Druckverluste wurden sowohl experimentell wie auch numerisch untersucht. Ein Katalog fasst die erhaltenen Druckverlustkoeffizienten in beiden Fliessrichtungen als Funktion der geometrischen Parameter zusammen. Zusätzlich wurden drei verschiedene empirische Beziehungen entwickelt, um den Druckverlustkoeffizienten für kantige, abgeschrägte und runde Blenden zu ermitteln und um Blenden als Drosseln zu dimensionieren.

Einerseits wurde die Länge der durch die Drossel im Stollen beeinträchtigten Zone experimentell ausgewertet, die zusammen mit der Blendenöffnung zunimmt. Andererseits wurde die Länge der Ablösezone numerisch bestimmt, welche nicht von der Abschrägung der Blende abhängt. Empirische Beziehungen, welche die beiden charakteristischen Längen voraussagen, konnten entwickelt werden.

Bei abgeschrägten Blenden wurden Experimente mit zeitlich variablen Abflüssen durchgeführt. Es konnte ein deutliches instationäres Verhalten beobachtet werden, welches bis zu

20% der stationären Druckverluste ausmachen kann. Der totale Druckverlust ist für einen beschleunigten Abfluss grösser und für einen verlangsamenden Abfluss kleiner, als der stationäre Druckverlust.

Für abgeschrägte Blenden wurde die Grenzkavitationszahl mit einphasigen numerischen Simulationen untersucht. Damit konnten empirische Beziehungen entwickeln werden, welche die Beurteilung des Kavitationsrisikos ermöglichen. Eine Kavitationszahl, welche die Kavitation der vena-contracta beschreibt wurde ebenfalls definiert. Es wird eine graphische Darstellung des Kavitationsrisikos empfohlen, um das Kavitationsrisiko von Wasserschlossdrosseln bei Massenschwingungen zu beurteilen.

Abschliessend, wurden numerische 1-D Simulationen an einem existierenden Hochdruckwasserkraftwerk mit der Software Hydraulic System durchgeführt, um die Drosseleffekte im gesamten Triebwassersystem zu beurteilen.

SICHWöRTER: *Hochdruckspeicherkraftwerke, Wasserschloss, Massenschwingungen, Drossel, Blende, stationären Druckverluste, beeinträchtigte, Ablösezone, stationären Druckverluste, Grenzkavitation*

Résumé

Les aménagements hydrauliques à haute chute sont le pilier principal de la production suisse électrique de pointe. Avec la stratégie énergétique 2050 acceptée par le peuple suisse, la production annuelle d'hydroélectricité devrait augmenter de 4% alors qu'environ 90% du potentiel techniquement faisable est déjà utilisé. Afin de pouvoir concentrer la production d'électricité sur les périodes de pointe et pour l'approvisionnement critique de la demi-année hivernale, il faut augmenter la flexibilité des aménagements hydrauliques de stockage en augmentant la capacité de production installée ou en relevant des barrages existants. Ces modernisations d'aménagements hydroélectriques existant peuvent engendrer des oscillations de masse plus critiques entre le réservoir amont et la cheminée d'équilibre, qui est un ouvrage hydraulique permettant de réduire les conséquences du coup de bélier dans la galerie d'amenée et d'amortir les changements rapides de débits dans l'aménagement. Un moyen simple de réduire l'amplitude de ces oscillations de masse est de mettre en œuvre un orifice à l'entrée de la cheminée d'équilibre.

Trois différentes géométries d'orifice, chanfreinée ou arrondie avec un côté tranchant ou avec deux chanfreins, ont été systématiquement étudiées dans des conduites avec des expériences en laboratoires et des simulations numériques. Le but est d'améliorer les connaissances sur le comportement des orifices tel que les pertes de charges en régime stationnaire et transitoire, les longueurs d'influence et de rattachement ainsi que le nombre d'apparition de la cavitation. Les pertes de charges en régime stationnaire ont été évaluées avec les deux approches. Un catalogue résume les coefficients de pertes de charge dans les deux directions d'écoulement en fonction des différents paramètres géométriques. De plus, trois différentes relations empiriques ont été développées pour prédire le coefficient de perte de charge pour des approches d'écoulement de type : tranchant, chanfreiné ou arrondi. Ces relations empiriques permettent aussi de dimensionner les orifices utilisés comme des étranglements de cheminée d'équilibre.

D'un côté, la longueur de la zone perturbée par l'orifice a été expérimentalement évaluée et augmente avec la section ouverte de l'orifice. D'un autre côté, la longueur de rattachement a été estimée numériquement and ne dépend pas de la présence d'un chanfrein. Des formules empiriques ont été dérivées pour prédire ces deux longueurs caractéristiques.

Des expériences en régime transitoire ont été réalisées sur des orifices avec un chanfrein et ont montré un comportement transitoire clair, qui peut aller jusqu'à 20% des pertes de charge en régime stationnaire. Les pertes de charge globales sont plus grandes pour des écoulements accélérés et plus petites pour des écoulements décélérés que les pertes de charge stationnaires correspondantes.

Le nombre d'apparition de la cavitation a été évalué pour des orifices chanfreinés avec des simulations CFD à une seule phase de fluide afin de développer des relations empiriques prédictives. Ceci permet l'évaluation du risque de cavitation. Un nombre d'apparition de la cavitation dans la veine contractée a aussi été déterminé. Une représentation graphique du risque de cavitation est proposée pour évaluer ce risque pour des étranglements de cheminée d'équilibre durant des oscillations de masse.

Finalement, des simulations numériques à une dimension (1D) ont été réalisées avec le logiciel Hydraulic System sur un aménagement hydraulique à haute chute existant pour mettre en évidence les effets de l'étranglement sur tout l'aménagement

MOTS CLEFS : Aménagements à hautes chutes et à accumulation, cheminée d'équilibre, étranglement, oscillation de masse, orifice, perte de charge stationnaire, longueur d'influence, longueur de rattachement, pertes de charges transitoires, apparition de la cavitation.

Contents

Abstract (English/Deutsch/Français) i

List of figures xiii

List of tables xxi

Notation xxiii

1 Introduction 1
- 1.1 Overview . . . 1
  - 1.1.1 Hydroelectricity . . . 2
  - 1.1.2 High-head power plant . . . 2
  - 1.1.3 Surge tank . . . 4
  - 1.1.4 Throttle and orifice . . . 5
- 1.2 Objectives of the study . . . 5
- 1.3 Organization of the report . . . 6

2 Theoretical bases 9
- 2.1 Transient flow within the waterway systems of hydroelectric power plants . . . 9
  - 2.1.1 Fundamental equations . . . 9
  - 2.1.2 Water hammer . . . 10
- 2.2 Surge tank . . . 11
  - 2.2.1 Purpose . . . 11
  - 2.2.2 Mass oscillations . . . 11
  - 2.2.3 Types of surge tanks . . . 13
  - 2.2.4 Stability criteria . . . 15
- 2.3 Throttled surge tanks . . . 16
  - 2.3.1 Classifications of throttles . . . 16
  - 2.3.2 Throttle location . . . 18
  - 2.3.3 Previous studies performed on surge-tank throttles . . . 19
- 2.4 Previous studies performed at the Laboratory of Hydraulic Constructions at EPFL 22
  - 2.4.1 Kárahnjúkar (2007) (throttle in a pressure-tunnel branch) . . . 22
  - 2.4.2 Lavey + (2011) . . . 22
  - 2.4.3 FMHL + (2012) . . . 24

2.4.4 Gondo (2014) . . . 25

3 Literature review 27

3.1 Use of orifices . . . 27

3.1.1 Flow meters . . . 27

3.1.2 Throttling device or producer of head losses . . . 28

3.2 Different flow types through orifices . . . 29

3.3 Head loss coefficient . . . 30

3.4 Recirculation or influence length . . . 32

3.5 Transient head losses . . . 33

3.6 Cavitation . . . 34

3.6.1 Cavitation number . . . 35

3.6.2 Cavitation regimes . . . 36

3.6.3 Incipient cavitation . . . 37

3.6.4 Prediction of the incipient cavitation number . . . 38

4 Experimental and numerical modeling 41

4.1 Experimental modeling . . . 41

4.1.1 Description of the experimental set-up . . . 41

4.1.2 Dimensional analysis . . . 43

4.1.3 Investigated parameters and test program . . . 45

4.1.4 Instrumentation . . . 49

4.1.5 Acquisition parameters . . . 51

4.1.6 Test procedure . . . 52

4.1.7 Measurement errors and uncertainties . . . 53

4.1.8 Scale effects . . . 53

4.2 Numerical simulations . . . 54

4.2.1 Presentation . . . 54

4.2.2 Geometry . . . 56

4.2.3 Mesh . . . 57

4.2.4 Pre-processing . . . 58

4.2.5 Solver . . . 60

4.2.6 Post-processing . . . 60

4.2.7 Validation . . . 63

5 Steady head losses of orifices 67

5.1 Introduction . . . 67

5.2 Methods . . . 67

5.3 Experimental results for orifices with a sharp side . . . 69

5.3.1 Performed tests . . . 69

5.3.2 Asymmetry . . . 70

5.3.3 Head losses for sharp flow direction (*AB*) . . . 72

5.3.4 Head losses for chamfer approach flow (*BA*) . . . 73

5.4 Experimental results for orifices with two chamfered angles 76
5.4.1 Influence of α_i on the head loss coefficients of orifices with chamfer, $\theta_R\, or\, \theta_L = 45°$ 76
5.4.2 Influence of α_i on the head loss coefficients of orifices with chamfer angle of 0°, 15°, 30° or 67° 78
5.4.3 Empirical relationship for head loss estimation 78
5.5 Experimental results for rounded orifices 81
5.6 Numerical 82
5.6.1 Comparison between the experimental and numerical results 82
5.6.2 Sharp approach flow - influence of the orifice inner thickness 88
5.6.3 Chamfer approach flow 89
5.7 Discussion 90
5.7.1 Chamfer orifices 90
5.7.2 Chamfer and rounded approach flow 91
5.8 Conclusion 92

6 Influence zone and flow reattachment lengths of orifice 97
6.1 Introduction 97
6.2 Methods 97
6.2.1 Reattachment and influence length 97
6.2.2 Dimensionless parameters 100
6.3 Influence length of orifice 101
6.3.1 Results from experiments 101
6.3.2 Results from numerical simulations 103
6.4 Reattachment length 107
6.5 Conclusions 110

7 Transient head losses through orifices 113
7.1 Introduction 113
7.2 Performed experiments 113
7.2.1 Experimental setup and tested configurations 113
7.2.2 Evaluation of head losses 114
7.2.3 Remarks on momentum and viscoelastic effects 115
7.3 Results 117
7.3.1 Head losses during the steady phases 117
7.3.2 Transient effects on the head losses through orifices 120
7.4 Discussion 123
7.4.1 Transient effect 123
7.4.2 Slow transient experiments for the evaluation of the steady head loss coefficient 124
7.5 Conclusions 124

8 Estimation of incipient cavitation number at orifices 125
8.1 Introduction 125
8.2 Assessment of cavitation 125
8.2.1 Prediction of the incipient and vena-contracta cavitation number 125
8.2.2 Cavitation risk in pipes 126
8.2.3 Cavitation risk in surge tank throttles 127
8.3 Results and analysis 128
8.3.1 Low pressure zones 128
8.3.2 Prediction of cavitation number 129
8.4 Discussion 134
8.5 Conclusions 135

9 Design guidelines and case studies 137
9.1 Design guidelines 137
9.1.1 Introduction 137
9.1.2 Required basic data 137
9.1.3 Numerical transient analysis 139
9.1.4 Design of the orifice producing the required head losses 139
9.1.5 Validation by hydraulic model tests or prototype measurements 146
9.1.6 Conclusion 146
9.2 Case Study 146
9.2.1 Effects of a throttle on the whole water way system 146
9.2.2 Design of throttle geometry 153
9.2.3 Influence and reattachment lengths 155
9.2.4 Determination of transient head losses for a down-surge (FMHL+) . . . 157
9.2.5 Estimation of the cavitation risk 159

10 Conclusions and outlook 163
10.1 Estimation of steady head loss coefficients for orifices 163
10.2 Determination of recirculation and influence lengths of the orifice 164
10.3 Transient head losses in orifices 165
10.4 Estimation of the cavitation risk 165
10.5 Practical recommendations 166
10.6 Outlook and future work 166

A Instrumentation 169
A.1 Presentation 169
A.1.1 Pressure transducers 169
A.1.2 Flow-meter 169
A.2 Calibration 170
A.2.1 Pressure transducers 170
A.2.2 FLow-meter 174
A.3 Sampling parameters 175

B Overview table of experiments and measured head losses 177

C Design of the numerical simulations 183

D Example of test sheet 187

E Transient experiments 191

F Theoretical bases for the cavitation limit 197

F.1 Straight pipe 197

F.1.1 Reference diameter - orifice diameter d 198

F.1.2 Reference diameter - pipe diameter D 198

F.2 Surge tank orifices 199

F.2.1 Surge tank emptying 199

F.2.2 Surge tank filling 200

F.3 Conclusions 200

G Expert sheet for orifice design 201

Bibliography 210

Acknowledgements 211

Curriculum Vitae 213

List of Figures

1.1 Phasing out of nuclear power in Switzerland according to the 2050 prediction as highlighted by the Swiss Federal Office of Energy (SFOE) for votation accepted by the Swiss on May, 21^{st} 2017 (adapted from (SFOE, 2015a)) 1
1.2 Schematic view of different waterway systems of high-head power plants 3
1.3 Schematic view of different waterway systems of high-head power plants 4
1.4 View of the Wevercé (Eastern Belgium) surge tank from the powerhouse 5
1.5 Structure of the report 7

2.1 Different types of surges tanks 13
2.2 (left) Picture of the orifice in the *Forces Motrices Hongrin-Léman* (hereafter, FMHL+) pumped-storage power plant (Hachem et al., 2013) and (right) drawing of the orifice of La Grande Dixence 17
2.3 Gondo power plant rack throttle (Adam et al., 2017): (left) picture before the on-site installation and (right) cross-section 18
2.4 Longitudinal section of a typical vortex throttle between the lower and upper chamber (adapted from Steyrer (1999)) 18
2.5 Schematic views of different locations of throttles according to the literature and existing power plants 19
2.6 Throttle of the Kárahnjúkar hydropower plant 23
2.7 Throttle at the entrance of the surge tank of the Lavey hydropower plant 23
2.8 Physical model of the new FMHL surge tank at LCH in EPFL (Hachem et al., 2013) 24
2.9 The two different Gondo throttle geometries (Adam et al., 2017) 26

3.1 The three different pressure tappings covered by the ISO (2003) (adapted from ISO (2003)). 28
3.2 Different flow types depending on the orifice thickness ratio 29
3.3 Chamfer and rounded orifices with a sharp side employed in this research study 30
3.4 Recirculation length, l_r, as a function of the contraction ratio, β, and the thickness ratio, α (adapted from Jianhua et al. (2010)) 33
3.5 Pressure line for water flowing through orifice 35
3.6 Identification of the cavitation regimes and limits (adapted from Instrument Society of America (1995) by Malavasi et al. (2015)) 37

3.7 Comparison of previous studies focusing on the evaluation of the incipient cavitation number σ_i as a function of the contraction ratio β 38
3.8 Flow through an orifice and localization of the different section used in the evaluation of σ_i and σ_{vc} 39

4.1 Overview of the experimental facility at LCH-EPFL 41
4.2 Sketch top view of the experimental facility at LCH-EPFL 42
4.3 Flow straighteners placed in the piping system 42
4.4 Orifice box within the orifice and the inner pipe 43
4.5 Detailed view of an orifice in a waterway system and definition of parameters . 44
4.6 Different reference orifice shapes tested with the dimensionless parameters and notations 46
4.7 Pressure tansducers used in the experimental campaign and dispatcher 50
4.8 Dimensionless positions of all the control cross-sections along the main pipe for $G1/4$" and $G1/2$" plugs 51
4.9 ENDRES + HAUSER - PROMAG 50 W flowmeter 52
4.10 Structure of the numerical modeling for each orifice from the orifice geometry (INPUT) to the results characterizing the orifice (OUTPUT) 56
4.11 Geometry of the numerical model (NUM001) 57
4.12 Views of the different meshes used for orifice NUM001 58
4.13 NUM_001 - Values of y^+ on pipe walls 62
4.14 Influence of the upstream and downstream length on the pressure line along the pipe axis in the numerical model compared to the experimental results (mean pressure and 95% confidence interval) for orifice EXP_007 - NUM_007 63
4.15 Influence of mesh refinement on head losses along the pipe axis and the most negative pressure on the numerical model compared to the experimental results for orifice EXP_007 - NUM_007 64
4.16 Influence of the turbulence model on head losses along the pipe axis if the numerical model compared to the experimental results for orifice EXP_007 - NUM_007 65

5.1 Flow through an orifice with a schematic indication of the pressure evolution along the pipe 68
5.2 EXP_001 - The pressure lines for five different discharges: (left) sharp approach flow (*AB*) and (right) chamfer approach flow (*BA*) 70
5.3 EXP_001 - The pair of head loss coefficients for: (a) the sharp approach flow (*AB*) and (b) the chamfer approach flow (*BA*) 71
5.4 Head loss coefficients for both flow directions and asymmetry: for the chamfered orifices from Table 5.1 with: C-R (reference chamfered orifice), C-A (variation of the angle, θ), C-B (variation of the contraction ratio, β), C-C (variation of the inner thickness ratio, α_i) C-D (variation of the thickness ratio, α); and for rounded orifices from Table 5.1 with R-i, the corresponding orifices related to the $C-i$ set of standard orifices (i is equal to A,B,C or D) 71

5.5 Highest (sharp) head loss coefficients for tested inner thickness ratio ($\alpha_i \in$ [0...0.2]): for chamfered and rounded orifices from Table 5.1 with: C(R)-R (reference chamfered and rounded orifices), C(R)-A (variation of the angle, θ), C(R)-B (variation of the contraction ratio, β), C(R)-C (variation of the inner thickness ratio, α_i) C(R)-D (variation of the thickness ratio, α); for a comparison between two formulae from Idel'cik (1969) (Eq. (3.3)) and Jianhua et al. (2010) (Eq. (3.7)) and an new empirical formula defined in the present study (Eq. (5.3)) 72

5.6 Comparison of the experimental results (data set C-B and R-B varying the contraction ratio β), present study equation (Eq. (5.3)) and existing equations (Section 3.3): Idel'cik (1969) (Eq. (3.3): $k' = 0.5$ and $\tau = 1.1$ and (3.4): $\tau = 0.707$), Blevins (1984) (Eq. (3.5): $C = 0.6$), and Jianhua et al. (2010) (Eq. (3.7): $\alpha = 0.5$) . 73

5.7 Influence of the chamfer angle, θ, on the chamfer head loss coefficient for a data set of standard orifices, R and A, fitted with a new empirical formula (Eq. (5.5)) and a comparison of the existing formulas from Idel'cik (1969) (Eq. (3.3): $k' = 0.5$ and $\tau = 1.285$ and (3.4): $\tau = 0.361$) 74

5.8 Evolution of the asymmetry ratio λ for the chamfer approach as a function of the inner thickness ratio, α_i, and the chamfer thickness ratio, α_θ (C-R, C-C and C-R series) 75

5.9 Head losses produced by a chamfered angle of $\theta_R \, or \, \theta_L = 45°$ 77

5.10 The asymmetry ratio, λ_θ, as a function of the chamfer thickness ratio α_θ for $\theta = 45°$ 77

5.11 Influence of the inner thickness ratio, α_i, on the sharp head loss coefficient ($\theta = 0°$) compared to between the empirical formula (Eq.(5.3))and different chamfer head loss coefficients ($\theta = 15°$, 30° or 67°) 79

5.12 Evolution of the coefficients, λ_θ^0 and $\kappa_{\alpha i}$, as a function of the chamfer angle, θ . 80

5.13 Rounded head loss coefficient, $k_{rounded}$, as a function of the inner thickness ratio α_i 81

5.14 Comparison between the experimental and predicted head loss coefficient values for the rounded orifices with the sharp and rounded approach flows 82

5.15 Orifices EXP_001 and NUM_001 ($\beta = 0.5$, $\alpha = 0.2$, $\alpha_i = 0.1$ and $\theta = 45°$) - comparison between the experimental results with 95% confidence interval ($\pm 1.96\sigma$) and the numerical results. 83

5.16 Orifices EXP_006 and NUM_006 ($\beta = 0.5$, $\alpha = 0.2$, $\alpha_i = 0.2$ and $\theta = 0°$) - Comparison between the experimental results with 95% confidence interval ($\pm 1.96\sigma$) and the numerical results. 84

5.17 Orifices EXP_007 and NUM_007 ($\beta = 0.5$, $\alpha = 0.2$, $\alpha_i = 0.1$ and $\theta = 15°$) - Comparison between the experimental results with 95% confidence interval ($\pm 1.96\sigma$) and the numerical results. 85

5.18 Orifices EXP_008 and NUM_008 $\beta = 0.5$, $\alpha = 0.2$, $\alpha_i = 0.1$ and ($\theta = 30°$) - Comparison between the experimental results with 95% confidence interval ($\pm 1.96\sigma$) and the numerical results. 86

5.19 Orifices EXP_009 and NUM_009 ($\beta = 0.5$, $\alpha = 0.2$, $\alpha_i = 0.1$ and $\theta = 67°$) - Comparison between the experimental results with 95% confidence interval ($\pm 1.96\sigma$) and the numerical results. 87
5.20 Comparison between the experimental and numerical head loss coefficients for the chamfered orifices for the sharp and chamfer approach flows (Table 4.2) . 88
5.21 Sharp head loss coefficients - comparison between the experimental and numerical results with the empirical formula (Eq.(5.3)) 89
5.22 Comparison between experimental and numerical head loss coefficients for all orifices tested either with the experimental or numerical model 90
5.23 Decomposition of an ideal orifice in a sudden contraction and enlargement with ① a far upstream pipe section, ② the most downstream orifice section as well as ③ a far downstream pipe section 91
5.24 Critical thickness ratio, α_c, as a function of the contraction ratio, β, based on the equality between Eq.(5.3) and (5.13) 91
5.25 Chamfer approach flow - vector colored by the value of the pipe axis velocity, u, for $\beta = 0.5$, $\alpha = 0.2$, $\alpha_i = 0.1$ and $\theta = 0°, 15°$ 94
5.26 Chamfer approach flow - vector colored by the value of the pipe axis velocity, u, for $\beta = 0.5$, $\alpha = 0.2$, $\alpha_i = 0.1$ and $\theta = 30°, 45°$ 95

6.1 Streamlines through orifice NUM_006, indicating the magnitude of the velocity (with colour scale), and the presence as well as the length of the reattachment zone 98
6.2 Evolution of the pressure, p, (above), and the axial velocity, u, (below), on the median plane of the pipe emphasizing to highlight the influence length 98
6.3 Schematic evolution of the pressure head along the pipe 99
6.4 Dimensionless pressure relative to the upstream pressure, p_u, for orifices EXP_0105 and NUM_0105: comparing the experimentally and numerically obtained influence length, L_j 101
6.5 Orifice EXP_0105 and NUM_0105: comparison between the experimental and numerical results and evaluation of the end of the influencing zone $l_j = \frac{L_j}{D}$ as a function of the Reynolds number (with 68% confidence interval) for the sharp approach flow 102
6.6 Experimental results of the dimensionless influence length, l_j, as a function of the contraction ratio β for all orifices with a sharp side: chamfer orifices, $C-i$ (square); rounded orifices $R-i$ (circle) and the two-chamfer orifices (triangle) (Table 4.4) 103
6.7 Comparison between the experimental and numerical influence length l_j . . . 104
6.8 The influence length, l_j, in the both flow direction as a function of the contraction ratio β for the numerically tested orifice 105
6.9 The asymmetrical ratio, λ_j, given in EQ.(6.6) as a function of the chamfer angle, θ, for the chamfer approach flow 106
6.10 Comparison of the numerically obtained influence length and the influence length predicted by Eqs.(6.4) and (6.7) for the sharp and chamfer approach flows 107

6.11 Reattachment length, l_r, as a function of the contraction ratio, β 108
6.12 The dimensionless reattachment length, l_r, as a function of the orifice height ratio γ_o and the comparison between the two-line model given in Eqs.(6.10) and (6.11) along with the graphical results from Jianhua et al. (2010) 109
6.13 Comparison of the dimensionless reattachment length, l_r, with the predicted value given by the empirical formulas (Eqs.(6.10) and (6.11)) 110

7.1 Tested geometries of the orifices of the transient experiments with $\alpha_i/\alpha = 0.5$ and $\theta = 45°$ 114
7.2 Procedure for the transient experiments 114
7.3 Positions of the $G1/4"$ transmitters for the transient experiments 115
7.4 Sharp approach flow: steady head losses determined with the transient experiments for orifices EXP_001, EXP_002, EXP_004, EXP_012 and EXP_032 compared with the steady head loss coefficients found in Chapter 5 118
7.5 Chamfer approach flow: steady head losses determined with the transient experiments for orifices EXP_001, EXP_002, EXP_004, EXP_012 and EXP_032 compared with the steady head loss coefficients found in Chapter 5 119
7.6 Orifice EXP_001, sharp approach flow: relationship between the instantaneous head losses and kinetic energy in the main pipe 120
7.7 Sharp approach flow - transient head losses determined during the transient experiments for orifices EXP_001, EXP_002, EXP_004, EXP_012 and EXP_032 compared to the steady head loss coefficients found in Chapter 5 121
7.8 Chamfer approach flow - transient head losses determined on the transient experiments for the orifices EXP_001, EXP_002, EXP_004, EXP_012 and EXP_032 compared to the steady head loss coefficients found in the Chapter 5 122

8.1 Schematic view of a Q-p_u plane for an orifice with the different areas of utilization with or without cavitation risk 127
8.2 Zones with expected low pressures: (a) gray zone where there are the lowest pressures; (b) white zone representing the *vena-contracta* 128
8.3 Comparison of the numerical result of the pressure loss coefficient (between the upstream and *vena-contracta* pressure) and the experimental formula-obtained values of Malavasi and Messa (2011) valid for $\beta \in [0.39, 0.7]$ and $\alpha \in [0.25, 1.5]$. 129
8.4 Value of the incipient cavitation number, σ_i, and the vena contracta cavitation number, σ_{vc}, as a function of the contraction ratio, β 130
8.5 Comparison of the numerical prediction and empirical prediction of the incipient cavitation number, σ_i, for the chamfer approach flow 131
8.6 Sharp approach flow - incipient cavitation number σ_i as a function of the contraction ratio, β, the thickness ratio α, the inner thickness ratio, α_i ,and the chamfer angle, θ 132
8.7 Chamfer approach flow - incipient cavitation number, σ_i, as a function of the contraction ratio, β, the thickness ratio, α, the inner thickness ratio, α_i, and the chamfer angle, θ 133

8.8 The *vena-contracta* cavitation number as a function of the chamfer angle, θ, and the contraction β for the chamfer approach flow 134
8.9 Comparison of numerical prediction with the empirical prediction of the incipient cavitation number, σ_i, for the sharp and chamfer approach flows 135
8.10 Comparison of numerical prediction and empirical prediction of the *vena-contracta* cavitation number, σ_{vc}, for the sharp and chamfer approach flows . . 135

9.1 Schematic view of the proposed orifice design procedure 138
9.2 Variation of sharp head loss coefficient for $\beta \in [0.4, 0.6]$ and $\alpha_i \in [0, 0.4]$ 140
9.3 Evolution of the coefficient λ_θ^0 and $\kappa_{\alpha i}$ as a function of the chamfer angle θ . . 142
9.4 Asymmetry ratio, λ, as a function of $\theta \in [0°, 90°]$ and $\alpha_i \in [0, 0.4]$ for $\alpha_\theta \geq 0.1$ . . 142
9.5 Incipient cavitation number, σ_i, for the sharp approach flow as a function of $\beta \in [0.4, 0.6]$ and $\alpha_i \in [0, 0.4]$ 143
9.6 Variation of the dimensionless reattachment length, l_r, for the sharp and chamfer approach flows with $\beta \in [0.4, 0.6]$ and $\alpha_i \in [0, 0.4]$ 144
9.7 Influence length of the orifice, l_j, for the sharp approach flow as a function of $\beta \in [0.4, 0.6]$ and $\alpha_i \in [0, 0.4]$ 145
9.8 Hydraulic System model of the Bieudron power house of Grande-Dixene scheme 147
9.9 The different equivalent diameters along the surge tank used for modeling with in Hydraulic System 148
9.10 Variation of the water level in the surge tank, z_{ST}, following a closure (duration 90s) for the existing surge tank and for the equivalent simple surge tank for different contraction ratios listed in Table 9.1 150
9.11 Variation of the pressure in the pressure tunnel close to the surge tank, p_{PT}, following a closure (duration 90s) for the existing surge tank and for the equivalent simple surge tank for different contraction ratios listed in Table 9.1 (the static pressure is relative to an upstream water level of 2156.6 m a.s.l.) 151
9.12 Maximum water level in the surge tank and the maximum pressure in the pressure tunnel as a function of the contraction ratio β. The reference elevation is the altitude of the tunnel axis below the surge tank (2156.6 m a.s.l.) 152
9.14 Maximal pressure in the pressure tunnel as a function of the contraction ratio β resulting in a maximum water level equivalent to the existing surge tank (2187.6 m a.s.l.) 152
9.13 Optimized equivalent diameter as a function of the contraction ratio β resulting in a maximum water level equivalent to the existing surge tank (2187.6 m a.s.l.). Also featured is a comparison of the required Thoma diameter (Eq.(9.3)), with the smallest diameter of the existing surge tank and the diameter of the existing lower and upper chambers 153
9.15 Plan view of the new FMHL surge tank at LCH of EPFL with the different orifice positions 156
9.16 Head loss coefficients characterizing the orifices as a function of the orifice position in the connecting tunnel (P_a to P_d in Figure 9.15) 157

9.17 Temporal evolution of the discharge and heads during the emptying of the new FMHL surge tank 158
9.18 Evolution of the head loss coefficient during emptying (0s after the end of the valve opening) 159
9.19 Graphical representation of the risk of cavitation (water at $20°C$)for a straight pipe using either the incipient cavitation number, σ_i, or the *vena-contracta* cavitation number, σ_{vc}, for four different numerically tested orifices: NUM_001 ($\beta = 0.5$), NUM_002 ($\beta = 0.4$), NUM_003 ($\beta = 0.45$) and NUM_004 ($\beta = 0.6$). The discharge was taken as positive for the sharp approach flow. 160
9.20 The risk of cavitation (water at $5°C$) for the Gondo surge tank subjected to a emergency shutdown leading to converging mass oscillations 161

10.1 Proposition of a new experimental testing setup for the assessment of the transient head losses during mass oscillations 167

A.1 Pressure transducers used in the experimental campaign 170
A.2 Calibration stand at LCH (EPFL) 171
A.3 Calibrations for the six G1/2" pressure transmitters 172
A.4 Calibrations for the six G1/4" pressure transmitters 173
A.5 Calibrations for the two flow-meters 174
A.6 Error on the mean pressure value compare the average taken on 15 minutes . . 175

E.1 Procedure of the transient experiments 191

F.1 Flow through an orifice and localization of the different section used in the evaluation of σ_i and $\sigma_{v.c.}$ 197
F.2 View of the idealized surge tank during when water flows in (a) or out (b) the surge tank 199

G.1 Print-screen of the expert-sheet, which is on-line available with the thesis (doi: 10.5075/epfl-thesis-8090) 202

List of Tables

2.1 Examples of existing orifice throttles 17
2.2 Existing studies on throttled surge tanks: goal of the study and means of investigation (+: Done; *o*: not presented in the paper and –: not done) 21

3.1 Limitations of flowmeter orifices defined by the ISO (2003) 28

4.1 Range of tested parameters 45
4.2 Set of sharp orifices tested during the experimental work 47
4.3 Set of rounded orifices tested during the experimental work 47
4.4 Set of sharp orifices tested during the experimental work 48
4.5 Range of tested discharges (*discharge tested numerically) 49
4.6 The record sequence for the G1/2" and G1/4" pressure transmitters for each discharge 51
4.7 Errors and uncertainties for the physical modeling 53
4.8 Previous studies performed on various types of orifices 55
4.9 Recent studies performed on a variety of orifice or throttled surge tanks 61
4.10 Number of cells with the four mesh refinements 64

5.1 Set of sharp orifices tested during the experimental work 69
5.2 Orifices considered for the analysis of the different chamfer angles 75

7.1 Opening and closure durations downstream for each orifice (note that all these values are theoretical, experimental results and values are shown in Appendix E) 115
7.2 The inertia coefficient $L_{①-②}\beta^2$ (Eq.(7.4)) is a function of the contraction ratio β116
7.3 Physical properties of the pipe wall of the experimental set-up 117
7.4 Comparison between the steady head loss coefficients found in Chapter 5 and the head loss coefficient fitted on the head losses during the steady phases with a limited set of discharges 119
7.5 Results for the transient head loss coefficient, k_t, for orifices EXP_001, EXP_002, EXP_004, EXP_012 and EXP_032 and compared to the transient coefficient, l_e, found by Yamaguchi (1976) (note: the effect of inertia, Table 7.2, is eliminated in the evaluation of k_t) 123

9.1 Simulation parameters - the contraction ratios β and two of the head loss coefficients . . . 149
9.2 Preliminary design of the Grande-Dixence throttle . . . 154
9.3 The positions of the orifice relative to the headrace tunnel and surge tank B . . 156
9.4 The influence and reattachment length, l_j and l_r, for $\beta = 0.70$ and $\beta = 0.73$ with a thickness ratio of $\alpha = 0.04$ . . . 156
9.5 Geometrical parameters of an equivalent orifice for the Gondo rack throttle . . 160

A.1 Calibrations of the six G1/2" pressure transmitters: Mean values and 5% - 95 % confidence intervals (CI) of the calibration linear parameters a and b 171
A.2 Calibrations of the six G1/4" pressure transmitters: Mean values and 5% - 95 % confidence intervals (CI) of the calibration linear parameters a and b 174
A.3 Calibrations of the two flow-meters: Mean values and 5% - 95 % confidence intervals (CI) of the calibration linear parameters a and b . . . 175

B.1 Set of sharp orifices tested during the experimental work . . . 178
B.2 Set of rounded orifices tested during the experimental work . . . 178
B.3 Set of sharp orifices tested during the experimental work . . . 179
B.4 Overview table sorted with descending highest head loss coefficient 180

E.1 Transient experiments performed on the orifice EXP_001 . . . 192
E.2 Transient experiments performed on the orifice EXP_002 . . . 193
E.3 Transient experiments performed on the orifice EXP_004 . . . 194
E.4 Transient experiments performed on the orifice EXP_012 . . . 195
E.5 Transient experiments performed on the orifice EXP_032 . . . 196

Notation

Roman letters

A_{PT}	[m^2]	pressure tunnel cross-section
A_{ST}	[m^2]	surge tank cross-section
A_{TH}	[m^2]	Thoma cross-section
A_i	[m]	position of the control cross-sections in the main pipe A for G1/2" transmitters
A_{ref}	[m^2]	reference cross-section of a surge tank throttle in SIMSEN
$A_{th,r}$	[m^2]	reference cross-section of a throttle
$A_{th,o}$	[m^2]	opening cross-section of a throttle
A_{tot}	[m^2]	total cross-section in Evangelisti correction (Eq. (2.9))
B_i	[m]	position of the control cross-sections in the main pipe B for G1/2" transmitters
C	[–]	coefficient depending on β in Blevins (1984)
C_D	[–]	discharge coefficient
D	[m]	pipe diameter
D_{LS}	[m]	laboratory supply diameter
Eu	[–]	Euler number
F	[–]	Froude number
H	[m]	total hydraulic head
H_n	[m]	head between the surge tank and the downstream reservoir at equilibrium
$H_{wh,max}$	[m]	maximum pressure during water hammer
K_D	[m]	kinetic energy in the main pipe (diameter D)
L_{fsd}	[m]	distance between a point and the closest free surface
L_j	[m]	length of the zone disturbed by the orifice
L_{PT}	[m]	length of the pressure tunnel
L_r	[m]	reattachment length
$L_{\textcircled{1}-\textcircled{2}}$	[m]	length for the inertial term between section ① and ②
Q	[m^{3}s^{-1}]	discharge
Q_c	[m^{3}s^{-1}]	discharge flowing into or out the surge tank
Q_T	[m^{3}s^{-1}]	discharge flowing through the turbine
Re	[–]	Reynolds number
Re_d	[–]	Reynolds number in the orifice
Re_D	[–]	Reynolds number in the main pipe
T_s	[s]	duration of the steady phase of discharge

$T_{t,dec.}$	[s]	duration of the transient decrease of the discharge
$T_{t,inc.}$	[s]	duration of the transient increase of the discharge
a	[ms^{-1}]	wave celerity
a_i	[m]	positio of the control cross-section in the main pipe A for G1/4" transmitters
$a_{l,i}$	[-]	empirical parameter for predicting the influence length
$a_{l,r}$	[-]	empirical parameter for predicting the reattachment length
a_r	[ms]	major elliptical axis for rounded orifices
b_i	[m]	position of the control cross-section in the main pipe B for G1/4" transmitters
$b_{l,i}$	[-]	empirical parameter for predicting the influence length
$b_{l,r}$	[-]	empirical parameter for predicting the reattachment length
b_r	[ms]	minor elliptical axis for rounded orifices
$c_{l,i}$	[-]	empirical parameter for predicting the influence length
$c_{l,r}$	[-]	empirical parameter for predicting the reattachment length
$d_{l,i}$	[-]	empirical parameter for predicting the influence length
d	[m]	orifice internal diameter
f	[–]	Darcy-Weisbach friction factor
g	[ms^{-2}]	gravity acceleration
k	[–]	head loss coefficient
k'	[–]	coefficient depending on the orifice upstream geometry
$k_{chamfer}$	[–]	head loss coefficient for chamfer approach flow
$k_{cont.}$	[–]	head loss coefficient for contracted approach flow, which is either chamfer or rounded approach flow
k_i	[–]	head loss coefficient for the friction losses given by Darcy-Weisbach, $\frac{fL}{D}$
$k_{rounded}$	[–]	head loss coefficient for rounded approach flow
k_s	[–]	steady head loss coefficient
$k_{s,i}$	[m]	sand roughness in the orifice inner wall
k_{sharp}	[–]	head loss coefficient for the sharp approach flow
k_t	[–]	transient head loss coefficient
$k_{t,t}$	[m]	coefficient multiplying the flow acceleration in transient modeling
$k_{t,x}$	[–]	coefficient multiplying the flow convection in transient modeling
$k_{s,p}$	[–]	sand roughness in the pipe wall
k_{PT}	[–]	head loss coefficient for the linear friction in the pressure tunnel
k_{ST}	[–]	head loss coefficient of the throttled surge tank
l_e	[m]	equivalent length of the orifice (Yamaguchi, 1976)
l_j	[–]	dimensionless influence length
$l_{j,sharp}$	[–]	dimensionless influence length for the sharp approach flow
$l_{j,chamfer}$	[–]	dimensionless influence length for the chamfer approach flow
l_r	[–]	dimensionless reattachment length
p	[Pa]	pressure
p_d	[Pa]	downstream pressure
p_u	[Pa]	upstream pressure
p_{vc}	[Pa]	vena-contracta pressure

p_{vg}	[Pa]	vapour pressure
p_i	[m]	average pressure at the section i
t	[m]	orifice thickness
t_c	[m]	orifice critical thickness
t_i	[m]	inner orifice thickness
t_θ	[m]	chamfer thickness
v	[ms^{-1}]	flow velocity
v_D	[ms^{-1}]	velocity flowing in the main pipe
v_d	[ms^{-1}]	velocity flowing in the orifice
v_{ST}	[ms^{-1}]	velocity flowing into/out of the surge tank
x	[m]	pipe axis
z	[m]	difference between the level in the surge tank and the reservoir level
z_i	[m a.s.l.]	elevation at the section i

Greek letters

ΔH	[m]	head losses
ΔH_s	[m]	steady head losses
ΔH_t	[m]	transient head losses
ΔH_{tot}	[m]	total head losses in Evangelisti correction (Eq. (2.9))
ΔH_{wh}	[m]	variation of the head due to the variation of flow velocity
Υ_{α_i}	[–]	parameter taking into account the effects of the inner thickness ratio α_i for sharp approach
α	[–]	orifice thickness ratio
α_a	[–]	dimensionless elliptical axis for rounded orifices
α_c	[–]	critical thickness ratio
α_i	[–]	inner thickness ratio
α_θ	[–]	chamfer thickness ratio
β	[–]	orifice diameter ratio
β_b	[–]	dimensionless elliptical axis for rounded orifices
γ_o	[–]	orifice height ratio
γ_{TH}	[–]	safety factor for the thoma cross-section
ϵ	[–]	expansion factor taking into account the flow compressibility
ε_i	[–]	dimensionless roughness for the orifice inner wall
ε_p	[–]	dimensionless roughness for the pipe wall
η	[–]	parameter depending on the diameter ratio and Reynolds number (Blevins, 1984)
θ	[°] or [rad]	orifice chamfer angle
$\theta_{R(resp.L)}$	[°] or [rad]	Right (resp. left) orifice chamfer angle
λ	[–]	asymmetry number
λ_a	[–]	asymmetry number defined for a variation of α_a
λ_i	[–]	Darcy friction factor
λ_j	[–]	asymmetry number for the influence length
λ_θ	[–]	asymmetry coefficient for a variation of the chamfer θ
λ_θ	[–]	asymmetry ratio for $\alpha_i = 0$ for a variation of the chamfer angle θ
$\kappa_{\alpha i}$	[–]	coefficient of the linear decrease of the head losses with α_i
ρ	[kg m^{-3}]	water density
σ	[–]	cavitation number
σ_c	[–]	critical cavitation number
σ_d	[–]	cavitation number (downstream definition)
σ_i	[–]	incipient cavitation number
σ_{mv}	[–]	maximum vibration cavitation number
σ_{vc}	[–]	vena-contracta cavitation number
σ_{vg}	[–]	cavitation number (vapour gaz)
τ	[–]	coefficient depending on α (Idel'cik, 1969)
ϕ	[°]	angle between the conduit axis and the horizontal

Acronyms and abbreviations

EPFL	École Polytechnique Fédérale de Lausanne
CFL	Courant-Friedrichs-Lewy condition
CFD	Computational Fluid Dynamics
DES	Detached Eddy Simulation
LCH	Laboratory of Hydraulic Constructions of EPFL
LES	Large Eddy Simulation
RANS	Reynolds Averaged Navier-Stokes
RNG	Renormalization group
RSM	Reynold Stress Method
SFOE	Swiss Federal Office of Energy
SST	Shear Stress Transport

1 Introduction

1.1 Overview

The Swiss confederation aims to phase out nuclear power production with its "2050 Energy Strategy" by increasing the renewable energy contribution to its overall energy generation. Even if the total electricity consumption does not increase significantly by 2050, nuclear power production, of which the yearly average production amounted to 33% in 2016, should end in 2035 (Figure 1.1). This ambitious schedule enforces replacement of a continuous generation of base load with intermittent renewable electricity generation, e.g. solar or wind energy, that depends on climatic conditions. Generation could thus not be able to follow the consumption and new storage schemes, and highly flexible hydropower plants should emerge. Hydroelectricity may aid in the transfer of excess production from intermittent generation when there is a need for production based on large-scale consumption.

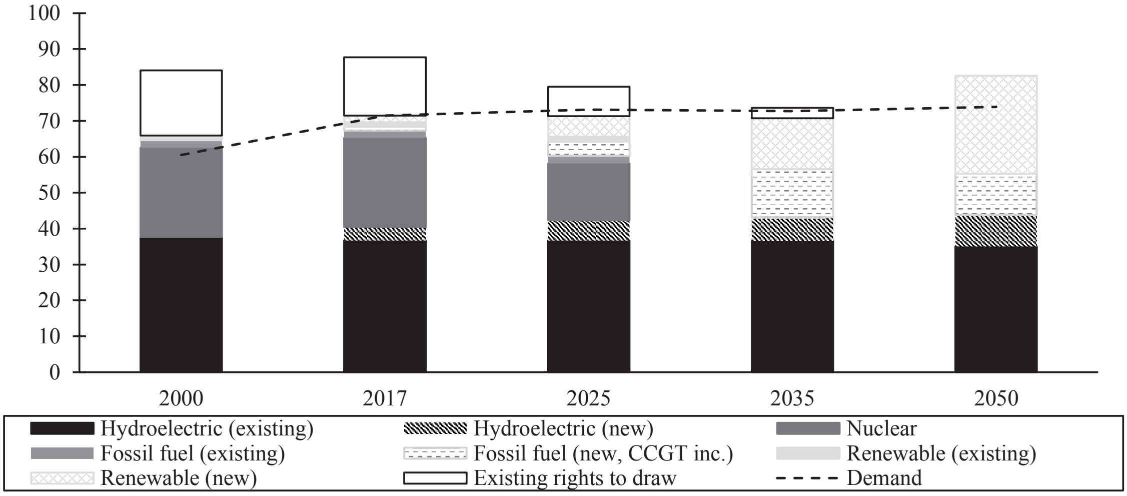

Figure 1.1 – Phasing out of nuclear power in Switzerland according to the 2050 prediction as highlighted by the Swiss Federal Office of Energy (SFOE) for votation accepted by the Swiss on May, 21^{st} 2017 (adapted from (SFOE, 2015a))

1.1.1 Hydroelectricity

In Switzerland, hydroelectricity has supplied approximately 60% of the domestic electricity production for the last 40 years and is the major source of renewable electricity (SFOE, 2015b). There are two main types of hydroelectric power plants, namely run-of-the-river or storage power plants that produce 40 and 60%, respectively, of Swiss hydroelectric generation.

With the "Energy Strategy 2050", the yearly expected average production should increase from approximately 36.0 TWh/year to 38.6 TWh/year, while the technically feasible potential is approximately 41.0 TWh/year (Hydropower and Dams, 2016). These objective could be achieved primarily either by refurbishing and extending existing power plants or by building new ones. New pumped-storage power plants, Veytaux II (Hachem et al., 2013), Nant de Drance and Limmern, have recently been commissioned to store production surpluses coming from new renewable energies and transferring it to peak hours.

This challenging strategy could strengthen the role of Swiss hydroelectricity in Central Europe. Historically, Switzerland has exported electricity to its neighbors during peak hours owing to storage power plants (including pump-storage plants) but has to import base-load electricity in the winter (Schleiss, 2007, 2012).

1.1.2 High-head power plant

As mentioned before, 60% of Swiss hydroelectricity is generated by high-head storage plants, and these can be found in the upstream part of river catchments (steep valleys).

Turbine operations, with start-up or shut-down, result in transient flows within the waterway system. In order to permit flexible operations of turbines (or pumps) and to protect the pressure tunnel against water hammer, different types of high-head power plants have been designed with a surge tank (Figures 1.2 and 1.3), which can be implemented upstream and downstream of the powerhouse as a free-surface surge tank or as an air-cushion chamber under very favorable rock conditions with high strength and in situ stress as well as low permeability. In Switzerland, the most common type is the high-head storage power plant with an upstream surge tank, the main interest in this study.

Figure 1.2a depicts a schematic view of a typical alpine high-head power plant (Schleiss, 2002). Generally, high-head power plants are composed of the following elements:

- an upstream reservoir;
- a pressure tunnel (or headrace tunnel) that is normally lined with concrete;
- a surge tank which could be defined as kind of a reservoir. Its role is to protect the pressure tunnel against the waterhammer coming from fast turbine maneuvers;
- a pressure shaft (or penstock) that is normally lined with steel;

- hydraulic machinery which produces electricity as a function of discharge and head; and
- a downstream tailrace tunnel.

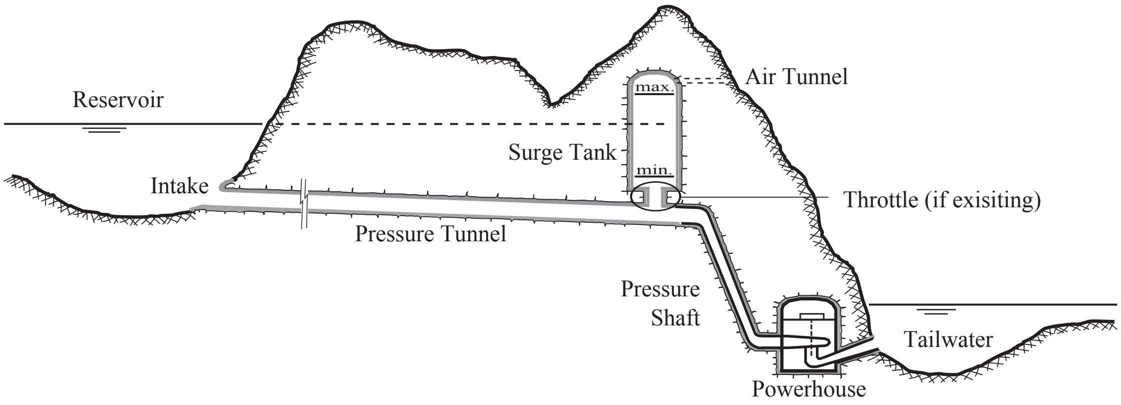
Reservoir
Air Tunnel
max.
Surge Tank
min.
Intake
Throttle (if exisiting)
Pressure Tunnel
Pressure
Shaft
Tailwater
Powerhouse

(a) Upstream surge tank (typically in alpine valleys) with courtesy of A.J. Pachoud

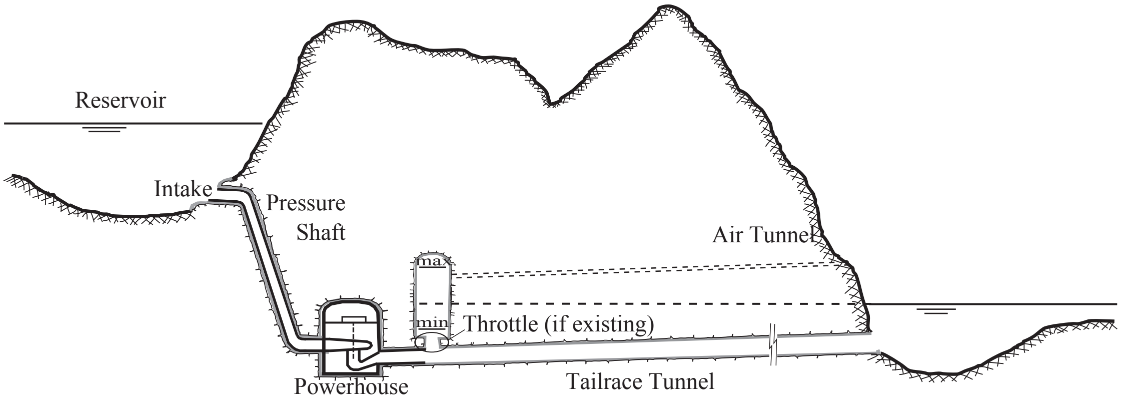
Reservoir
Intake
Pressure
Shaft
Air Tunnel
max
min
Throttle (if existing)
Powerhouse
Tailrace Tunnel

(b) Downstream surge tank

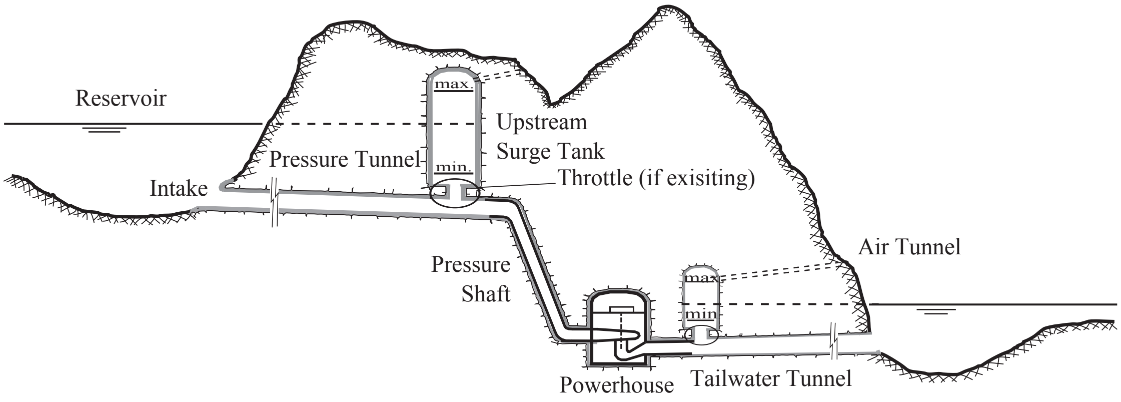
Reservoir
max.
Upstream
Surge Tank
Pressure Tunnel
min.
Throttle (if exisiting)
Intake
Air Tunnel
Pressure
Shaft
max
min
Powerhouse
Tailwater Tunnel

(c) Two surge tanks

Figure 1.2 – Schematic view of different waterway systems of high-head power plants

The waterway has similar elements whether the plants are pumping or turbining (pumped-storage plants). In actual facts, other design-load cases could be critical based on the pumping mode.

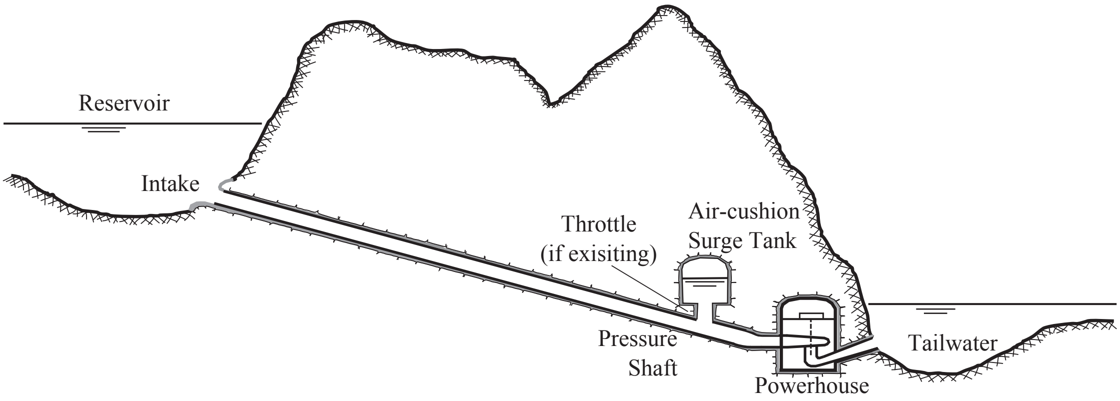

(a) Air-cushion surge tank

Figure 1.3 – Schematic view of different waterway systems of high-head power plants

1.1.3 Surge tank

A surge tank is an excavated shaft that is eventually combined with chambers connected to the waterway of a hydroelectric power plant, especially a high-head power plant. According to Chaudhry (2014), the two main roles of a surge tank are:

- Diminish the amplitude of pressure fluctuations in the waterway system. It reflects incoming pressure waves such as water hammer waves. These waves, which emanate from the pressure shaft owing to changes in turbine flow, are reflected back at the surge tank and reduces the pressure transmitted to the pressure tunnel; and
- improve the regulation of hydraulic turbines. The determining length for the water-starting time is depending on the surge tank and not to the upstream reservoir.

Nevertheless, as a free surface is introduced into the waterway system, a mass oscillation with the reservoir appears for any changes of discharge within the system, such as the water hammer, but they are two distinct phenomena (Jaeger, 1933, 1977). However, the mass oscillation may limit the turbine restart after a shut-down.

There are different types of surge tanks including those with free-water surfaces, e.g. simple, throttled, differential surge tanks or those with expansions (chambers), as well as pressurized air like air-cushion surge tanks. Each type is meant to enhance the dampening of mass oscillations so as to decrease the consequences of its introduction. They can also decrease the surge tank geometry in order for it to stay within the topography, which is generally the case in the alpine region (Figure 1.2a) but difficult in other parts of the world (Figure 1.4).

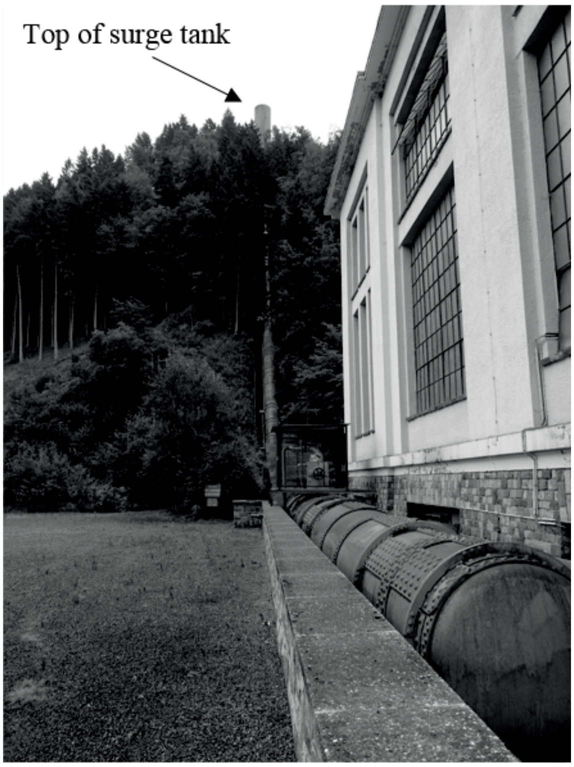

Figure 1.4 – View of the Weveré (Eastern Belgium) surge tank from the powerhouse

1.1.4 Throttle and orifice

As stated earlier, throttled surge tanks can thus enhance the dampening of mass oscillations. This allows for the optimization of surge tank geometry in term of maximum amplitude of mass oscillations. In this study, a throttle is the generic term for the hydraulic device producing head losses at the entrance of a surge tank. Different throttle geometries have been highlighted in the literature, such as orifices, rack or bar-screen and vortex throttles (Adam et al., 2016).

This study focuses on orifices, which facilitates the easy introduction of different head losses in the two flow directions, i.e. when the water flows into or out of the surge tank.

1.2 Objectives of the study

Throttling a surge tank is an economical measure for adapting existing surge tanks to increased turbine capacity based on discharge or head increase as the construction of a new surge tank can be avoided (Adam et al., 2017). Different types of throttling exist, though orifices placed at the entrance of the surge tank are often employed because of their simplicity. However, as suggested by Vereide (2016), there is a need for improvement in the design methods pursued to find an optimal throttle installed at the entrance of the surge tank in an efficient way. This begins with the hydraulic characterization of throttles and especially of orifices.

Orifices are commonly used to evaluate the discharge flowing through or producing head losses. Nevertheless, most studies that have utilized them have focused only on one flow direction and did not consider their possible asymmetrical behavior, which is an important characteristics in the case of a throttling device.

The present research study aimed to fill in these gaps of knowledge by means of an experimental and numerical study to improve the knowledge of orifices' behavior as a throttle. The study objectives can be synthesized by answering the following questions:

- Which geometrical parameters influence the head loss coefficients and how to identify an orifice with a certain asymmetry ratio ?
- How long is the reattachment length at the downstream end of the orifice and what is the influence zone of the orifice conduit ?
- Is there a transient behavior of head losses at orifices?; and
- How can the cavitation risk be assessed to provide guidelines for the choice of orifice geometry ?

1.3 Organization of the report

The report is divided into ten chapters (Figure 1.5).

Chapters 1, 2 and 3 introduce the framework of this research as well as the state of the art regarding the steady and transient head losses produced by orifices, influence and reattachment lengths at the downstream of orifices and cavitation risk. Chapters 4 and 5 present the experimental modeling and numerical simulations with the purpose of evaluating systematically the behavior of an orifice.

Chapter 6 discusses the steady head losses produced by orifices using the experimental and numerical results, while Chapter 7 covers the effect of the orifice geometry on the disturbed zone and reattachment length. Chapter 8 highlights the transient behaviors of the head losses produced by the orifices. Chapter 9 describes a new way to take into account cavitation and avoid incipient cavitation. Chapters 6 to 9 were prepared as publications.

Chapter 10 offers the main findings of the work presented herein and design guidelines applicable to throttles and orifices. Then, in Chapter 11, different case studies on various steps in the analysis of orifices and throttling devices are featured.

Finally, Chapter 12 summarizes the conclusions of this research and provides a number of outlooks for future investigations.

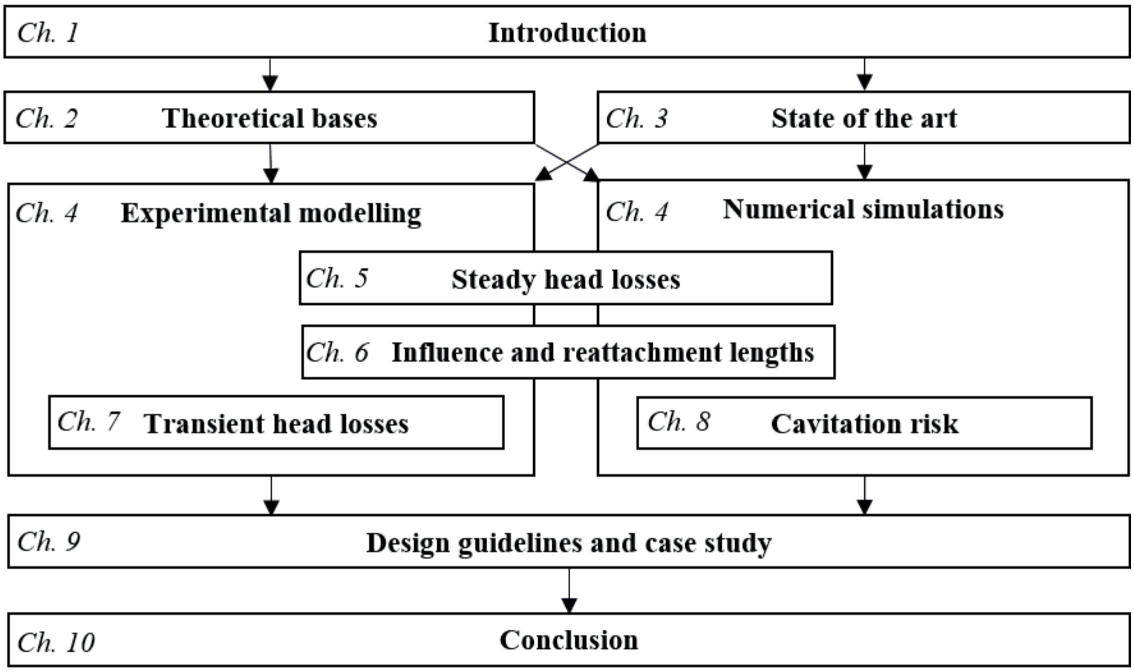
Ch. 1 Introduction
Ch. 2 Theoretical bases
Ch. 3 State of the art
Ch. 4 Experimental modelling
Ch. 4 Numerical simulations
Ch. 5 Steady head losses
Ch. 6 Influence and reattachment lengths
Ch. 7 Transient head losses
Ch. 8 Cavitation risk
Ch. 9 Design guidelines and case study
Ch. 10 Conclusion

Figure 1.5 – Structure of the report

2 Theoretical bases[1]

2.1 Transient flow within the waterway systems of hydroelectric power plants

2.1.1 Fundamental equations

Turbine operations, in order to satisfy grid demand, induce transient flows in pressure conduits of hydropower schemes. Consequently, water hammer occurs in conduits when the flow discharge changes abruptly. The greatest water hammer arises when the maneuver duration is less than the time taken by a pressure wave to transit back and forth within the conduit (reflexion time).

Many authors (Popescu et al., 2003; Boillat and de Souza, 2004; Nicolet, 2007; Chaudhry, 2014) have proposed the continuity (Eq.(2.1)) and momentum (Eq.(2.2)) equations for pressurized conduits.

The continuity equation Eq.(2.1) is applied to a control volume of the conduit and was developed for slightly compressible fluid and elastic conduit walls. Furthermore, the flow is assumed to be 1D and with uniform pressure across the pipe cross-section.

$$\frac{\partial p}{\partial t} + v\frac{\partial p}{\partial x} + \rho a^2 \frac{\partial v}{\partial x} = 0 \tag{2.1}$$

where: p is the pressure, v the flow velocity, ρ the fluid density, a the wave celerity and x the conduit axis

The momentum equation, Eq.(2.2), is for the same control volume and obtained by applying

---

[1] This Chapter is based on a submitted scientific paper: "Adam, N.J. De Cesare,G. & Schleis, A.J. (under revision). Throttles in surge tanks to reduce mass oscillations. Submitted to the *Canadian Journal of Civil Engineering*". The work and analysis presented hereafter is original and was performed by the author.

Newton's second law of motion:

$$\frac{\partial v}{\partial t}+v\frac{\partial v}{\partial x}+\frac{1}{\rho}\frac{\partial p}{\partial x}+g\sin\phi+f\frac{v|v|}{2D}=0 \tag{2.2}$$

where: g is the gravitational constant, ϕ the angle between the conduit axis and the horizontal, f the Darcy-Weisbach friction factor and D the conduit diameter

Chaudhry (2014) assumed that transient head losses are equal to steady head losses of the momentum equation for transient flows in closed conduits (this assumption is discussed in Section 3.5). With this simplification, a system of hyperbolic partial differential equations (Eq.(2.1) and (2.2)) is obtained. Different resolution methods can be carried out, such as the arithmetic method (Allievi, 1913), graphical method (Bergeron, 1950), the method of characteristic (Chaudhry, 2014; Boillat and de Souza, 2004) or by employing the Finite-Difference method and analogous to electrical schemes (Nicolet, 2007). These methods all enable conducting numerical simulations for studying transient flows within the waterways of hydroelectric power plants, such as the water hammer (Section 2.1.2) or mass oscillations (Section 2.2.2).

2.1.2 Water hammer

A water hammer is a surge pressure wave with a succession of overpressure and under pressure. The amount of pressure produced in a pipe depends on a variety of parameters, such as pipe geometry, pipe wall rigidity and the duration and shape of closure (or opening). As explained in Jaeger (1933) and Stucky (1950), the main goal of a surge tank is to prevent the water hammer coming from the valve into the long pressure tunnel to avoid heavy linings, like steel liner, in the pressure tunnel. When an overpressure starts at the downstream valve, it propagates up the pressure shaft to the surge tank. This overpressure is divided into both the pressure tunnel and the surge tank as a function of each section. Normally, the surge tank section is much larger than the pressure tunnel and thus any water hammer is avoided in the pressure tunnel.

As demonstrated in Stucky (1950) and Nicolet (2007) by applying the mass and momentum conservation to the pipe during a valve closure, the overpressure, ΔH_{wh}, for an instantaneous closure or opening, is a function of the wave speed, a, and the velocity change, Δv, in the tunnel as shown in Eq.(2.3). The main assumption is made based on transient energy losses, which are assumed to be equal to steady losses.

$$\Delta H_{wh}=-\frac{a\cdot\Delta v}{g} \tag{2.3}$$

where: ΔH_{wh} is the variation of head owing to the variation of flow velocity, Δv

For a full closure of the valve, the maximum overpressure is given by (2.4):

$$H_{wh,max} = \frac{a \cdot v_0}{g} \tag{2.4}$$

where v_0 is the initial flow velocity prior to closure.

By studying the temporal resolution of both governing equations, the momentum and conservation of mass, and by applying the method of characteristic (Stucky, 1950; Nicolet, 2007), this maximum overpressure observed to take place only when the closure time is less than a critical time as given by (2.5):

$$t_{crit} = \frac{2L_{fsd}}{a} \tag{2.5}$$

where L_{fsd} is the distance between the valve and the first free surface (*free-surface distance*) such as the surge tank, or, if not existent, the upstream reservoir.

2.2 Surge tank

2.2.1 Purpose

According to Section 2.1.1, the implementation of a surge tank enables decreasing the duration of closure for the same overpressure within the pressure shaft or decreasing the overpressure for the closure time. It analogously leads to underpressure for an opening. In other words, a surge tank reduces the amplitude of pressure fluctuations. The pressure waves, induced by a discharge variation within the waterway, are reflected in the pressure shaft and, thus, decreases the pressure entering in the pressure tunnel.

However, a consequence of surge tank implementation is that the pressure wave energy is transfered via a mass oscillation between the surge tank and reservoir. These mass oscillations are much slower than the water hammer pressure fluctuations.

2.2.2 Mass oscillations

Mass oscillation in a surge tank occurs every time the discharge from the plant is changed. A mass oscillation is a transient event that takes place between a first equilibrium level and a second because of a change of flow within the system. This phenomenon is critical for full closure or for consecutive operations.

From Jaeger (1933) and Stucky (1950), it is known that the water hammer and mass oscillation are interconnected and must be studied simultaneously in the case of a throttle (Schleiss, 2002).

While a water hammer is an elastic phenomenon, a mass oscillation follows the principle of communicating reservoirs, where the water can be considered incompressible. Based on the different time scales (a few seconds for a water hammer and a few minutes for a mass oscillation), these phenomena are often studied separately.

Simplified governing equations can be found in the literature (e.g. in (Stucky, 1950; Zicman, 1953; Jaeger, 1977; Boillat and de Souza, 2004; Popescu et al., 2003)). Different assumptions, described as follows, have been made by relevant authors:

- water is considered incompressible and pipe walls are infinitely rigid;
- water inertia in the surge tank is small compared to the inertia of the pressure tunnel;
- water levels in the surge tank are always horizontal and kinetic energy can be neglected;
- major and minor losses can be expressed according to the unsteady regime with the same relation as in the steady regime;
- system is always entirely filled with water; and
- all parameters, variables, i.e. geometric and hydraulic, are continuous and differentiable.

The two main relations are: (i) *Newton's second low applied to the pressure tunnel* (2.6) ; and *(ii) The conservation of mass locally under the surge tank* (2.7):

$$\frac{L_{PT}}{g} \cdot \frac{dv}{dt} + z + \Delta H = 0 \tag{2.6}$$

$$v = \frac{A_{ST}}{A_{PT}} \cdot \frac{dz}{dt} + \frac{Q_T}{a} \tag{2.7}$$

where v is the velocity in the pressure tunnel, L_{PT} the length of the pressure tunnel, z the difference between the level in the surge tank and the reservoir level (counted positive when the level in the surge tank is higher than the upstream level), ΔH the total amount of head losses, A_{ST} the surge tank cross-section, A_{PT} the pressure tunnel cross-section and Q_T the discharge going through the turbines. This term, ΔH, can be divided into two main components such as major losses (head loss because of friction in the pressure tunnel) and secondary losses (head loss at the entrance of the surge tank).

The evolution of the free surface in the surge tank can be found by combining Eq. (2.7) and (2.6).

2.2.3 Types of surge tanks

According to Giesecke et al. (2014), Figure 2.1 portrays the four main types of surge tanks. Yet another type is the air-cushion surge tank (Figure 1.3a). The main goal of more complex surge tanks is to improve the oscillation dampening caused by a discharge change within the waterway, just as mentioned earlier. Gardel (1956) showed that the main effect of the more complex surge tanks, for example those with throttle, with expansion(s) or differential, is that the pressure in the pressure tunnel at the entrance the surge tank rises faster than in the case of a simple surge tank.

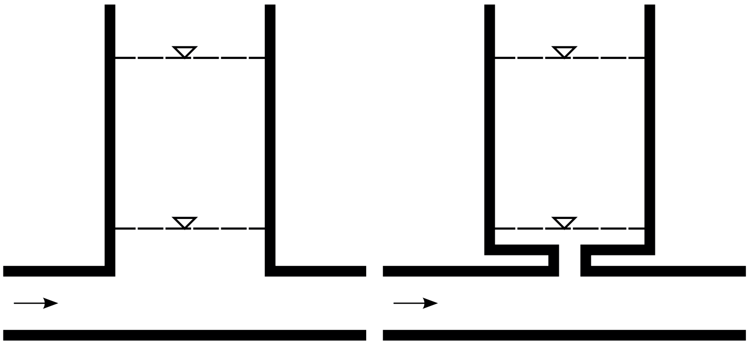

(a) Simple shaft

(b) Throttled shaft

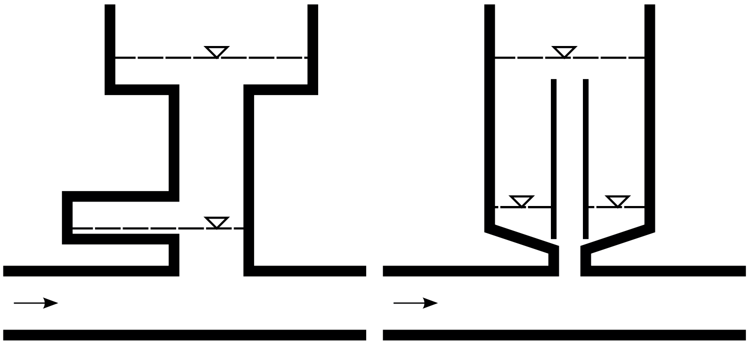

(c) Shaft with chamber(s) or expansion(s)

(d) Differential surge shaft

Figure 2.1 – Different types of surges tanks

Simple surge tank This is the simplest surge tank due to its cylindrical shape, though it can be inclined or vertical. Inclined surge tanks feature a larger surface and, thus, higher stability. Nowadays, simple surge tanks are mostly employed for low and middle heads and Francis turbines. Nevertheless, their simple shape permits the development of and understanding the major phenomena (Stucky, 1950; Gardel, 1956; Boillat and de Souza, 2004).

Surge tank with expansions Expansions permit diminishing total construction costs by saving excavation volume while ensuring waterway stability (Jaeger, 1977). There are two predominant forms of expansion, i.e. widening of the main surge shaft and chambers with tunnels. According to Jaeger (1977), the reduced area of the intermediate shafts have to be as small as possible to more rapidly accelerate (or decelerate) the flow in the pressure tunnel. Put another way, for the same water volume flowing within the pressure tunnel, the level in a surge tank with expansions would be higher than that in a simple surge tank. Thus, the pressure under the surge tank is higher and the dampening effect would be more quick (Vereide et al., 2015b). However, this reduced area should not be smaller than a certain limit that would cause excessive oscillations (Thoma, 1910). The unsteady waves of the expansion chambers have to be evaluated during filling and emptying of the surge tank (Montes and Delphin, 1983; Vereide et al., 2015b). Throttles may be placed either at the entrance of the surge tank (Hachem et al., 2013; Giesecke et al., 2014; De Cesare et al., 2015) or between the expansions (Steyrer, 1999; Vereide et al., 2015b).

Throttled surge tank Placing a throttle, at the entrance of surge tanks assists in ensuring there are similar effects as those from expansion chambers (by accelerating the dampening effect of the surge tank). When the water is flowing in (or out) the surge tank through the orifice, it is set up a higher (or lower) pressure that dampens the mass oscillations more effectively. Furthermore, the implementation of throttle fosters, without modifications of the surge tank volume, a moderate rise in the installed capacity of existing plants (Alligne et al., 2014; De Cesare et al., 2015). The orifice may produce either symmetric or asymmetric head losses (Steyrer, 1999; Gabl, 2012). The main disadvantage of a throttle is that the proportion of water hammer pressure entering in the pressure tunnel increases, and this is mainly because of the restriction of the area that stops a fraction of the water hammer before reaching the surge tank. Schleiss (2002) proposed that the presence of a throttle or surge tank orifice requires investigating both mass oscillation and water hammer together, as these two phenomena are always interconnected (Jaeger, 1933).

Differential surge tank This type of surge tank is often composed of a shaft and a larger chamber. In the case of total closure, the water level within the shaft rises rapidly until discharge into the main chamber. This permits there to be maximum levels with a minimum volume so as to reduce the discharge within the pressure shaft (Stucky, 1950).

Air-cushion surge tank This surge tank is constructed in a rock cavern filled with pressurized air and mainly found in Norway (Vereide et al., 2015b; Goodall et al., 1988). For the design and analysis of mass oscillations, the thermodynamic behavior of the pressurized air has to be considered (Vereide et al., 2015a; Vereide, 2016). Air-cushion surge tanks necessitate highly resistant rock with low permeability or a steel-lined chamber.

2.2.4 Stability criteria

Thoma's cross-section area: A third equation, following Eq. (2.6) and (2.7), could be arrived at if output power is assumed as a constant. This assumption was made by Thoma (1910). In this scenario, any variation in levels within the surge tank is counterbalanced by a variation of flow discharge of the system to produce exactly the same power.

Thoma (1910) developed a criterion for hydraulic stability of surge tanks with a integration of small oscillations from Eq.(2.6) and (2.7). Thoma's area ensures that small oscillations are stable. Indeed, if the level drops, the discharge rises. The level has to decrease again to elevate the discharge, etc. At the end, this first small oscillation can empty the surge tank, which cannot be acceptable. Thoma's area is defined as

$$A_{TH} = \frac{L_{PT} \cdot A_{PT}}{2g \cdot k \cdot H_n} \tag{2.8}$$

where L_{PT} is the length of the pressure tunnel, A_{PT} the cross-section area of the pressure tunnel , k the head losses coefficient between the reservoir and surge tank and H_n the net head between the surge tank and the downstream reservoir of the equilibrium (steady) state (Thoma, 1910; Stucky, 1950)

Practical recommendations: This stability criterion is widely used to design surge tanks all around the world, even if certain authors have doubted its validity (Jaeger, 1943; Stucky, 1950; Anderson, 1984). Evangelisti showed that, if the pressure shaft length is important compared to the pressure tunnel, Thoma's cross-section has to be multiplied by a correction factor (2.9) (Schleiss, 2002).

$$\alpha_{EV} = \frac{1 + \dfrac{L_{PT+PS} \cdot A_{PT}}{L_{PT} \cdot A_{tot}}}{1 - \dfrac{\Delta H_{tot}}{H - \Delta H}} \tag{2.9}$$

where A_{PT} is the cross-section of the pressure tunnel, a_{tot} the total cross-section of the pressure tunnel and shaft, ΔH_{tot} the total head losses between the upstream reservoir and the plant and ΔH the head losses within the pressure tunnel.

Furthermore, Jaeger (1960) and Schleiss (2002) posited that the minimal cross-section of the surge tank has to be increased by a safety factor γ_{TH}, from 1.5 to 2.0.

Note that other stability criterion exist, such as the Svee criteria including the velocity head that Thoma (1910) neglected (Leknes, 2016).

2.3 Throttled surge tanks[2]

For throttle surge tanks, taking into account the local head losses introduced at the entrance of the surge tank, Eq.(2.7) and (2.6) become Eq.(2.10).

$$\frac{L_{PT}}{gA_{PT}}\Big(A_{ST}\frac{d^2z}{dt'2}+\frac{dQ_T}{dt}\Big)z+(k_{PT}+1)\frac{v|v|}{2g}+k_{ST}\frac{v_{ST}|v_{ST}|}{2g}=0 \tag{2.10}$$

where: v is the flow velocity in the pressure tunnel, A_{PT} the pressure tunnel cross-section, LPT the pressure tunnel length, z the difference between the water level within the surge tank and the upstream reservoir level (counted positive when the level in the surge tank is higher than in the reservoir), ΔH_{PT} the total amount of head losses (frictional and local) between the reservoir and surge tank, A_{ST} the surge tank cross-section, Q_T the discharge flowing through the turbine and $\Delta H_{ST} = k_{ST}\frac{v_{ST}^2}{2g}$ is the head losses produced by the surge tank throttle.

Concerning surge tank stability, Piccolier (1966) and Montes (1980) theoretically demonstrated that the area of a throttled surge tank should not be smaller than the area required by Thoma's criterion. However, An et al. (2013b) numerically found that a throttle at the entrance can reduce Thoma's criterion . They introduced a correction factor for throttle surge tank, which is not equal to unity when there is not a throttle or an orifice at the surge tank entrance. Furthermore, according to Vereide et al. (2017), the placement of a throttle enhances the turbine power control.

2.3.1 Classifications of throttles

There are different ways to generate head losses at the entrance of surge tanks. The overall general denomination is throttle, but they are composed by different local geometrical devices:

- Orifices (Figure 2.2) are local geometry restrictions which may be circular, square, etc. with the same expansion conditions in all directions (see Section 3.1). However, asymmetrical orifice shapes permit the introduction of different head losses in the two flow directions. An orifice is mainly characterized by its contraction ratio β (Figure 2.2(right) , $\beta = 0.53$) and its chamfer angle θ. Table 2.1 features the different existing orifice throttles. The asymmetry of an orifice is defined case-by-case generally with higher head losses when the water flows out of the surge tank.
- Racks or bar-screen throttles are composed by a frame of spaced bars or beams that

---

[2] This section is based on a published conference paper: "Adam, N.J., De Cesare,G. & Schleis, AJ.(2016). Surge tank throttles for safe and flexible operation of storage plants. *Hydro Conference 2016.* Montreux, Switzerland" and a scientific paper accepted for publication "Adam, N. J., De Cesare, G., Nicolet, C., Billeter, P., Angermayr, A., Valluy, B., and Schleiss, A. J. (2017). Design of a throttled surge tank for the refurbishment by power increase of a high-head power plant (accepted for publication). Journal of Hydraulic Engineering.". The work presented hereafter is original and was performed by the author.

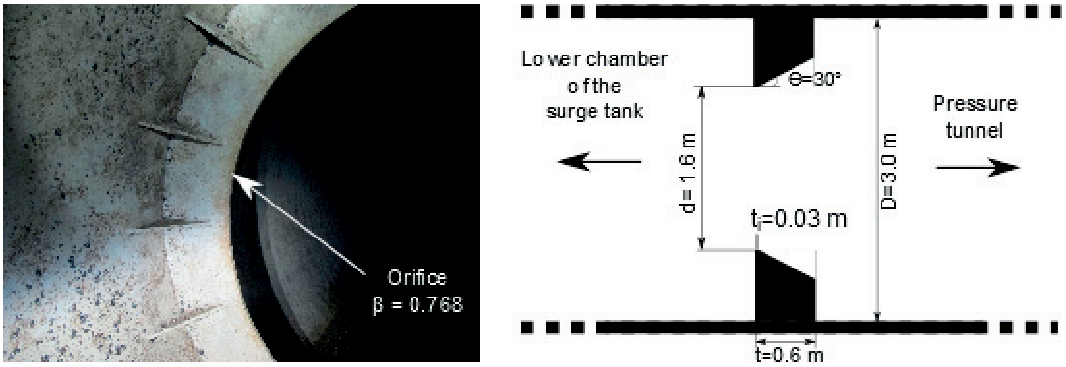

Figure 2.2 – (left) Picture of the orifice in the *Forces Motrices Hongrin-Léman* (hereafter, FMHL+) pumped-storage power plant (Hachem et al., 2013) and (right) drawing of the orifice of La Grande Dixence

Table 2.1 – Examples of existing orifice throttles

Symmetric orifices	Asymmetric orifices
Acaray (Paraguay)	Atdorf (Austria) (Schneider et al., 2014)
Etzelwerk (Switzerland)	Guadalami (Italy)
FMHL+ (Switzerland)	La Grande Dixence (Switzerland)
Lavey+ (Switzerland)	Obervermunt II (Austria) (Richter et al., 2015; Gomsrud, 2015)
	Wassen I (Switzerland)

are parallel or cross each other. Expansions interact and vary across either direction. This type of throttle was used in Amsteg (Billeter et al., 1996) or in Gondo (Figure 2.3, (De Cesare et al., 2015; Adam et al., 2017)).

- Vortex throttles, as defined in Steyrer (1999), are mostly utilized in Austria. As portrayed in Figure 2.4, this type of throttle is very complex with many different pipes and a rotating flow. Owing to its complexity and space requirements, it is not suitable for an extension or adaptation of an existing surge tank. Haakh (2003) carried out numerical simulations in order to study the water level evolution during mass oscillations for such a vortex throttle. Wójtowicz and Kotowski (2009) highlighted the influencing parameters of vortex throttles and presented empirical formulas evaluating head losses produced by them.

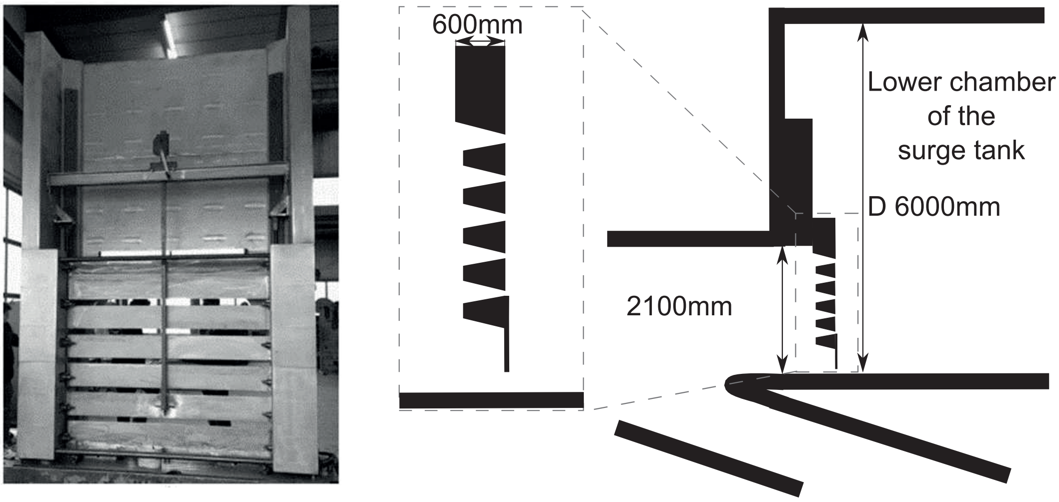
600mm
Lower chamber of the surge tank
D 6000mm
2100mm

Figure 2.3 – Gondo power plant rack throttle (Adam et al., 2017): (left) picture before the on-site installation and (right) cross-section

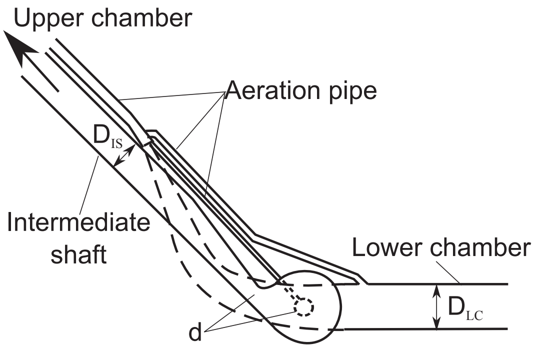
Upper chamber
Aeration pipe
D_{IS}
Intermediate shaft
Lower chamber
D_{LC}
d

Figure 2.4 – Longitudinal section of a typical vortex throttle between the lower and upper chamber (adapted from Steyrer (1999))

2.3.2 Throttle location

At least three different locations have been underscored in the literature (Figure 2.5):

- At the surge tank bottom (entrance) (De Cesare et al., 2015);
- In the connecting tunnel between two expansions chambers (Steyrer, 1999; Vereide et al., 2015b); and
- In a connecting tunnel between the surge tank and the pressure tunnel (Billeter et al., 1996; Hachem et al., 2013)

The throttling effect is instantaneous in the case that the throttle is placed at the bottom (Figure 2.5a) and within a connecting tunnel (Figure 2.5c) even for small oscillations in the lower part

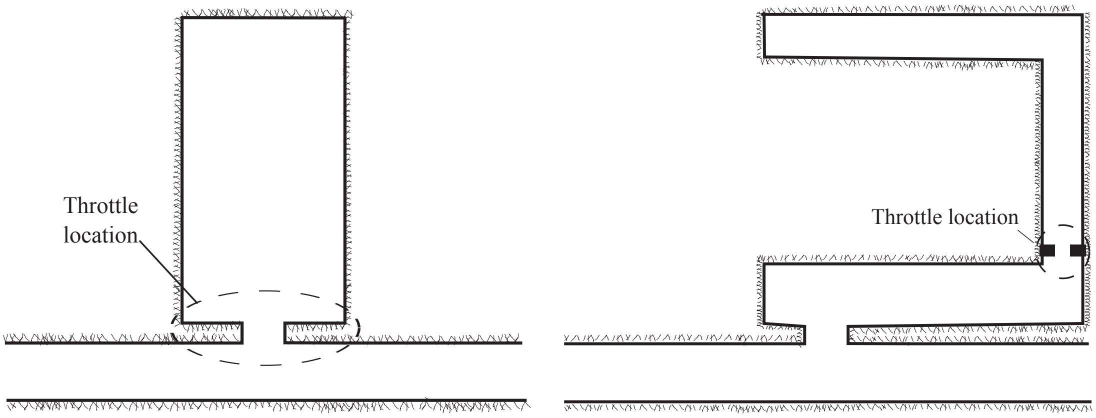

(a) At the surge tank entrance (b) Between two expansion chambers

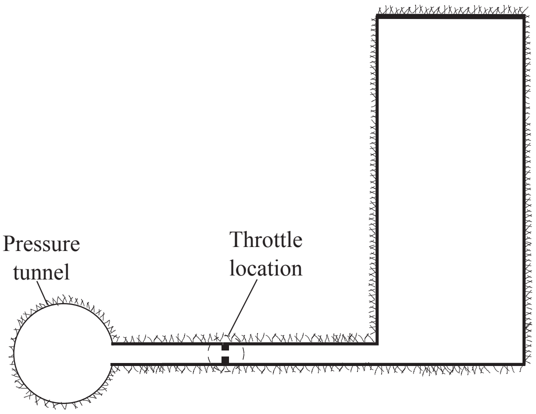

(c) In the connecting tunnel

Figure 2.5 – Schematic views of different locations of throttles according to the literature and existing power plants

of the surge tank. However, if the throttle is placed in an intermediate shaft connecting two expansions (Figure 2.5b), there is no impact from throttling on the lower expansion.

2.3.3 Previous studies performed on surge-tank throttles

Many studies have been performed on throttled surge tanks (Table 2.2). Throttling a surge tank, and thus implementing distinct head losses, might help handle extreme water levels (Chaudhry, 2014; De Martino and Fontana, 2012; Jaeger, 1977). Vereide et al. (2015b) and Gabl et al. (2014) noted there are at least three tools, i.e. physical scale models, 1D numerical simulations (Cao et al., 2013; Kim, 2010; Chaudhry, 2011; De Martino and Fontana, 2012) or 3D numerical simulations, to investigate the effects of throttle geometry on head losses. The required head losses of the throttle are often evaluated with 1D numerical simulations while geometry optimization is determined by either physical scale models, 3D numerical simulations or both. Table 2.2 lists several studies performed over the last few years on throttled surge tanks and throttle optimization. The majority of studies used physical scale models but a few performed prototype measurements to validate the physical model. For the numerical simulations, Table 2.2 indicates that either 1D transient models or 3D CFD models were utilized (only one single study used both forms of modeling).

Table 2.2 – Existing studies on throttled surge tanks: goal of the study and means of investigation (+: Done; *o*: not presented in the paper and –: not done)

			Numerical		
	Goal(s)	Physical scale	1-D	3-D (CFD)	Prototype validation
Klasinc and Bilus (2009)	Geometry optimization and flow visualization	+	-	+	-
Huber (2010)	Comparison	+	-	+	-
Kim (2010)	Throttle optimization	-	+	-	-
Gabl et al. (2011)	Throttle optimization	-	-	+	-
Nabi et al. (2016)	Throttle optimization	-	+	-	-
Richter et al. (2012)	Flow visualization	+	o	-	-
An et al. (2013b)	Geometry optimization	-	-	+	-
Hachem et al. (2013)	Geometry optimization	+	+	-	-
Kendir and Ozdamar (2013)	Geometry optimization	+	+	-	-
Alligne et al. (2014)	Geometry optimization and flow visualization	+	+	+	-
Schneider et al. (2014)	Geometry optimization and flow visualization	+	-	+	-
Meusburger (2015)	Geometry optimization and flow visualization	+	-	+	-
Adam et al. (2017)	Geometry optimization	+	+	-	+

2.4 Previous studies performed at the Laboratory of Hydraulic Constructions at EPFL

The Laboratory of Hydraulic Constructions (hereafter, LCH) has performed several physical model tests for surge-tank throttles. The main studies are reported in the following sections.

2.4.1 Kárahnjúkar (2007) (throttle in a pressure-tunnel branch)

This throttle, installed at the Kárahnjúkar hydropower plant (Middle-East of Iceland), is shown in Figure 2.6. The main characteristics of the throttle, which is a succession of sudden and gradual contractions (or expansion), are:

- diameter of the main pipe: $D = 6\,m$,
- smaller diameter of the throttle: $d = 2.1\,m$ and, thus, a contraction ratio $\beta = 0.35$,
- thickness of the throttle: $t \approx 48.8\,m$ and, thus, a thickness ratio $\alpha \approx 8$,

Based on the large thickness of the throttle, it can be classified as a plug and not as an orifice. The head losses are higher in the normal than in the reverse flow condition (Figure 2.6). The major proportion of head loss production in the reverse flow condition is logically created through the sudden expansion. The asymmetry ratio, which is the ratio between the smallest and the largest head loss coefficients, of this throttle is 0.19. For the physical modeling, a geometrical scale of $1:20$ was used with a Froude similarity. This scale ensured a minimum Reynold number of 10^5 in order to be independent from it. Seven discharges were employed to determine the head loss coefficients.

2.4.2 Lavey + (2011)

The throttle placed at the entrance of the surge tank of the Lavey hydropower plant is comprised of a local contraction of the surge-tank entrance, however, there is no blockage at the bottom of the throttle. Even if the throttle is symmetric, the local configuration, between the pressure tunnel, pressure shaft and the surge tank, induces asymmetric behavior. The head losses are higher for the water flowing out of the surge tank with an asymmetry ratio of around 0.7. The main characteristics of the throttle were:

- area of the main pipe (connection gallery to the surge tank): $A_{th,r} \approx 47.8\,m^2$,
- area of the throttle: $A_{th,o} = 16.8\,m^2$ and, thus, an equivalent contraction ratio of $\beta_{eq} = 0.59$,
- thickness of the throttle: $t = 0.5\,m$ and, hence, $\alpha \approx 0.064$.

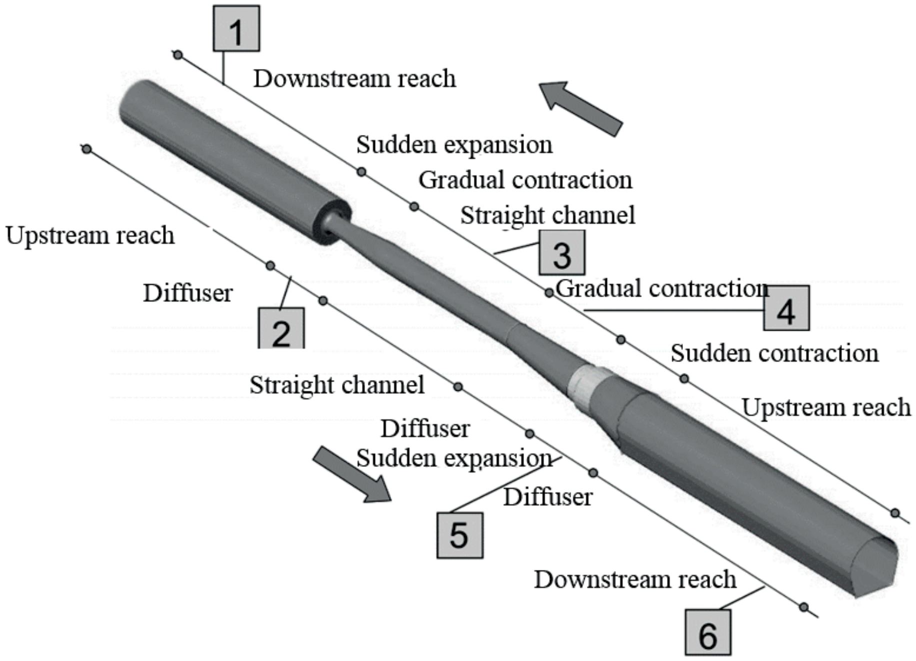
1
Downstream reach
Sudden expansion
Gradual contraction
Straight channel
Upstream reach
Diffuser
3
2
Gradual contraction
4
Sudden contraction
Straight channel
Upstream reach
Diffuser
Sudden expansion
Diffuser
5
Downstream reach
6

Figure 2.6 – Throttle of the Kárahnjúkar hydropower plant

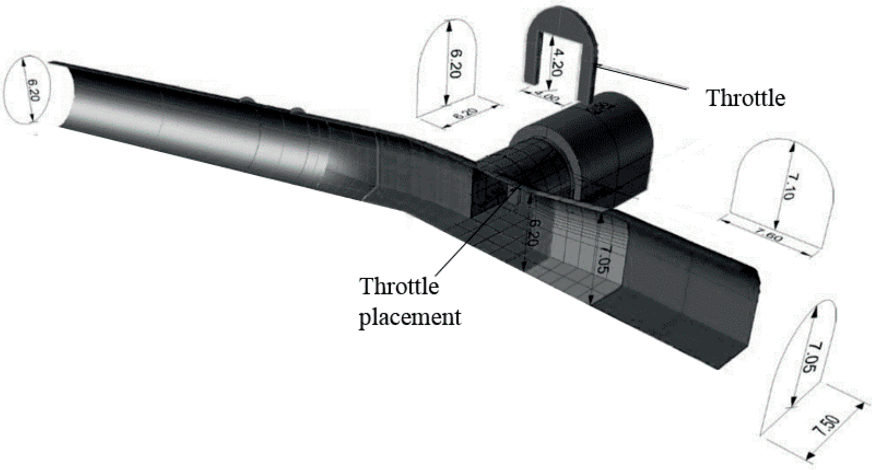
6.20
6.20
6.20
4.20
4.00
Throttle
7.10
7.60
6.20
7.05
Throttle
placement
7.05
7.50

Figure 2.7 – Throttle at the entrance of the surge tank of the Lavey hydropower plant

For the physical modeling, a geometrical scale of 1 : 32.2 was used with a Froude similarity that ensured an independence of the Reynold number as its minimum value is at 10^5.

2.4.3 FMHL + (2012)

The Forces Motrices Hongrin Léman (FMHL) decided to double the installed generation capacity of the power plant located along the shore of Lake Geneva. A new surge tank connected to the former one was added to this pumped-storage plant, with a net head of 883 m. An orifice was placed into the connecting tunnel (Figure 2.8) so as to improve the behavior of these two surge tanks. The experimental design of the orifice was performed at LCH of EPFL (Figure 2.8). The main characteristics of the orifice were:

- diameter of the connecting tunnel: $D = 2.2\,m$;
- inner diameter of the throttle: $d = 1.69\,m$ and, thus, a contraction ratio of $\beta = 0.77$; and
- thickness of the throttle: $t \approx 0.09\,m$ and, hence, a thickness ratio of $\alpha \approx 0.04$.

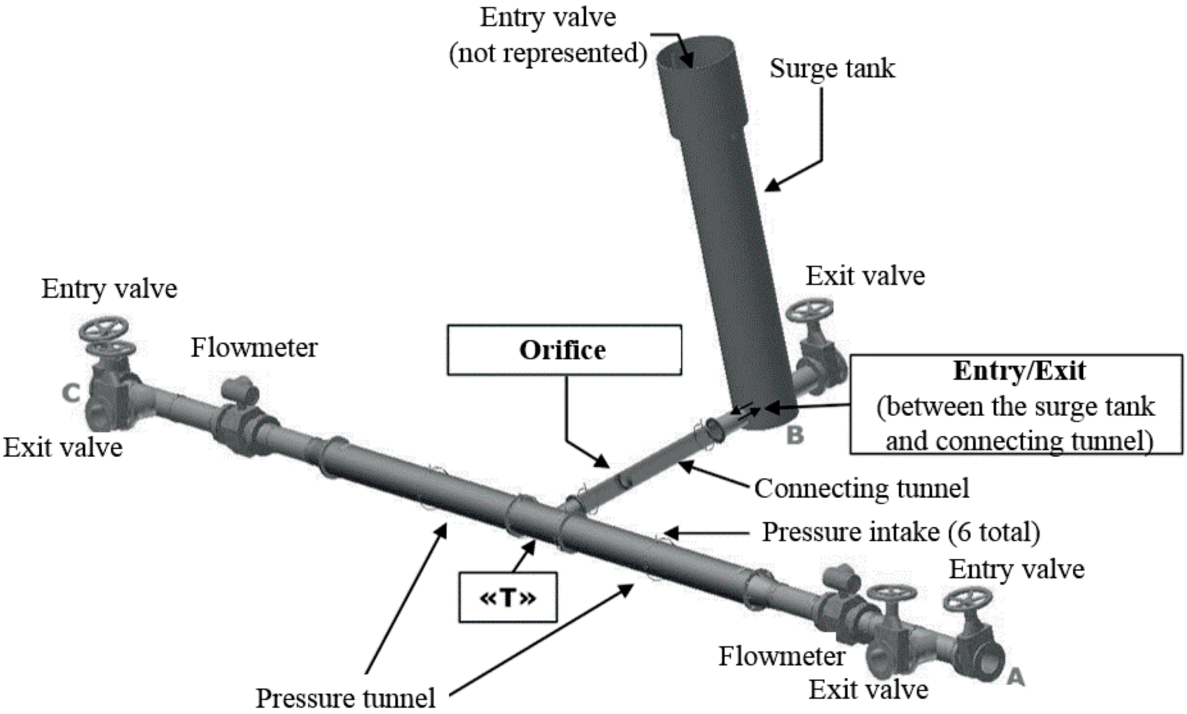
Entry valve
(not represented)
Surge tank
Exit valve
Entry valve
Flowmeter
Orifice
C
Entry/Exit
(between the surge tank
and connecting tunnel)
Exit valve
B
Connecting tunnel
Pressure intake (6 total)
Entry valve
«T»
Flowmeter
Exit valve
A
Pressure tunnel

Figure 2.8 – Physical model of the new FMHL surge tank at LCH in EPFL (Hachem et al., 2013)

For the physical modeling, a geometrical scale of 1 : 18.2 was used with a Froude similarity. This scale ensured a minimum Reynold number of 10^5 in order to be independent of it.

2.4.4 Gondo (2014)[3]

The refurbishment of the existing Gondo hydropower plant would facilitate an increase in the existing installed generation capacity with the renewal of the third turbine installed during the 1980s. This would result in an increase within the discharge flowing in the headrace system from 12 m^3/s up to 14.7 m^3/s, with a 470 m head between the upstream reservoir and the Gondo power plant. The existing headrace system had to be carefully verified with regards to the dynamic pressure by means of a 1-D numerical transient model.

This numerical transient model was the result of a throttle producing a head loss coefficients of 40 for the water flowing in and 30 for the water flowing out of the surge tank. Physical experiments were performed on two different throttle geometries, i.e. a gate and a rack throttle (Figure 2.9). It was necessary to distribute the head loss on the height as the gate throttle did not produce enough head losses. Nine different throttle geometries, i.e. three gate throttles and six rack throttles were tested.

The main characteristics of the final throttle (Figure 2.3) are:

- area of the entrance section of the surge tank: $A_{th,r} = 3.94\,m^2$;
- opening area of the throttle: $A_{th,o} = 0.735\,m^2$ and, thus, an equivalent contraction ratio of $\beta_{eq} = 0.43$;
- thickness of the throttle: $t \approx 0.32\,m$ and, thus, a thickness ratio of $\alpha \approx 0.143$; and
- angle of $\theta = 12°$.

The asymmetry ratio between the water flowing in and out of the surge tank is 0.75.

For the physical modeling, a geometrical scale of 1 : 12 is used with a Froude similarity. The minimum Reynold number in the reference cross-section is 10^5 to ensure an independence of it.

---

[3] This subsection is based on a scientific paper accepted for publication “Adam, N. J., De Cesare, G., Nicolet, C., Billeter, P., Angermayr, A., Valluy, B., and Schleiss, A. J. (accepted for publication). Design of a throttled surge tank for the refurbishment by power increase of a high head power plant. Journal of Hydraulic Engineering.”. The experimental work presented hereafter is original and was performed by the author.

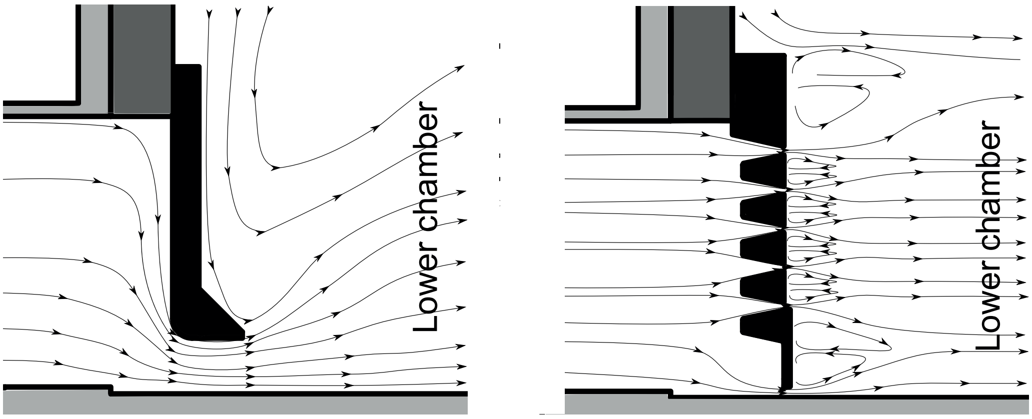
Lower chamber
Lower chamber

(a) Gate throttle (b) Rack throttle

Figure 2.9 – The two different Gondo throttle geometries (Adam et al., 2017)

3 Literature review

As seen in Section 2.3.1, there are at least three different types of throttle used in throttled surge tanks. In this thesis, we focus on orifices used as throttles. Orifices have the simplest throttle geometry, allowing the perform of different analyses to highlight systematically the influence of all the geometrical parameters.

3.1 Use of orifices

Orifices introduce a sudden and local variation of the pipe cross-section. The discharge flowing through orifices, with a shape that was defined by ISO (2003) is deduced with the pressure drop between the upstream orifice pressure and the vena contracta pressure.

3.1.1 Flow meters

Orifices have largely been studied for the application of flowmeters, e.g. Reader-Harris (2015); ISO (2003); Reader-Harris et al. (1995) with the geometrical or flow limitations shown in Table 3.1. Different types of pressure tappings exist for the evaluation of the discharge as depicted in Figure 3.1.

ISO (2003) determined Equ. (3.1), which yields the discharge related to the differential pressure in the limitations given of Table 3.1.

$$Q = \frac{C_D}{\sqrt{1-\beta^4}}\varepsilon\rho\frac{\pi}{4}d^2\sqrt{2\Delta p} \tag{3.1}$$

where: Q is the discharge flowing through the orifice, C_D the discharge coefficient, $\beta = d/D$ the contraction ratio (Figure 3.1), ε the expansion factor taking into account the compressibility of the fluid ($\varepsilon = 1$ for incompressible flow), ρ the water density, d the inner orifice diameter, and Δp the differential pressure (Figure 3.1).

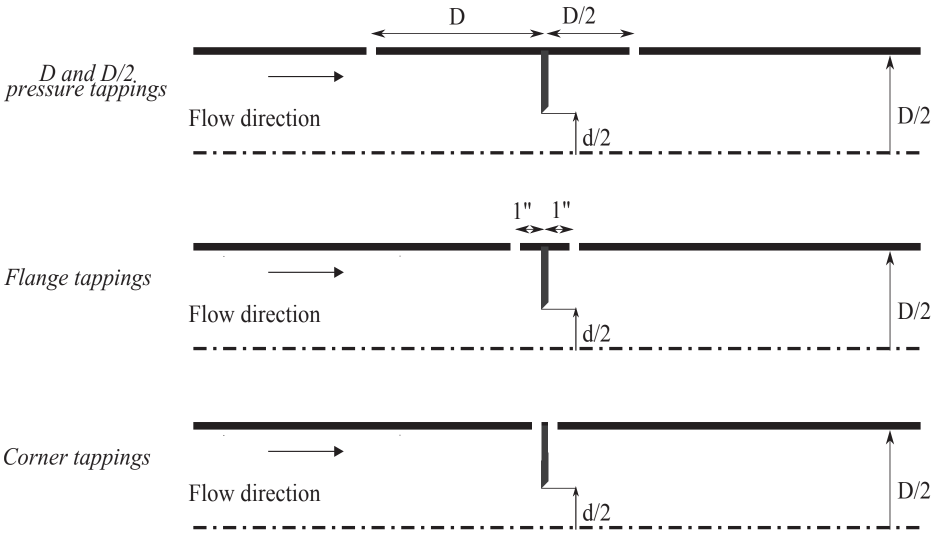

Figure 3.1 – The three different pressure tappings covered by the ISO (2003) (adapted from ISO (2003)).

Table 3.1 – Limitations of flowmeter orifices defined by the ISO (2003)

Parameter	Corner or D and D/2 pressure tappings	Flange tapping
Inner orifice diameter	$d \geq 12.5\,mm$	
Pipe diameter	$50\,mm \leq D \leq 1000\,mm$	
Contraction ratio	$0.1 \leq \beta \leq 0.75$	
Reynolds number	$Re_D \geq 5000$ for $0.1 \leq \beta \leq 0.56$ or $Re_D \geq 16000\beta^2$ for $\beta > 0.56$	$Re_D \geq 5000$ and $Re_D \geq 170\beta^2 D$

For standard orifices, the discharge coefficient, C_D, is given in ISO (2003) for different pipe diameter, D, Reynolds number, Re, and contraction ratios, β. Reader-Harris et al. (1995) developed experimentally empirical equations for the discharge coefficient, C_D, depending on the contraction ratio, β, and the Reynolds number, Re_D.

3.1.2 Throttling device or producer of head losses

As explained in Chapter 2, the implementation of an orifice is an efficient way for throttling an existing surge tank, which protects pressure tunnels from pressure waves produced by discharge variations in hydroelectric power plants (Hachem et al., 2013; Alligne et al., 2014; Gabl et al., 2011). Orifices could have different shapes, such as those defined by ISO (2003) or other shapes tested either with physical (Gabl et al., 2014; Gabl, 2012; Huber, 2010; Malavasi and Messa, 2011; Malavasi et al., 2015) or numerical experiments (Malavasi and Messa, 2011; Gabl, 2012; Huber, 2010).

Urner (1997) linked this pressure drop with the total produced head losses.

3.2 Different flow types through orifices

Figure 3.2 depicts the various possible types of flow through an orifice depending on its thickness.

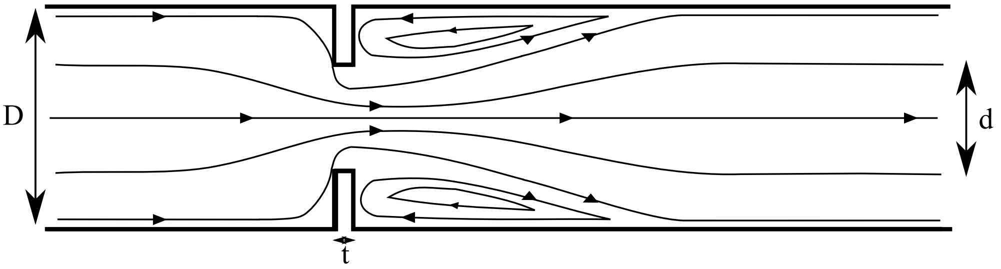

(a) Orifice Flow, $\alpha < \alpha_c$

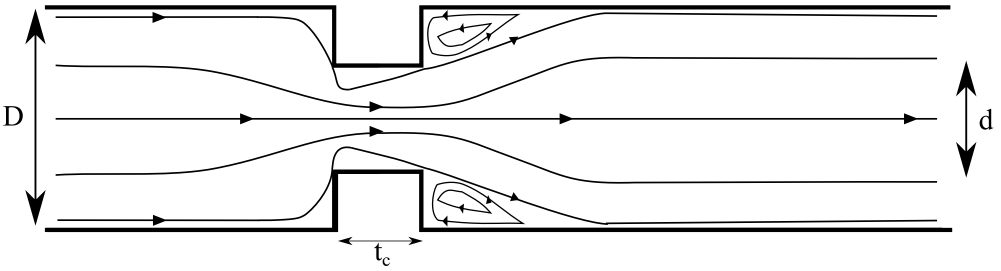

(b) Critical flow, $\alpha = \alpha_c$

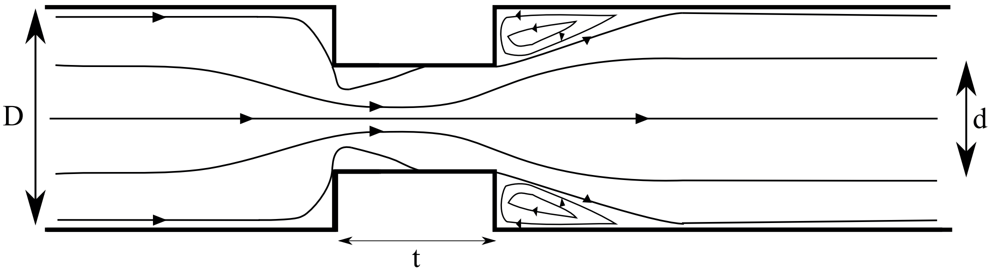

(c) Plug Flow, $\alpha > \alpha_c$

Figure 3.2 – Different flow types depending on the orifice thickness ratio α (defined in Figure 3.3)

The critical thickness, t_c (and the corresponding dimensionless parameter, α_c) is the required thickness for which the orifice jet reattaches at the end of the orifice. For small thicknesses, the contraction before and the expansion of streamlines after the orifice are interdependent and influence each other. On the contrary, for plug flow, there is an attachment point where the water jet is connected to the inner orifice wall. Tian et al. (2009) and Fossa and Guglielmini (2002) defined a plug flow when $t > 0.5D$ while Wu and Ai (2010) performed numerical simulations to fit an empirical function depending on β, α and Re. Wu and Ai (2010) showed that α_c increases with Re when β decreases.

Gan and Riffat (1997) showed that the thinner an orifice is, the higher the head losses are. However, the minimum head losses seem to be around $\alpha/\beta = 1\ldots1.5$ (Gan and Riffat, 1997; Fratino and Pagano, 2011). The head losses drop to approximately 25% from $\alpha/\beta = 0.5$ to 1.5. Fratino and Pagano (2011) demonstrated that for thick plug orifices the total head losses have to take into account friction losses along the plug orifice, as evaluated using Darcy friction, f, and the equivalent sand roughness, ε_i (Brown, 2002).

3.3 Head loss coefficient

The head loss coefficient, k, is the ratio between the head losses, ΔH, produced by an orifice (or any changes in geometry or flow direction) and the kinetic energy, $\frac{v^2}{2g}$, in a reference section. This reference section is usually the surrounding cross-section; hereafter the reference cross-section is the main pipe cross-section.

$$\Delta H = k \cdot \frac{v_D^2}{2g} \tag{3.2}$$

Figure 3.3 features the two main orifice geometries, used in this research study. Each chamfer orifice (Figure 3.3a) is characterized by four geometrical parameters: β the contraction ratio, α, the thickness ratio, α_i, the inner thicknes ratio and the chamfer angle, θ. Each rounded orifice (Figure 3.3b) is also characterized by four geometrical parameters : β, the contraction ratio, α_i, the inner thickness ratio and the elliptical semi-axes, α_a and β_b.

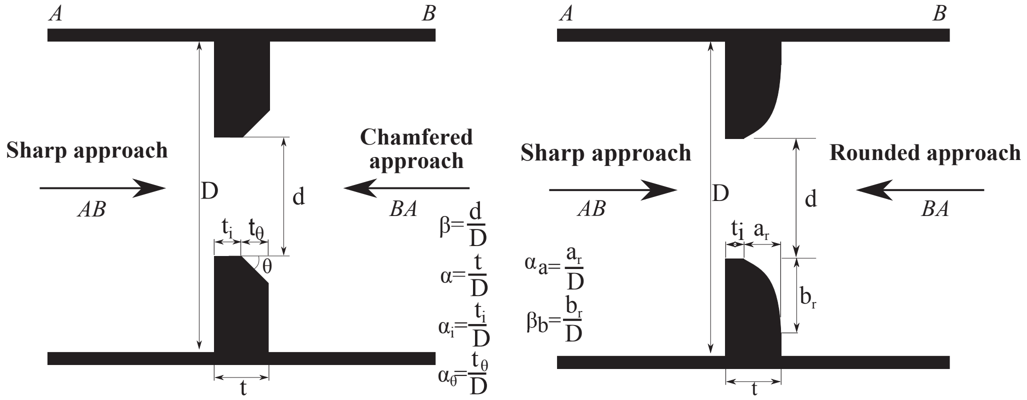
A
B
Sharp approach
AB
D
d
t_i
t_θ
θ
t
Chamfered approach
BA
$\beta=\frac{d}{D}$
$\alpha=\frac{t}{D}$
$\alpha_i=\frac{t_i}{D}$
$\alpha_\theta=\frac{t_\theta}{D}$
A
B
Sharp approach
AB
D
d
t_i
a_r
b_r
t
Rounded approach
BA
$\alpha_a=\frac{a_r}{D}$
$\beta_b=\frac{b_r}{D}$

(a) Chamfer orifice

(b) Rounded-edged orifice

Figure 3.3 – Chamfer and rounded orifices with a sharp side employed in this research study

The contraction ratio, β, is the most critical parameter impacting the head losses produced by an orifice (Idel'cik, 1969; Blevins, 1984; Şahin, 1989). The head loss coefficient is inversely proportional to β^4 and α (Jianhua et al., 2010; Blevins, 1984). Many authors have put forth empirical relationships for the estimation of the head loss coefficient.

Idel'cik (1969) offered different head losses evaluations as a function of β, α and the orifice shape for both flow directions. Idel'cik (1969) defined head loss coefficients either for upstream, orifice or downstream cross-sections. Herein, the reference cross-section is always defined as the upstream one. The following points are a summary of the empirical formulas provided by Idel'cik (1969):

- Eq.(3.3) presents a formula of head loss coefficient for an orifice plate and plug orifice respectively, which is valid for a symmetric device ($\theta = 0°$) and for $\mathsf{Re}_d > 10^5$:

$$k = \frac{\left(k' + \tau\sqrt{1-\beta^2}\right) \cdot (1-\beta^2) + (1-\beta^2)^2 + k_i}{\beta^4} \tag{3.3}$$

  where k' depends on the upstream orifice shape ($k' = 0.5$ for a square-edged orifice or $k' \approx 0.4$ for a 45-degree-chamfer orifice), τ depends on α ($\tau = 1.35$ for a thin orifice of $\alpha << 1$ or $\tau \approx 0$ for a thicker orifice of $\alpha > 2$) and k_i represents friction losses evaluated with the Darcy-Weisbach equation for the inner orifice pipe, $k_i = f \cdot \alpha_i$, where f depends on the inner orifice roughness, ε_i.

- For chamfer orifices, Eq.(3.4) generates head loss coefficients for the sharp and chamfer flow approaches. The formula is valid for thin orifices ($\alpha/\beta \leq 0.015$ and $\alpha_i = 0$) and for $\mathsf{Re}_d > 10^5$. For the shape approach with an angle, only angles, θ, between 20° and 30° were taken into account. No information was given on the radius for the rounded approach.

$$k = \frac{(1 + \tau\sqrt{1-\beta^2} - \beta^2)^2}{\beta^4} \tag{3.4}$$

  where $\tau = 0.707$ for sharp approach and, for shape approach, τ varied from 0.678 to 0.4 as a function of α and τ varied from from 0.663 to 0.245 as a function of α.

Blevins (1984) gave a simplified relation for a thin square-edged orifice that is valid for $\mathsf{Re}_D > 10^4$ and $\alpha \in [0.01, 0.02]$:

$$k = \frac{\eta}{C^2}\frac{1-\beta^4}{\beta^4} \tag{3.5}$$

where η is a function of β ($\eta = 0.93$ for $\beta = 0.2$ and $\eta = 0.38$ for $\beta = 0.8$) and C depends on β and Re($C = 0.6$ for $\mathsf{Re}_D > 10^5$)

Urner (1997) found equation (3.6) for standard orifices by developing a head loss evaluation for an ideal nozzle. The field of application was the same as defined by ISO (2003) (see Table 3.1).

$$k = \left[\frac{\sqrt{1-\beta^4(1-C^2)}}{C_D\beta^2} - 1 \right]^2 \tag{3.6}$$

where: k is the head loss coefficient (ξ in Urner (1997)), β the contraction ratio and C_D the discharge coefficient.

Jianhua et al. (2010) fit a new equation depending on α and β (equation (3.7)), which is valid for $\alpha \in [0.05, 0.25], \beta \in [0.4, 0.8]$ and $\mathrm{Re}_D > 10^5$.

$$k = \frac{0.7418}{\alpha^{0.1142}} \left(\frac{3.196}{\beta^4} - \frac{5.646}{\beta^2} + 2.45 \right) \tag{3.7}$$

Other authors, e.g. Malavasi et al. (2012); Zeghloul et al. (2017); Malavasi and Messa (2011); Roul and Dash (2012), have evaluated the maximum pressure drop in the *vena-contracta*, that Urner (1997) linked to the head loss coefficient as shown with Eq.(3.8). Theoretically, the head loss coefficient could be found from the pressure drop under the assumption of a standard discharge coefficient (defined by ISO (2003))

$$\frac{\Delta H}{\Delta p} = \frac{\sqrt{1-\beta^4(1-C_D^2)} - C_D\beta^2}{\sqrt{1-\beta^4(1-C_D^2)} + C_D\beta^2} \tag{3.8}$$

where: ΔH is the head losses, Δp the pressure drop in the vena contracta, β the contraction ratio and C_D the discharge coefficient.

3.4 Recirculation or influence length

A minimum straight pipe length upstream and downstream of an orifice should be ensured to decrease the uncertainties of the discharge coefficient of a standard orifice (ISO, 2003). According to ISO (2003), the downstream straight should be longer than $4D$ if $\beta = 0.2$ to $8D$ for $\beta = 0.75$ in order to have no additional uncertainties. This length could be diminished by 2 if a 5% uncertainty is accepted. Furthermore, these values are 60% higher than those provided by the *American Petroleum Institute* (Reader-Harris, 2015). These lengths can be taken only as an order of magnitude of the zone that influences an orifice.

Jianhua et al. (2010) showed that the recirculation length does not depend on the Reynolds number Re (for $\mathrm{Re} \in [1.8\cdot 10^5, 2.76\cdot 10^6]$). Figure 3.4, created by Jianhua et al. (2010), depicts the evolution of l_r as a function of the contraction ratio, β, and the thickness ratio, α. The recirculation length, l_r, increases if α or β decreases. The recirculation length, l_r, tends logically to 0 when β tends to 1, a pipe without an orifice.

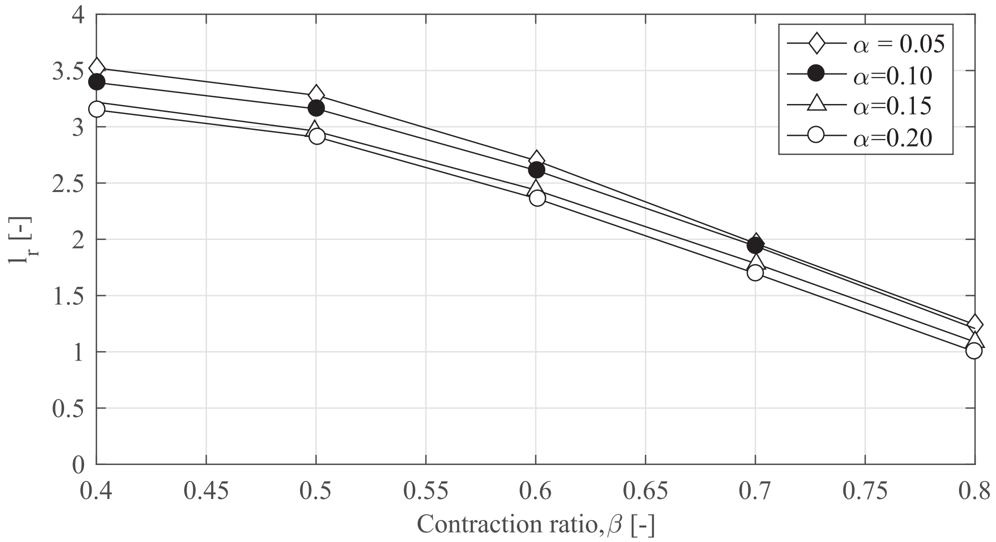

Figure 3.4 – Recirculation length, l_r, as a function of the contraction ratio, β, and the thickness ratio, α (adapted from Jianhua et al. (2010))

3.5 Transient head losses

For fast transient flows, the behaviour of losses, in general friction losses, is often non-linear (Ferràs Segura, 2016). However, the approximation with steady losses seems to be still sufficient, with a 1-D modeling, for the first oscillation that yield the maximum and minimum pressures (Chaudhry, 2014). However, the pressures for other oscillations or obtained for multiple operations, e.g. an emergency shut-down following a turbine start or a restart following a load rejection, are less reliable.

Many investigations, which have been performed on unsteady head (friction) losses during water hammer, have employed several methods taking into account these effects in transient flow computations. They can be classified into three (Chaudhry, 2014), four (Ferràs Segura, 2016) or six (Bergant et al., 2001) categories. A decomposition between steady and transient head losses, as in Eq.(3.9), is frequently adopted in the literature.

$$\Delta H = \Delta H_s + \Delta H_t \tag{3.9}$$

According to Bergant et al. (2001) and Chaudhry (2014), the transient head losses, ΔH_t, is modeled by either instantaneous-acceleration-based (IAB) model, i.e. the instantaneous mean flow velocity v or with the instantaneous acceleration, $\frac{\partial v}{\partial t}$, and/or with the convective acceleration $\frac{\partial v}{\partial x}$; or convolution methods employing instantaneous mean flow velocity and weighted past flow velocity changes; or quasi-two-dimensional (2D) model, which provides accurate results but is time-consuming. The typical expression for ΔH_t evaluated with IAB methods are shown in Eq.(3.10). This research project focused only on local head losses. Thus, in Eq.(3.10), the partial derivative, $\frac{\partial v}{\partial x}$, can be neglected.

$$\Delta H_t = \frac{1}{g}\left[k_{t,t}\frac{\partial v}{\partial t} + k_{t,x}\frac{v|v|}{v^2}\left|a\frac{\partial v}{\partial x}\right|\right] \tag{3.10}$$

where: $k_{t,t}$ and $k_{t,x}$ should be equal or different.

Schönfeld (1949) assessed the transient effects of head losses produced in fully turbulent flows in pipes or in open canals. This resulted in a correction of the inertial term, $\frac{dQ}{dt}$ (Similar to Eq.(3.11)).

Concerning orifices, Yamaguchi (1976) gave an evaluation of the term, l_e, based on the concept of equivalent length for air flows.

$$\Delta H = k_s \cdot \frac{v_d^2}{2g} + \frac{l_e}{gA_d}\frac{dQ}{dt} \tag{3.11}$$

where: k_s refers to the steady head losses relative to the orifice area, v_d the average flow velocity in the orifice and t_e the equivalent thickness of the orifice defined as in Eq.(3.12).

$$l_e = t + d \cdot (\frac{8}{3}\pi - 1.06 \cdot \beta) \tag{3.12}$$

where d is the orifice diameter and β the contraction ratio.

3.6 Cavitation

When the discharge flowing through an orifice increases, the head losses produced by the orifice cover three main regions (Malavasi and Messa, 2011). In the first region ($\mathrm{Re}_D < 10^4$), the Reynolds number in the pipe, Re_D, have a large influence on head losses (Idel'cik, 1969). In the second region ($\mathrm{Re}_D > 10^4$), for fully turbulent flows (Idel'cik, 1969; Blevins, 1984), the head losses do not depend on the Reynolds number. Finally, for high Re_D, the head losses increase because of cavitation.

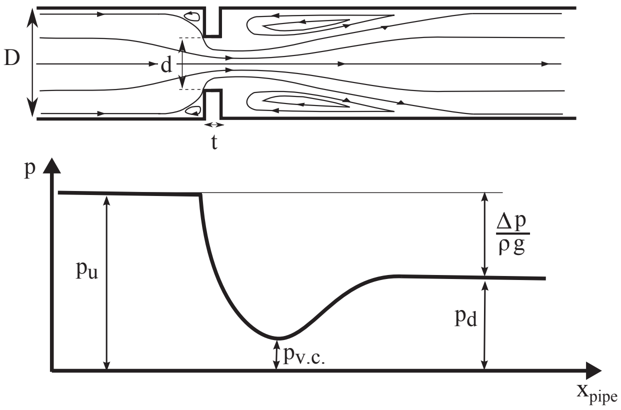

Figure 3.5 – Pressure line for water flowing through orifice

As defined in Tullis (1989):

> *"Cavitation consists of rapid vaporization and condensation of a liquid. [...] It normally occurs when liquid at constant temperature is subjected to vapour pressure either by a static or a dynamic pressure"*

Cavitation can cause damage to the structures of the throttle itself or to the pipe but also can significantly increase head losses. This sudden rise could have the same effect as valve closure and induce a water hammer within the pressure tunnel.

3.6.1 Cavitation number

According to Malavasi et al. (2015), there are various definitions for the cavitation number as shown in Eq.(3.13) (Ferrarese et al., 2015), (3.14) (Tullis, 1989) and (3.15) (Yan and Thorpe, 1990) :

$$\sigma = \frac{p_u - p_{vg}}{p_u - p_d} \tag{3.13}$$

where: p_u is the upstream pressure, p_d the downstream pressure and p_{vg} the vapour pressure.

$$\sigma_d = \frac{p_d - p_{vg}}{p_u - p_d} = \sigma - 1 \tag{3.14}$$

$$\sigma_{vg} = \frac{p_u - p_{vg}}{\frac{1}{2}\rho v^2} = Eu \cdot \sigma \tag{3.15}$$

where: ρ is the fluid density, v the mean pipe velocity and Eu the Euler number defined as follows: $Eu = \frac{p_u - p_d}{1/2 \rho v^2}$

In Eqs.(3.13) to (3.15), the positions of the upstream and downstream pressures have varying definition:

- p_u is the upstream pressure taken at just upstream of the orifice (Tullis, 1989), at $1D$ upstream (Yan and Thorpe, 1990) or at $2D$ upstream (Ferrarese et al., 2015)
- p_d is the downstream pressure taken at $6D$ downstream of the orifice (Ferrarese et al., 2015), at $10D$ downstream (Numachi et al., 1960; Tullis, 1989) or at $15D$ downstream (Yan and Thorpe, 1990).

In this study, the definition given by Ferrarese et al. (2015) was used. The values coming from other authors (Numachi et al., 1960; Tullis, 1989; Yan and Thorpe, 1990; Maynes et al., 2013) will be transformed with the relation from Eqs.(3.14) and (3.15).

3.6.2 Cavitation regimes

There are different cavitation regimes (Figure 3.6) (Tullis, 1989; Instrument Society of America, 1995):

- Regime I: No cavitation;
- Regime II: Incipient cavitation number σ_i commences the regime till light cavitation, which ends at the critical cavitation number, σ_c. According to Numachi et al. (1960), small cavitation bubbles appear in the flow and are visible with human eyes;
- Regime III: Covers light till the maximum intensity of cavitation, where there is large acceleration of the sound pressure levels and cavitation takes place from the orifice edges (Numachi et al., 1960). It ends with the maximum vibration (or choking) cavitation number, σ_{mv}; and
- Regime IV: Choking cavitation with a drop in intensity where the pipe is almost filled with cavitation bubbles.

According to Tullis (1989), limiting the flow of regime I is very conservative. The life of an orifice in regime II would not decrease. However, in the work presented here, the goal is to make a comparison between orifice geometries producing the same amount of head losses in each flow direction rather than study the effect of cavitation on head loss coefficients (see explanation in Chapter 8).

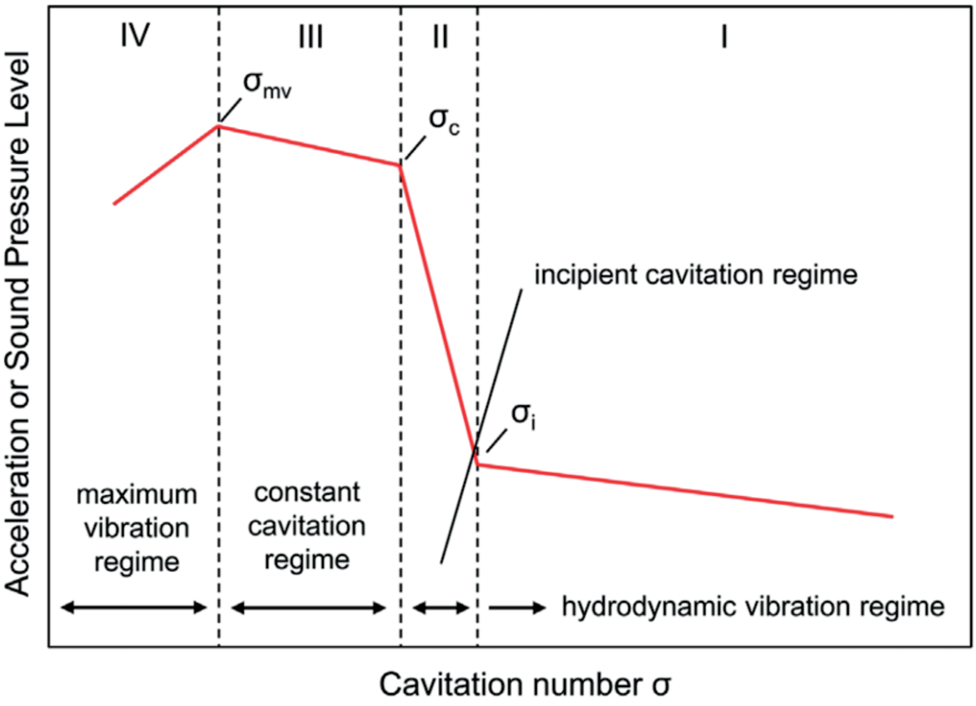
IV
III
II
I
σ_{mv}
σ_c
incipient cavitation regime
σ_i
maximum vibration regime
constant cavitation regime
hydrodynamic vibration regime
Acceleration or Sound Pressure Level
Cavitation number σ

Figure 3.6 – Identification of the cavitation regimes and limits (adapted from Instrument Society of America (1995) by Malavasi et al. (2015))

3.6.3 Incipient cavitation

As described in Section 3.6.2, the incipient cavitation is the limit between no cavitation and light cavitation. As explained in Section 3.6.1, there are different definitions of the cavitation number. The values of the incipient cavitation number are adapted to the definition given by Eq.(3.13).

Figure 3.7 portrays the relation of the incipient cavitation numbers, σ_i, evaluated in previous studies (Numachi et al., 1960; Tullis, 1989; Yan and Thorpe, 1990; Maynes et al., 2013; Ferrarese et al., 2015) and the contraction ratio, β.

The incipient cavitation number, σ_i, seems globally to increase when β increases. Depending on the author, there is major variation in σ_i for a given β. Tullis (1989) stated that cavitation can be highly affected by scale effects. However, here, it does not seem to be the cause of the discrepancies as the pipe diameter is more or less the same (Figure 3.7). Moreover, the two external diameters give more or less the same σ_i (Numachi et al., 1960; Yan and Thorpe, 1990).

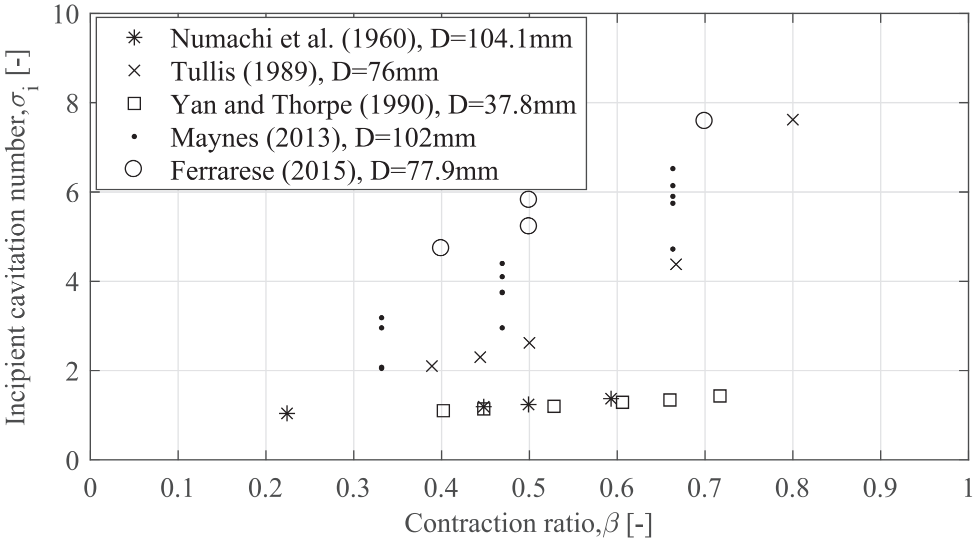

Figure 3.7 – Comparison of previous studies focusing on the evaluation of the incipient cavitation number σ_i as a function of the contraction ratio β

3.6.4 Prediction of the incipient cavitation number

Method based on physical characteristics A variety of authors have developed methods based on the physical characteristics of orifices, such as the contraction ratio, β, the discharge coefficient, C_D, or the orifice contraction coefficient C_C (Kuroda et al., 1978; Sánchez et al., 2008; Malavasi et al., 2015).

Method based on CFD simulations Ferrarese et al. (2015) proposed a new method for the prediction of the incipient cavitation number, σ_i. The pressure involved in the evaluation of σ is based on numerical simulations of single-phase incompressible flow. They showed that a single discharge CFD simulation is sufficient to predict σ_i. However, the three discharges, which are defined in Section 4.1.3, are utilized in this study to predict σ_i. Eq.(3.16) defines the incipient cavitation number, σ_i, with the position of each section in Figure 3.8:

$$\sigma_i = \frac{p_u - p_{vg}}{p_u - p_d} \tag{3.16}$$

where: p_u is the upstream pressure, p_d the downstream pressure and p_{vg} the vapour pressure.

In a single-phase incompressible flow simulation, without any model of cavitation, the pressure field, p^*, is always defined by imposing a fixed pressure somewhere in the computed domain, generally in the downstream section. In other words, a constant, p_c, can be added or subtracted from the domain without changing the value of the other flow variables, e.g.

velocities. Eq.(3.17) reflects the infinite possibilities of a pressure field, $\tilde{p}$.

$$\tilde{p} = p^* + p_c \tag{3.17}$$

With the method developed by Ferrarese et al. (2015), the constant, p_c, was chosen in order to have the minimal pressure of the pressure field equal to the vapor pressure, p_{vg}. This condition leads to having the apparition of cavitation regime II (Section 3.6.2) and the first bubbles of cavitation. This transformation is therefore given by Eq.(3.18). The incipient cavitation number, σ_i, can thus be predicted by Eq.(3.19) as shown in Ferrarese et al. (2015).

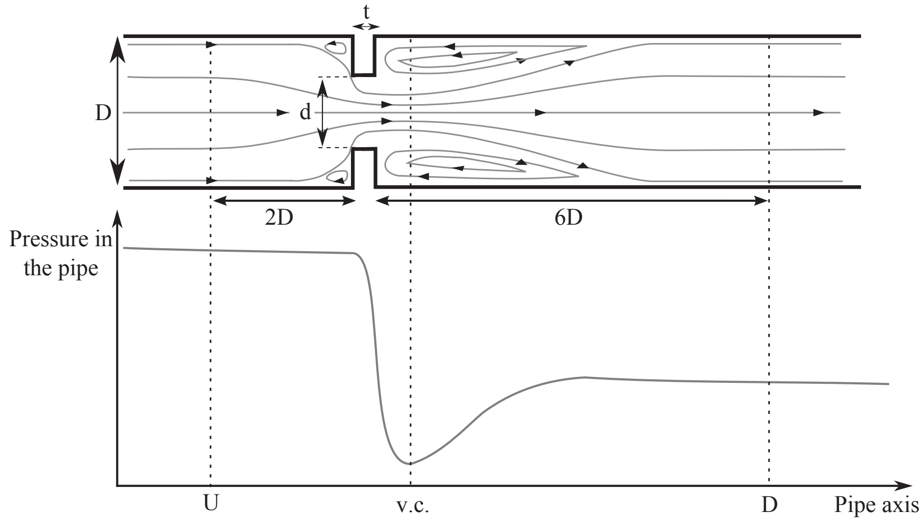

Figure 3.8 – Flow through an orifice and localization of the different section used in the evaluation of σ_i and σ_{vc}

$$\tilde{p} = p^* + p_{vg} - p_m^* \tag{3.18}$$

where p_m^* is the minimal pressure in the computed domain.

$$\sigma_i = \frac{\tilde{p_u} - p_{vg}}{\tilde{p_u} - \tilde{p_d}} = \frac{\left(p_u^* + p_{vg} - p_m^*\right) - p_{vg}}{\left(p_u^* + p_{vg} - p_m^*\right) - \left(p_d^* + p_{vg} - p_m^*\right)} = \frac{p_u^* - p_m^*}{p_u^* - p_d^*} \tag{3.19}$$

where p_u is the upstream pressure, p_d the downstream pressure and p_{vg} the vapour pressure.

Furthermore, in this research project, by assuming that the pressure drop in the *vena contracta* is relatively unaffected by the incipient cavitation, the cavitation number characterizing the cavitation of the *vena contracta* is evaluated by Eq.(3.20).

$$\sigma_{vc} = \frac{p_u^* - p_{vc}^*}{p_u^* - p_d^*} \tag{3.20}$$

where p_{vc}^* is the *vena-contracta* pressure

4 Experimental and numerical modeling

4.1 Experimental modeling

4.1.1 Description of the experimental set-up

The experimental work was carried out in a straight pipe located at the LCH of EPFL (Figures 4.1 and 4.2). The main pipe was made of two polyvinyl chloride (PVC) translucent pipes and an acrylic orifice box. The inner diameter of the main pipe was $D = 0.216\,m$ and the length was $L = 4\,m$ between the two expansion devices linking the experimental pipe to the laboratory supply conduits.

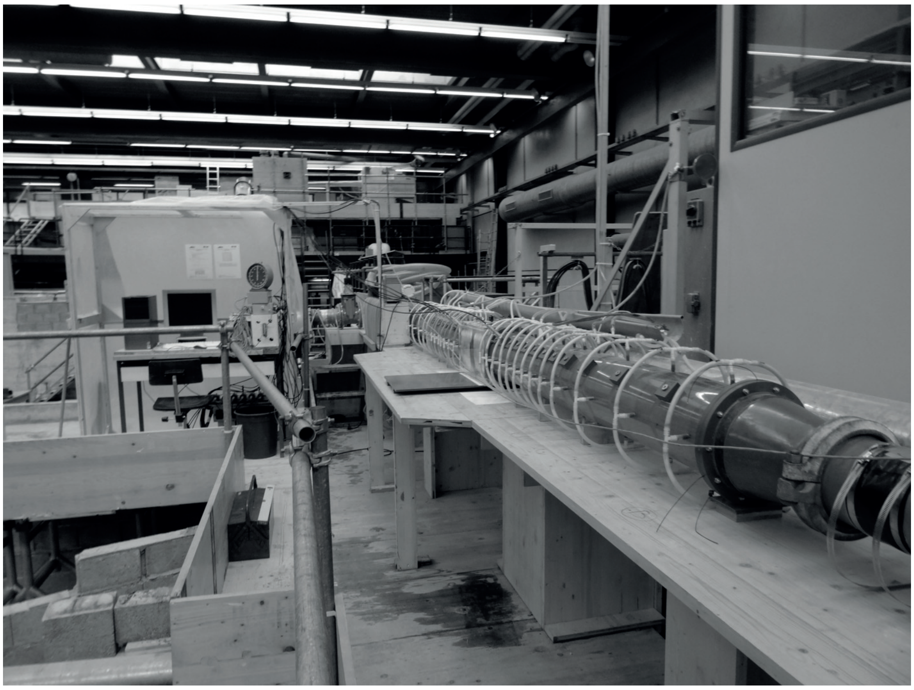

Figure 4.1 – Overview of the experimental facility at LCH-EPFL

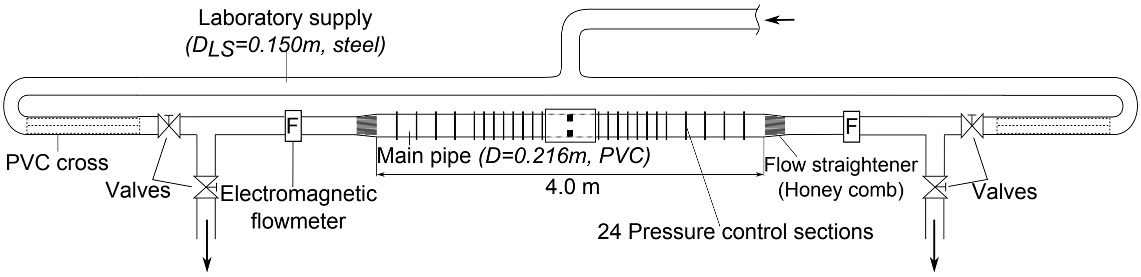
Laboratory supply
(D_LS=0.150m, steel)
PVC cross
Valves
F
Electromagnetic flowmeter
Main pipe (D=0.216m, PVC)
4.0 m
Flow straightener (Honey comb)
24 Pressure control sections
Valves

Figure 4.2 – Sketch top view of the experimental facility at LCH-EPFL

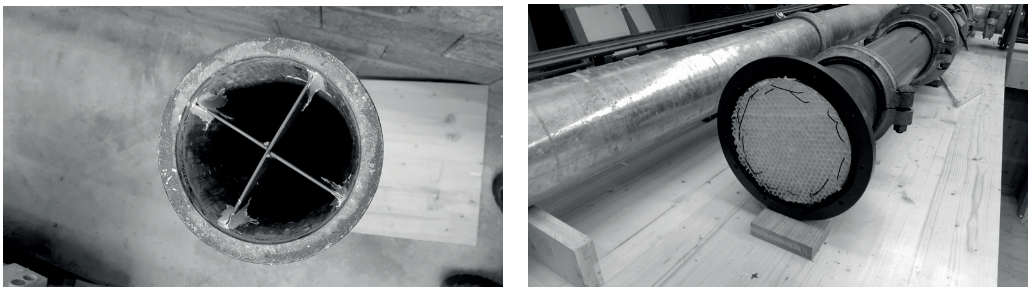

(a) PVC crosses

(b) Honey comb in the divergent pipe

Figure 4.3 – Flow straighteners placed in the piping system

Laboratory water supply

The main pipe was connected to the pump through a 150 mm supply conduit (D_{LS}). As shown in Figure 4.2, two 90-degree bends were located 2.7 m ($\approx 18D_{LS}$) far from the starting section of the main pipe.

Two types of flow straighteners are used to improve the hydraulic flow conditions in the pipe: (1) two PVC crosses (Figure 4.3a) are placed inside the laboratory supply to prevent the development of swirling flows because of the bends; and (2) honey combs (Figure 4.3b with a thickness of $0.1 m$ and single-hole openings of $\approx 2.6 \cdot 10^{-4}\, m^2$) were placed in the gradual divergent pipe to eliminate the possibility of small flow recirculations in the main pipe.

ISO (2003) lists the influences of the surrounding pipe waterway on the evaluation of the discharge coefficient, which is related to the head loss coefficient (Urner, 1997), of a standard orifice. Hence, in order to limit the uncertainties on the evaluation of the discharge (or head losses), the length upstream of the orifice should be higher than:

- $25D$, at least following two 90-degree bends without any flow straightener (for $\beta \in [0.2...0.67]$); and
- from 8 to $14D$ (for $\beta \in [0.2...0.67]$) following concentric expanders with an expanding ratio of 2, while the expanding ratio of our experimental setup was 1.44.

In the same way, in order to mitigate any additional uncertainty, the length downstream of the orifice should be higher than 7 D.

The experimental set-up fulfilled the criteria of the upstream and downstream lengths from ISO (2003) as two different types of flow straighteners were placed before the experimental pipe to improve flow conditions.

Orifice box

A special orifice box (Figure 4.4) was designed for testing efficiently numerous orifice thicknesses (Tables 4.1). An inner pipe was placed inside the box to ensure the same inner diameter within the main pipe and box. The orifice box and the inner pipes were made of Plexiglas for clear visibility of the flow. The watertightness between all parts was made certain by O-rings.

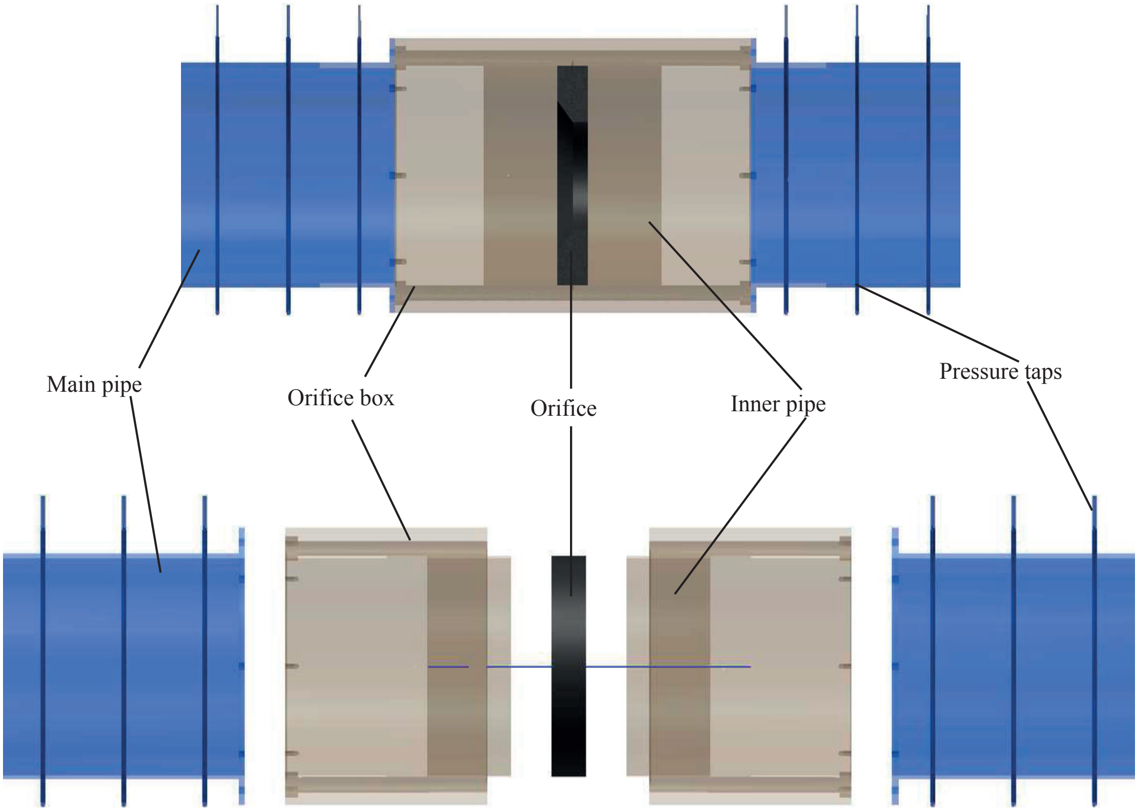

Figure 4.4 – Orifice box within the orifice and the inner pipe

4.1.2 Dimensional analysis

Dimensional analysis allows determination of the main influencing dimensionless parameters of shape. According to the literature, and particular, ISO (2003), the parameters characterizing an orifice situated inside a waterway (Figure 4.5) are:

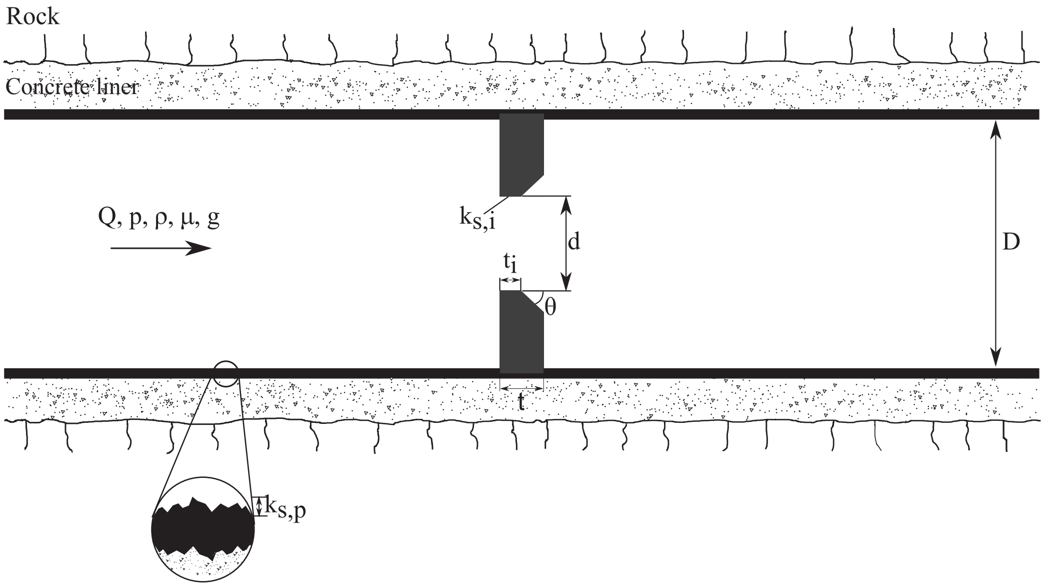

Figure 4.5 – Detailed view of an orifice in a waterway system and definition of parameters

- fluid (water in the thesis): ρ, μ;
- flow: Q, p;
- orifice: d, t, t_i, θ, $k_{s,i}$, shape; and
- surrounding pipe: D, $k_{s,p}$

And the dependent results are:

- head losses: ΔH;
- pressure drop in the vena contracta: Δp_{vc};
- influence orifice length: L_j; and
- reattachment length: L_r

We used the Buckingham Π-theorem to emphasize the dimensionless parameters according to Figure 4.5 (Buckingham, 1915).

$$\Delta H, \Delta p_{vc}, L_j, L_r = F(D, d, t, t_i, \theta, k_{s,p}, k_{s,i}, Q, p, \rho, \mu, g) \tag{4.1}$$

Table 4.1 – Range of tested parameters

Parameter name		Experimental	Numerical
Contraction ratio	$\beta = \frac{d}{D}$	0.4...0.6	0.2...0.8
Thickness ratio	$\alpha = \frac{t}{D}$	0.05...0.4	0.025...0.8
Inner thickness ratio	$\alpha_i = \frac{t_i}{D}$	0.025...0.4	0.025...0.8
Angle	θ	0°...90°	0°...90°
Shape		Sharp or rounded	Sharp

As seen in Eq. (4.1), there are 12 parameters pertaining to this problem. According to Buckingham (1915), there are nine possible dimensionless parameters as there are only independent fundamental units, i.e. meter, second and kilogram. Finally, we find Eq. (4.2) and (4.3).

$$\Delta H, \Delta p_{vc}, L_j = f\left(\frac{d}{D}, \frac{t}{D}, \frac{t_i}{D}, \theta, \frac{k_{s,p}}{D}, \frac{k_{s,i}}{D}, \frac{v \cdot D}{\frac{\mu}{\rho}}, \frac{v}{\sqrt{g \cdot D}}, \frac{\Delta p}{\frac{1}{2} \cdot \rho \cdot v^2}\right) \tag{4.2}$$

Eq. (4.2) highlights important numbers characterizing orifice issues. The first four number are the main geometrical parameters: $\beta = \frac{d}{D}$, the orifice diameter ratio, $\alpha = \frac{t}{D}$, the orifice thickness ratio, $\alpha_i = \frac{t_i}{D}$, the inner thickness ratio and θ, the orifice sharp angle. The next two dimensionless numbers are the dimensionless roughness for the pipe and the inner orifice surface $\varepsilon_p = \frac{k_{s,p}}{D}$ and $\varepsilon_i = \frac{k_{s,i}}{D}$, while the last three numbers are well known in hydraulics as Reynolds, Froude and Euler number. Note that the Euler number is another definition of the head loss coefficient. All these parameters are outlined in Eq. (4.3).

$$\Delta H, \Delta p_{vc}, L_j = f(\beta, \alpha, \alpha_i, \theta, \varepsilon_{s,p}, \varepsilon_{s,i}, \mathsf{Re}, \mathsf{Fr}, \mathsf{Eu}) \tag{4.3}$$

4.1.3 Investigated parameters and test program

The nine dimensionless parameters obtained with the dimensional analysis are found in Figure 4.5. The four geometrical independent parameters characterising an orifice (β, α, α_i and θ), as well as the orifice shape, were systematically tested (see Table 4.1). The experimental campaign concentrated on three different series of orifices: sharp-edged (Figure 4.6a and Table 4.2), rounded (Figure 4.6b and Table 4.3) and a combination of sharp-edged orifices (Figure 4.6c and Table 4.4). The design of experiments and the experimental results are summarized in Appendix B.

According to Figure 4.6, the following notations were used to clearly distinguish between the different flow approaches:

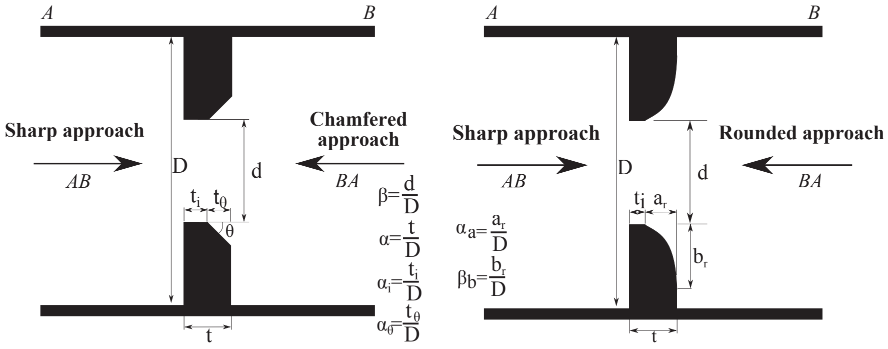
A
B
Sharp approach
AB
Chamfered approach
BA
D
d
t_i
t_θ
θ
t
$\beta=\frac{d}{D}$
$\alpha=\frac{t}{D}$
$\alpha_i=\frac{t_i}{D}$
$\alpha_\theta=\frac{t_\theta}{D}$
A
B
Sharp approach
AB
Rounded approach
BA
D
d
t_i
a_r
b_r
t
$\alpha a=\frac{a_r}{D}$
$\beta b=\frac{b_r}{D}$

(a) Sharp-edged orifice

(b) Rounded-edged orifice

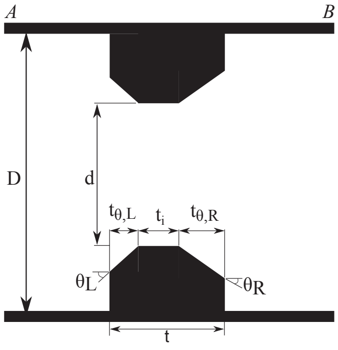
A
B
D
d
$t_{\theta,L}$
t_i
$t_{\theta,R}$
θL
θR
t

(c) Combination

Figure 4.6 – Different reference orifice shapes tested with the dimensionless parameters and notations

- Sharp approach flow (*AB*) when water flows by the sharp or square-edged side of the orifice;
- Chamfer approach flow (*BA*) when water flows according to the sloping-approach owing to the chamfer (if there are two chamfers, an additional distinction is used by the mean of the chamfer angle); and
- Rounded -approach flow (*BA*) when water flows through the rounded approach.

Table 4.5 shows the different discharges for the experiments and numerically and relates the kinetic energy values, along with the Reynold and Froude numbers. For both approaches, the Reynold number in the main pipe is higher than 10^4, thereby ensuring full turbulent flow. However, the influence of the dimensionless roughness ε_p and ε_i was considered in this study.

Table 4.2 – Set of sharp orifices tested during the experimental work

Orifice name	Shape	Varying parameter	$\beta\,[-]$	$\alpha\,[-]$	$\alpha_i\,[-]$	$\theta\,[°]$	α_i/α
EXP_001	sharp	Reference	0.50	0.20	0.10	45	0.5
EXP_002	sharp	β	0.45	0.20	0.10	45	0.5
EXP_003	sharp	β	0.40	0.20	0.10	45	0.5
EXP_004	sharp	β	0.59	0.20	0.10	45	0.5
EXP_005	sharp	β	0.54	0.20	0.10	45	0.5
EXP_006	sharp	θ	0.50	0.20	0.20	0	1.0
EXP_007	sharp	θ	0.50	0.20	0.10	15	0.5
EXP_008	sharp	θ	0.50	0.20	0.10	30	0.5
EXP_009	sharp	θ	0.50	0.20	0.10	67	0.5
EXP_010	sharp	α_i	0.50	0.20	0.15	45	0.74
EXP_010.5	sharp	α_i	0.50	0.20	0.00	45	0.00
EXP_011	sharp	α_i	0.50	0.20	0.05	45	0.26
EXP_012	sharp	α	0.50	0.10	0.05	45	0.51
EXP_013	sharp	α	0.50	0.05	0.025	45	0.49
EXP_032	sharp	α	0.50	0.40	0.20	45	0.50
EXP_026	sharp	α, θ	0.50	0.40	0.40	0	1.0

Table 4.3 – Set of rounded orifices tested during the experimental work

Orifice name	Shape	Varying parameter	$\beta\,[-]$	$\alpha\,[-]$	$\alpha_i\,[-]$	$\beta_b\,[-]$	α_i/α
EXP_014	rounded	Rounded shape	0.50	0.20	0.04	0.10	0.19
EXP_015	rounded	Shape, β	0.45	0.20	0.01	0.14	0.07
EXP_016	rounded	Shape, β	0.40	0.20	0.04	0.15	0.19
EXP_017	rounded	Shape, β	0.59	0.20	0.06	0.03	0.32
EXP_018	rounded	Shape, β	0.54	0.20	0.04	0.07	0.19
EXP_019	rounded	Shape, θ	0.50	0.20	0.04	0.21	0.20
EXP_020	rounded	Shape, θ	0.50	0.20	0.04	0.16	0.19
EXP_021	rounded	Shape, θ	0.50	0.20	0.05	-0.09	0.23
EXP_022	rounded	Shape, α_i	0.50	0.20	0.12	0.18	0.60
EXP_023	rounded	Shape, α_i	0.50	0.20	-0.04	0.02	-0.19
EXP_024	rounded	Shape, α	0.50	0.10	0.02	0.18	0.19
EXP_025	rounded	Shape, α	0.50	0.05	0.01	0.21	0.14
EXP_932	rounded	Shape, α	0.50	0.40	0.24	0.10	0.60

Table 4.4 – Set of sharp orifices tested during the experimental work

Orifice name	Right	Left	$\beta\,[-]$	$\alpha\,[-]$	$\alpha_i\,[-]$	$\alpha_L\,[-]$	$\theta_L\,[°]$	$\alpha_R\,[-]$	$\theta_R\,[°]$
EXP_026	SHARP006	SHARP006	0.50	0.40	0.40	0.20	0	0.20	0
EXP_027	SHARP006	SHARP001	0.50	0.40	0.30	0.20	0	0.10	45
EXP_028	SHARP006	SHARP007	0.50	0.40	0.30	0.20	0	0.10	15
EXP_029	SHARP006	SHARP008	0.50	0.40	0.30	0.20	0	0.10	30
EXP_030	SHARP006	SHARP009	0.50	0.40	0.30	0.20	0	0.10	67
EXP_031	SHARP006	SHARP010	0.50	0.40	0.35	0.20	0	0.05	45
EXP_032	SHARP006	SHARP011	0.50	0.40	0.25	0.20	0	0.15	45
EXP_033	SHARP006	SHARP010.5	0.50	0.50	0.20	0.20	0	0.20	45
EXP_034	SHARP012	SHARP006	0.50	0.50	0.25	0.05	45	0.20	0
EXP_035	SHARP013	SHARP006	0.50	0.50	0.23	0.03	45	0.20	45
EXP_036	SHARP001	SHARP007	0.50	0.40	0.20	0.10	45	0.10	15
EXP_037	SHARP001	SHARP009	0.50	0.40	0.20	0.10	45	0.10	67
EXP_038	SHARP001	SHARP011	0.50	0.40	0.15	0.10	45	0.15	45
EXP_039	SHARP012	SHARP001	0.50	0.30	0.15	0.05	45	0.10	45
EXP_040	SHARP007	SHARP008	0.50	0.40	0.20	0.10	15	0.10	30
EXP_041	SHARP007	SHARP010	0.50	0.40	0.25	0.10	15	0.05	45
EXP_042	SHARP007	SHARP010.5	0.50	0.40	0.10	0.10	15	0.20	45
EXP_043	SHARP0013	SHARP007	0.50	0.40	0.20	0.10	45	0.10	15
EXP_044	SHARP008	SHARP009	0.50	0.40	0.20	0.10	30	0.10	67
EXP_045	SHARP008	SHARP011	0.50	0.40	0.15	0.10	30	0.15	45
EXP_046	SHARP012	SHARP008	0.50	0.30	0.15	0.05	45	0.10	45
EXP_047	SHARP009	SHARP010	0.50	0.40	0.25	0.10	67	0.05	45
EXP_048	SHARP009	SHARP010.5	0.50	0.40	0.10	0.10	67	0.20	45
EXP_049	SHARP012	SHARP009	0.50	0.30	0.15	0.05	45	0.10	67
EXP_050	SHARP010	SHARP011	0.50	0.40	0.20	0.05	45	0.15	45
EXP_051	SHARP012	SHARP010	0.50	0.30	0.20	0.05	45	0.05	45
EXP_052	SHARP011	SHARP010.5	0.50	0.40	0.05	0.15	45	0.20	45
EXP_053	SHARP013	SHARP011	0.50	0.25	0.08	0.03	45	0.15	45
EXP_054	SHARP012	SHARP010.5	0.50	0.30	0.05	0.05	45	0.20	45
EXP_055	SHARP013	SHARP012	0.50	0.15	0.08	0.03	45	0.05	45

Table 4.5 – Range of tested discharges (*discharge tested numerically)

♯	$Q\,[m^3/s]$	$v\,[m/s]$	$K_D\,[m]$	Re [−]	Fr [−]
0	0	0	0	0	0
1	$9.5\cdot10^{-3}$	0.259	$3.43\cdot10^{-3}$	$5.60\cdot10^{4}$	$1.78\cdot10^{-1}$
2*	$13.4\cdot10^{-3}$	0.366	$6.82\cdot10^{-3}$	$7.90\cdot10^{4}$	$2.51\cdot10^{-1}$
3	$16.4\cdot10^{-3}$	0.448	$1.02\cdot10^{-2}$	$9.67\cdot10^{4}$	$3.07\cdot10^{-1}$
4	$19.0\cdot10^{-3}$	0.519	$1.37\cdot10^{-2}$	$1.12\cdot10^{5}$	$3.56\cdot10^{-1}$
5	$21.2\cdot10^{-3}$	0.579	$1.71\cdot10^{-2}$	$1.25\cdot10^{5}$	$3.97\cdot10^{-1}$
6*	$23.2\cdot10^{-3}$	0.633	$2.04\cdot10^{-2}$	$1.37\cdot10^{5}$	$4.35\cdot10^{-1}$
7	$25.1\cdot10^{-3}$	0.685	$2.39\cdot10^{-2}$	$1.48\cdot10^{5}$	$4.71\cdot10^{-1}$
8	$26.8\cdot10^{-3}$	0.731	$2.73\cdot10^{-2}$	$1.58\cdot10^{5}$	$5.02\cdot10^{-1}$
9	$28.5\cdot10^{-3}$	0.778	$3.08\cdot10^{-2}$	$1.68\cdot10^{5}$	$5.34\cdot10^{-1}$
10*	$30.0\cdot10^{-3}$	0.819	$3.42\cdot10^{-2}$	$1.77\cdot10^{5}$	$5.62\cdot10^{-1}$

4.1.4 Instrumentation

Appendix A features additional information surrounding the instrumentation, its calibration and the definition of the record duration and sampling frequency.

Pressure transducers

12 piezoresistive pressure transmitters of the *KELLER - series 25*, six $G1/4$" plugs and six $G1/2$" plugs, were utilized to measure the pressure along the pipe.

- The six $G1/4$" plugs were directly connected to the main pipe with an eight-millimeter hole at 45 degrees from the top of the pipe (Figure 4.7b). For each test, one plug was placed upstream and five downstream of the orifice depending on the flow direction. The position reliant on the flow direction is shown in Figure 4.8 and described in Table 4.6. Air bubbles trapped in the hole were removed at the beginning of each orifice test.
- The six $G1/2$" plugs (Figure 4.7a) were connected to two by 24 cross-sections distributed along the pipe (Figure 4.8) through a dispatcher composed of 20 solenoid valves (Figure 4.7c). Six recordings were necessary for recording once per cross-sections as seen in Table 4.6.

Both type of transmitters were calibrated for pressures between 2 mH_2O (resp. 19.62 kPa) and 0.4 mH_2O (resp. 3.92 kPa) as explained in Appendix A.

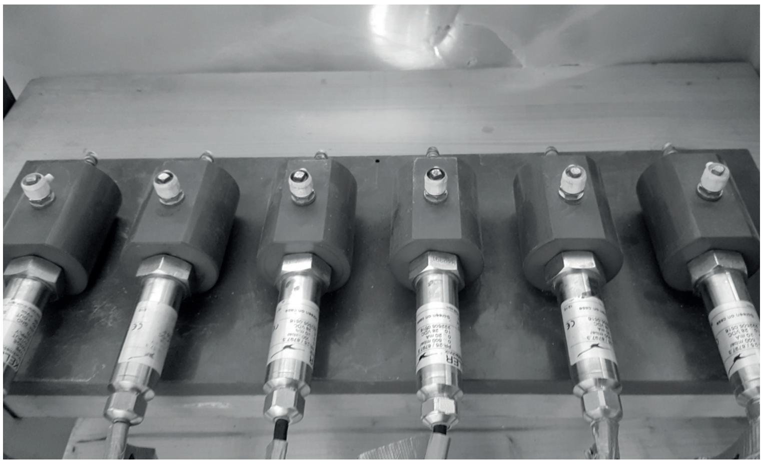

(a) Six piezo-resistive transducers

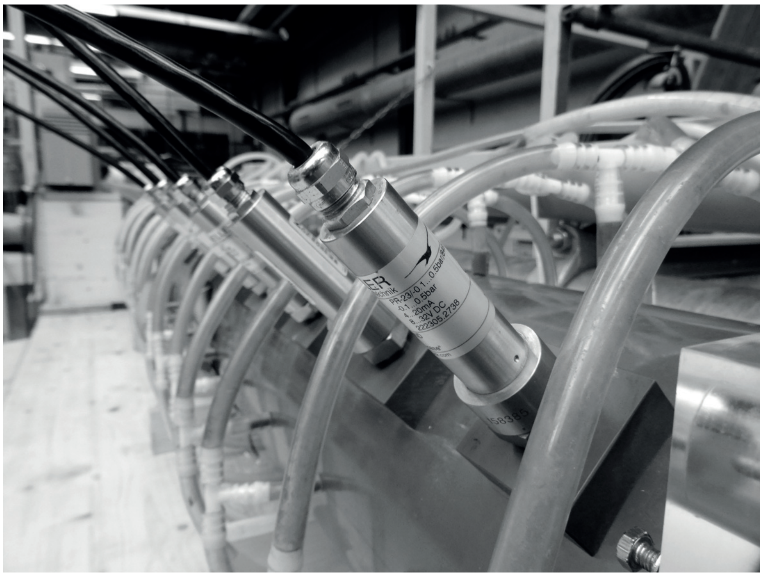

(b) G1/4" piezo-resitive transducers

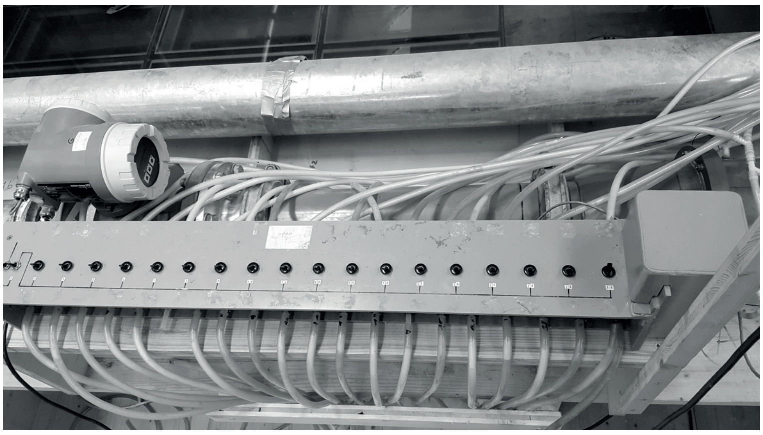

(c) Dispatcher

Figure 4.7 – Pressure tansducers used in the experimental campaign and dispatcher

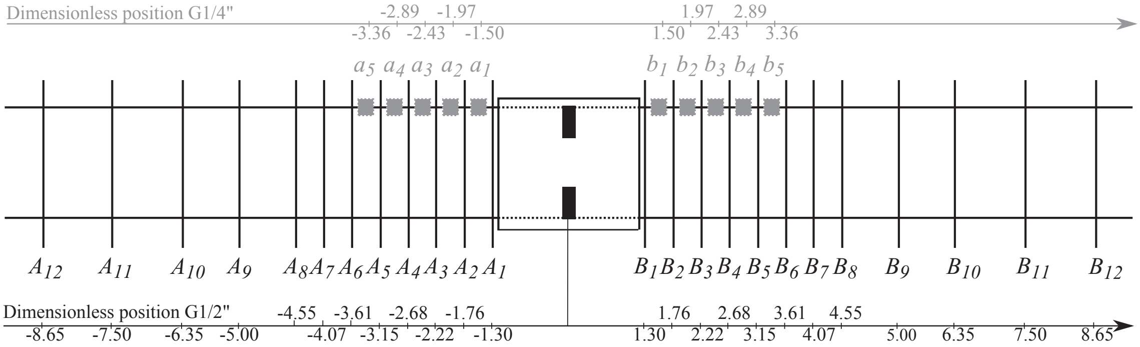
Dimensionless position G1/4"
-2.89 -1.97
-3.36 -2.43 -1.50
1.97 2.89
1.50 2.43 3.36
a_5 a_4 a_3 a_2 a_1
b_1 b_2 b_3 b_4 b_5
A_{12} A_{11} A_{10} A_9 A_8 A_7 A_6 A_5 A_4 A_3 A_2 A_1
B_1 B_2 B_3 B_4 B_5 B_6 B_7 B_8 B_9 B_{10} B_{11} B_{12}
Dimensionless position G1/2"
-4.55 -3.61 -2.68 -1.76
1.76 2.68 3.61 4.55
-8.65 -7.50 -6.35 -5.00 -4.07 -3.15 -2.22 -1.30
1.30 2.22 3.15 4.07 5.00 6.35 7.50 8.65

Figure 4.8 – Dimensionless positions of all the control cross-sections along the main pipe for $G1/4"$ and $G1/2"$ plugs

Table 4.6 – The record sequence for the G1/2" and G1/4" pressure transmitters for each discharge

Recording	G1/2"(1)	G1/2"(2)	G1/2"(3)	G1/2"(4)	G1/2"(5)	G1/2"(6)
$AB_1(BA_1)$	A_{11}	A_9	A_4	B_4	B_9	B_{11}
$AB_2(BA_2)$	A_{11}	A_8	A_3	B_3	B_8	B_{11}
$AB_3(BA_3)$	A_{11}	A_7	A_2	B_2	B_7	B_{10}
$AB_4(BA_4)$	A_{11}	A_6	A_1	B_1	B_6	B_{12}
$AB_5(BA_5)$	A_{10}	A_6	A_1	B_1	B_6	B_{11}
$AB_6(BA_6)$	A_{12}	A_5	A_1	B_1	B_5	B_{11}
	G1/4"(1)	G1/4"(2)	G1/4"(3)	G1/4"(4)	G1/4"(5)	G1/4"(6)
AB	a_1	b_1	b_2	b_3	b_4	b_5
BA	a_1	b_1	a_5	a_4	a_3	a_2

Flow meters

The water discharge, Q, was measured by electromagnetic flow meters, *Endres + Hauser - PROMAG 50 W* (Figure 4.9) on the laboratory supply conduit (DN 150). The two flow meters were adjusted to assess discharges up to 0.04 m^3/s. However, the flowmeter could measure discharges up to 0.167 m^3/s for DN 150 conduits. The measurement uncertainty was ±0.5% of the measured discharge (thus, $2 \cdot 10^{-4}\ m^3/s$). The measured flow meter was always the flowmeter at the end of the downstream pipe (Figure 4.2)

The flowmeter was calibrated for five discharges (from 0.009 to 0.03 m^3/s) before the experimental campaign as reported in Appendix A.

4.1.5 Acquisition parameters

The sampling frequency varied from 100 Hz (for steady-state measurement) to 1000 Hz (for transient measurement).

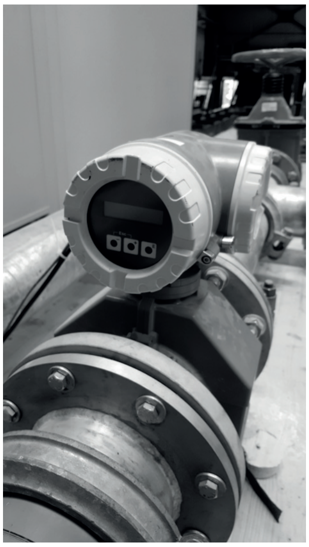

Figure 4.9 – ENDRES + HAUSER - PROMAG 50 W flowmeter

The recording duration was 30 s as indicated in Appendix A.

4.1.6 Test procedure

Each physical test was carried out according to the following this test procedure:

1. The model was prepared with the required orifice with in the box. The six G1/4" pressure transducers are placed at their positions relative to the first testing flow direction;
2. The model was filled with water from the upstream pipe;
3. The air bubbles were blown away by the internal pressure (higher than the surrounding air pressure). The bubbles could be drained either by the two box taps or by all the 24 control cross-sections by means of the dispatcher;
4. The G1/4" pressure transducers were tightened after blowing the air away;
5. All the discharges were tested following a rise and a fall of the whole set of discharge;
6. For each discharge, steady flow conditions were reached in order to perform six recordings of 30 s each with a sampling rate of 100 Hz. This permitted recording, at least once, each of the 24 control cross-sections. The acquisition of the pinhole pressures, the four-points-averaged pressures and the discharges were recorded; and
7. For the chosen orifices (Chapter 7), transient recordings were with a sampling rate of 1 kHz.

Table 4.7 – Errors and uncertainties for the physical modeling

Type	Unit	Standard error σ_ε
Geometrical	mm	±0.1
Pressure transmitters	%	±0.2
Flow-meter	%	±0.5
Pressure fluctuations	%	±5
Discharge fluctuations	%	±1

4.1.7 Measurement errors and uncertainties

The measurement errors and uncertainties in this research may be divided into three different classes:

- geometrical errors: All the pieces were built in the EPFL workshop with a tolerance of $\pm 0.1\,mm$. However, the tolerance for the inner pipe thickness (see Figure 4.4) was $-0.1\,mm$ to avoid blockages within the orifice box;
- instrumentation uncertainties: Both types of instrumentation, i.e. flowmeter and pressure transmitters, were submitted to uncertainties, supplied by the manufacturer as described in Appendix A and summarized in Table 4.7;
- experimental pressure fluctuations: The six-blades pump creates fluctuations in laboratory supply. The pressure uncertainties, are independent of the discharge. The average uncertainties are roughly 5% of the tested discharges; and
- experimental discharge fluctuations: Also based the six-blade pump and the uncertainties regarding discharge are 1%.

The uncertainties of the head losses and kinetic energy are, respectively, 5% and 1%, leading to an uncertainty of the head loss coefficient at 6%. However, the head loss coefficients are fitted for 2 x 10 discharges, thus the uncertainty can be divided by $\sqrt{N}$ with $N = 20$. The final uncertainty is therefore 1.3%.

4.1.8 Scale effects

Various researchers have carried out physical or numerical experiments (see Table 4.8). The Reynold number in the main pipe is higher than 10^4 for most of the studies in order to ensure a fully turbulent behavior of the local head losses produced by the orifice. Hence, the local head losses are independent of the Reynold number. Furthermore, the primary diameter of the experiments used in this study is on the same order of magnitude as those shown in Table 4.8.

The upscaling of the experimental results can be performed according to Froude similitude. For pressurized flow, there would be a need to conserve the ratio of the inertial forces to the viscous forces. Nevertheless, the experimental results can indeed be upscaled; as fully turbulent flow is always facilitated during the experiments.

Finally, it should be noticed that the ratio between the main pipe diameter, D, and existing diameter of the surge tank entrance are on the same order of magnitude as those of previous model tests performed at LCH (Section 2.4).

4.2 Numerical simulations

4.2.1 Presentation

The numerical simulations were performed with the CFD software ANSYS CFX (either version 15.0 or 17.1) and using ANSYS Workbench. The numerical model was developed in collaboration with Prof. Cécile Munch-Alligné from HES-SO Valais/Wallis. The structure of the numerical modeling can be summarized as follows (see also Figure 4.10):

1. The design of the numerical experiments gives the geometrical parameters for a larger set of chamfered orifices than the experimental modelling (Chapter 4.1). The interactions between geometrical parameters could be highlighted;
2. A straight pipe geometry is generated from the orifice geometrical parameters (Section 4.2.2);
3. The geometry is meshed with hexahedron elements (Section 4.2.3);
4. The pre-processing allows the definition of the boundary conditions, the turbulence model and the parameters of the simulation, e.g. the convergence criteria;
5. The solver of ANSYS CFX;
6. The post-processing where the variables characterizing the orifice flow can be exported;
7. From the exported variables, the orifice flow is analyzed to achieve the goal of numerical modeling:
    - Comparison with the experimental results (*validation of the numerical model)*
    - *Simulation of an extended set of chamfered orifices to evaluate the interaction between the geometrical parameters, to extend and validate the empirical formulae fitted on the experimental results*
    - *Evaluation of the incipient cavitation number in order to characterize each orifice in terms of the risk of cavitation*

Table 4.8 – Previous studies performed on various types of orifices

Study	Flow	Geometry		Object	$Re_D[-]$	$D\,[mm]$	$\beta[-]$
Hobbs and Humphreys (1990)	water	sharp	P	C	$Re_d \approx 5\cdot 10^5$	304.8	$[0.4, 0.75]$
Morrison et al. (1990)	air	sharp	P	C	$[5\cdot 10^4, 1.23x\cdot 10^5]$	50.4	0.5&0.75
Morrison et al. (1995)	air	sharp	P	C	$9.1\cdot 10^4$, $1.2\cdot 10^5$	52.5	$[0.43, 0.726]$
Gan and Riffat (1997)(1)	gas	Square-edged	N,P	k	$9.1\cdot 10^4$, $1.2\cdot 10^5$	$c = 300$	$\beta_{eq} = 0.706$
Zhang and Cai (1999)	water	different	N,P	$C, k, shape$	-	102	$[0.5, 0.8]$
Fossa and Guglielmini (2002)	water	orifice	P	k, 2-phase flow	$[3\cdot 10^4, 2\cdot 10^5]$	40, 60	0.735, 0.845
Singh et al. (2006)(2)	water and oil	V-cone	P	C	$[1.25\cdot 10^3, 2.6\cdot 10^5]$	50	0.36
Qing et al. (2006)	water	Square-edged	P, N	Jet frequency	$> 10^5$	90	0.255, 0.335
Jianhua et al. (2010)	water	Square-edged	P,N	k, L_j	$1.8\cdot 10^5$	210	$[0.4, 0.8]$

(1) Gan and Riffat (1997) performed experiments on orifice and perforated plates in a square duct.

(2) Singh et al. (2006) used another definition for the contraction ratio $\beta = d_{max}/D$ instead of the common definition $\beta = d_{min}/D$.

The author then reverted to the common definition.

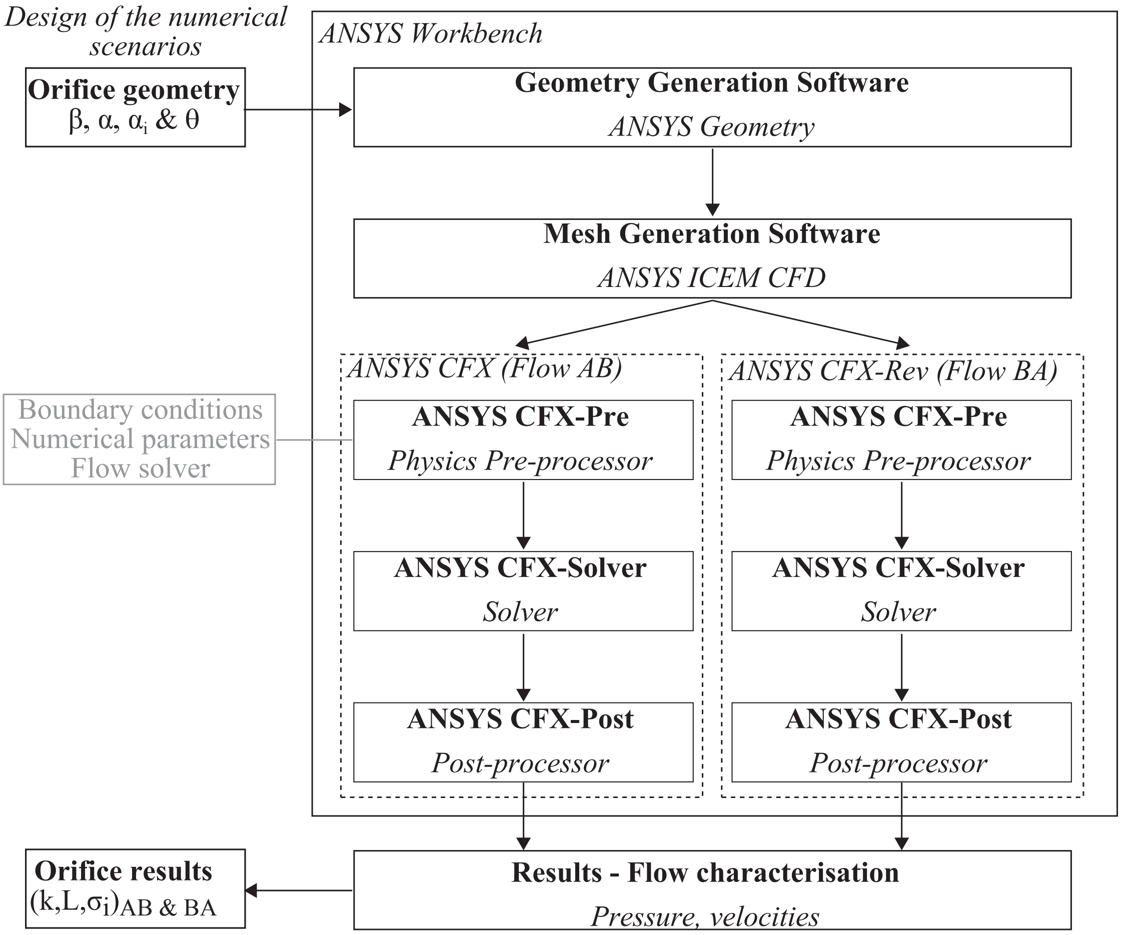
Design of the numerical scenarios
Orifice geometry
β, α, α_i & θ
ANSYS Workbench
Geometry Generation Software
ANSYS Geometry
Mesh Generation Software
ANSYS ICEM CFD
ANSYS CFX (Flow AB)
ANSYS CFX-Rev (Flow BA)
Boundary conditions
Numerical parameters
Flow solver
ANSYS CFX-Pre
Physics Pre-processor
ANSYS CFX-Pre
Physics Pre-processor
ANSYS CFX-Solver
Solver
ANSYS CFX-Solver
Solver
ANSYS CFX-Post
Post-processor
ANSYS CFX-Post
Post-processor
Orifice results
$(k,L,\sigma_i)_{AB\ \&\ BA}$
Results - Flow characterisation
Pressure, velocities

Figure 4.10 – Structure of the numerical modeling for each orifice from the orifice geometry (INPUT) to the results characterizing the orifice (OUTPUT)

4.2.2 Geometry

For the numerical simulations, the geometry was composed of the main pipe (Figure 4.2 and 4.11). The inner pipe diameter was equal to the experimental diameter, $D = 0.216\,m$. The orifice is placed at the central section of the pipe and both boundary cross-sections were at $10\,D$ (2.16 m). All the upstream and downstream experimental installations (Figure 4.2) were not considered for the numerical model. The influence of the distance of the boundaries upstream and downstream of the orifice was studied in Section 4.2.7.

The design of the numerical simulations is described in Appendix C. The contraction ratios, β, and interactions with the other geometrical parameters were evaluated to determine how to mitigate the lack of results in Chapter 5.

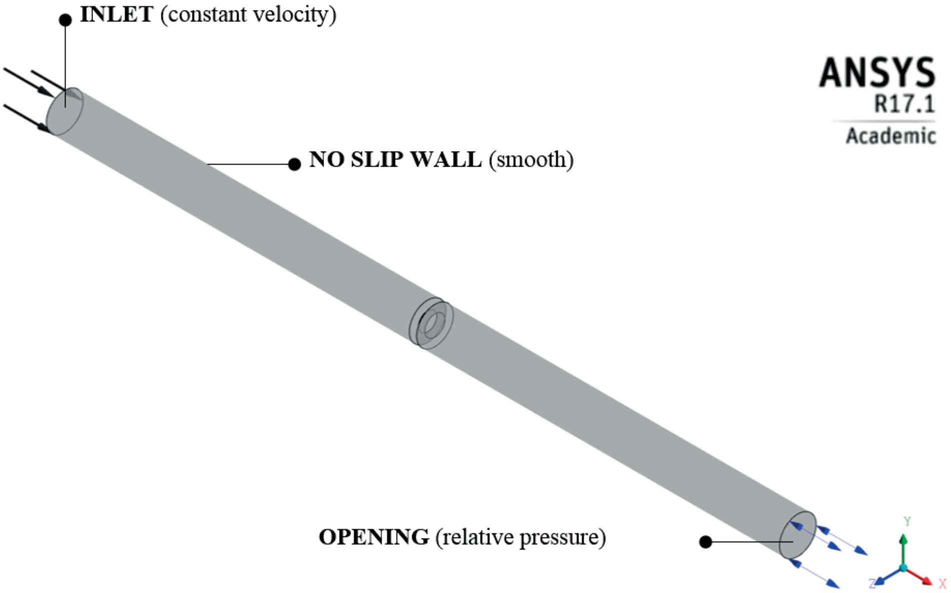
INLET (constant velocity)
ANSYS
R17.1
Academic
NO SLIP WALL (smooth)
OPENING (relative pressure)
Y
Z
X

Figure 4.11 – Geometry of the numerical model (NUM001)

4.2.3 Mesh

The fluid volume was meshed with a structured hexagonal grid. There are four different blocks, i.e. the upstream pipe, the straight component and the chamfered part of the orifice as well as the downstream pipe. The cross-section of the pipe of the mesh was of the O-mesh (ANSYS, 2016a) variety so as to enhance mesh quality (Figure 4.12).

There were three different walls (Figure 4.12c), i.e. pipe wall, orifice side wall and orifice wall, where a near-wall inflation was necessary to model the viscous layer of the flow:

- the pipe wall inflation going from the pipe wall to the pipe axis and finishing with the O-mesh grid (1, blue in Figure 4.12c);

- the orifice side inflation going from the orifice sides to the boundaries (2, red in Figure 4.12c), and the maximum cell length in this direction was limited to 0.015 m; and

- the orifice wall inflation, which is the most important for capturing flow detachment and modeling the head losses, from the orifice wall to the pipe core (3, green in Figure 4.12c)

Note that the minimum cell length, excepting inflation, was 0.001 m either for the O-mesh core or within the orifice. The total number of cells were, on average, roughly 1.5 million.

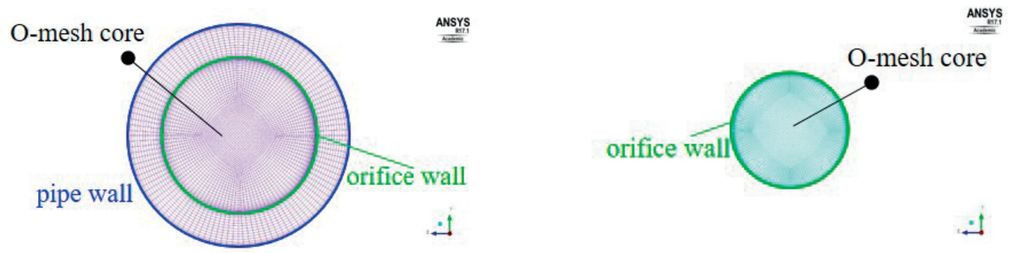

(a) Cross-section of the downstream pipe mesh (b) Cross-section of the orifice mesh

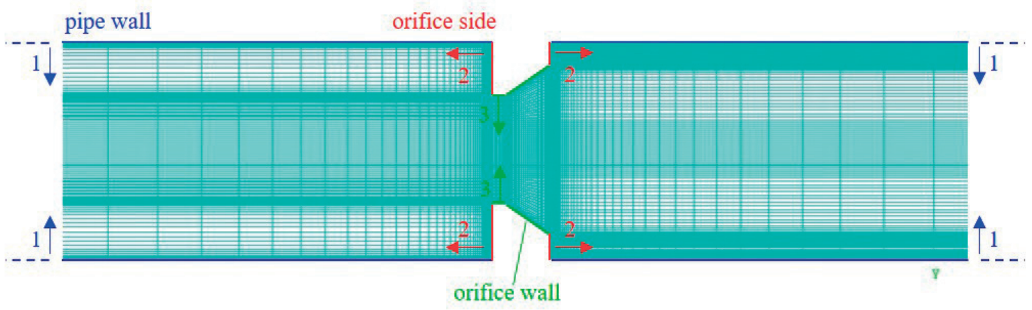

(c) Longitudinal section close to the orifice

Figure 4.12 – Views of the different meshes used for orifice NUM001

4.2.4 Pre-processing

Boundary conditions

ANSYS CFX permits the employment of different types of boundary conditions (ANSYS, 2016b), i.e. an inflow and outflow, which depends on the flow direction, and a wall condition (Figure 4.11).

- At the upstream boundary cross-section, which depends on the flow direction, an inlet was utilized with a velocity-specified condition. The average velocity on the whole pipe cross-section was applied to the boundary cross-section. The influence of the upstream length was evaluated (see Section 4.2.7). Three discharges, and thus three average velocities, were tested for each geometry as seen in Table 4.5.
- At the downstream boundary cross-section, which is also reliant on the flow direction, an opening was used instead of an outlet which can numerically diverge because of the erection of a temporary wall for avoiding an inflow (ANSYS, 2016c). This generally results in a failure, though this effect was only based on numerical considerations.
- Along the pipe wall and on the orifice surface, a no slip-wall condition was applied with a smooth wall (without wall roughness). This eliminates the influence of roughness on the linear head losses but reproduces the linear head losses generated by the flow, e.g. by its viscosity.

Physical properties of the fluid

The fluid in the numerical simulations was water, just as in the experimental modeling. All properties of water were assessed at $20°C$, while the temperature during the experimental evaluations were between $15°C$ and $20°C$. Even for Chapter 8, which deals with cavitation, the fluid was continuous, and single phase, while there was no cavitation model for negative pressures, only relative pressures. Water flowing in the pressurized pipe was driven by the pressure and not the gravity, like in open-channel flow, and the buoyancy of the fluid was set with non-buoyant fluid (ANSYS, 2016c).

Turbulence model

Turbulence models predict the effects of all turbulence without solving all the turbulence scales. Many models are based on turbulence approximations made with Reynolds Averaged Navier-Stokes (RANS) equations but there are also models that are not based on RANS equations, e.g. Large Eddy Simulation (LES) or Detached Eddy Simulation (DES) models (ANSYS, 2016c). The models based on RANS equations can also be divided into eddy-viscosity and Reynolds Stress (RSM) models:

- Eddy-viscosity models with no additional equation (Smith and Cebeci, 1967; ABSI, 2006);
- Eddy-viscosity models with one additional equation, e.g. Prandtl or Sparlart-Allmaras (Spalart et al., 1994) model;
- Eddy-viscosity models with two additional equations, e.g. the k-ε models (standard, realizable or RNG[1]) or k-ω models (Shear Stress Transport, or SST, model included);
- RSM simulates all the individual components of the Reynolds stress tensor and are more accurate for flows with high degrees of anisotropy (Craft et al., 1996).

Table 4.9 lists the simulation characteristics of a number of previous studies, wherein performed were numerical simulations on orifices or throttles with similar Reynolds numbers (fully turbulent, $\mathsf{Re}_D > 10^4$). Many authors have used the k-ε models, however ANSYS (2016c) has suggested the SST model, which yields better results for flows with boundary layer separation. According to Table 4.9 and ANSYS (2016c), the SST model was employed as the turbulence model for this project.

Near-wall treatment: Wall treatments are used to take into account the viscous effects close to the wall and to solve the rapid variation of flow variables in the boundary layer. ANSYS (2016c) maintains there are two different approaches, commonly used to model the near-wall region:

---

[1] based on renormalization group analysis of the Navier-Stokes equations (ANSYS, 2016d)

- wall functions, which are based on empirical formulas, decreasing the necessary computational time; and
- the low Reynolds Number method, which solves the boundary layer profile, via thin inflation layers close to the walls.

Based on ANSYS (2016c), for the SST model, an automatic near-wall treatment was applied.

4.2.5 Solver

ANSYS CFX features two analysis types (ANSYS, 2016b):

- *Steady state* for numerical problems that likely results in steady flow solutions. If there are any unsteady effects, that do not depend on the mesh, a transient analysis should be performed. All parameters, that have an influence on numerical stability, e.g. the timestep or the CFL number, are automatically handled by the software; and
- *Transient* for other numerical problems that lead to unsteady solutions. All the parameters influencing numerical stability are defined by the user. An adaptive or constant timestep can be employed. The maximum or RMS Courant number should be established in order to ensure numerical divergence and accuracy.

In the thesis, steady state analysis was preferred. If there was any doubt related to the numerical or real transient phenomena, transient analysis was performed. The convergence criteria was either when the maximum residual was $1e^{-7}$ or for maximal iterations of 1000. The convergence of the head losses between the upstream and downstream part of the pipe and the steadiness of the solution was always verified subsequently.

4.2.6 Post-processing

Wall function - y^+

ANSYS (2016c) presented various guidelines for ensuring the best accuracy of wall treatment for mesh generation. As can be seen from Table 4.9, the authors used different values of y^+. Before, when standard wall functions were employed, it was advised to avoid y^+ values smaller than 20, but with automatic wall treatment, these values are only provided for information pertaining to near-wall resolutions (ANSYS, 2016c).

Figure 4.13 portrays the value of y^+ on the pipe wall along the pipe axis for NUM_001. For all the numerical simulations, the value of y^+ was locally limited to 100 and 30 on average. Furthermore, the maximal value was locally obtained on the edge.

Table 4.9 – Recent studies performed on a variety of orifice or throttled surge tanks

Study	Software	Interest	Turbulence model	Reynolds number Re_D [-]	y_+ [-]
Erdal and Andersson (1997)	Phoenics 2.1.3	Orifice: C_D	k-ε	$10^4 \ldots 10^6$	/
Huber (2010)	Fluent 6.3.26	Throttled ST: k	/	$4\cdot10^5 \ldots 4\cdot10^6$	2-10
Wu and Ai (2010)	/	Orifice: α_c	RNG k-ε	$1.75\cdot10^7 \ldots 3.51\cdot10^7$	/
Jianhua et al. (2010)	/	Orifice: k,l_r	RNG k-ε	$9\cdot10^4 \ldots 2.76\cdot10^6$	7
Gabl et al. (2011)	ANSYS CFX 12.1	Orifice: k, λ	SST	/	< 20
Alligne et al. (2012)	ANSYS CFX 14.0	Throttled ST: k	SST	$> 10^5$	20...100
Li et al. (2012)	ANSYS CFX	Orifice: C_D	k-ε	/	/
Shah et al. (2012)	OpenFOAM 1.6	Orifice: C_D	k-ε	$4.5\cdot10^4 \ldots 9\cdot10^4$	< 5
An et al. (2013a)	Fluent	Throttled ST: k	realizable k-ε	/	/
Nygård and Andersson (2013)	/	Orifice flow	/	$5\cdot10^3 \ldots 1.5\cdot10^4$	≤ 5
Lancial et al. (2016)	Code_Saturne	Orifice: k,C_D	k-ε	$8.69\cdot10^5$	20, 40, 60

where: k is the head loss coefficient, α_c the critical thickness ratio, l_r the reattachment length, λ the asymmetry ratio, and C_D the discharge coefficient.
/: No direct information in the article

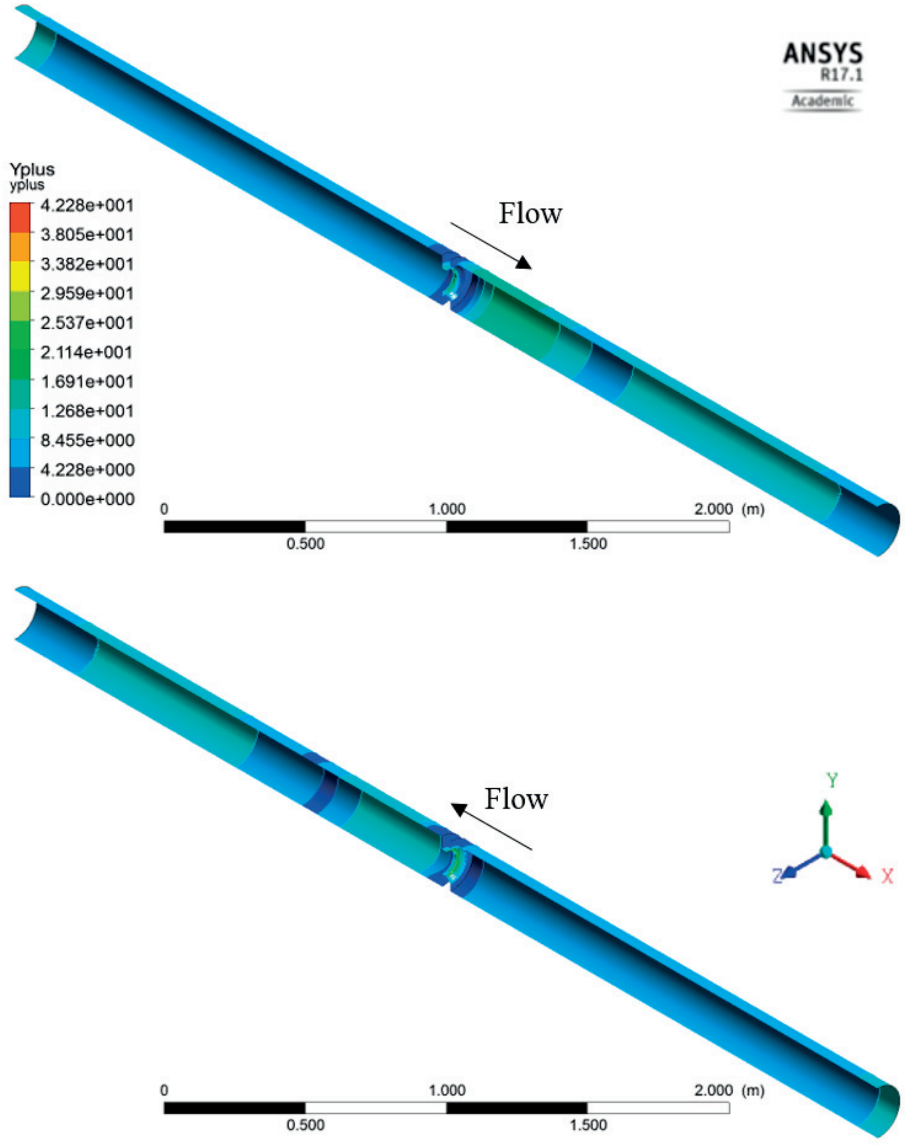
ANSYS
R17.1
Academic
Yplus
yplus
4.228e+001
3.805e+001
3.382e+001
2.959e+001
2.537e+001
2.114e+001
1.691e+001
1.268e+001
8.455e+000
4.228e+000
0.000e+000
Flow
0
1.000
2.000 (m)
0.500
1.500
Flow
Y
Z
X
0
1.000
2.000 (m)
0.500
1.500

(a) Overall

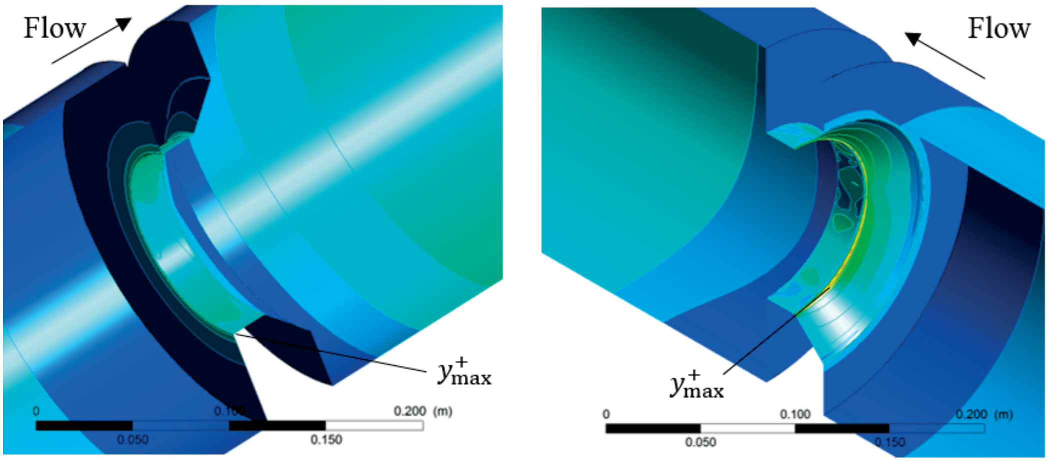
Flow
$y^+_{\max}$
0
0.100
0.200 (m)
0.050
0.150
Flow
$y^+_{\max}$
0
0.100
0.200 (m)
0.050
0.150

(b) Sharp approach - detail

(c) Chamfer approach - detail

Figure 4.13 – NUM_001 - Values of y^+ on pipe walls

Mesh

For all the meshes, the mesh quality was inspected prior to the simulation. Before each simulation, three criteria, i.e. the mesh orthogonality, the aspect ratio and the expansion factor, are verified by ANSYS in order to determine if the mesh is good, acceptable or questionable (as defined in ANSYS (2016b)). The meshes where the quality is insufficient were always re-meshed in order to be, at the very least, acceptable.

4.2.7 Validation

Validation comparing the numerical and experimental results of the sharp and chamfer approach flow directions were performed (see Section 5.6.1). However, the effects of the upstream and downstream lengths, mesh refinement and turbulence models were also evaluated (see Section 4.2.7). All the numerical simulations for the validation were performed with orifice EXP_007-NUM_007 (see right margin). The discharge was always equivalent to 30 l/s for the validation. Furthermore, the boundary conditions were those found in Figure 4.11.

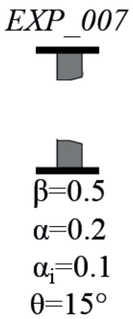

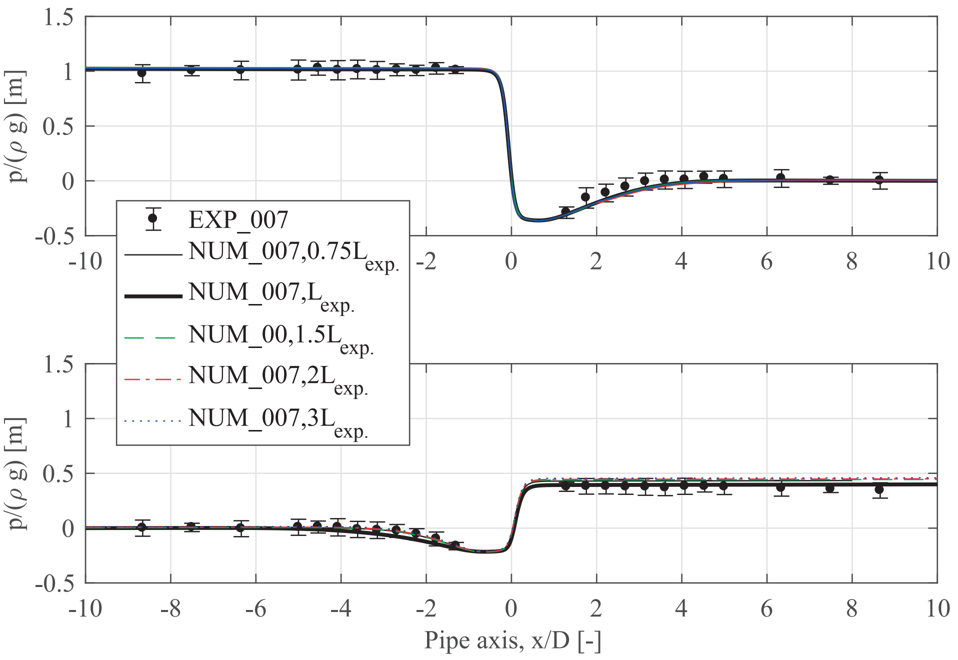

Figure 4.14 – Influence of the upstream and downstream length on the pressure line along the pipe axis in the numerical model compared to the experimental results (mean pressure and 95% confidence interval) for orifice EXP_007 - NUM_007

Influence of upstream and downstream distance

Four different upstream and downstream lengths, from 7.5 D to 30 D, are tested to evaluate their influence on the head losses produced by the orifice. Figure 4.14 shows a comparison of the pressure line for the different lengths. The downstream boundary condition is an opening anyway. There is no major difference of head losses for all the upstream and downstream lengths. Consequently, taking the length of the main experimental pipe allows approaching the experimental conditions and being independent of the boundary conditions of the numerical model.

Mesh sensitivity

Four mesh refinements were tested as outlined in Table 4.10. Figure 4.10 demonstrates that when the number of cells is higher than 10^6, there is solid agreement with the experimental results for the head losses and minimum pressure in the pipe. For all refinements, the inflation close to the walls was not modified, leading to comparable values of y^+. The Medium-2 mesh was utilized in this study.

Table 4.10 – Number of cells with the four mesh refinements

Name	# of cells
Fine	3.5 M
Medium-1	2.5 M
Medium-2	1.5 M
Coarse	0.7 M

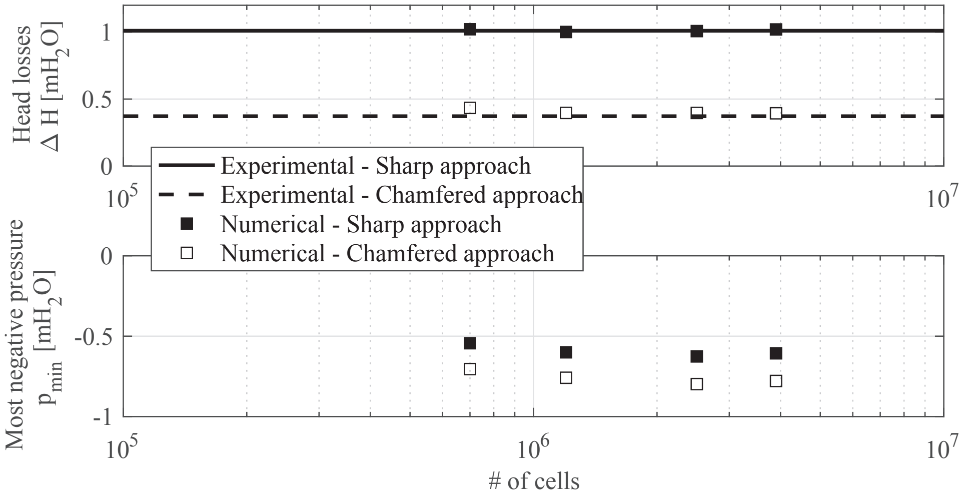

Figure 4.15 – Influence of mesh refinement on head losses along the pipe axis and the most negative pressure on the numerical model compared to the experimental results for orifice EXP_007 - NUM_007

Turbulence model

Numerical simulations with orifice NUM_007 were performed with four different turbulence models, i.e. standard k-ε, standard k-ω, SST and the Baseline Explicit Algebraic Reynolds stress model (BSL EARSM). Figure 4.16 compares the experimental results for orifice EXP_007 (Table 4.2) and the numerical results for orifice NUM_007.

For the sharp approach flow, it can be seen that k-ε underestimates head losses by 10%. With this, the other turbulence models are in line with the upstream pressure. For the downstream component of the flow, the increase in pressure after the *vena-contracta* is quite well-approximated by all turbulence models.

For the chamfered approach, the k-ε and k-ω models overestimates the upstream pressure by almost 10% while the SST model overestimates it by 5%. There is no major difference for the downstream increase in pressure.

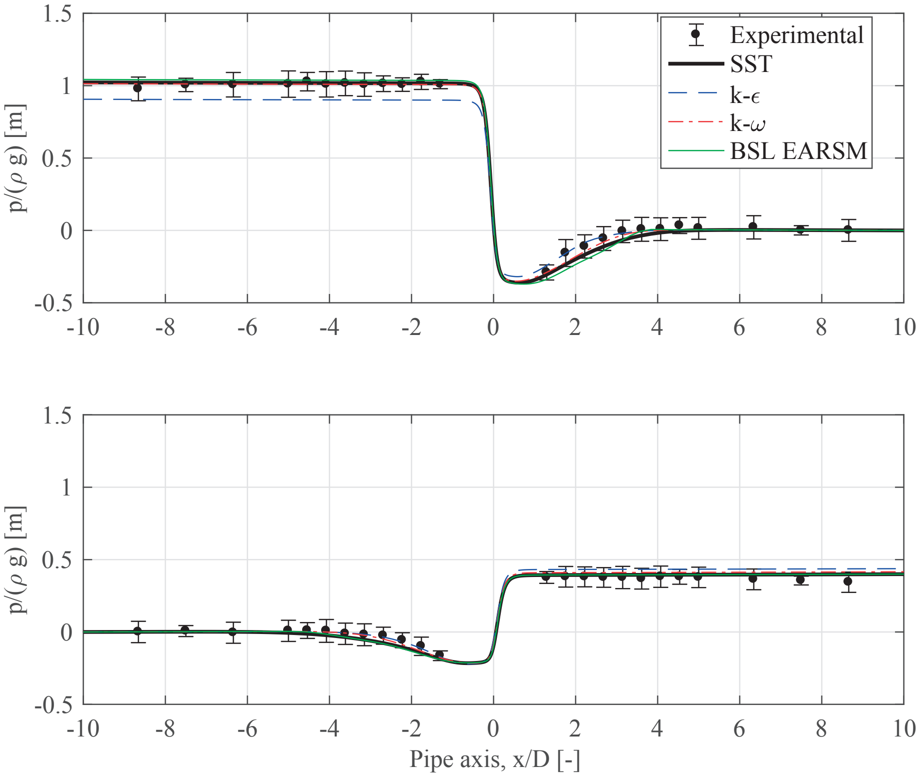

Figure 4.16 – Influence of the turbulence model on head losses along the pipe axis if the numerical model compared to the experimental results for orifice EXP_007 - NUM_007

5 Steady head losses of orifices[1]

5.1 Introduction

An orifice can be used as a throttling device at the entrance of a surge tank. During the design phase or in the analysis of a refurbishment, engineers conduct numerical simulations to simulate the behavior of the surge tank. A throttle introducing head losses can be necessary at the entrance of the surge tank to optimize its role. The results of this phase are generally a pair of head losses, i.e. one loss when the water flows in and one when the water flows out of the surge tank.

This chapter focuses on the evaluation of the pair of head losses for different orifice geometries (see Section 4.1.3). In a first step, two different orifice shapes, i.e. a chamfered shape defined by ISO (2003) and rounded orifices, with the shape fitted on the corresponding chamfered orifices, were experimentally studied. Enhanced empirical formulas for the estimation of head losses, based on Idel'cik (1969), are given. Then, the effect of an orifice with two chamfers (one on each side) is also experimentally evaluated. Practically speaking, these two chamfered orifices are juxtapositions of two single-chamfered orifices. Finally, a larger data set of chamfered orifice was numerically assessed in order to verify and extend the validity of the empirical formula derived during the first step.

5.2 Methods

As explained in Chapter 4.1, 10 different discharges were tested twice, in order to examine the local head losses produced by the orifice of the experimental model. For one discharge, the global head losses can be evaluated from the pressure line (Figure 5.1).

---

[1] This chapter is based on a submitted scientific paper: "Adam, N.J. De Cesare,G. & Schleis, A.J. (under revision). Influence of geometrical parameters of standard orifices on head losses of standard orifices. Submitted to the *Journal of Hydraulic Research*". The experimental and numerical work and the analyses presented hereafter is original and was performed by the author.

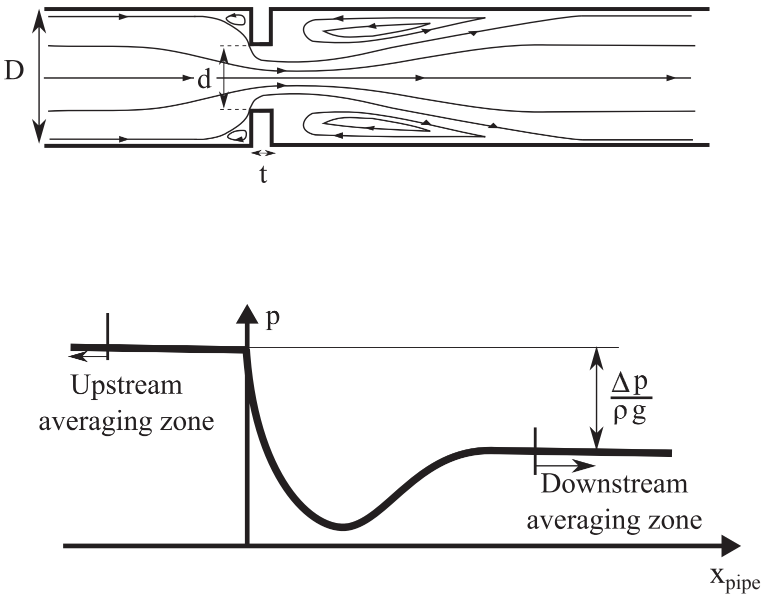

Figure 5.1 – Flow through an orifice with a schematic indication of the pressure evolution along the pipe

$$\frac{\Delta p}{\rho \cdot g} = k \cdot \frac{v_D^2}{2g} = k \cdot K_D \tag{5.1}$$

The head loss coefficient, k, was evaluated with Eq.(5.1) based on the kinetic energy in the main pipe and pressure drop between the upstream and downstream averaging zones:

- Upstream pressure (head): all the 12 control sections were used for the averaging. The last control section was $1.2\,D$ away from the upstream orifice side;
- Downstream pressure (head): only control sections after the jet wake were employed (Figure 5.1). The first control section was determined case by case. For the contraction ratio, $\beta = 0.5$, the reattachment length was approximately $3.15\,D$ according to Jianhua et al. (2010). For $\beta = 0.5$, eight control sections were utilized with the closest being $3.25\,D$ from the upstream orifice side.

For both averaging zones, the linear head losses produced by the pipe roughness and flow viscosity are taken into account even though the linear losses were equal to $0.004\,m$ between the two furthest sections with the greatest discharge according to Darcy-Weisbach.

For a given orifice, the asymmetry number, λ, is the ratio between the two head loss coefficients defined in Gabl et al. (2011). The value of the asymmetry ratio is always below 1, which means the head losses are symmetrical.

$$\lambda = \frac{k_{cont.}}{k_{sharp}} \tag{5.2}$$

5.3 Experimental results for orifices with a sharp side

5.3.1 Performed tests

In this first part of the experimental testing, there are only orifices with one sharp side (Table 4.2 and 4.3). For the analyses, the orifices were split into eight groups (Table 5.1).

Table 5.1 – Set of sharp orifices tested during the experimental work

Group name	Varying parameter	Interval	Orifices
C-R	Reference	/	EXP_001
C-A	θ	0°...67°	EXP_006, EXP_007, EXP_008, EXP_009
C-B	β	0.4...0.6	EXP_002, EXP_003, EXP_004, EXP_005
C-C	α_i	0...0.2	EXP_010, EXP_0105, EXP_011, EXP_006
C-D	α	0.05...0.4	EXP_012, EXP_013, EXP_032, EXP_026
R-R	Reference, shape	/	EXP_014
R-A	θ, shape	/	EXP_019, EXP_020, EXP_021
R-B	β, shape	0.4...0.6	EXP_015, EXP_016, EXP_017, EXP_018
R-C	α_i, shape	0...0.2	EXP_022, EXP_023, EXP_006
R-D	α, shape	0.015...0.2	EXP_024, EXP_025, EXP_932

For each orifice, during the experimental campaign, the pressure lines were recorded for the various assessed discharges. Figure 5.2 portrays the results of orifice EXP_001 (see right margin) for five different discharges and both flow directions (sharp and chamfer approach flow). These results were typical for all orifices for which the sharp head losses were higher than the chamfer head losses. Next, the local head losses produced by the orifice were determined for each discharge (Section 5.2). Finally, the head loss coefficients of the orifice were evaluated using the least-squares method as demonstrated in Figure 5.3. The experimental results are summarized in Appendix B, while the test-sheets (see Appendix D) with the experimental results are available on-line with the thesis (doi:10.5075/epfl-thesis-8090).

EXP_001

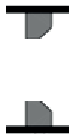

β=0.5
α=0.2
α_i=0.1
θ=45°

5.3.2 Asymmetry

As can be seen in Figure 5.4 and as expected, the head losses for the sharp approach flow were more than those from the contracted approach flow (chamfer and rounded). The contraction ratio, β, has a large influence on the head loss coefficient in both flow directions. Chamfered orifices permit producing a large range of asymmetry values, λ, between 0.35 and 1.0 while rounded orifice shapes have a more or less constant asymmetry value λ between 0.25 and 0.4 for series R-R, R-A, R-B and R-C series. For the R-D series, the asymmetry value varied from 0.33 to 0.53 while α varied from 0.2 to 0.05. These two orifice shapes cover a large area of asymmetry with ratios ranging from 1:4 to 1:1. The variation of the chamfered angle, θ (A series), and the inner thickness ratio, α_i (C series), had a higher influence on the asymmetry value, λ, than β.

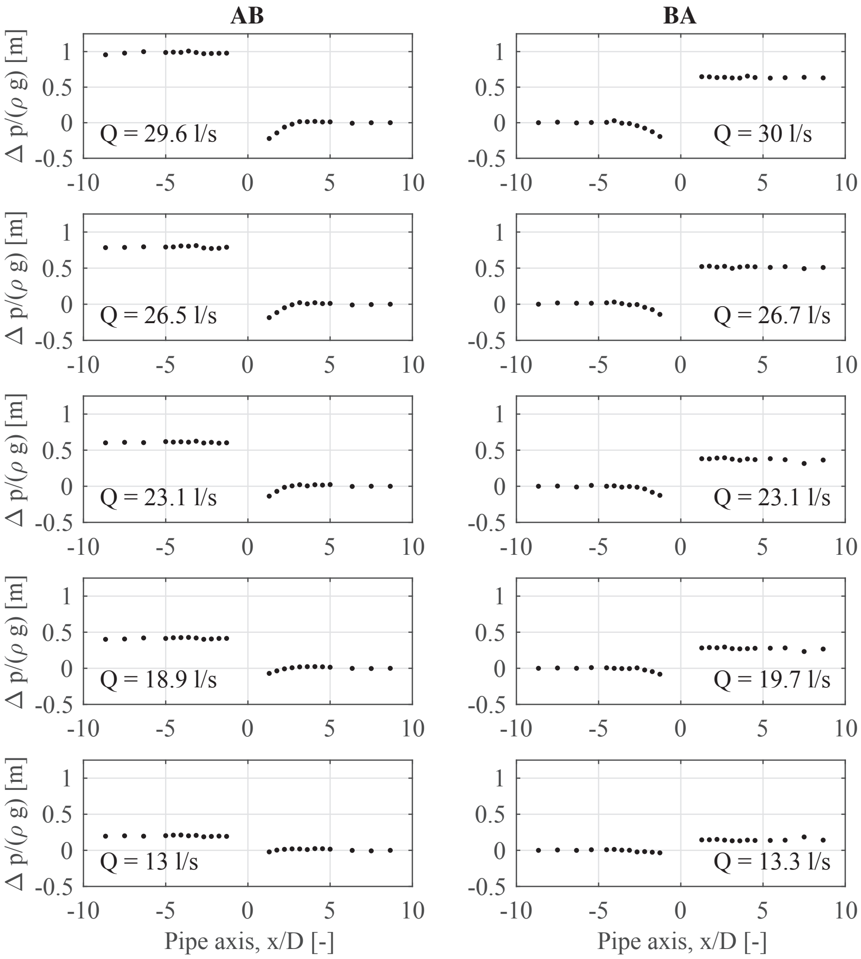

Figure 5.2 – EXP_001 - The pressure lines for five different discharges: (left) sharp approach flow (*AB*) and (right) chamfer approach flow (*BA*)

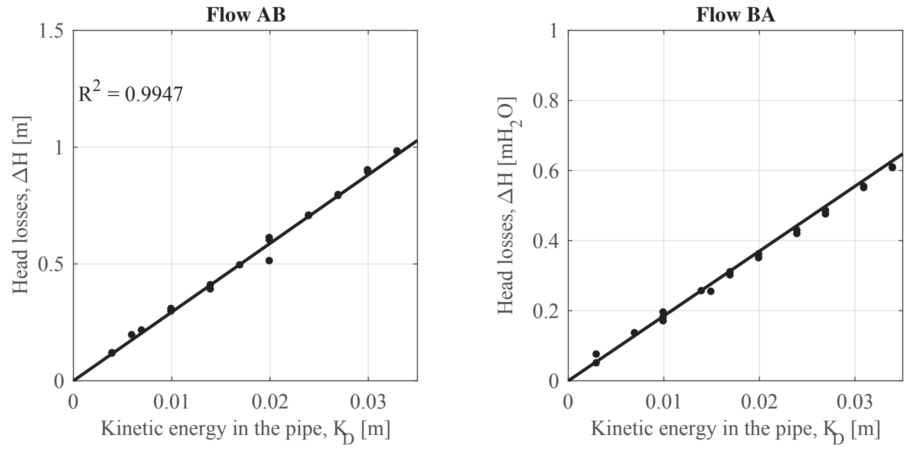

(a) Sharp approach flow (k_{sharp} = 29.4) (b) Chamfer approach flow ($k_{chamf.}$ = 18.2)

Figure 5.3 – EXP_001 - The pair of head loss coefficients for: (a) the sharp approach flow (*AB*) and (b) the chamfer approach flow (*BA*)

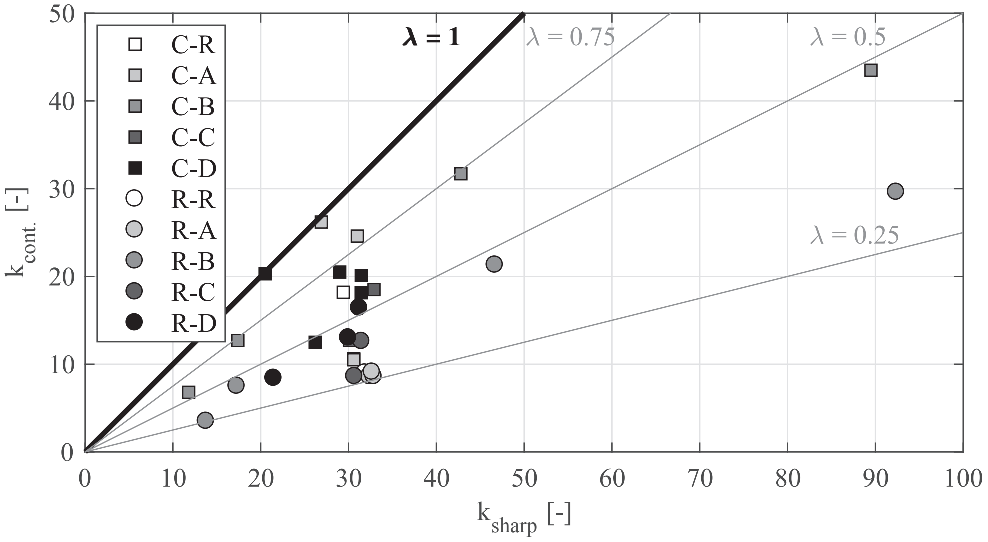

Figure 5.4 – Head loss coefficients for both flow directions and asymmetry: for the chamfered orifices from Table 5.1 with: C-R (reference chamfered orifice), C-A (variation of the angle, θ), C-B (variation of the contraction ratio, β), C-C (variation of the inner thickness ratio, α_i) C-D (variation of the thickness ratio, α); and for rounded orifices from Table 5.1 with R-i, the corresponding orifices related to the $C-i$ set of standard orifices (i is equal to A,B,C or D)

5.3.3 Head losses for sharp flow direction (*AB*)

The relationship between the inner thickness ratio, α_i, and the head losses for the sharp approach flow is portrayed in Figure 5.5. For chamfered and rounded orifices, head loss coefficients decrease linearly while α_i is increasing. This reduction is greater than that described by Idel'cik (1969).

Eq.(5.3) is similar to Eq.(3.3) in Idel'cik (1969) for evaluating head loss coefficients corresponding to different orifice geometries (see Eq. (3.3) and (3.4)). Eq. (3.4) shows that only the parameter τ, which depends on the shape and thickness of the orifice, can be modified. The present study introduced a new correction factor, $\Upsilon_{\alpha i}$, fitted on the experimental results (Table 5.1) and depending on the inner thickness ratio as given by Eq.(5.4).

$$k_{sharp} = \Upsilon_{\alpha i} \cdot \frac{(1+\tau\sqrt{(1-\beta^2)}-\beta^2)^2}{\beta^4} \tag{5.3}$$

where $\Upsilon_{\alpha i}$ is given by Eq.(5.4), and $\tau = 0.745$.

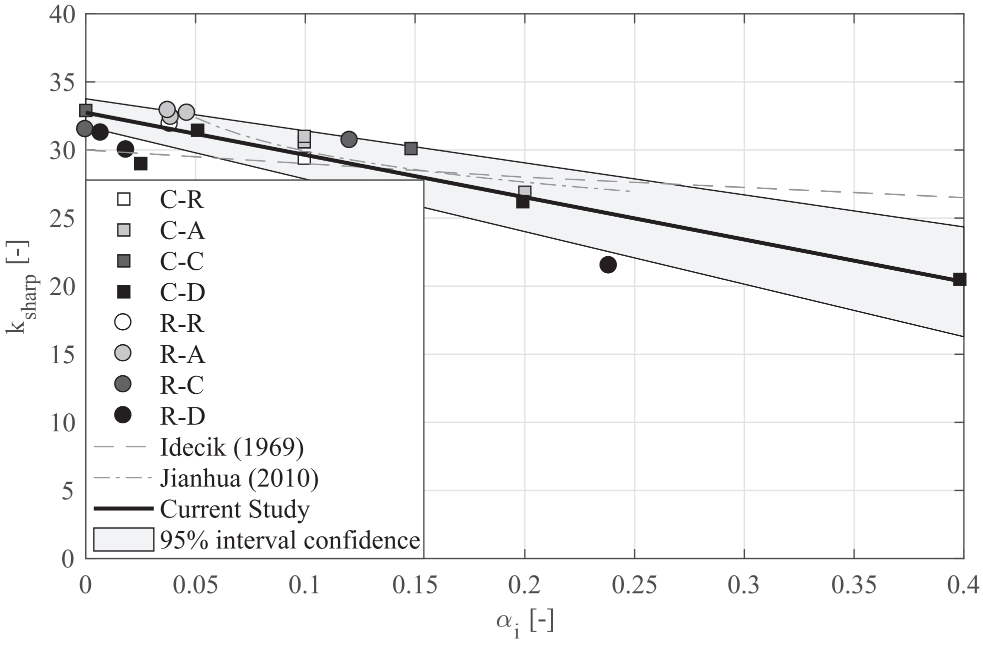

Figure 5.5 – Highest (sharp) head loss coefficients for tested inner thickness ratio ($\alpha_i \in$ [0...0.2]): for chamfered and rounded orifices from Table 5.1 with: C(R)-R (reference chamfered and rounded orifices), C(R)-A (variation of the angle, θ), C(R)-B (variation of the contraction ratio, β), C(R)-C (variation of the inner thickness ratio, α_i) C(R)-D (variation of the thickness ratio, α); for a comparison between two formulae from Idel'cik (1969) (Eq. (3.3)) and Jianhua et al. (2010) (Eq. (3.7)) and an new empirical formula defined in the present study (Eq. (5.3))

$$\Upsilon_{\alpha i} = 1 - \kappa_{\alpha i} \cdot \alpha_i \tag{5.4}$$

where $\kappa_{\alpha i} = 0.9486$ is fitted on the experimental results for sharp approach flow

The empirical formula (5.3) is applied to the B series (Table 5.1). Robust agreement between the results and the predicted head loss coefficient evident in Figure 5.6. A comparison was performed with the other formulas described in Chapter 3.1. No large discrepancy is apparent. The decrease of head loss coefficients depend mainly on α_i and not on α if there is no interaction between the chamfer edge and flow.

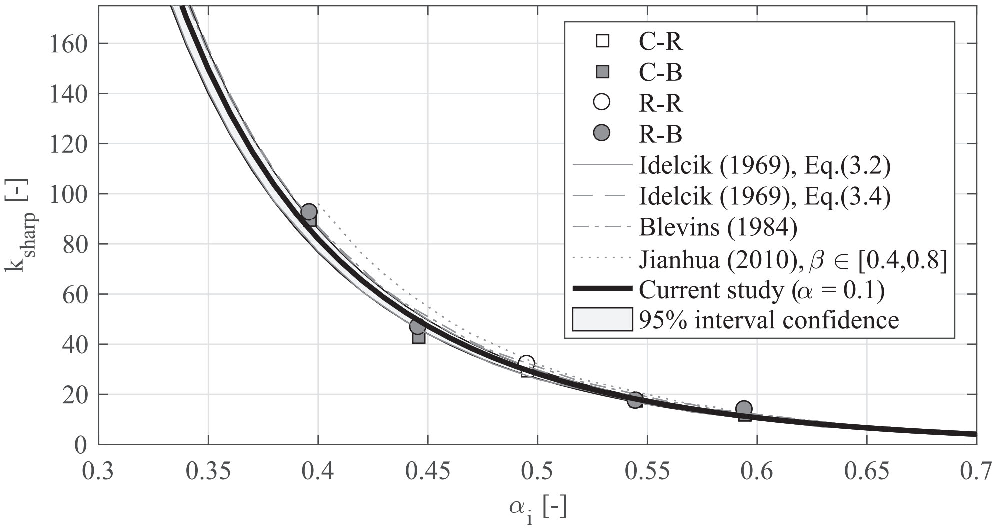

Figure 5.6 – Comparison of the experimental results (data set C-B and R-B varying the contraction ratio β), present study equation (Eq. (5.3)) and existing equations (Section 3.3): Idel'cik (1969) (Eq. (3.3): $k' = 0.5$ and $\tau = 1.1$ and (3.4): $\tau = 0.707$), Blevins (1984) (Eq. (3.5): $C = 0.6$), and Jianhua et al. (2010) (Eq. (3.7): $\alpha = 0.5$)

5.3.4 Head losses for chamfer approach flow (*BA*)

Influence of the angle The influence of the chamfer angle, θ, on the chamfer head loss coefficient can be seen in Figure 5.7. The results show there is a decrease of head loss coefficient from 0 to 15 degrees, and a minimum value between 15 and 30 degrees. From 30 degrees onwards, the head loss coefficient rises until the head loss coefficient related to a 90-degrees chamfer angle (constant orifice thickness equivalent to $\alpha = 0.1$). Furthermore, there is a variation of head losses for angles between 40 and 60 degrees while Idel'cik (1969) reported constant losses.

A new parameter, λ_θ, representing the asymmetry value, which relies upon the angles and fits the experimental results, is introduced via Eq.(5.5). This new parameter corrects the sharp head loss coefficient, Eq.(5.3), without modification.

$$k_{chamfer} = \lambda_\theta \cdot \left[\Upsilon_{\alpha i} \cdot \frac{(1+\tau\sqrt{(1-\beta^2)}-\beta^2)^2}{\beta^4} \right] \tag{5.5}$$

where λ_θ is given by Eq.(5.6) along with $\Upsilon_{\alpha i}$ and τ are given by Eq.(5.3) for $\alpha_i = 0.1$.

$$\lambda_\theta = \sin(\theta - \theta^{'}) + e^{-\kappa_\theta \cdot \theta} \tag{5.6}$$

where $\theta^{'} = \frac{1}{18}\pi$ and $\kappa_\theta = \frac{3}{2}\pi$. The angle, θ, must be in radians.

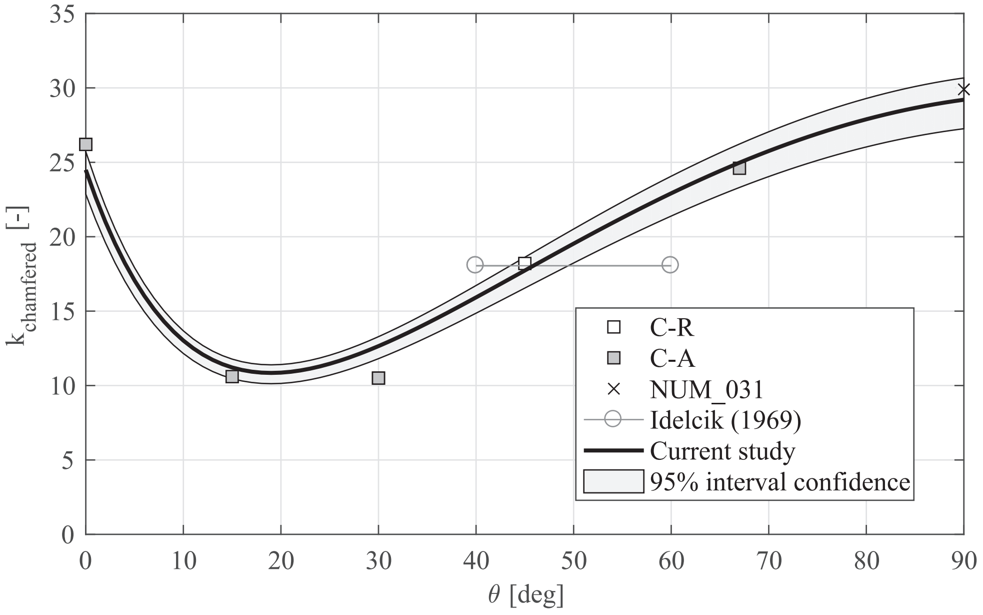

Figure 5.7 – Influence of the chamfer angle, θ, on the chamfer head loss coefficient for a data set of standard orifices, R and A, fitted with a new empirical formula (Eq. (5.5)) and a comparison of the existing formulas from Idel'cik (1969) (Eq. (3.3): $k' = 0.5$ and $\tau = 1.285$ and (3.4): $\tau = 0.361$)

Influence of the inner orifice thickness, α_i, and the chamfer thickness, α_θ Figure 5.8 illustrates the influence of the inner orifice thickness, α_i, and the chamfer thickness, α_θ, on the head loss coefficient for the chamfer approach flow. Two trends can be distinguished: Firstly, the asymmetry ratio, λ, decreases with α_i for a given angle[2] (here, $\theta = 45°$); Secondly, the asymmetry ratio, λ, tends to 1 when α_θ tends to 0, which is logical because of the disappearance of the chamfer angle.

It seems to have interactions between the influences of α_i and α_θ on the contracted head loss coefficient, and these interactions were evaluated (see Section 5.4).

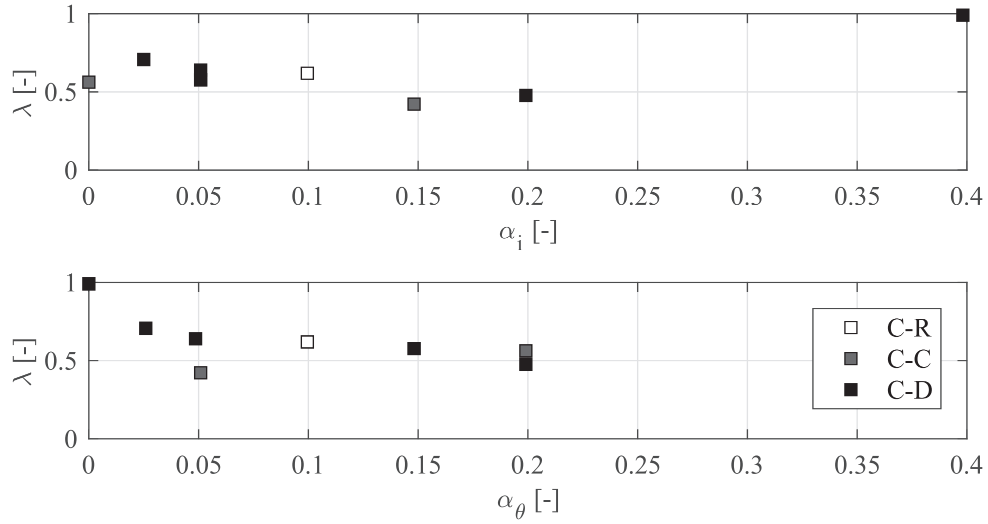

Figure 5.8 – Evolution of the asymmetry ratio λ for the chamfer approach as a function of the inner thickness ratio, α_i, and the chamfer thickness ratio, α_θ (C-R, C-C and C-R series)

Table 5.2 – Orifices considered for the analysis of the different chamfer angles

Angle θ	Right chamfer (θ_R)	Left chamfer (θ_L)
0°	EXP_001 to EXP_035 & EXP_932	
15°	EXP_007, EXP_028, EXP_043	EXP_040, EXP_041 & EXP_042
30°	EXP_008, EXP_030, EXP_040 & EXP_046	EXP_044 & EXP_045
45°	EXP_034, EXP_035, EXP_036, EXP_037, EXP_038, EXP_039, EXP_043, EXP_046, EXP_049, EXP_050, EXP_052, EXP_053, EXP_054 & EXP_055	EXP_001, EXP_010, EXP_0105, EXP_011, EXP_012, EXP_013, EXP_027, EXP_031, EXP_032, EXP_033, EXP_038, EXP_045, EXP_047, EXP_050, EXP_051, EXP_052, EXP_053, EXP_054 & EXP_055
67°	EXP_009, EXP_030, EXP_044 & EXP_049	EXP_047 & EXP_048

---

[2] The point $\alpha_i = 0.4$ and $\lambda = 1$ is orifice EXP_026 with two sharp-edged angles ($\theta = 0°$)

5.4 Experimental results for orifices with two chamfered angles

Table 4.4 outlines the orifices with two chamfered angles. Those orifices are characterized by the juxtaposition of two chamfer orifices, which are fixed by their sharp side. In the previous Section, it could be concluded that the chamfer angle, θ, does not have an influence on the head loss coefficient for the sharp approach flow. This means that each angle should be independently taken.

The goal of the present section was to evaluate the influence of the inner thickness ratio on the head loss coefficient produced in the chamfer ($\theta_R(\theta_L) = 15°, 30°, 45°$ or $67°$) or sharp ($\theta_L = 0°$) approach flow, upon which the empirical formula (Eq.(5.3)) was verified for the other α_i.

The influence of the chamfer thickness ratio, α_θ, can be highlighted for the angle 45°, as there are different α_θ values for this angle.

Note that the distinction between left and right has no influence on the results.

5.4.1 Influence of α_i on the head loss coefficients of orifices with chamfer, $\theta_R\, or\, \theta_L = 45°$

Figure 5.9 depicts the results for orifices with a chamfer angle, $\theta = 45°$ (Table 5.2). For this angle, different chamfer thickness ratios α_θ were tested. As can be seen in Figure 5.9, α_θ has little impact on the head losses. When α_θ rises, the head loss coefficient diminishes. However, α_θ loses its influence for high ratios ($\alpha_\theta \geq 0.1$) (Figure 5.10). It can be also observed in Figure 5.9 that the head loss coefficients with different α_θ values decrease with almost the same slope $\kappa_{\alpha i}$. However, for $\alpha_\theta = 0$, the value of $\kappa_{\alpha i}$ has to be equal to the value defined in Section 5.3.3.

The relationship between the asymmetry ratio, λ_θ^0, created by the chamfer angle, $\theta = 45°$, is shown in Figure 5.10 and Eq.(5.7). The superscript 0 means that this asymmetry ratio is relative to $\alpha_i = 0$. The empirical formula, developed for the chamfer approach flow, is discussed herein (see Section 5.4.3).

$$\lambda_\theta(\alpha_\theta) = \frac{\lambda_\theta^0 \cdot \alpha_\theta + 0.0125}{\alpha_\theta + 0.0125} \tag{5.7}$$

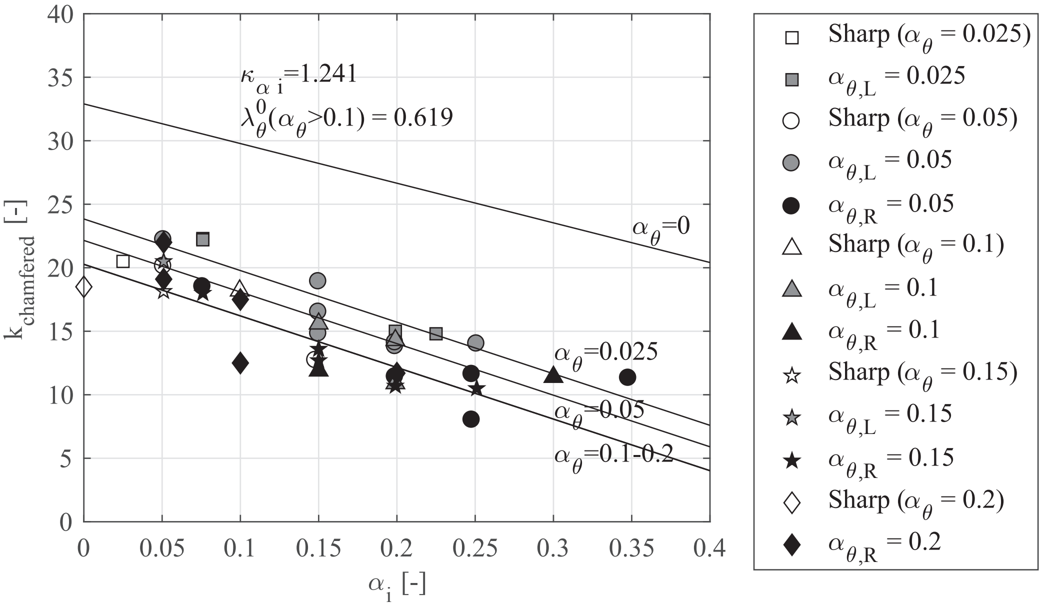

Figure 5.9 – Head losses produced by a chamfered angle of $\theta_R\ or\ \theta_L = 45°$

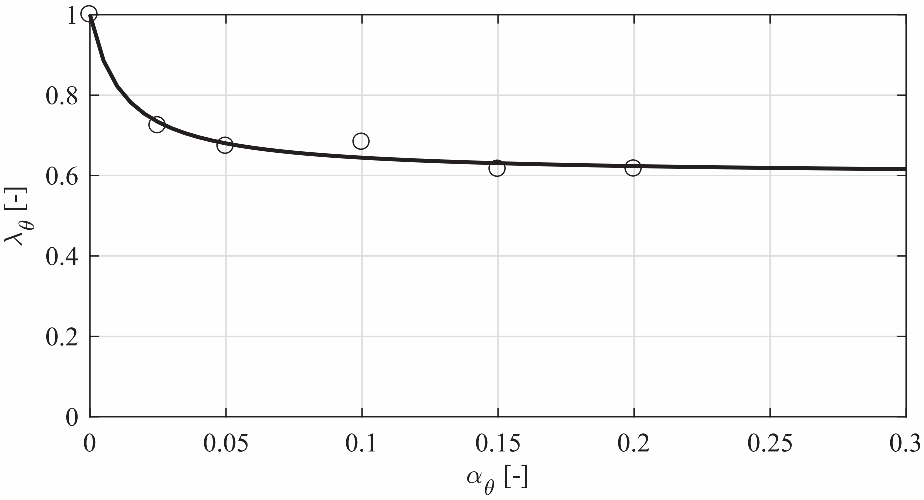

Figure 5.10 – The asymmetry ratio, λ_θ, as a function of the chamfer thickness ratio α_θ for $\theta = 45°$

5.4.2 Influence of α_i on the head loss coefficients of orifices with chamfer angle of $0°$, $15°$, $30°$ or $67°$

The orifices considered for the analysis for each chamfer angle, θ, are located in Table 5.2. In Figure 5.11, the evolution of the head losses produced by a chamfer of 0°, 15°, 30° and 67° for different inner thickness ratios, α_i, but for the same α_θ is portrayed.

For each angle, it is possible to define λ_θ^0 and $\kappa_{\alpha i}$, which respectively are the head loss coefficient for $\alpha_i = 0$ and the slope of the decrease with α_i. The least-squares method was used for all the linear fitting. The relevant observations are as follows:

- for the sharp approach flow (0°), the fitting performed on the chamfered and rounded orifices (Section 5.3) was still well-adapted to the extended set of sharp orifices;
- for the chamfer approach flow with the angles producing the smallest head losses, the head loss coefficient did not really depends on α_i. This can be explained by the fact that, for the small angles ($\theta = 15°$ or $30°$), the flow did not detach from the orifice wall (as described in Section 5.7.2); and
- for the highest angles, the behavior had the same shape as the sharp approach flow ($\theta = 0°$). However, the slope was higher, thereby indicating a faster decrease in head loss coefficient than with the sharp approach flow.

5.4.3 Empirical relationship for head loss estimation

Figures 5.9 and 5.11 reveal that two coefficients have an influence on the chamfered head loss coefficient:

- The asymmetry ratio, λ_θ^0, which varies with α_θ and depends on θ as shown in Eq.(5.7), were taken for $\alpha_i = 0$ in order to separate the influence from α_i and α_θ. The evolution of λ_θ^0 as a function of θ is depicted in Figure 5.12 for $\alpha_\theta \geq 0.1$. The empirical relationship (Eq.(5.8)) is more aligned with the experimental results than Eq.(5.5).

$$\lambda_\theta^0(\theta) = 1.304\theta^4 - 5.97\theta^3 + 9.054\theta^2 - 4.55\theta + 1 \tag{5.8}$$

where: θ is in radians

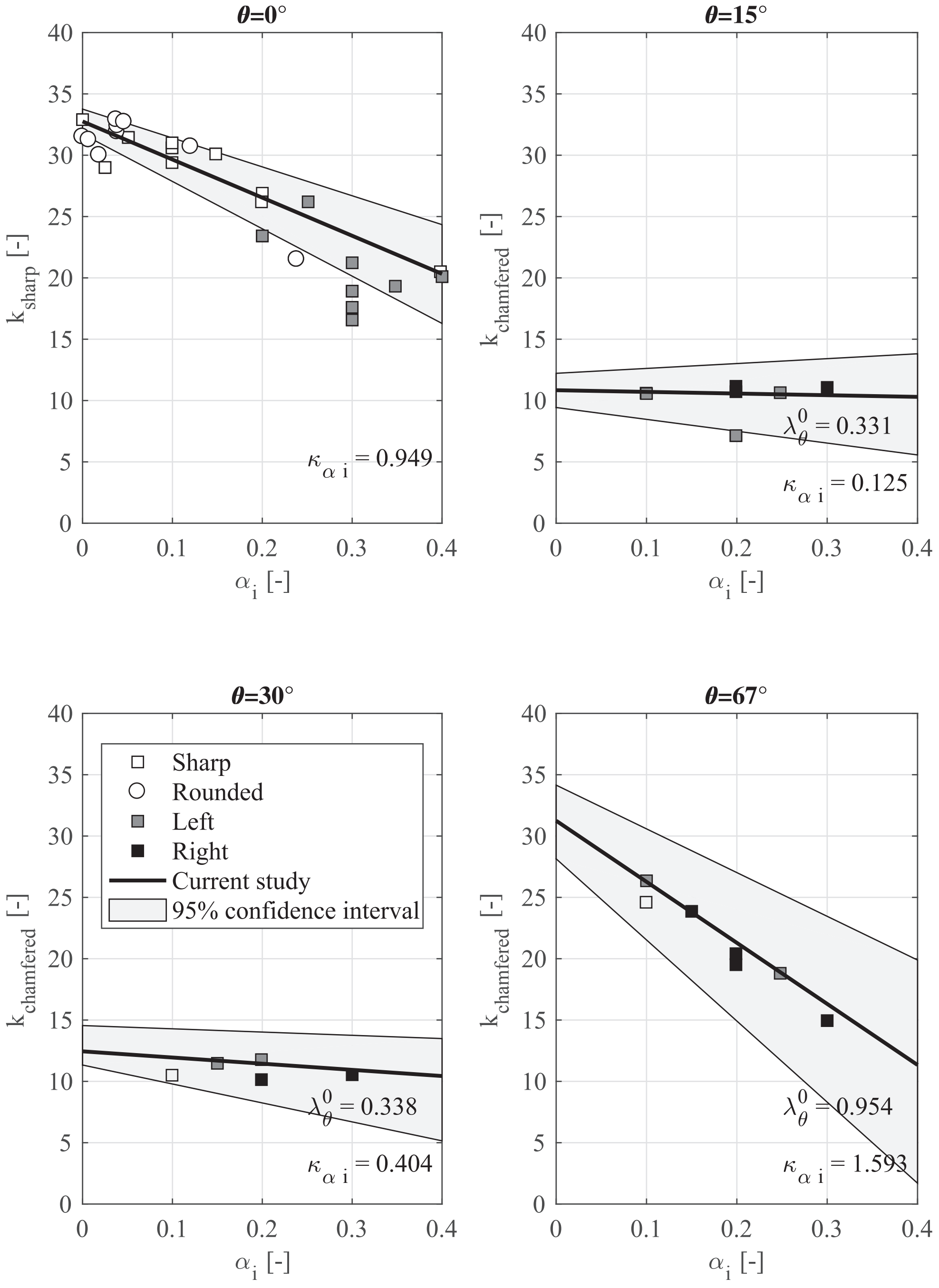

Figure 5.11 – Influence of the inner thickness ratio, α_i, on the sharp head loss coefficient ($\theta = 0°$) compared to between the empirical formula (Eq.(5.3))and different chamfer head loss coefficients ($\theta = 15°, 30°$ or $67°$)

- The decreased slope, $\kappa_{\alpha i}$, which describes the linear fall of the head losses with the increase of α_i. The relationship between $\kappa_{\alpha i}$ and θ is shown in Figure 5.12. The empirical relationship (Eq.(5.9)), fitted on the experimental results, yields the slope for all the angles($\theta \in [0°, 90°]$). Furthermore, $\kappa_{\alpha i}$ also depends on α_θ: if $\alpha_\theta \in [0, 0.1[$, a linear interpolation is performed between the two values.

$$\kappa_{\alpha i}(\theta) = 3.18\theta^4 - 13.88\theta^3 + 18.60\theta^2 - 7.29\theta + 0.949 \tag{5.9}$$

where: θ is in radians

Therefore, Eq.(5.10) is an empirical relationship evaluating the chamfered head loss coefficient for a given orifice geometry. Note that if there is no chamfer angle, the relationship is equivalent to the empirical relationship found for the sharp head loss coefficient (Eq.(5.3)).

$$k_{chamfer} = \lambda_\theta \cdot \Upsilon_{\alpha i} \cdot \frac{(1 + \tau\sqrt{(1-\beta^2)} - \beta^2)^2}{\beta^4} \tag{5.10}$$

where $\lambda_\theta = \frac{\lambda_\theta^0 \cdot \alpha_\theta + 0.0125}{\alpha_\theta + 0.0125}$, λ_θ^0 given by Eq.(5.8), $\Upsilon_{\alpha i} = 1 - \kappa_{\alpha i} \cdot \alpha_i$, $\kappa_{\alpha i}$ given by Eq.(5.9) and $\tau = 0.745$.

The fit of the empirical relationship Eq.(5.10) portrayed in Section 5.6.3 (Figure 5.22) for all the experimental and numerical results.

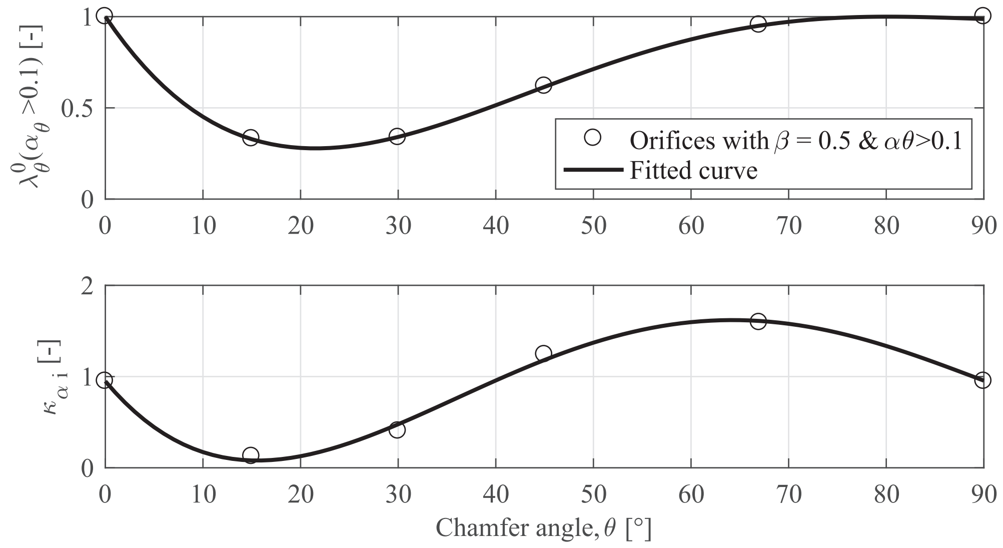

Figure 5.12 – Evolution of the coefficients, λ_θ^0 and $\kappa_{\alpha i}$, as a function of the chamfer angle, θ

5.5 Experimental results for rounded orifices

In Section 5.3.3, it was demonstrated that there was no difference when evaluating the sharp head loss coefficients for the chamfered and rounded orifices. However, Figure 5.4 shows that the head loss coefficients for the rounded approach flow were almost constant and less than with the chamfer approach flow. The method used for chamfer approach flow (Section 5.4) was applied to the rounded approach flow. Figure 5.13 shows the evaluation of λ_a (which is equivalent to λ_θ) and the slope, $\kappa_{\alpha i}$, for $\alpha_\theta > 0.1$. An empirical relationship similar to Eq.(5.10) was found as seen in Eq.(5.11). However, for the rounded approach, the coefficients, λ_a, were taken as constant. A linear variation was also taken between $\kappa_{\alpha i}(\alpha_a > 0.1)$ and $\kappa_{\alpha i}(\alpha_a = 0)$.

$$k_{rounded} = \lambda_a \cdot \Upsilon_{\alpha i} \cdot \frac{(1+\tau\sqrt{(1-\beta^2)}-\beta^2)^2}{\beta^4} \tag{5.11}$$

where λ_a is given by Eq.(5.12), $\Upsilon_{\alpha i} = 1 - \kappa_{\alpha i} \cdot \alpha_i$, $\kappa_{\alpha i}$ comes from Figure 5.13 with $\tau = 0.745$.

$$\lambda_a = \frac{\lambda_a^0 \cdot \alpha_\theta + 0.0125}{\alpha_\theta + 0.0125} \tag{5.12}$$

where λ_a^0 is given by Figure 5.13

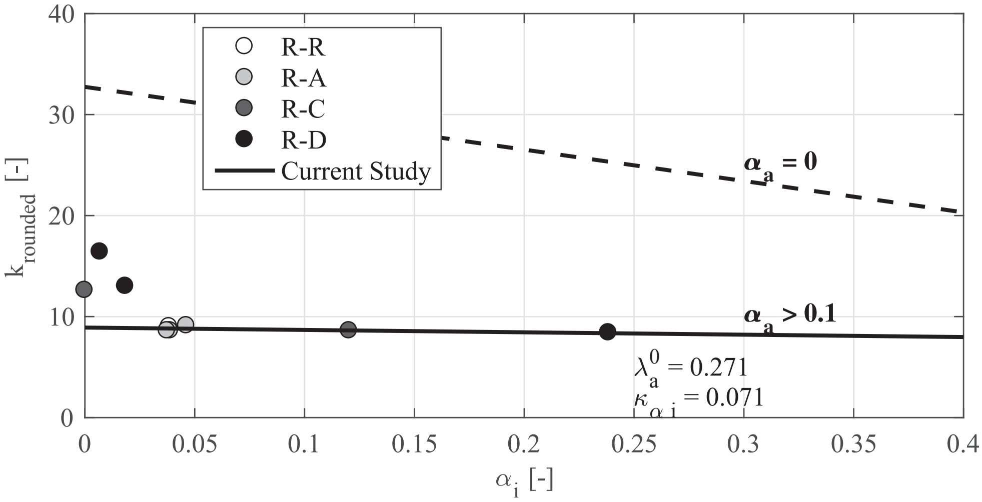

Figure 5.13 – Rounded head loss coefficient, $k_{rounded}$, as a function of the inner thickness ratio α_i

Figure 5.14 illustrates the comparison between the experimental and predicted values. It can be seen that 90% of the predicted values are within the ±20% lines, while 70% are within the ±10% lines.

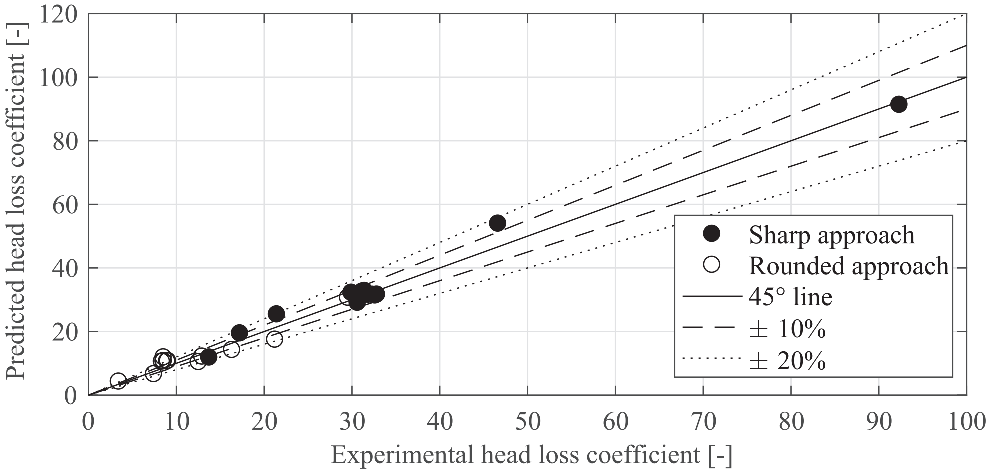

Figure 5.14 – Comparison between the experimental and predicted head loss coefficient values for the rounded orifices with the sharp and rounded approach flows

5.6 Numerical

5.6.1 Comparison between the experimental and numerical results

For the validation of the numerical model, the chamfered orifices, which were tested during the experimental campaign, were numerically tested and compared to the experimental pressure lines.

Figures 5.15 to 5.19 depict the comparison between the experimental and numerical results for the A series (see Table 5.1). For the sharp approach, the numerical model tended to be model precisely the pressure line and, hence, the head losses. For the chamfer approach flow, there was a strong accuracy (differences less than 5%) for the low and high angles ($\theta = 15°, 30°$ and $67°$). However, there were significant discrepancies, equating to roughly 25%, for the middle angle ($\theta = 45°$). This can be explained by the intermediate behavior of this angle (Section 5.7.2).

The numerical model fits the pressure well in the orifice jet for both flow direction and for all tested chamfer angles.

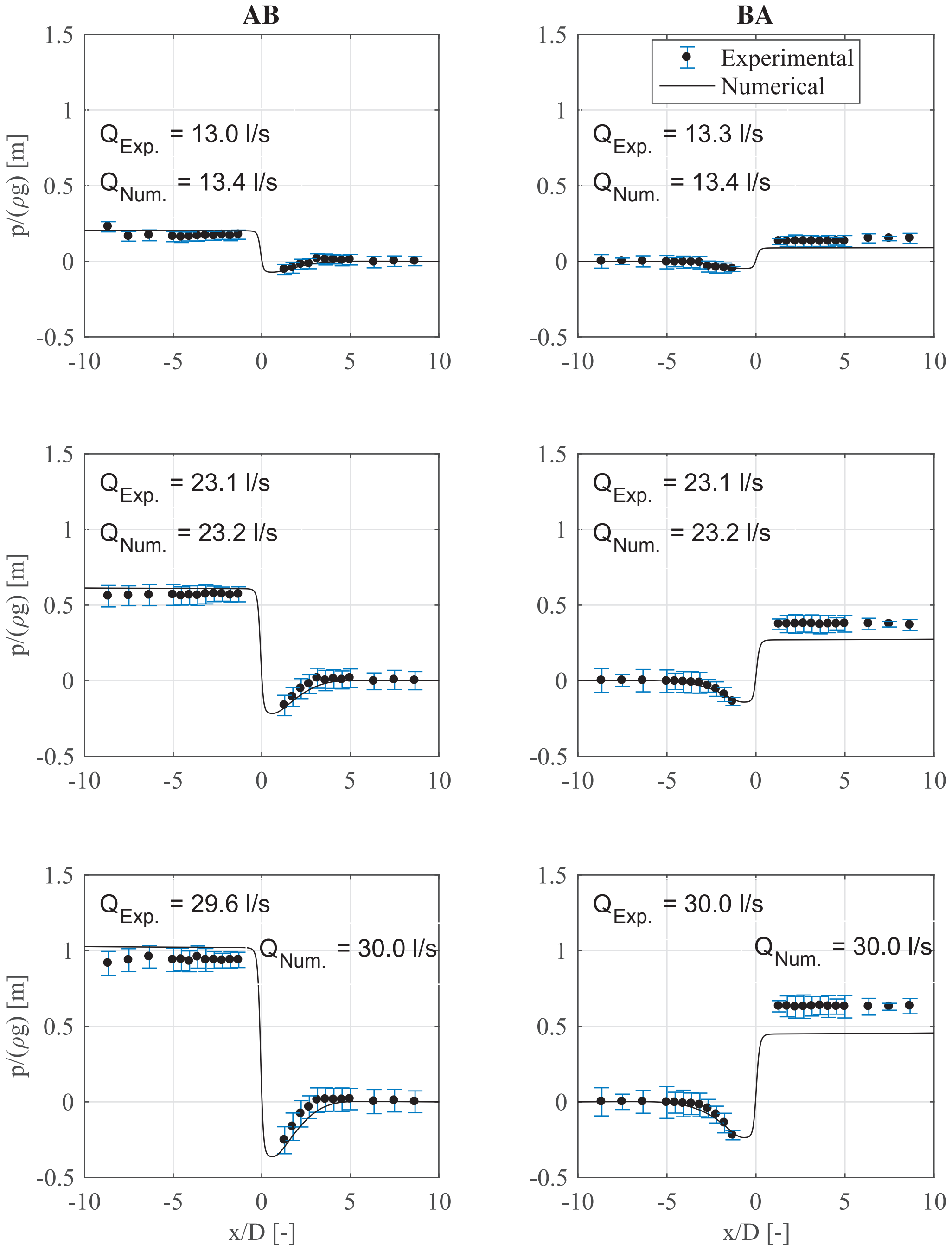

Figure 5.15 – Orifices EXP_001 and NUM_001 ($\beta = 0.5$, $\alpha = 0.2$, $\alpha_i = 0.1$ and $\theta = 45°$) - comparison between the experimental results with 95% confidence interval ($\pm 1.96\sigma$) and the numerical results.

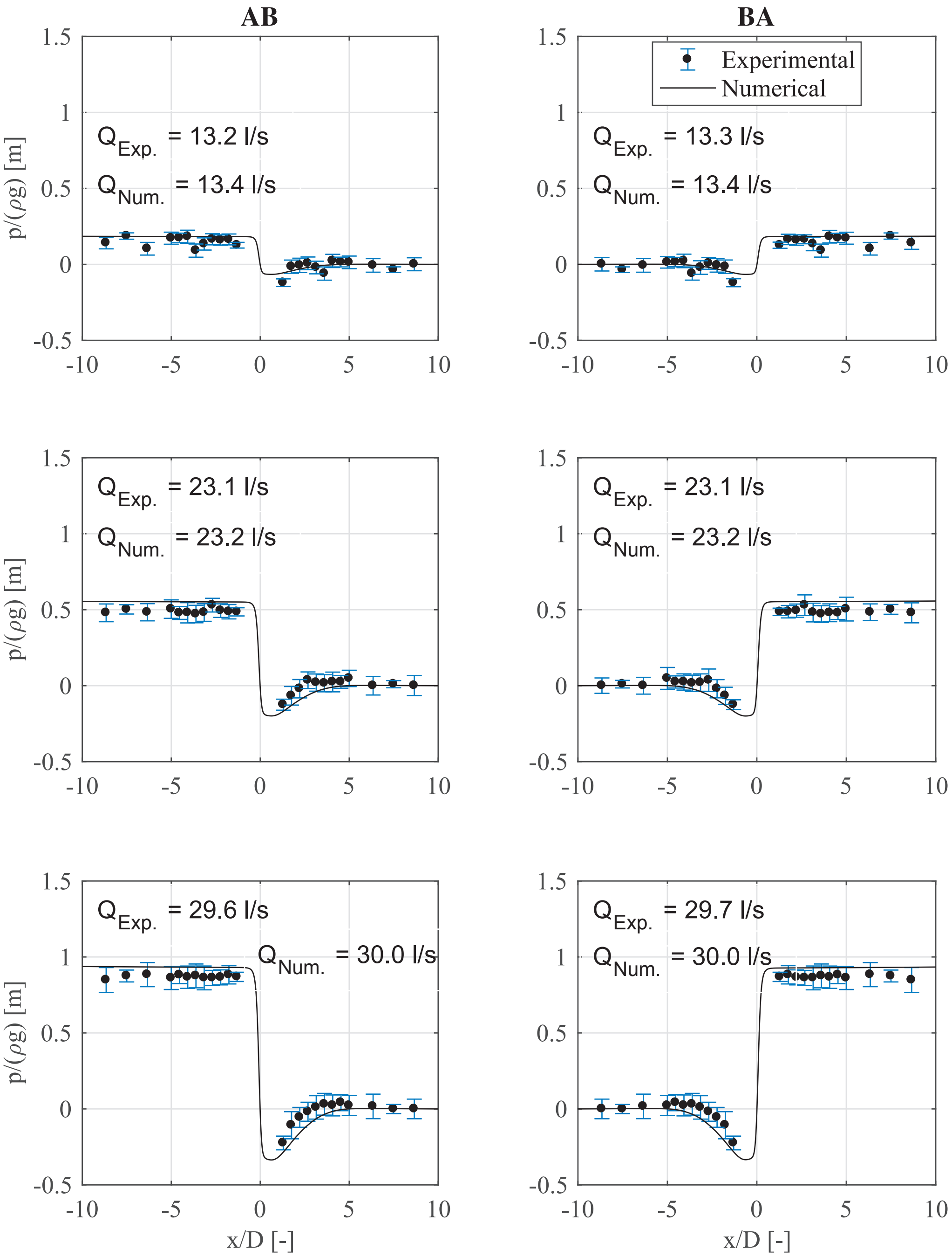

Figure 5.16 – Orifices EXP_006 and NUM_006 ($\beta = 0.5$, $\alpha = 0.2$, $\alpha_i = 0.2$ and $\theta = 0°$) - Comparison between the experimental results with 95% confidence interval ($\pm 1.96\sigma$) and the numerical results.

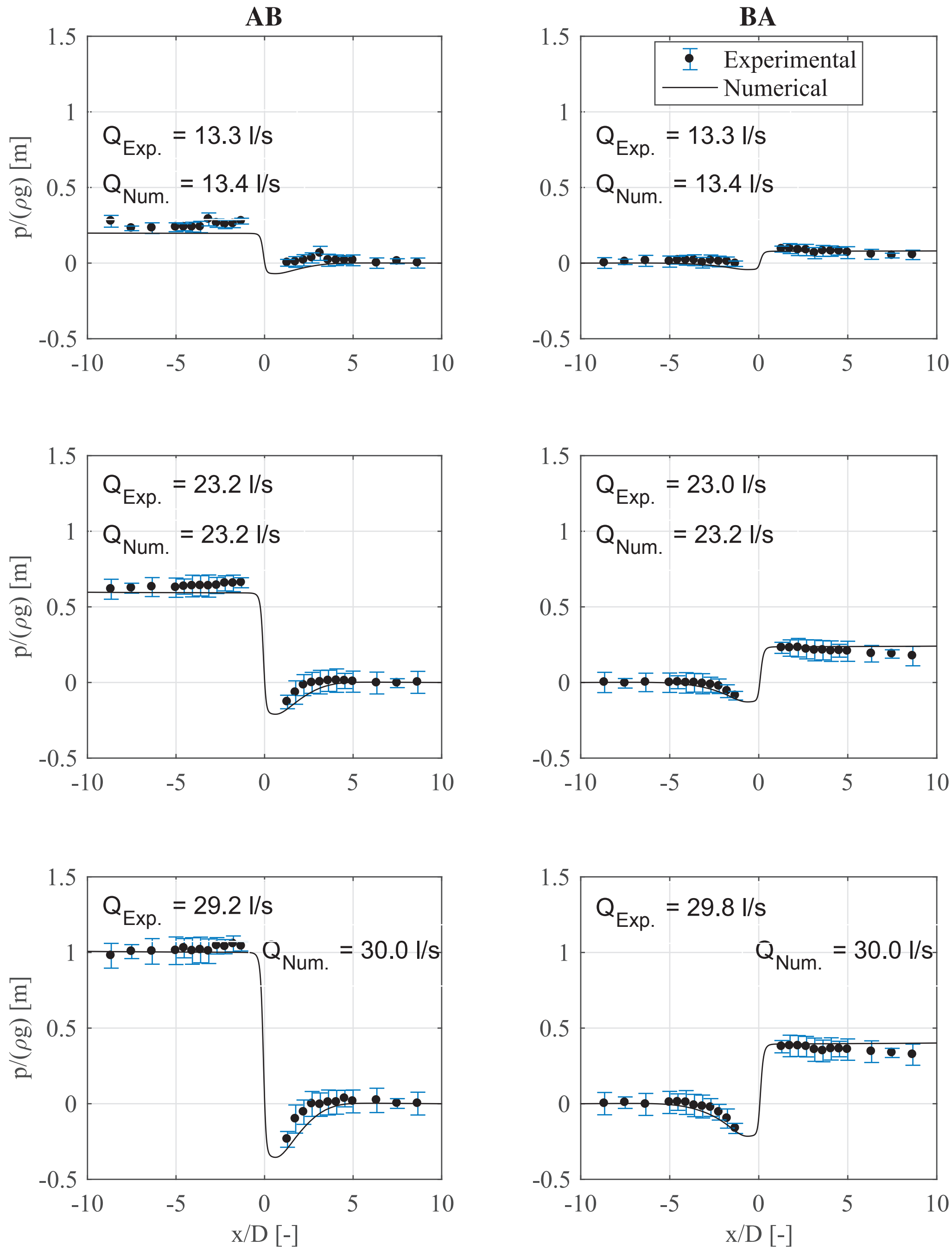

Figure 5.17 – Orifices EXP_007 and NUM_007 ($\beta = 0.5$, $\alpha = 0.2$, $\alpha_i = 0.1$ and $\theta = 15°$) - Comparison between the experimental results with 95% confidence interval ($\pm 1.96\sigma$) and the numerical results.

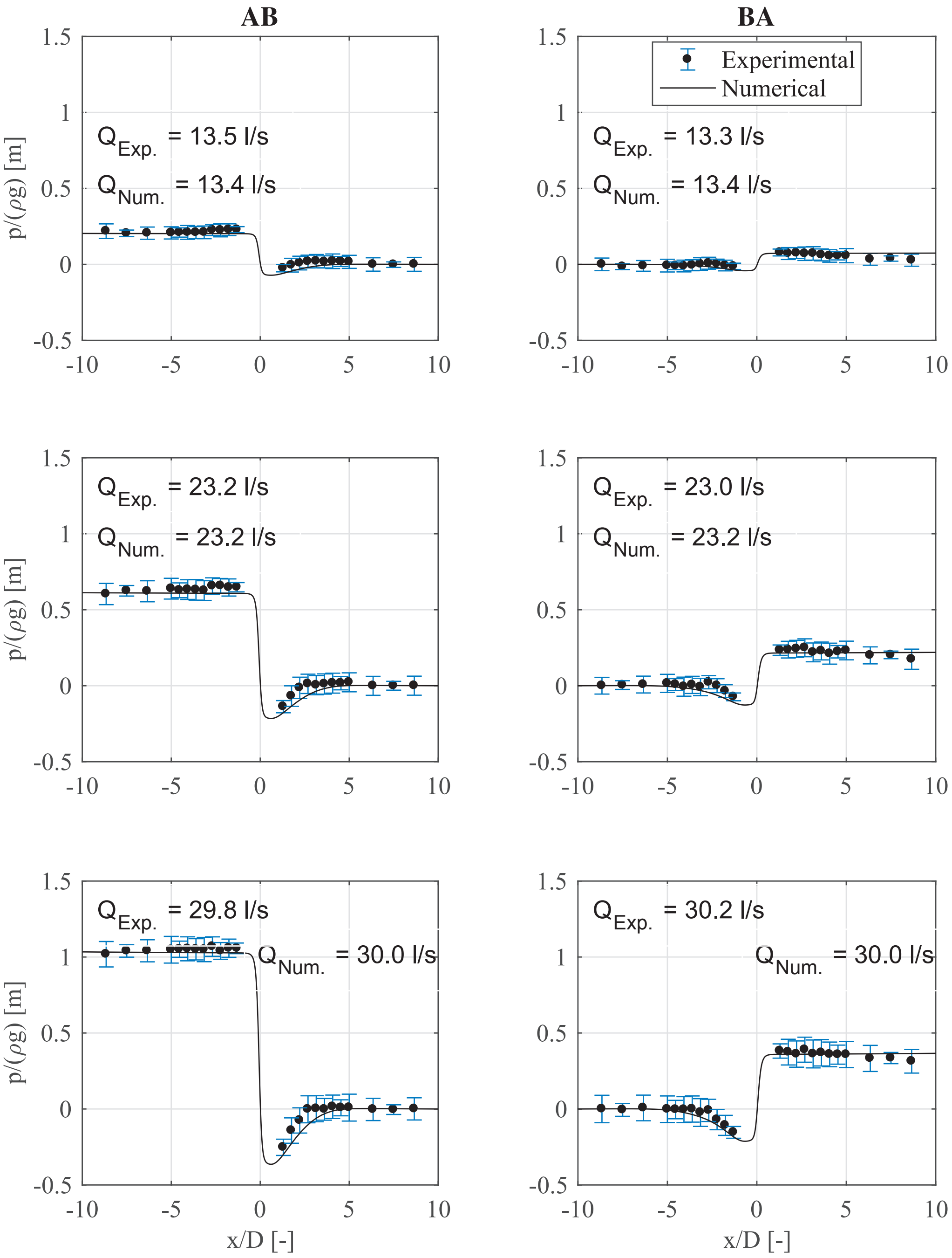

Figure 5.18 – Orifices EXP_008 and NUM_008 $\beta = 0.5$, $\alpha = 0.2$, $\alpha_i = 0.1$ and ($\theta = 30°$) - Comparison between the experimental results with 95% confidence interval ($\pm 1.96\sigma$) and the numerical results.

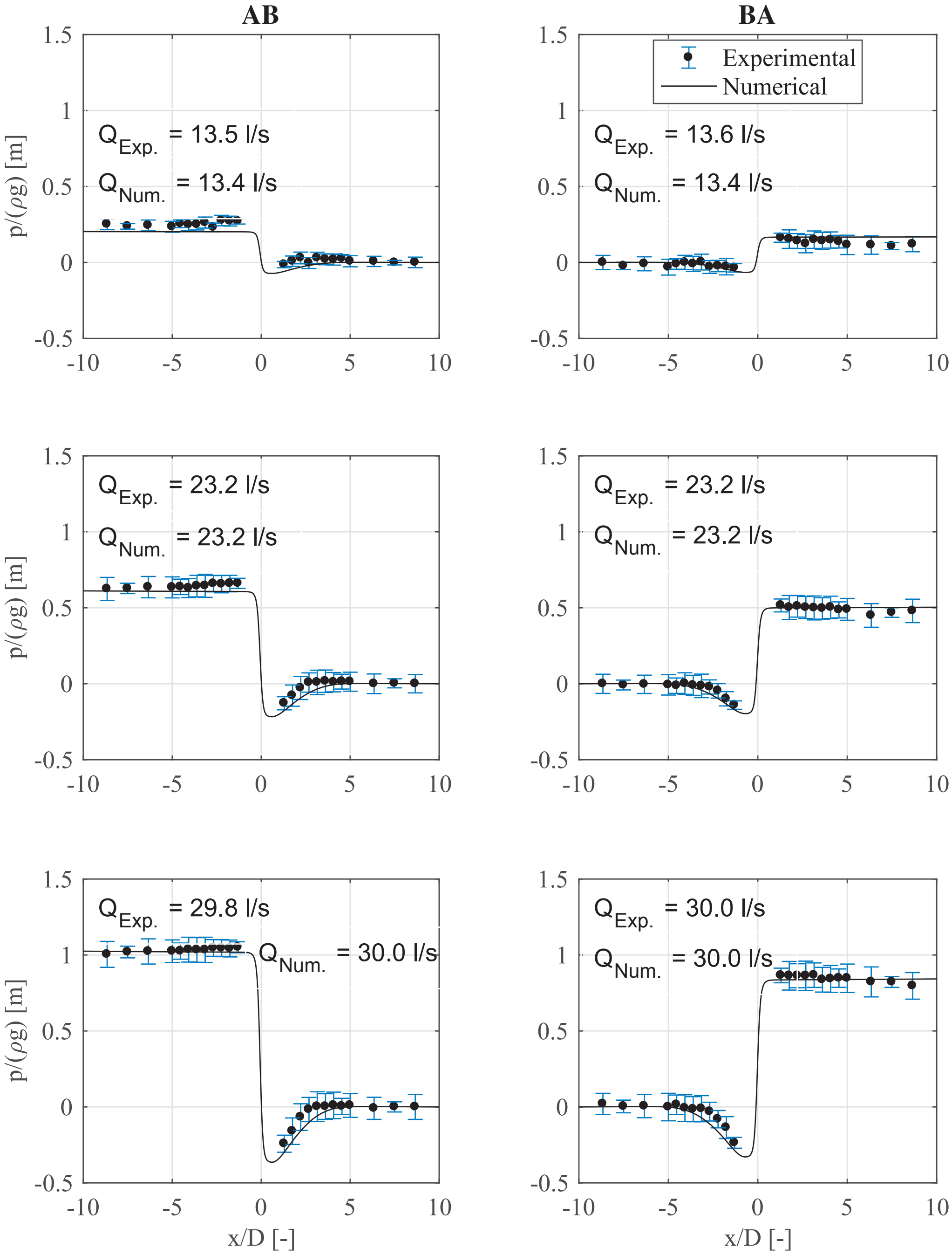

Figure 5.19 – Orifices EXP_009 and NUM_009 ($\beta = 0.5$, $\alpha = 0.2$, $\alpha_i = 0.1$ and $\theta = 67°$) - Comparison between the experimental results with 95% confidence interval ($\pm 1.96\sigma$) and the numerical results.

Figure 5.20 compares the experimental and numerical head loss coefficients. For the sharp approach flow, the discrepancies between the experimental and numerical results are within ±10%. For the chamfer approach flow,the orifices, which are outside the ±20%, are orifice within $\theta = 45°$.

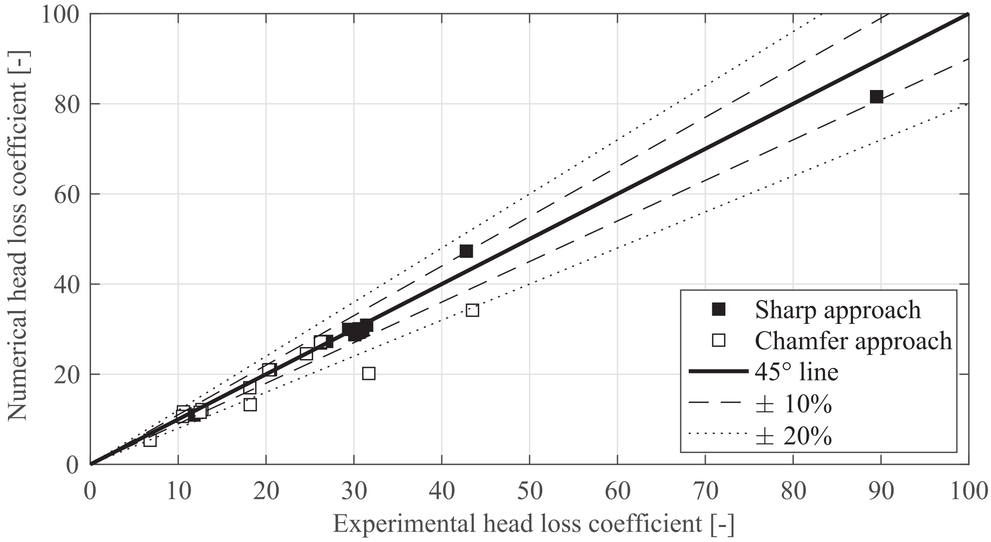

Figure 5.20 – Comparison between the experimental and numerical head loss coefficients for the chamfered orifices for the sharp and chamfer approach flows (Table 4.2)

5.6.2 Sharp approach flow - influence of the orifice inner thickness

An empirical formula (Eq.(5.3)) based on an equation of Idel'cik (1969) was proposed in Section 5.3.3. Figure 5.21 describes the very strong agreement between the formula (Eq.(5.3)) and the numerical results.

The empirical formula was fitted on the chamfered and rounded orifices for the sharp approach flow (orifices with $\beta = 0.5$ in Tables 4.2 and 4.3). According to Figure 5.21, the use of these two parameters (τ and $\kappa_{\alpha i}$) remains acceptable for the different contraction ratios β (from 0.3 to 0.7), that were numerically tested. For $\beta = 0.6$ or 0.7, the slope, $\kappa_{\alpha i}$, seemed slightly smaller.

The validity of the formula was limited to this fall of head loss with increasing inner thickness ratio, α_i. According to Gan and Riffat (1997), the head loss coefficient was minimal when $\alpha_i/\beta \approx 1...1.5$. For higher α_i/β, the friction losses in the orifice, which becomes a plug, should be taken into account and increase the global head losses. The minimum head losses may be approximated (see Section 5.7).

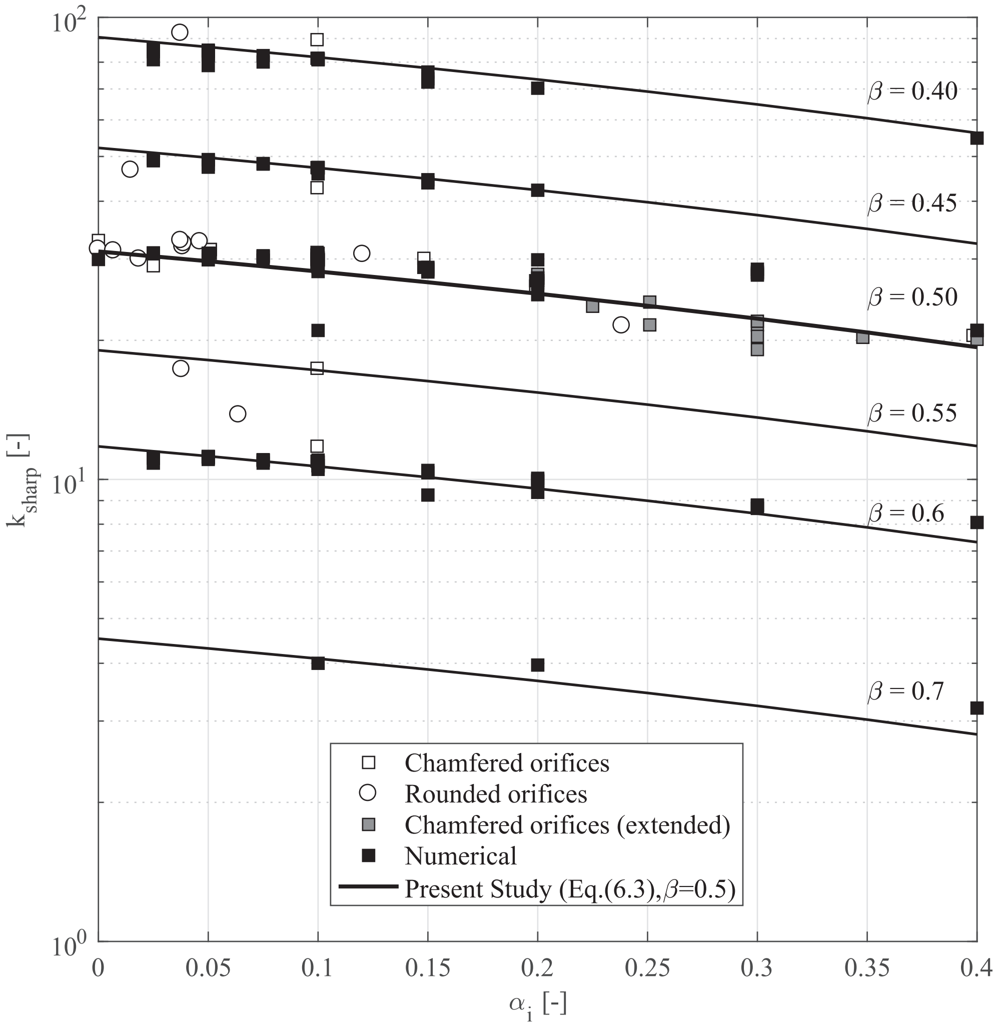

Figure 5.21 – Sharp head loss coefficients - comparison between the experimental and numerical results with the empirical formula (Eq.(5.3))

5.6.3 Chamfer approach flow

The same empirical formula (Eq.(5.10)) equivalent to that found for the sharp approach flow was applied to all the experimental and numerical results. Figure 5.22 suggests that there are differences between the predicted values with the empirical relationship and the experimental or numerical head loss coefficients. However, 80% of the predicted values are within the ±20%, which seems acceptable for a first approximation of the chamfer head loss coefficient.

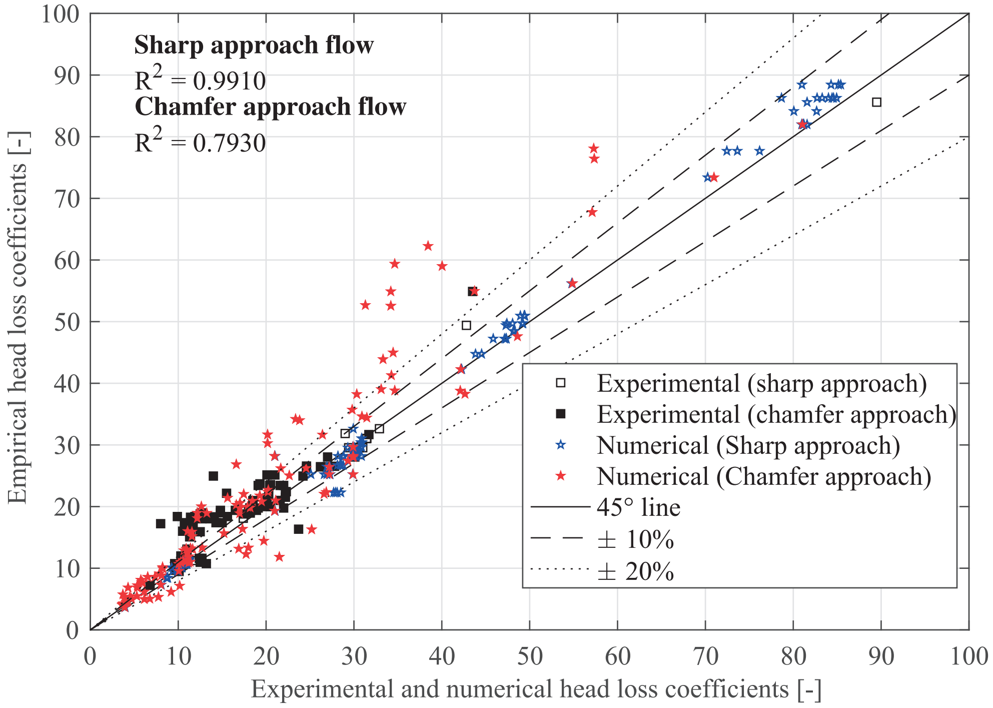

Figure 5.22 – Comparison between experimental and numerical head loss coefficients for all orifices tested either with the experimental or numerical model

5.7 Discussion

5.7.1 Chamfer orifices

As seen in Figure 5.21, the empirical formula (Eq.(5.3)) fits well with the different contraction ratio, β, and inner thickness ratio, α_i, values even if the slope appears to decrease less when β is reduced. However, as explained in Section 3.2, the head losses diminish only for α_i/β values smaller than 1 to 1.5.

It is possible to estimate the critical thickness, α_c, that corresponds to the inner thickness producing the smallest head losses for a given contraction ratio, β. The smallest sharp head loss coefficient can be theoretically approximated by considering a sharp sudden contraction (from 1 to 2) followed by a sharp sudden enlargement (from 2 to 3) of the pipe (Figure 5.23 and Eq.(5.13)). The critical thickness ratio, α_c, can be calculated by equating Eq.(5.3) and (5.13). The evolution of α_c as a function of β is outlined in Figure 5.24.

$$k_{min}(\beta) = k_{contraction} + k_{enlargement} = \left[\frac{1}{2}\left(1-\beta^2\right)^2 + \left(1-\beta^2\right)^2\right] \cdot \frac{v_d^2}{2g} = \frac{3}{2}\frac{(1-\beta^2)^2}{\beta^4} \cdot \frac{v_D^2}{2g} \quad (5.13)$$

Even if the head losses decrease until $\alpha = \alpha_c$, the empirical relationships of Eq.(5.3), (5.10) and (5.11) are limited to the tested ranges, being: $\alpha \in [0, 0.4]$ and $\alpha_i \in [0, 0.4]$.

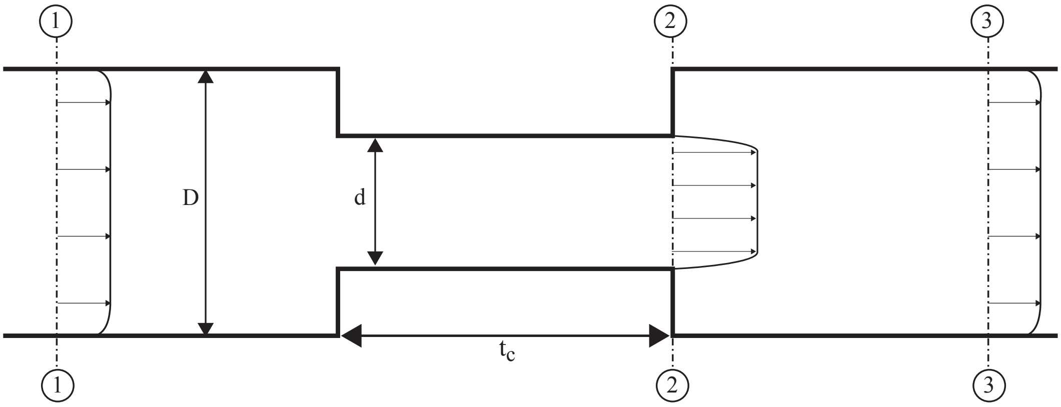

Figure 5.23 – Decomposition of an ideal orifice in a sudden contraction and enlargement with ① a far upstream pipe section, ② the most downstream orifice section as well as ③ a far downstream pipe section

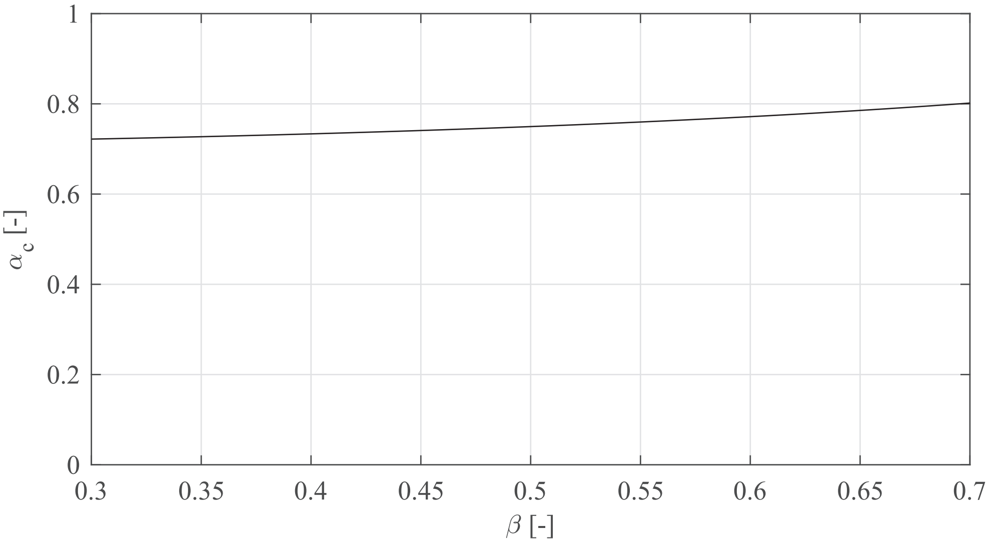

Figure 5.24 – Critical thickness ratio, α_c, as a function of the contraction ratio, β, based on the equality between Eq.(5.3) and (5.13)

5.7.2 Chamfer and rounded approach flow

Chamfered orifices allow introducing different asymmetry ratios λ from 0.33 to 1.0. These values that vary between the head loss coefficient for the chamfer and sharp approach flows can be explained with Figures 5.25 and 5.26:

- without any chamfer angle ($\theta = 0°$), there is a recirculation zone, with a length that is comparable to the orifice thickness, close to the orifice wall;
- with $\theta = 15°$, the recirculation zone is reduced and located on the chamfer edge, the flow is attached to the orifice wall;
- for $\theta = 30°$, Figure 5.26a clearly indicates that the recirculation zone within the orifice wall is small and the flow is almost perfectly contracted;
- if θ rises, the flow is attached to the chamfer wall but a recirculation zone appears close to the inner orifice wall; and
- finally, for higher θ the flow is not contracted any longer by the chamfer wall and the flow behavior tends to the behavior of $\theta = 0°$.

There is a change of behavior when going from a recirculation zone on the chamfer edge to a recirculation zone on the inner orifice edge. Furthermore, for rounded orifices, the contracted head loss coefficient is still smaller than for that of a small angle. The flow seems to be perfectly contracted for this shape.

5.8 Conclusion

It is evident that a chamfer with various angles, fosters the introduction of an asymmetry by reducing the chamfered approach head losses by up to 35% of sharp approach head losses.

For the sharp approach flow, the head loss coefficient increases with the chamfer as was highlighted that with how sharp head losses decrease based upon the inner thickness ratio, α_i, regardless of the shape, being chamfered or rounded. With the sharp approach flow, an equation derived by Idel'cik (1969) was modified to predict the sharp head loss coefficient for the two orifice geometries via Eq.(5.3) and (5.4).

For the chamfer approach flow, the head loss coefficient is also reduced with α_i. However, the slope of the decrease depends on the chamfer angle, θ, leading to a large range of asymmetry ratios between 0.35 and 1.0. A correction of the sharp head loss coefficient is suggested to evaluate the chamfer head loss coefficient by Eq.5.10.

With the rounded approach flow, the asymmetry ratio is less sensitive to the geometry parameters, i.e. the two elliptical axes, and varies from 0.25 to 0.4. A correction of the sharp head loss coefficient is also indicate to assess the rounded head loss coefficient as given by Eq. (5.11).

It could be stated for the two-chamfer orifices, each chamfer angle, θ, leads to a chamfer head loss coefficient independent of the other chamfer angle, θ. The two head loss coefficients can be evaluated by the alterations of the chamfer approach flow with Eq.(5.10).

Finally, numerical simulations enable to acquisition of flow characteristics, e.g. flow velocities or pressure, everywhere within the domain. This allows for understanding the different flow behaviors close to the orifice. The analysis of the velocity field of the orifice for different angles, θ, shows that the difference in the produced head losses originates from how the flow is constricted by the orifice geometry. The numerical results were in tight agreement with the empirical formula developed with the experimental results and could be extended the testing of the set of geometrical parameters.

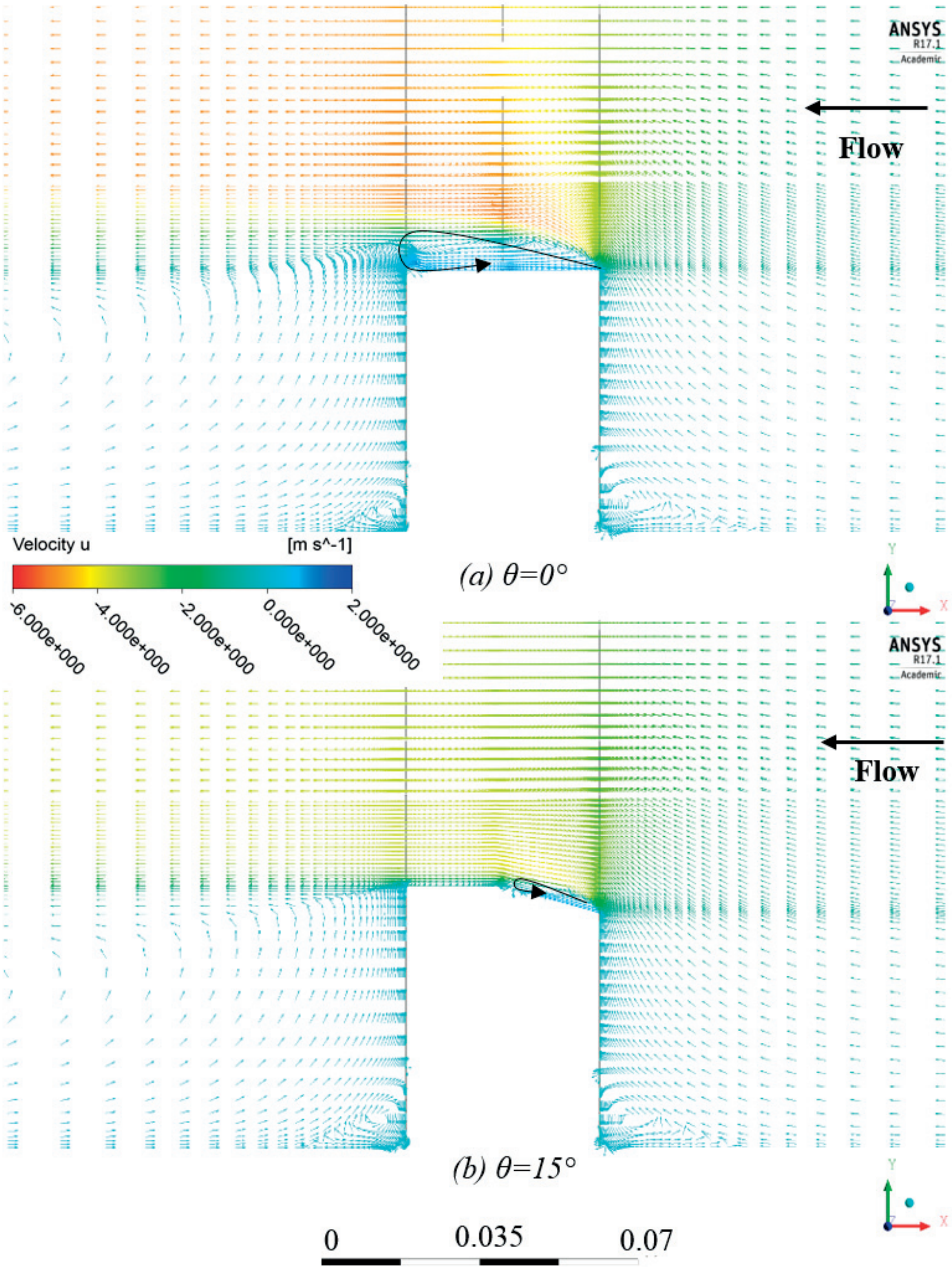

(a) θ=0°

(b) θ=15°

Figure 5.25 – Chamfer approach flow - vector colored by the value of the pipe axis velocity, u, for $\beta = 0.5$, $\alpha = 0.2$, $\alpha_i = 0.1$ and $\theta = 0°, 15°$

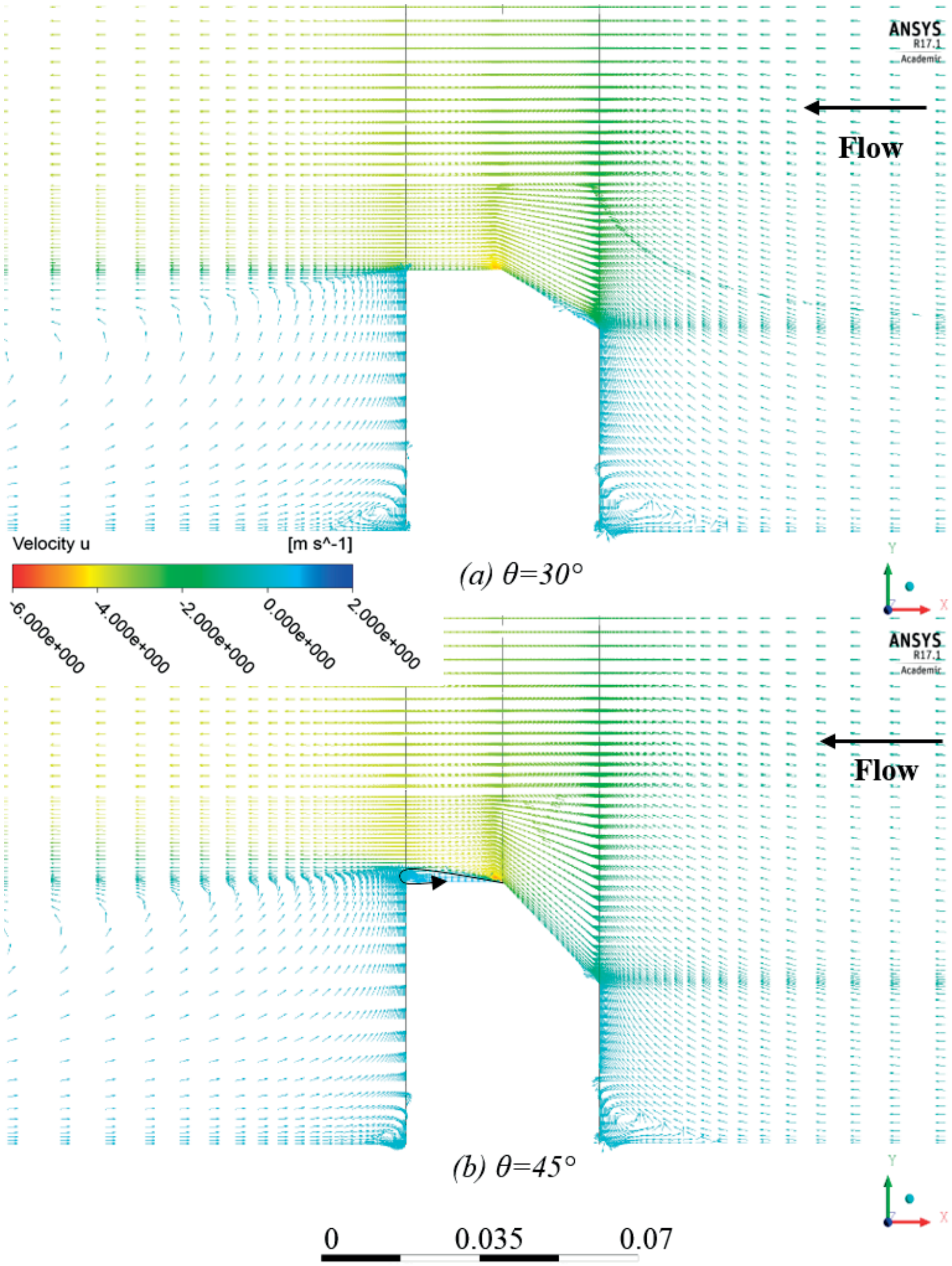

(a) θ=30°

(b) θ=45°

Figure 5.26 – Chamfer approach flow - vector colored by the value of the pipe axis velocity, u, for $\beta = 0.5$, $\alpha = 0.2$, $\alpha_i = 0.1$ and $\theta = 30°, 45°$

6 Influence zone and flow reattachment lengths of orifice

6.1 Introduction

An orifice is a local restriction in a pipe. Water flowing through it accelerates and creates a jet. It can be distinguished between two different lengths characterizing this jet, namely the influence length, L_j, and the reattachment length, L_r. Knowing these jet lengths is required for an appropriate design:

- the recirculation zone is characterized by large turbulences and lower pressures. Knowing the reattachment length, L_r, the tunnel can be lined with steel in order to protect it from high turbulence flow and low pressure in the case of cavitation risk; and
- the upstream and downstream flow conditions have an impact on the head loss coefficient. If the downstream pipe length is at least higher than the recirculation zone, it can be assumed that the head loss coefficient is not affected by downstream conditions. Hereafter, the notation influence length, L_j, is used to characterize this zone.

In order to determine the influence length, the results of the physical experiments and numerical simulations are employed. The reattachment length can be estimated strictly numerically.

6.2 Methods

6.2.1 Reattachment and influence length

In Figure 6.1, the streamlines underscore the presence of a recirculation zone downstream of the orifice depicted. On the one hand, it can be seen that the reattachment length, L_r, is the length between the downstream orifice side and the abscissa where the main flow reattaches to the pipe wall (Jianhua et al., 2010). On the other hand, Figure 6.2 reveals that the zone, which is influenced by the presence of the orifice, is longer than the reattachment zone.

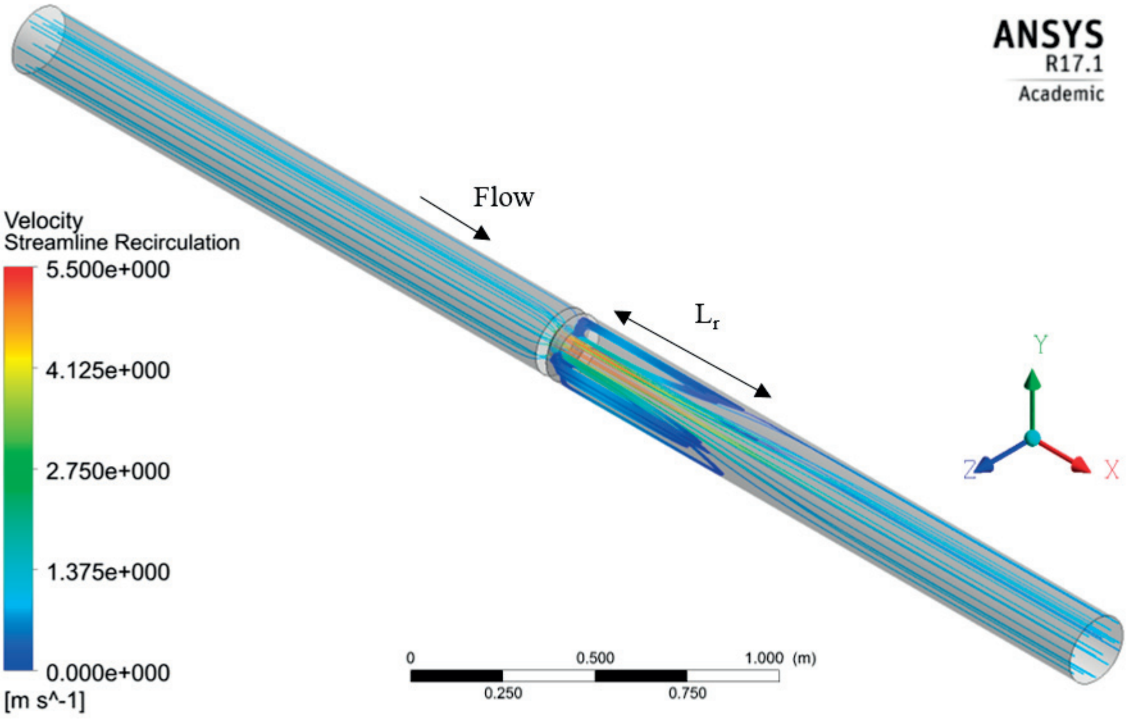
ANSYS
R17.1
Academic
Flow
L_r
Velocity
Streamline Recirculation
5.500e+000
4.125e+000
2.750e+000
1.375e+000
0.000e+000
[m s^-1]
0
0.500
1.000 (m)
0.250
0.750
Y
Z
X

Figure 6.1 – Streamlines through orifice NUM_006, indicating the magnitude of the velocity (with colour scale), and the presence as well as the length of the reattachment zone

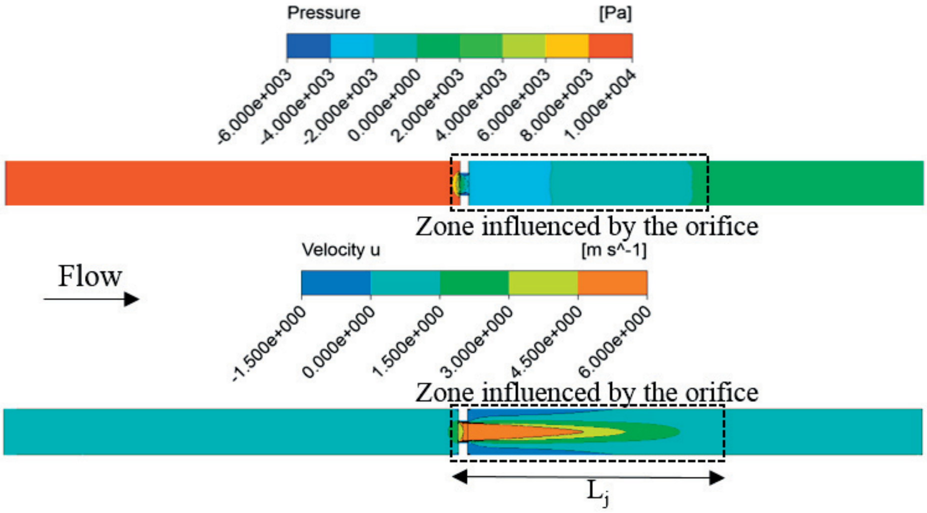

Figure 6.2 – Evolution of the pressure, p, (above), and the axial velocity, u, (below), on the median plane of the pipe emphasizing to highlight the influence length

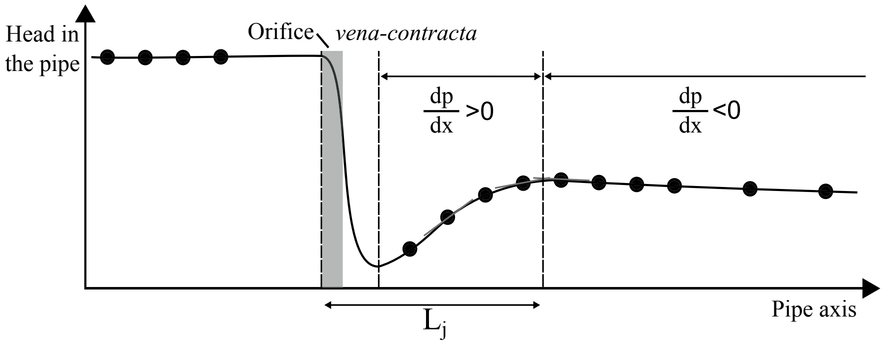

Figure 6.3 – Schematic evolution of the pressure head along the pipe

Figure 6.3 offers a schematic view of the pressure line along the pipe through the orifice. The influence length, L_j, is defined as the distance between the upstream orifice side and the point where the first derivative of the pressure line is equal to zero, as the pressure line must a local maximum downstream of the orifice. After the *vena-contracta*, the pressure increases in the orifice jet as the axial velocity decreases. However, further along the pipe, the pressure diminishes owing to friction and viscosity losses. The end of the zone influenced by the orifice is located where the pressure line begins to decrease linearly because of friction losses.

As the pressure is experimentally recorded by pressure transmitters (see Chapter 4.1 and Appendix A), the first derivative is evaluated by the mean of the first central finite difference (Eq.(6.1)). Conversely, for the most upstream (or downstream) measured points, the forward (or backward) difference is utilized.

$$\frac{dp}{dx} \approx \frac{p(x+\Delta x)-p(x-\Delta x)}{2\Delta x} \tag{6.1}$$

The end of the zone is usually between two discrete points, and the length is calculated with a linear regression to find the abscissa of the local maximum. An error on the pressure can, thus, significantly impact the results of the influence length. The same definition is employed for the numerical results but as Δx is smaller, the error related to the abscissa may also be less.

The influence length is evaluated only for discharges with $\mathsf{Re}_D > 10^5$. Subsequently, the influence length does not depend on Re (Table 4.5) and the average value $\mu \pm \sigma$ of L_j is obtained for the analysis (see Section 6.3.1).

Finally, the experimental results, from evaluating the length of the zone influenced by the orifice jet L_j were compared to those of the numerical results.

6.2.2 Dimensionless parameters

Eq.(6.2) and (6.3) give, respectively, the definition of the dimensionless influence and reattachment length, l_j and l_r.

$$l_j = \frac{L_j}{D} \tag{6.2}$$

$$l_r = \frac{L_r}{D} \tag{6.3}$$

6.3 Influence length of orifice

6.3.1 Results from experiments

Treatment of the experimental results Figure 6.4 illustrates the dimensionless pressure line for orifices EXP_0105 and NUM_0105 (see right margin) according the sharp approach flow. It can be seen that the influence length L_j significantly depends on the discharge. For three discharges, there is a difference of 26% in terms of the experimental prediction of the influence length L_j, while there is no difference for the two corresponding numerical discharges.

EXP_0105

β=0.5
α=0.2
α_i=0.0
θ=45°

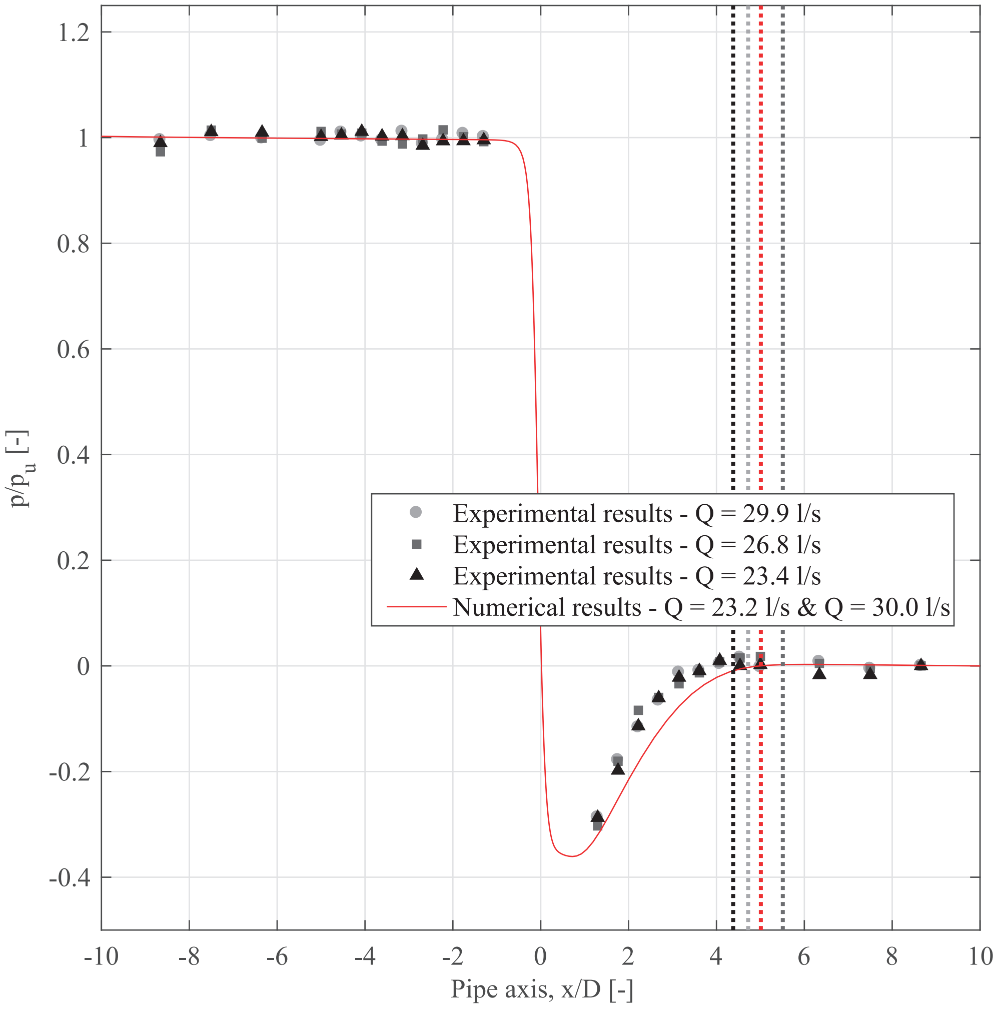

Figure 6.4 – Dimensionless pressure relative to the upstream pressure, p_u, for orifices EXP_0105 and NUM_0105: comparing the experimentally and numerically obtained influence length, L_j

The experimentally obtained influence length depends largely on the uncertainty of the pressure within the influence zone, just as expected. Therefore, only the values within the confidence interval $\pm\sigma$ were used for the evaluation of the experimental influence length for a more accurate estimation. Figure 6.5 shows the extreme neglected value of L_j for the sharp approach flow and orifices EXP_0105 and NUM_0105.

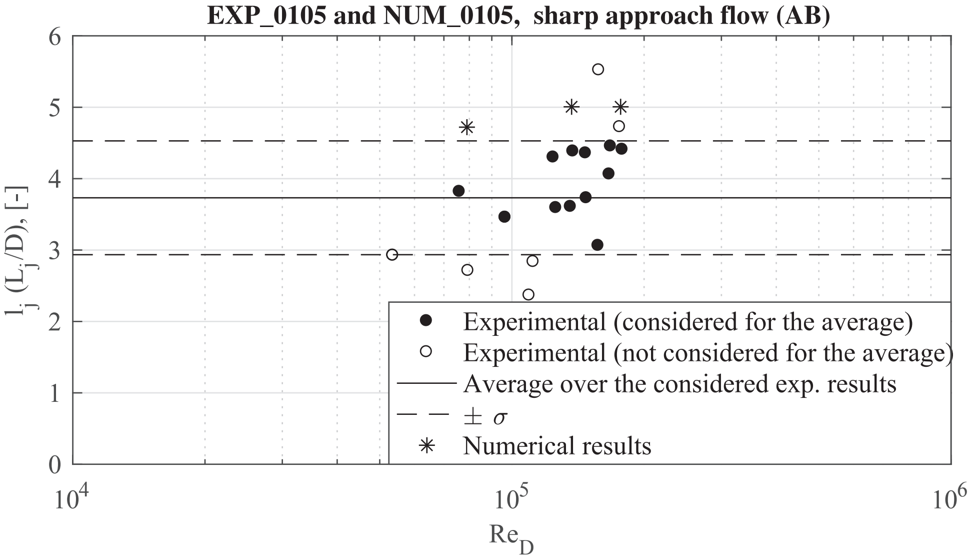

Figure 6.5 – Orifice EXP_0105 and NUM_0105: comparison between the experimental and numerical results and evaluation of the end of the influencing zone $l_j = \frac{L_j}{D}$ as a function of the Reynolds number (with 68% confidence interval) for the sharp approach flow

Analysis of experimental results Figure 6.6 demonstrates the evolution of l_j as a function of β for the sharp and chamfer approach flows. The orifice series corresponds to the chamfer and rounded orifices (see Table 5.1) and to the two-chamfer orifices (see Table 4.4). The following was observed:

- for both approach flow directions, the influence length, L_j, increases when β rises and there is little difference between the chamfered and rounded orifices, which is similar to the head loss coefficients, that do not depend on the downstream shape. This seems consistent because, theoretically, for $\beta = 0$, there is no perturbation downstream of the orifice, and for $\beta = 1$, the perturbation could be considered to be infinite;
- there were large discrepancies for the contraction ratio $\beta = 0.5$. Even if this was not possible to identify with the experimental results, the other geometrical parameters, e.g. α or α_i, should have a lesser influence on the influence length L_j; and
- the influence length was longer for the chamfer approach flow than for the sharp approach flow.

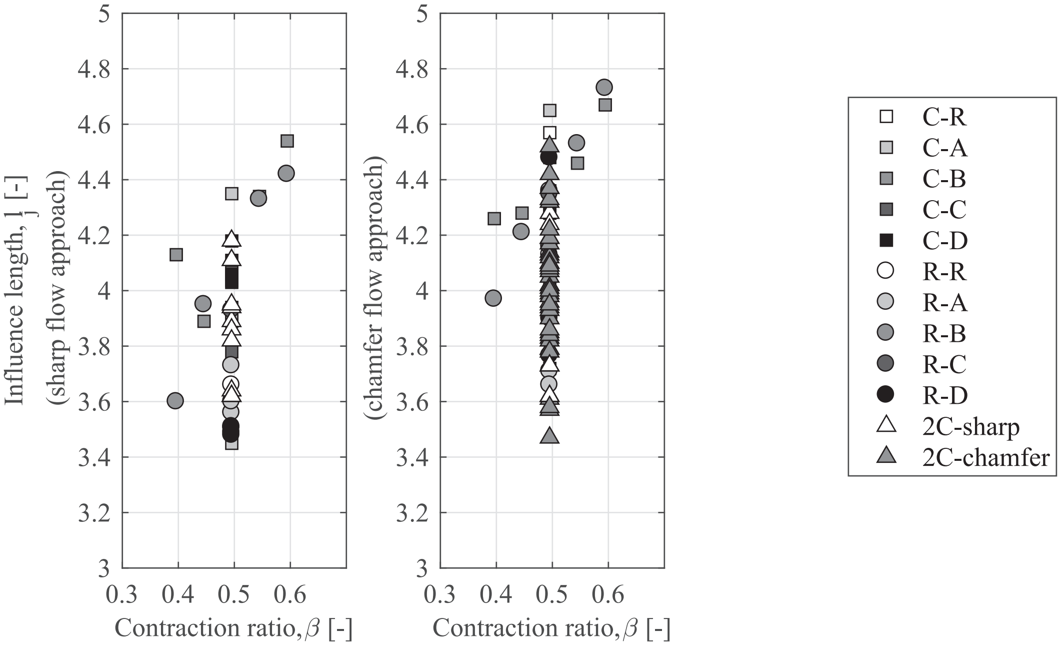

Figure 6.6 – Experimental results of the dimensionless influence length, l_j, as a function of the contraction ratio β for all orifices with a sharp side: chamfer orifices, $C-i$ (square); rounded orifices $R-i$ (circle) and the two-chamfer orifices (triangle) (Table 4.4)

6.3.2 Results from numerical simulations

Comparison with the experimental results Figure 6.7 gives compares the experimentally and numerically obtained results of the dimensionless influence length, l_j. There are quite large differences as was expected from the large variation in the experimental results for the same orifice (see Figure 6.5). The distance between the two sections, where the pressure was recorded, was at least $0.46D$. An error in the pressure recording could thus lead to very major differences. It should be noted that the differences were, on average, higher for the chamfer approach than for the sharp approach. This can be explained by the fact that the pressure drop, downstream of the orifice, is much higher with the sharp approach flow. The same error regarding pressure has less if an influence on the final results, as the pressure rise was higher.

Owing to the large variability of the results, analysis should be performed on the numerical results. This is nevertheless a conservative hypothesis as the numerical length was longer than the physical length (Figure 6.7).

Analysis of the influence length Figure 6.8 describes all the numerically obtained influence length, L_j. It can be seen that L_j rises with the contraction ratio, β, and is also longer for the chamfer approach flow than for the sharp approach flow as already seen with the experimental

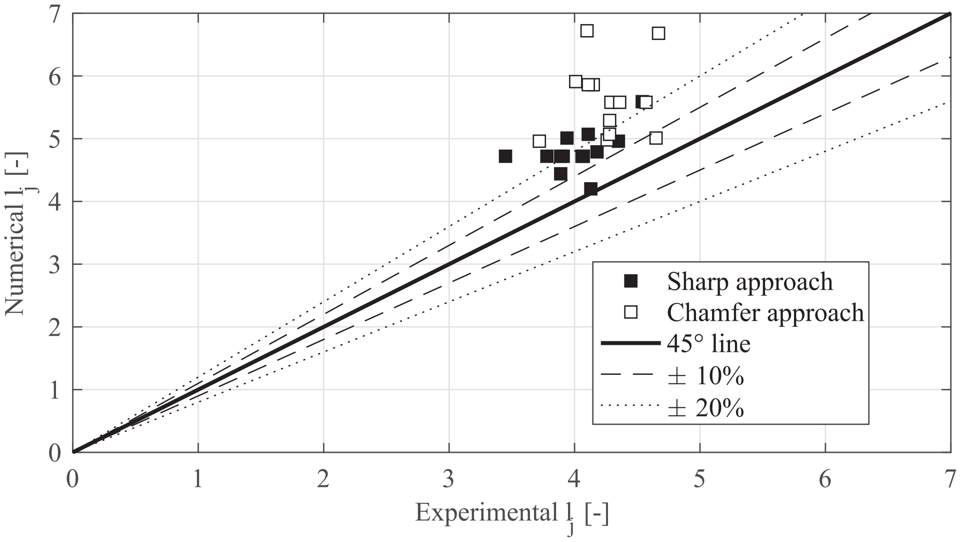

Figure 6.7 – Comparison between the experimental and numerical influence length l_j

results (see Figure 6.6). The influence length does not depend on the Reynolds number if $\mathrm{Re}_D > 10^5$ (see Figure 6.5).

For the sharp approach flow and for each contraction ratio β, the maximum difference between all the numerical results was ±5%. This difference can be understood via the small effect of α_i. It can be assumed that β and α_i were the geometrical parameters, which have an influence on l_j for the sharp approach flow within the tested range of parameters ($\beta \in [0.3\ldots0.7]$ and $\alpha \in [0.05\ldots0.4]$). However, the contraction ratio, β, has a greater impact than the inner thickness ratio, α_i, on l_j. The empirically obtained influence length, l_j, may be described with Eq.(6.4) as a function of β and α_i for the sharp approach flow. The parameters $a_{l,j}$, $b_{l,j}$ and $c_{l,j}$ are fitted on the numerical results and shown in Eq.(6.5). Specifically, the fit is demonstrated in Figure 6.10.

$$l_{j,sharp} = \frac{L_{j,sharp}}{D} = a_{l,j} + b_{l,j} \cdot \beta + c_{l,j} \cdot \alpha_i \tag{6.4}$$

$$\begin{aligned} a_{l,j} &= 1.47 \\ b_{l,j} &= 6.90 \\ c_{l,j} &= 0.77 \end{aligned} \tag{6.5}$$

The asymmetrical ratio, λ_j, is the ratio between the influence length for the chamfer and for

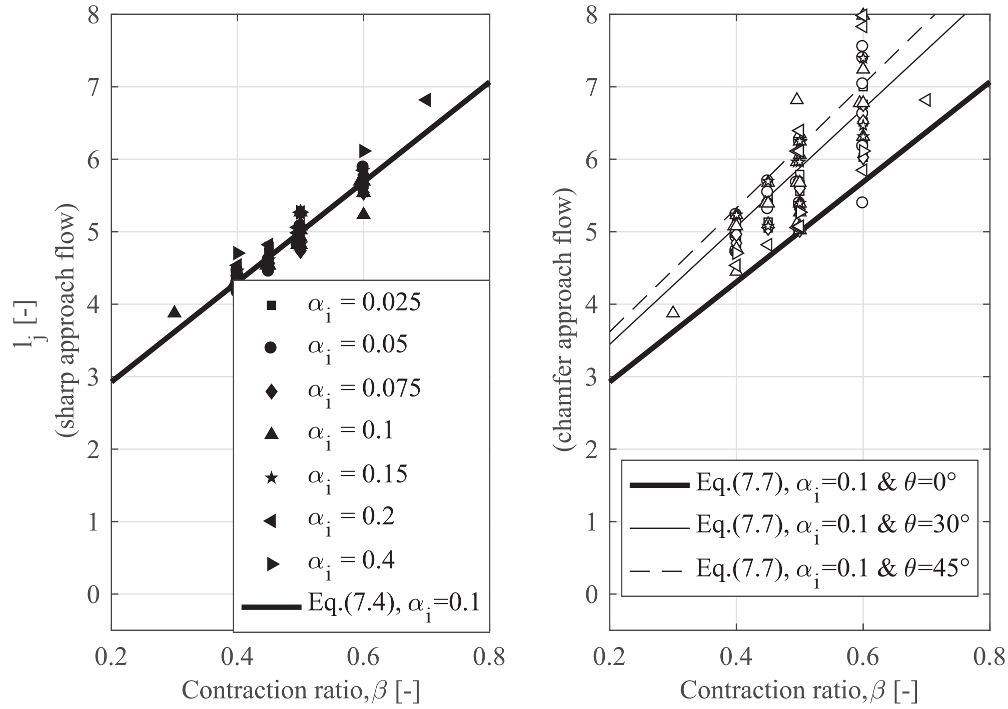

Figure 6.8 – The influence length, l_j, in the both flow direction as a function of the contraction ratio β for the numerically tested orifice

the sharp approach flows as derived in Eq.(6.6).

$$\lambda_j = \frac{L_{j,chamfer}}{L_{j,sharp}} \tag{6.6}$$

The influence length increases with α_θ, just as can be seen in Figure 6.9 . At the maximum, the influence length for the chamfer approach flow is 40% higher than with the sharp approach flow. An empirical relationship is given in Eq.(6.7) for estimating the dimensionless influence length, l_j, based on the numerical simulation results and taking into account the chamfer angle, θ, and the inner thickness ratio, α_i. The parameters $a_{l,j}$, $b_{l,j}$ and $c_{l,j}$ are found in Eq.(6.5) and $d_{l,j}$ was fitted on the numerical results as per Eq.(6.8). One more, the fit is exhibited in Figure 6.10.

$$l_{j,chamfer} = \left[a_{l,j} + b_{l,j} \cdot \beta + c_{l,j} \cdot \alpha_i\right] \cdot \lambda_j \tag{6.7}$$

where: $a_{l,j}$, $b_{l,j}$ and $c_{l,j}$ are given by Eq.(6.5) and λ_j is given by Eq,(6.8).

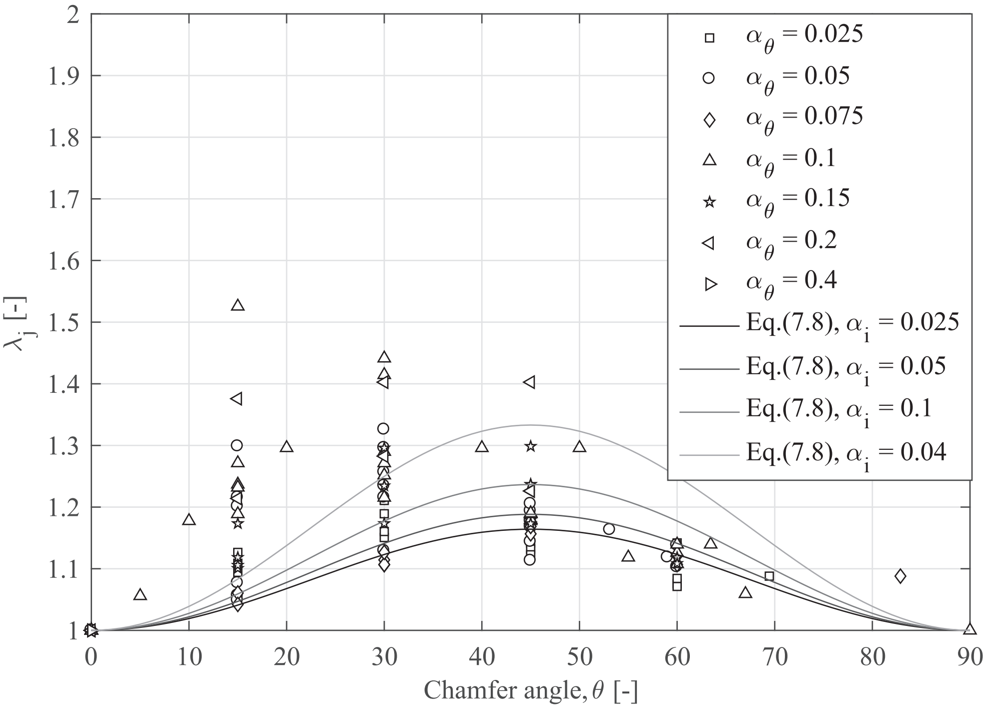

Figure 6.9 – The asymmetrical ratio, λ_j, given in EQ.(6.6) as a function of the chamfer angle, θ, for the chamfer approach flow

$$\begin{aligned}\lambda_j &= \left(1 + d_{l,j} \cdot \sin^2(2\theta)\right) \\ d_{l,j} &= 0.97 \cdot \alpha_i + 0.14\end{aligned} \tag{6.8}$$

Discussion A comparison between the numerically obtained dimensionless influence length, l_j, and the predicted dimensionless influence length, $\hat{l}_j$, obtained by Eqs.(6.4) and Eq.(6.7) is given in Figure 6.10 for the sharp and chamfer approach flow directions. Predictions of the dimensionless influence length, l_j, for the sharp approach flow were better than for the chamfer approach flow. However, the predicted influence lengths for the sharp approach flow were within the ± 10 % of the numerical influence length. Further, for the chamfer approach flow, 80% of $\hat{l}_j$ were within ± 10 %, while only 3% were outside the ±20% limits.

As well, the numerically obtained influence lengths were on the same order of magnitude as the required downstream length for a standard orifice used as a flowmeter (ISO, 2003).

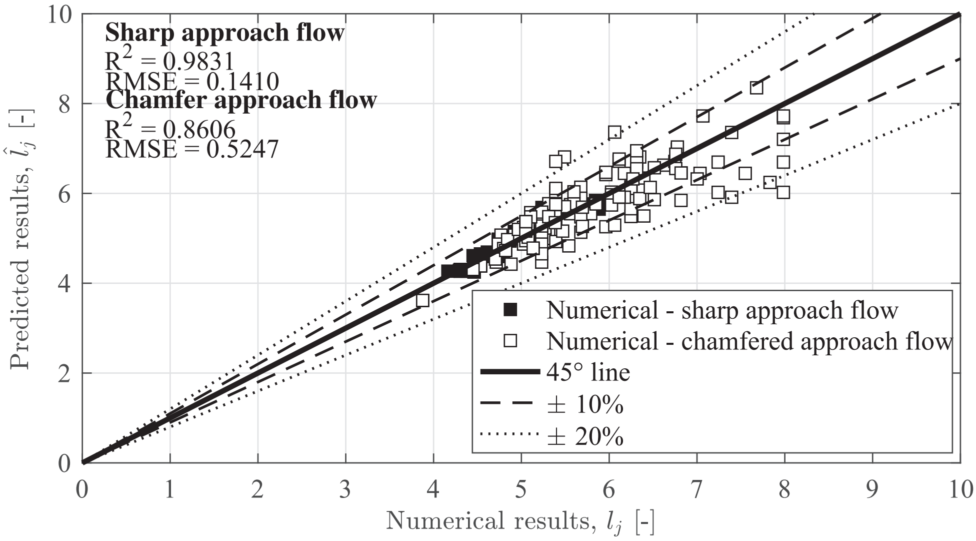

Figure 6.10 – Comparison of the numerically obtained influence length and the influence length predicted by Eqs.(6.4) and (6.7) for the sharp and chamfer approach flows

6.4 Reattachment length

Analysis of the reattachment length The reattachment length of the jet behind the orifice was smaller than the recirculation zone, which was disturbed by the presence of the orifice within the pipe (see Figures 6.8 and 6.11). Except for the larger β, the chamfer angle θ did not have a major effect on the reattachment length. The following observations can be made for Figure 6.11:

- for $\beta > 0.5$, the reattachment length, L_r, decreases linearly while β converges to $\beta = 1$ and $L_r = 0$, where there is no recirculation zone because of the lack of orifices in the pipe. The other geometrical parameters, namely the inner thickness ratio, α_i, the thickness ratio, α, and the chamfer angle, θ, does not have an influence on L_r;
- for $\beta < 0.5$, the decrease of l_r as a function of β is smaller than for $\beta > 0.5$. It even seems that there is a maximum reattachment length with a constant value for $\beta > 0.4$;
- unlike the influence length, there was no significant difference between the sharp and chamfer approach flows. The height of the orifice wall seems to be the main influence.

The same was already observed by Jianhua et al. (2010) for symmetrical orifices.

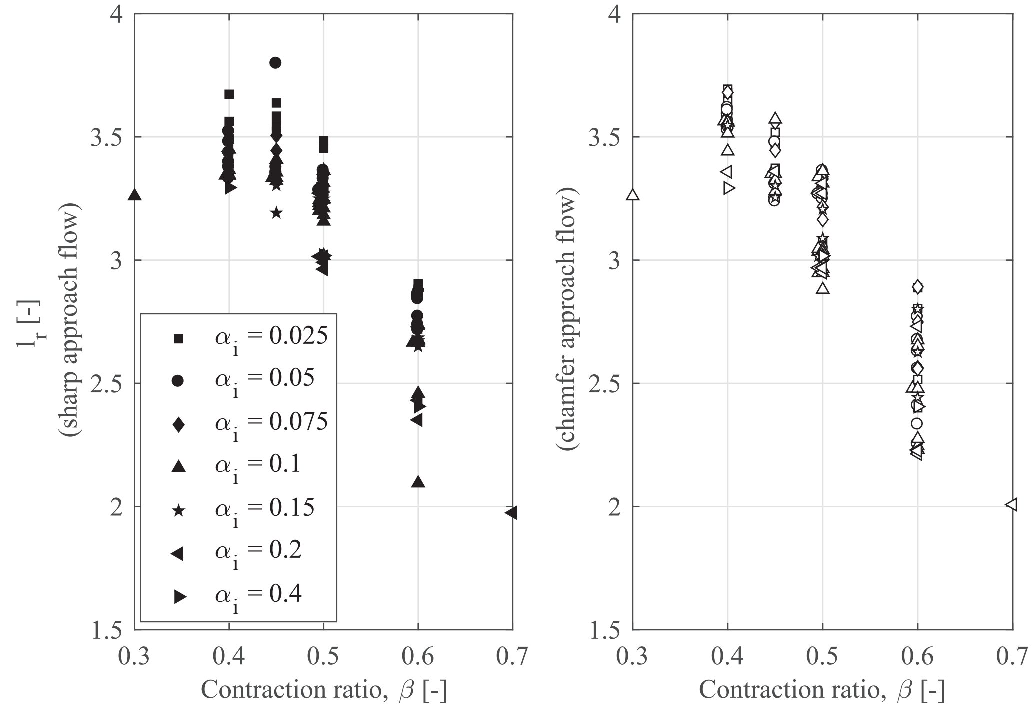

Figure 6.11 – Reattachment length, l_r, as a function of the contraction ratio, β

Development of a predictive empirical formula A model characterizing the dimensionless reattachment length, l_r, was found with two lines inspired by the numerical results and those of Jianhua et al. (2010). The two lines join at $\beta = 0.5$ because of the previous observations. For the understanding of the phenomenon, it is useful to define the orifice height ratio γ_o (Eq.(6.9)). The two-line model relies on γ_o as suggested in Eq.(6.10).

$$\gamma_o = \frac{1-\beta}{2} \tag{6.9}$$

$$\begin{aligned} l_r &= a_{l,r} \cdot \gamma_o,\ if\ \beta \geq 0.5\,(\gamma_o \leq 0.25) \\ l_r &= b_{l,r} \cdot \gamma_o + c_{l,r},\ if\ \beta < 0.5\,(\gamma_o > 0.25) \end{aligned} \tag{6.10}$$

where: $a_{l,r}$ and $b_{l,r}$ are the line slopes, that depend on α_i, and $c_{l,r}$ depends on $a_{l,r}$ and $b_{l,r}$. The three parameters $a_{l,r}$, $b_{l,r}$ and $c_{l,r}$ are given in Eq.(6.11).

Figure 6.12 portrays the variation of l_r with γ_o. Logically, it can be observed that there is no reattachment zone for $\beta = 1$ (no orifice). For $\gamma_o \leq 0.25$, which corresponds to $\beta \geq 0.5$, the reattachment length, L_r, is directly proportional to γ_o. The inner thickness ratio, α_i, directly influences the slopes $a_{l,r}$ and $b_{l,r}$ defined in Eq.(6.10). Eq.(6.11) features the slopes $a_{l,r}$ and $b_{l,r}$ as a function of the inner thickness ratio, α_i, fitted on the numerical results. For the sake of continuity, the results at $\beta = 0.5$ ($\gamma_o = 0.25$), $c_{l,r}$ are defined by Eq.(6.11).

$$\begin{aligned} a_{l,r} &= -5.46 \cdot \alpha_i + 14.10 \\ b_{l,r} &= 3.95 \cdot \alpha_i + 2.32 \\ c_{l,r} &= \frac{a_l - b_l}{4} \end{aligned} \tag{6.11}$$

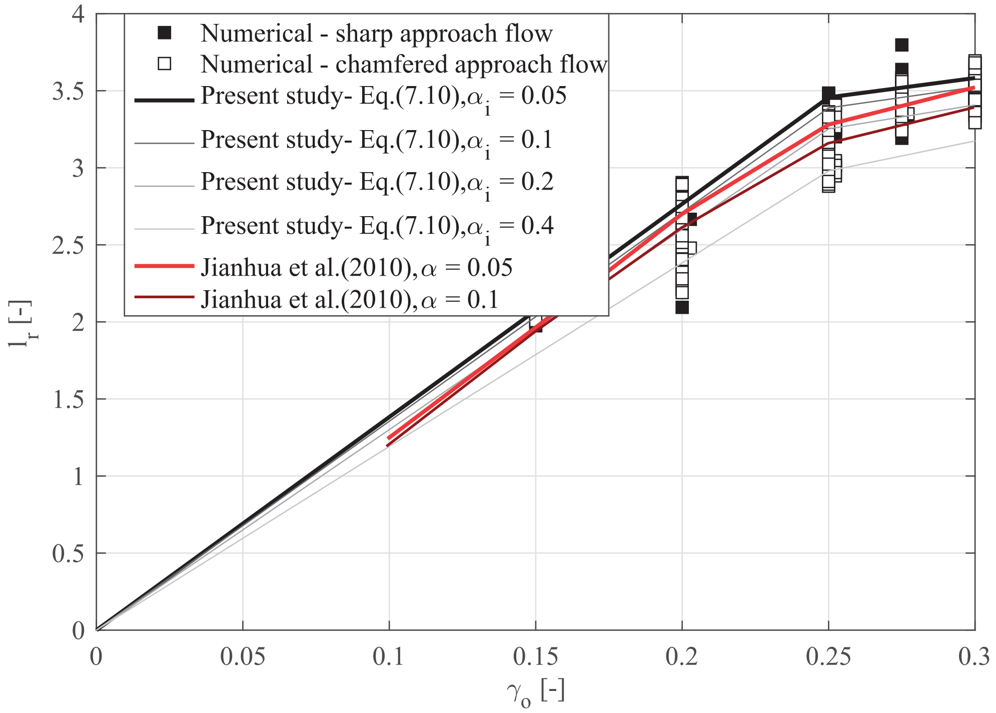

Figure 6.12 – The dimensionless reattachment length, l_r, as a function of the orifice height ratio γ_o and the comparison between the two-line model given in Eqs.(6.10) and (6.11) along with the graphical results from Jianhua et al. (2010)

Figure 6.12 features a comparison of the results of Jianhua et al. (2010) with those presented herein. The model developed in this research is quite different with a higher (roughly 10%) reattachment length that is close to $\beta = 0.5$. Moreover, the empirical formulas given by Eqs.(6.10) and (6.11) enable the direct determination of the reattachment lengths by avoiding graphical interpolation.

Discussion The linear decrease for $\beta > 0.5$ can be explained by a constant diffusion angle of the jet within the pipe. The value of this angle is approximately 4 to 5°.

Figure 6.13 demonstrates there is a good alignment between the numerical reattachment length and the predicted reattachment length, which were established by Eqs.(6.10) and (6.11). Most of the predicted reattachment lengths are within ±10% limits. However, the two-line model developed in this project tends to yield longer reattachment lengths.

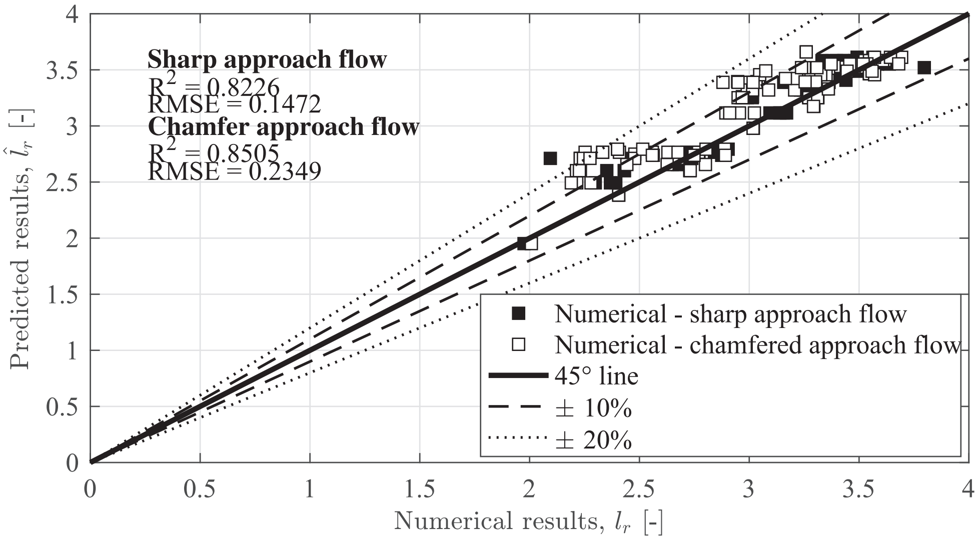

Figure 6.13 – Comparison of the dimensionless reattachment length, l_r, with the predicted value given by the empirical formulas (Eqs.(6.10) and (6.11))

6.5 Conclusions

The disturbance zone, because of the orifice jet, is longer than the recirculation zone, i.e. reattachment length.

The influence length, L_j, characterizing the disturbance zone rises with the contraction ratio, β, while L_r decreases when β is increased. A comparison between the dimensionless influence length, l_j, obtained experimentally and numerically uncovered that the experimental model was not adequate for this evaluation.

For the sharp approach flow, the numerically obtained influence length, L_j, depends mainly on β and the inner thickness ratio, α_i, while L_j relies upon the chamfer angle, θ, for the chamfer approach flow. The influence length, l_j, would be valuable for the placement of serial independent orifices in the tunnel or the implementation of a pressure transmitter in an undisturbed zone:

- for the sharp flow approach, the dimensionless influence length $l_{j,sharp}$ can be predicted by the suggested empirical formula Eq.(6.4); and
- for the chamfer flow approach, the dimensionless influence length, $l_{j,chamfer}$, can be acquired with the empirical formulas Eqs.(6.7) and (6.8).

The reattachment length, L_r, does not depend on the chamfer angle of the orifice, θ, and depends primarily on β and α_i. The recirculation zone is characterized by highly turbulent flows in which cavitation can take place. The estimation of L_r permits the establishment of where the tunnel should be steel-lined for resisting turbulent flows and low pressures. A two-line model was developed to predict l_r as given by Eqs.(6.10) and (6.11). This model was then compared with the graphical results of Jianhua et al. (2010) stressing there was the same variation of l_r as a function of β and α_i. A large decrease in l_r for $\beta \leq 0.5$ and an almost constant value for $\beta < 0.5$ was evident.

An application of these two characterizing lengths, namely the influence and reattachment lengths, through experimental work is found in Chapter 9.2.

7 Transient head losses through orifices

7.1 Introduction

A number of previous experiments have been performed with different steady discharges. Chaudhry (2014) assumed that head losses for steady flow (friction in the original text) may be used to compute transient phenomena. However, steady head losses could be insufficient for the simulation of multiple operations, e.g. starting the pumps following a power failure. However, steady head losses may be adequate for an initial approximation of the first amplitude of a mass oscillation, which is generally restrictive in terms of the design of surge tanks.

Different types of models have been formulated to investigate the unsteadiness of the flow in transient simulations: quasi-two-dimensional models, convolution integral and instantaneous acceleration-based methods (IAB) models. These have all focused exclusively on friction losses and not local head losses (Bergant et al., 2001; Chaudhry, 2014; Ferràs Segura, 2016).

7.2 Performed experiments

7.2.1 Experimental setup and tested configurations

The experimental setup and instrumentation employed are presented in Chapter 4.1 and Appendix A. The transient experiments were carried out on five orifices, i.e. EXP_001, EXP_002, EXP_004, EXP_012 and EXP_032 (Figure 7.1),with different contraction and thickness ratios, β and α (Figure 7.1 and Table 4.2). Figure 7.2 shows a typical schematic evolution of the discharge during such transient experiments. For the longest duration, specifically 30 s, the duration of the steady discharge was at least 30 s for the evaluation of the steady head loss coefficients.

Four rise and fall durations (Table 7.1) were tested three times in order to determine the transient effect on head losses. The average acceleration of the orifice velocity was from approximately $0.02\,m/s^2$ to nearly $0.4\,m/s^2$. The rise (or fall) of discharge is obtained by

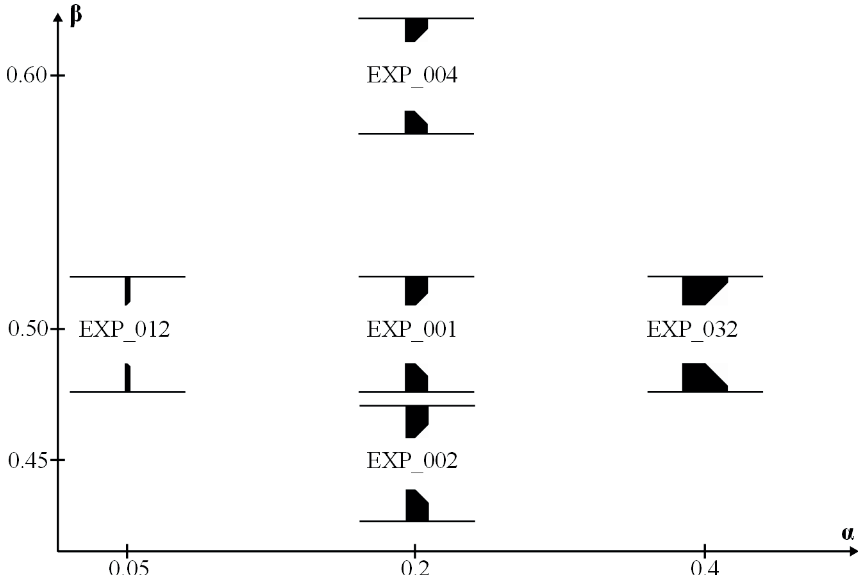
β
0.60
0.50
0.45
EXP_004
EXP_012
EXP_001
EXP_032
EXP_002
α
0.05
0.2
0.4

Figure 7.1 – Tested geometries of the orifices of the transient experiments with $\alpha_i/\alpha = 0.5$ and $\theta = 45°$

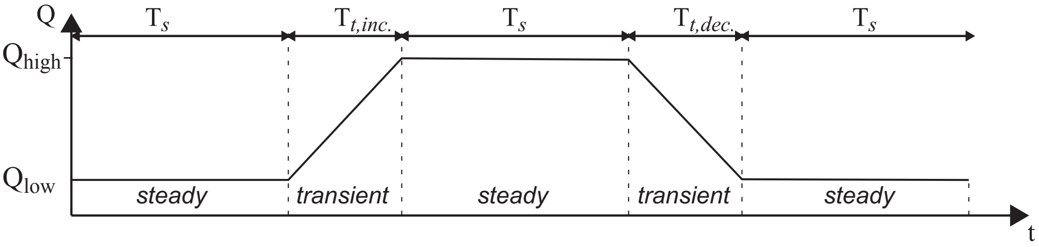
Q
Q_high
Q_low
T_s
T_t,inc.
T_s
T_t,dec.
T_s
steady
transient
steady
transient
steady
t

Figure 7.2 – Procedure for the transient experiments

opening (or closing) manually the downstream valve of the experimental set-up. All the information surrounding the experimental characteristics, e.g. steady discharges or opening and closure durations are reported in Appendix E.

As per Chapter 5, the pressure and discharge were recorded on the same computer with the same sampling properties: the sampling frequency, f_s, is $1000 Hz$ and the sampling number, N_s, is $150'000$ for all orifices and durations. The discharge was always recorded by the flow meter downstream of the pipe, while the pressure was recorded by the $G1/4"$ pressure transmitters placed 45° from the pipe cap(Chapter 4.1 and Appendix A). For the transient experiments, $G1/4"$ pressure transmitters were placed as described in Figure 7.3.

7.2.2 Evaluation of head losses

Instantaneous head losses were evaluated between the upstream and downstream transmitters and compared to the steady head losses from Chapter 5. This comparison highlights the

Table 7.1 – Opening and closure durations downstream for each orifice (note that all these values are theoretical, experimental results and values are shown in Appendix E)

Orifice	Q_{high}	Q_{low}	Sharp flow direction (AB)				Contracted flow direction (BA)			
			$5\,s$	$10\,s$	$20\,s$	$30\,s$	$5\,s$	$10\,s$	$20\,s$	$30\,s$
EXP_001	28.2	19.1	✓	✓	✓	✓	✓	✓	✓	✓
EXP_002	28.2	19.1	✓	✓	✓	✓	✓	✓	✓	✓
EXP_004	28.2	19.1	✓	✓	✓	✓	✓	✓	✓	✓
EXP_012	28.2	19.1	✓	✓	✓	✓	✓	✓	✓	✓
EXP_032	28.2	19.1	✓	✓	✓	✓	✓	✓	✓	✓
	25.1	19.1	✓		✓		✓		✓	

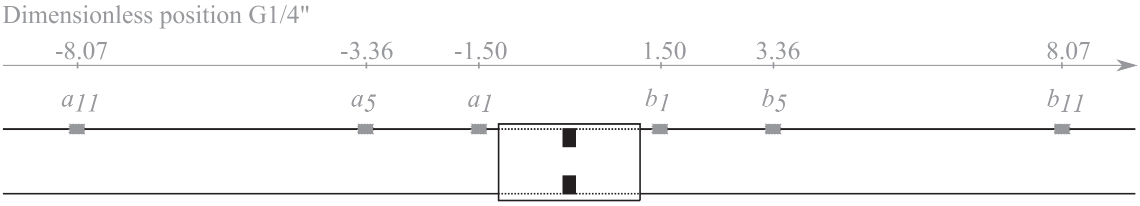

Figure 7.3 – Positions of the $G1/4$" transmitters for the transient experiments

difference between transient and steady head losses. The head loss coefficients fitted on the different steady phases can be slightly different from the head loss coefficient found in Chapter 5. The uncertainty of the head loss coefficient can be greater as the fitting is only performed on two (three for EXP_032) discharges and on four pressure transmitters (three upstream and one downstream).

As explained in Section 3.5, the local head losses can be obtained by Eq.(7.1), which distinguish the steady and transient behaviors

$$\Delta H = \Delta H_s + \Delta H_t = k\frac{v^2}{2g} + \frac{k_t}{g}\frac{dv_d}{dt} \tag{7.1}$$

where: k is the steady head loss coefficient (as in Chapter 5), v the velocity in the surrounding pipe, k_t the transient head loss coefficient and dv_d/dt the flow acceleration through the orifice.

7.2.3 Remarks on momentum and viscoelastic effects

During transient experiments, inertia and water hammer effects are present. On one side, the inertia effect is obtained by integrating the momentum equation and, on the other side, the discharge changes lead to a small water hammer in the pipe resulting in overpressure (as shown in Eq.(2.3)). Seeing that the main pipe was made of PVC, it was important to verify whether the viscoelastic effect was small enough to be neglected.

Momentum effect Eq.(2.2) is the momentum equation applied to a control volume. It can be rewritten as Eq.(7.2) by considering a horizontal pipe and ignoring the friction losses in the pipe.

$$\frac{\partial v}{\partial t} + v\frac{\partial v}{\partial x} + \frac{1}{\rho}\frac{\partial p}{\partial x} = 0 \tag{7.2}$$

Eq.(7.2) can be integrated between two random sections of the pipe ① and ②. The length $L_{①-②}$ is the distance between the two sections. Eq.(7.3) is the result of the integration of Eq.(7.2) by assuming there is no interaction between this and the effect of the transient head losses.

$$\frac{\partial Q}{\partial t} = \frac{A_D}{\rho L_{①-②}}(p_{①} - p_{②}) \tag{7.3}$$

where A_D is the main pipe cross-section, ρ the water density, $L_{①-②}$ the distance between the two sections 1 and 2 and p the pressure in the section 1 or 2.

The temporal integration of Eq.(7.3) is the well-known *pressure-time method* (Adamkowski, 2012; Landry, 2015).

The application of Eq.(7.3) to the experimental set-up (see Figure 7.3) between the two most distanced cross-sections, a_{11} and b_{11}, is shown in Eq.(7.4).

$$\frac{\Delta p}{\rho g} = \frac{p_{a11} - p_{b11}}{\rho g} = \frac{L_{①-②}}{g A_D}\frac{dQ}{dt} = \frac{L_{①-②}}{g A_D}\cdot\frac{A_d}{A_d}\frac{dQ}{dt} = \frac{L_{①-②}\beta^2}{g}\cdot\frac{dv_d}{dt} \tag{7.4}$$

The value of the coefficient, $L_{①-②}\beta^2$, is reported in Table 7.2 for the different contraction ratios.

Table 7.2 – The inertia coefficient $L_{①-②}\beta^2$ (Eq.(7.4)) is a function of the contraction ratio β

β	$L_{①-②}\beta^2$
0.45	0.706
0.5	0.872
0.59	1.214

Table 7.3 – Physical properties of the pipe wall of the experimental set-up

Properties		Unit	Values
Thickness	e	[mm]	5
Mean radius	r_m	[mm]	110.5
Yield strength	f_y	[MPa]	35^*
Young modulus	E	[MPa]	2000^*
Maximum working pressure	p_w	[Mpa]	0.05

*: Assumption

Viscoelastic effect The pipe wall of the experimental model is composed of PVC. Table 7.3 lists the physical properties of the pipe. By using the formula of the thin-walled tube (Massonet and Cescotto, 1994), the maximum (failure) pressure was approximately 155 mH_2O (see Eq.(7.5), 15.8 bar) while the pressure was limited to 5 m during the experiments. For 5 m pressure head and assuming elastic behavior of the PVC, the radial deformation was roughly $5.6 \cdot 10^{-4}$ % of the initial diameter (Eq.(7.6)).

$$p_{max} = \frac{f_y \cdot e}{r_m} = 1.58\, MPa \tag{7.5}$$

$$\Delta r_{p=5\,m} = \frac{p_w r_m^2}{Ee} \approx 0.06 \cdot 10^{-3}\, m \tag{7.6}$$

According to these results as well as the low variation of pressure within the experimental set-up regarding the maximum pressure evaluated with the PVC yield limit, the viscoelastic effects were not be taken into account in this study.

7.3 Results

7.3.1 Head losses during the steady phases

During each experiment, there were, at least, three phases of 30 s with two different discharges. By combining all the experiments (at least 36 steady phases for each orifice), it was possible to evaluate the steady head loss coefficients. Compared to Chapter 5, there were only two different discharges and a maximum of six control sections. This increased the uncertainty of the head loss coefficient evaluation.

Figures 7.4 and 7.5 show the linear regression for both flow directions (see Table 7.4 and a comparison with the head loss coefficients found in Chapter 5). According to Table 7.4, the discrepancies between the two values of head loss coefficient was maximum of 13% but 5% on average. For the analysis during this chapter, the head loss coefficients, which were fitted on the three steady discharges per experiment, were utilized. However, the difference between the results was considered to be small enough.

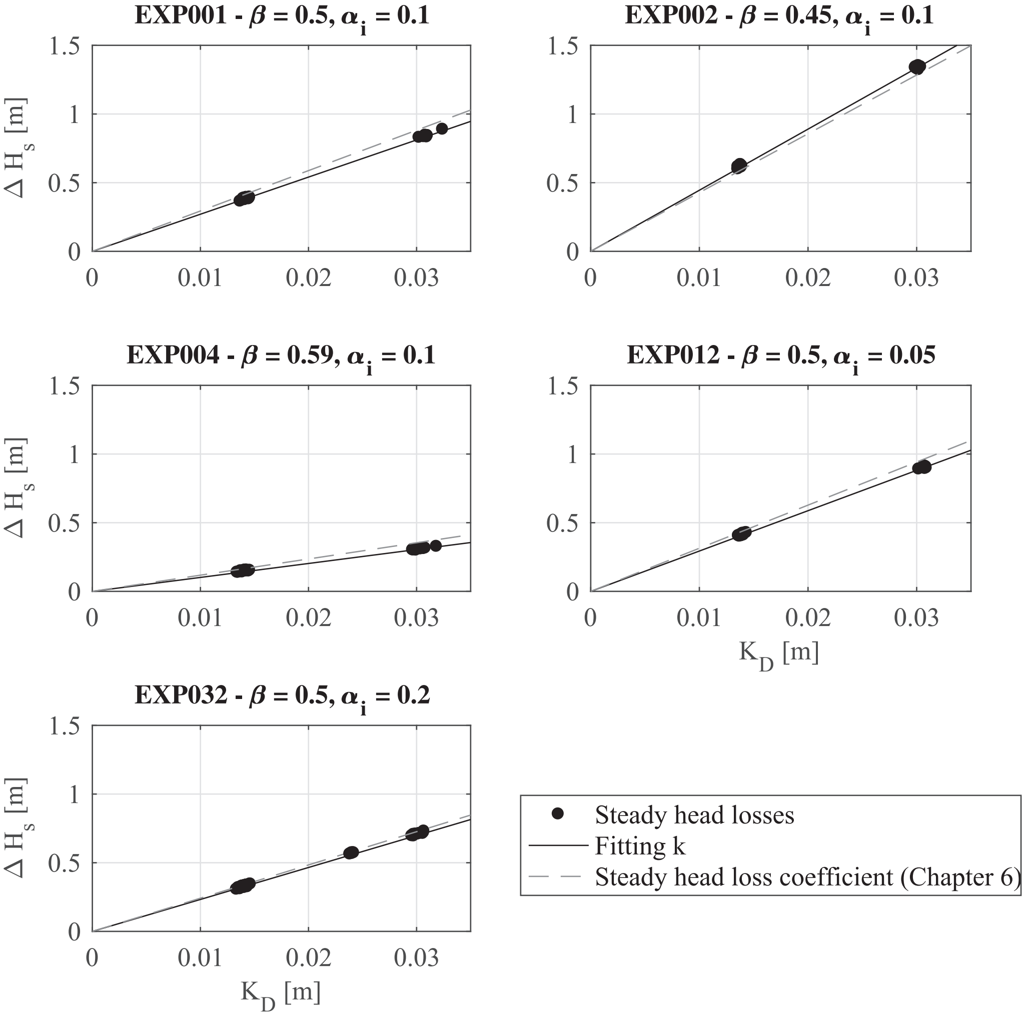

Figure 7.4 – Sharp approach flow: steady head losses determined with the transient experiments for orifices EXP_001, EXP_002, EXP_004, EXP_012 and EXP_032 compared with the steady head loss coefficients found in Chapter 5

Table 7.4 – Comparison between the steady head loss coefficients found in Chapter 5 and the head loss coefficient fitted on the head losses during the steady phases with a limited set of discharges

Orifice	Sharp flow direction			Contracted flow direction		
	$k_{Shapr.}^{exp.}$	$k_{Sharp.}^{fit.}$	$diff.$	$k_{Cont..}^{exp.}$	$k_{Cont.}^{fit.}$	$diff.$
EXP_001	29.4	27.0	−8.2%	18.2	17.9	−1.6%
EXP_002	42.8	44.5	+3.9%	31.7	30.1	−5.0%
EXP_004	11.8	10.2	+13%	6.8	6.7	−1.5%
EXP_012	31.4	29.4	−6.4%	20.1	20.6	+2.5%
EXP_032	26.2	23.4	−10.7%	12.5	12.5	0%

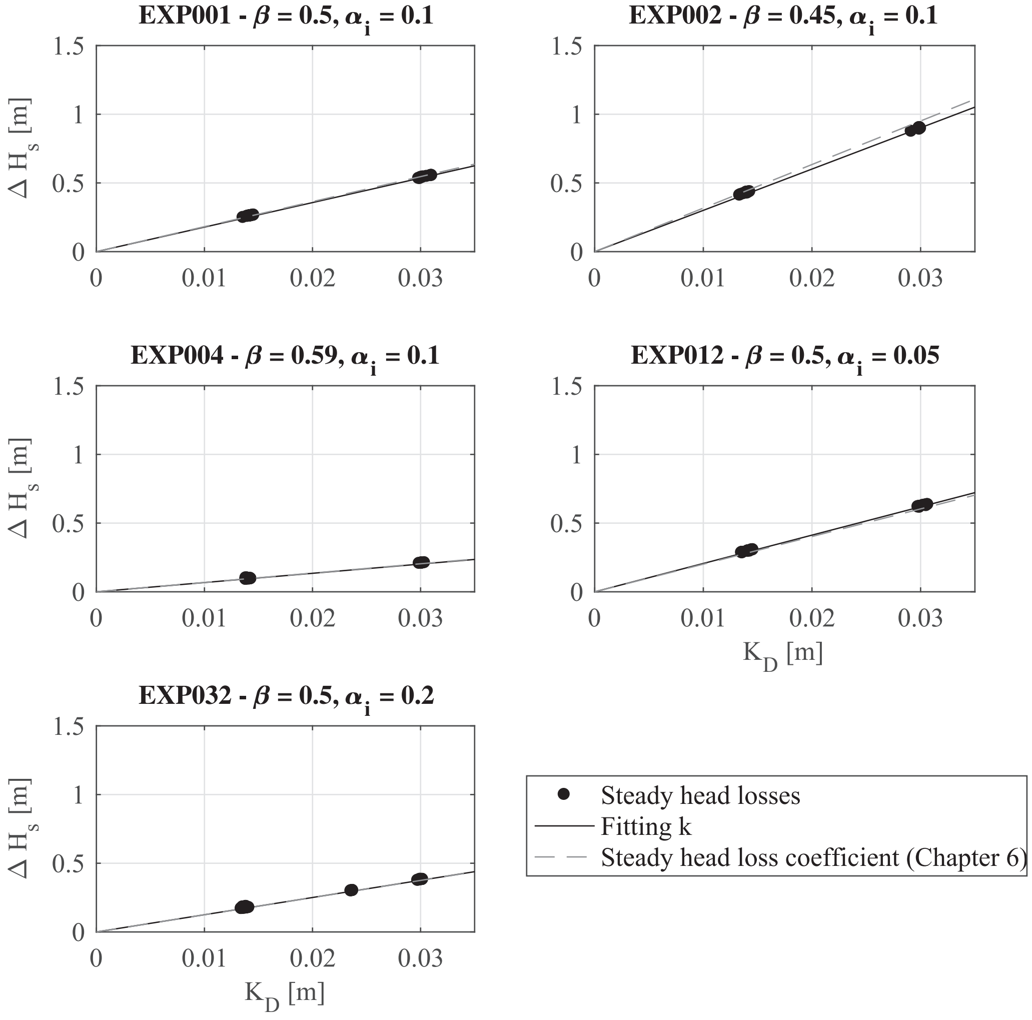

Figure 7.5 – Chamfer approach flow: steady head losses determined with the transient experiments for orifices EXP_001, EXP_002, EXP_004, EXP_012 and EXP_032 compared with the steady head loss coefficients found in Chapter 5

7.3.2 Transient effects on the head losses through orifices

Figure 7.6 shows, for orifice EXP_001, the relationship between the instantaneous local head losses produced by the orifice and the kinetic energy in the main pipe for the different opening and closure durations. It can be noticed that the head losses increase (or decrease) faster than the kinetic energy when the acceleration is positive (or negative). Furthermore, the transient effects are more significant when the flow acceleration, dv_d/dt, increases in the orifice. For the longest durations, the transient effect becomes negligible and tends to merge within the steady pressure fluctuations. This observation leads to a suggestion of a faster experimental method for the evaluation of head loss coefficients (Section 7.4.2).

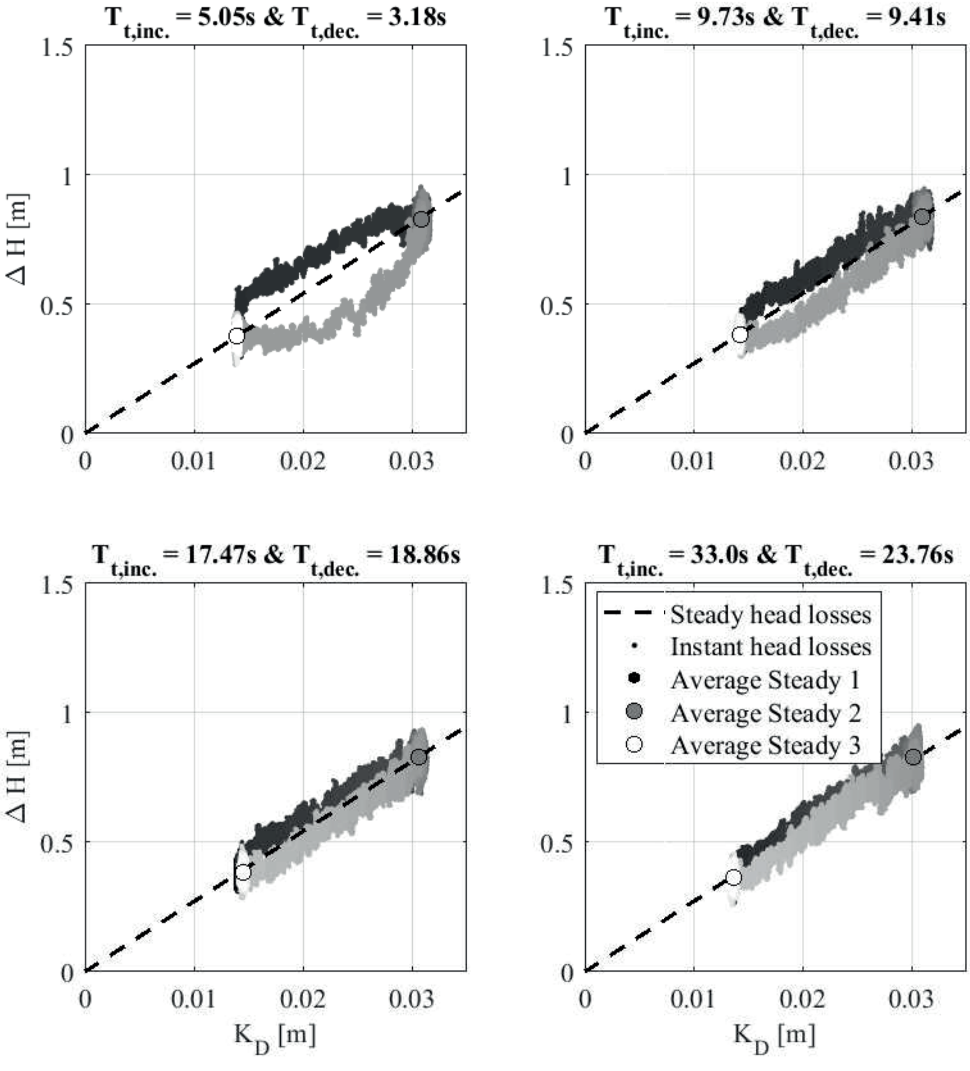

Figure 7.6 – Orifice EXP_001, sharp approach flow: relationship between the instantaneous head losses and kinetic energy in the main pipe

By stressing the transient effects, the transient head loss coefficient, k_t, is defined in Eq.(7.1) and can be evaluated. For the evaluation of k_t, the evolution of the average transient head losses, ΔH_t, defined in Eq.(7.1), as a function of the orifice acceleration, dv_d/dt, as shown in Figures 7.7 and 7.8. ΔH_t is linearly proportional to the orifice flow acceleration while ΔH_s rises with the square of the flow velocity (Section 3.3). Table 7.5 summarizes the obtained values of the transient head loss coefficients for the tested orifices.

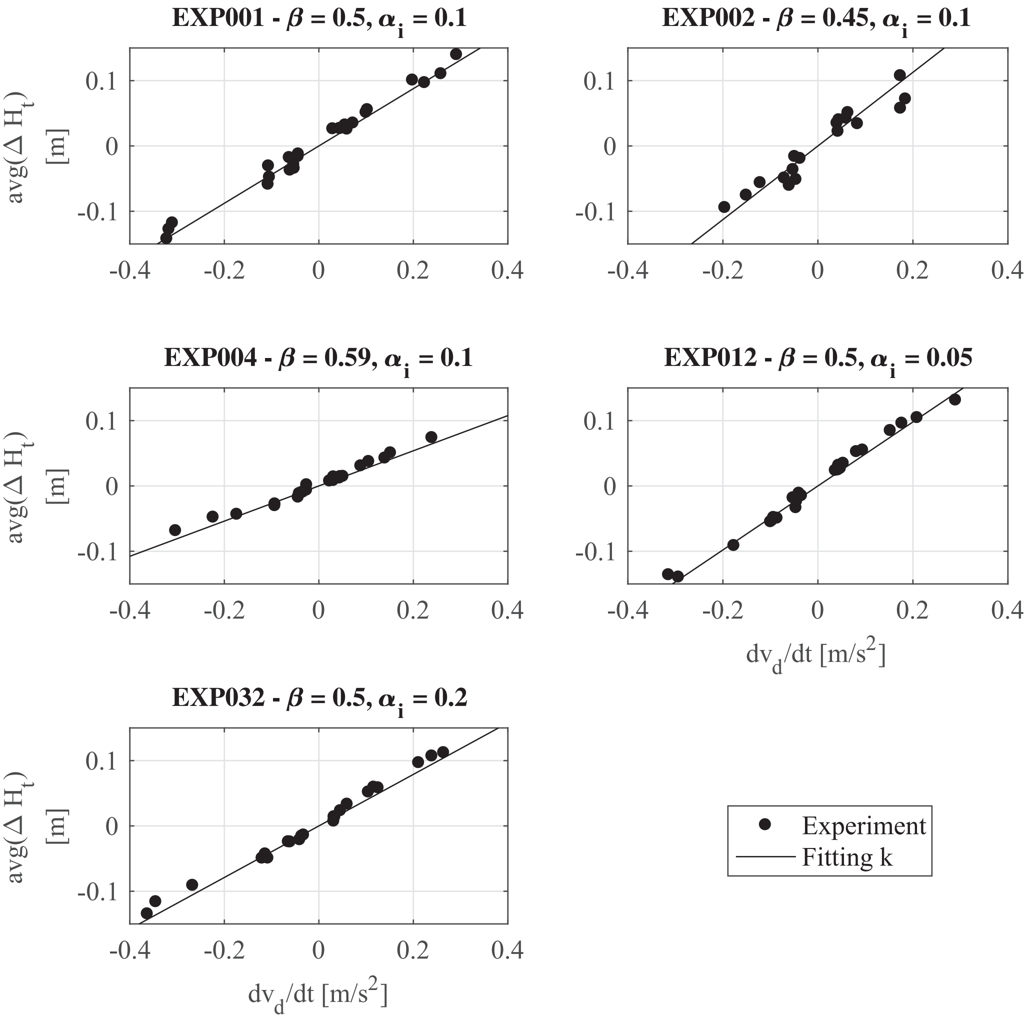

Figure 7.7 – Sharp approach flow - transient head losses determined during the transient experiments for orifices EXP_001, EXP_002, EXP_004, EXP_012 and EXP_032 compared to the steady head loss coefficients found in Chapter 5

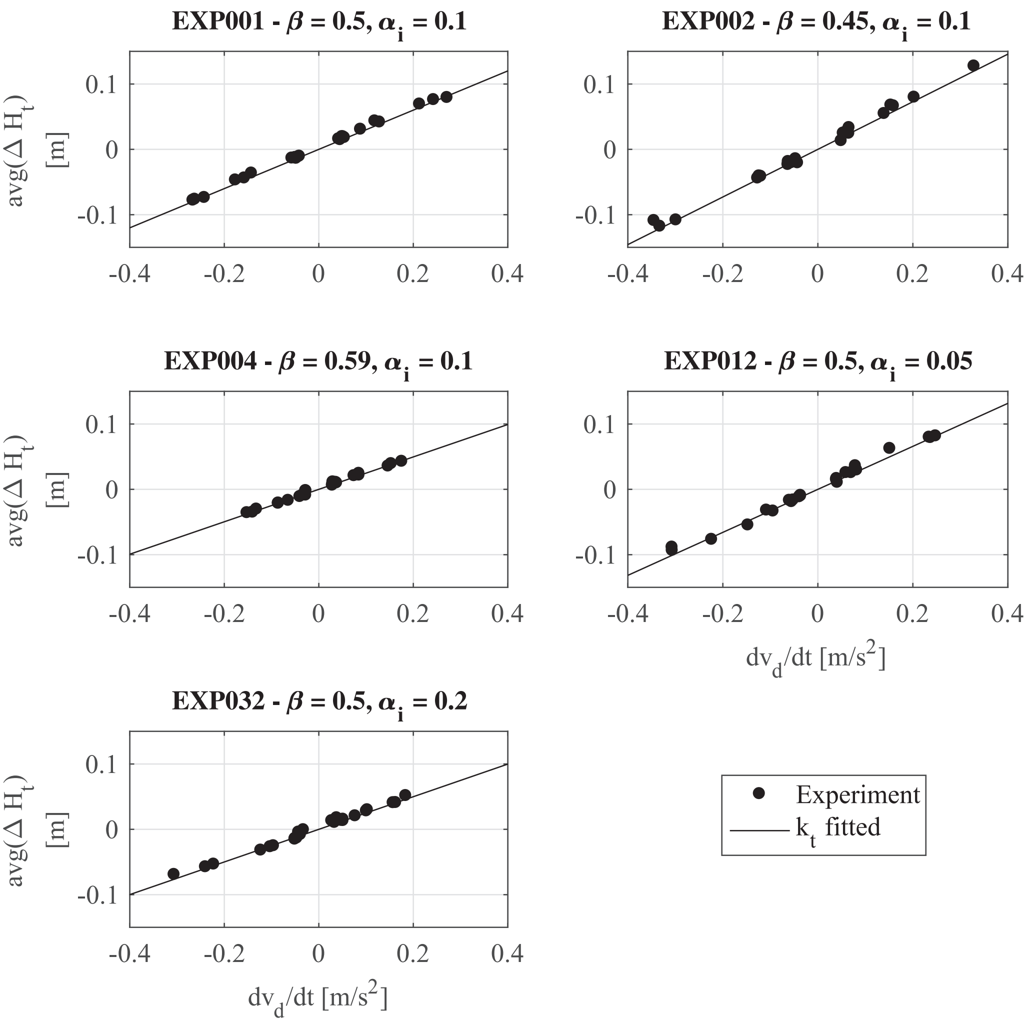

Figure 7.8 – Chamfer approach flow - transient head losses determined on the transient experiments for the orifices EXP_001, EXP_002, EXP_004, EXP_012 and EXP_032 compared to the steady head loss coefficients found in the Chapter 5

Table 7.5 – Results for the transient head loss coefficient, k_t, for orifices EXP_001, EXP_002, EXP_004, EXP_012 and EXP_032 and compared to the transient coefficient, l_e, found by Yamaguchi (1976) (note: the effect of inertia, Table 7.2, is eliminated in the evaluation of k_t)

Orifice	Sharp flow direction	Chamfered flow direction	l_e (Yamaguchi, 1976)
EXP_001	3.43	2.08	0.89
EXP_002	4.82	2.87	0.90
EXP_004	1.43	1.22	0.88
EXP_012	3.94	2.36	0.86
EXP_032	3.00	1.58	0.93

According to Figures 7.7 and 7.8 along with Table 7.5, the following observations could be made:

- the transient head loss coefficient, k_t, increases when the contraction ratio β increases. The new coefficient does not seem to be proportional to β^4 as is the case for the steady head loss coefficient; and

- the transient head loss coefficient, k_t, diminishes when the inner thickness and thickness ratios, α_i and α, increase akin to the steady head loss coefficient.

7.4 Discussion

7.4.1 Transient effect

For all orifices, transient behaviors of head losses were examined. Transient effects depending on the flow acceleration and the velocity diffusion (dv/dx) are well-known (Ferràs Segura, 2016; Chaudhry, 2014). However, very few studies have been performed on the transient effect on local head losses (Daily et al., 1955; Yamaguchi, 1976). Yamaguchi (1976) evaluated the transient head loss coefficient, k_t, for air flows based on the concept of the equivalent length of an orifice. A comparison with the coefficient obtained in this study shows that this coefficient seems higher in the case of water flows than with air flows (Table 7.5).

Using the 1D numerical simulations performed for the Gondo hydropower plant (Adam et al., 2017), the maximum flow acceleration related to the entrance of the surge tank was determined to be roughly 0.13 m/s^2, which is in the range of the experiments herein.

7.4.2 Slow transient experiments for the evaluation of the steady head loss coefficient

The transient effects of head losses decrease with the absolute value of the flow acceleration, dQ/dt. It should be possible to evaluate the head loss coefficient in one flow direction with small accelerations leading to negligible additional uncertainties between steady and unsteady results similar to what Hasmatuchi et al. (2016) performed with respect to the hydraulic characteristics of turbines.

During this study, the experimental procedure was performed according to Chapter 4.1. The total recording duration for the experimental setup was 120 minutes for each orifice without changes to the discharge for flow directions. The real duration of each orifice test was actually 240 minutes from the beginning of the test preparation to the end of the test itself. However, the evolution of the pressure line along the pipe axis was lost with slow transient experiments only.

It could be useful to decrease this duration by combining long steady measurements (for example, three discharges) and two slow transient measurements (for instance, between the minimum and median discharges and between the median and maximum discharge). Pressure lines for the three discharges would be recorded and could be compared to the numerical results while the experimental duration and uncertainty would remain as low as possible.

7.5 Conclusions

It could be shown that there is a clear influence of flow acceleration on head losses. The total head losses were thus divided into steady head losses proportional to the flow kinetic energy and transient head losses proportional to flow acceleration.

An increase (or decrease) in flow velocity leads to more head losses (or less) significantly than the steady head losses evaluated in Chapter 5. This effect is pronouncedly greater than the inertial effect evaluated by the integration of the momentum equation; it works as the orifice temporarily blocks the information originating downstream.

A method for estimating the steady head loss coefficient is suggested in order to decrease the duration of the experimental tests. Even if the experimental procedure presented in Chapter 4.1 is still relevant, its duration could decrease from 240 minutes to at least 90 minutes without increasing the uncertainty too much in terms of the steady head loss coefficients. However, the pressure line information for a given discharge would be lost. An intermediate procedure testing less steady discharges and various transient tests would be adequate.

8 Estimation of incipient cavitation number at orifices

8.1 Introduction

The previous chapters focused on the head losses and influence length of different orifice geometries. Different combinations of the contraction ratio, β, inner thickness ratios, α_i, and chamfered angle, θ, can produce the same head losses in both directions, i.e. for the water flowing into or out of a surge tank. Nevertheless, certain geometries are more subjected to cavitation than others. Hence, the cavitation risk has to be known.

Cavitation may be accepted for certain cases but it should not disturb the hydraulic behavior of the orifice throttle for which it was designed. As explained in Chapter 2, 1D numerical simulations are performed to determine the require head losses produced by the throttle. Yet, these 1D models are not able to reproduce the effect of cavitation.

The cavitation number is defined differently depending on the authors (see Section 3.6.1). In the following, the definition given by Ferrarese et al. (2015) is used to allow for a comparison with previous studies that employ other definitions of cavitation numbers, with the transformations as given in Section 3.6.1 to accompany them.

A graphical representation of the cavitation risk in the plane discharge - upstream pressure or discharge - water level in the surge tank is suggested. This representation visualizes the cavitation risk based on the results, water level and discharge in the surge tank, as per the 1D numerical simulations.

8.2 Assessment of cavitation

8.2.1 Prediction of the incipient and vena-contracta cavitation number

As described in Section 3.6.4, a method developed by Ferrarese et al. (2015), that predicts the incipient cavitation number, σ_i, was employed as in Eq.(8.1). Along with this prediction, there was another prediction of the *vena-contracta* cavitation number characterizing the appearance of the cavitation in the *vena-contracta* as in Eq.(8.2). The computed pressure field is obtained with CFD numerical simulations for chamfered orifices.

$$\sigma_i = \frac{p_u^* - p_m^*}{p_u^* - p_d^*} \tag{8.1}$$

where p_u^* is the upstream computed pressure, p_m^* the minimum computed pressure and p_d^* the downstream computed pressure

$$\sigma_{vc} = \frac{p_u^* - p_{vc}^*}{p_u^* - p_d^*} \tag{8.2}$$

where: p_{vc}^* is the computed pressure in the *vena-contracta*

The prediction of the incipient cavitation number, σ_i, and the *vena-contracta* cavitation number, σ_{vc}, given by Eqs.(8.1) and (8.2) do not focus on the vapour pressure p_{vg}. This term is present by the mean of the constant pressure added in the development performed by Ferrarese et al. (2015) and summarized in Section 3.6.4. Furthermore, σ_i and σ_{vc} are evaluated under numerical steady flow. The pressure fluctuations are hence not considered even if they could cause cavitation. However, this effect is less severe for transient flows.

8.2.2 Cavitation risk in pipes

Once the incipient cavitation number has been predicted either by numerical CFD simulations or by an empirical formula (Section 8.3.2), a graphical representation can assess the risk of cavitation. Figure 8.1 shows schematically its possible utilization. If the point of utilization (Q, p_u) is in the white area, there is no risk of cavitation while there is indeed risk in the grey area. In the work presented here, the discharge is positive for the chamfer approach flow.

Eq.(8.3), which was developed from Eq.(8.1), establishes the boundary with the area where there is a risk of cavitation (grey zone in Figure 8.1) and the area with low or no cavitation risk. The development of Eq.(8.3) is shown in Appendix F.

$$p_u = \sigma_i \cdot \frac{8\beta^4}{g\pi^2 d^4} k \cdot Q^2 + p_{vg} \tag{8.3}$$

where: p_u is the upstream pressure, σ_i the incipient cavitation number, β the contraction ratio, k the head loss coefficient (Chapter 5), Q the discharge, d the orifice diameter and $p_{v.g.}$ the vapour pressure.

An application of this formulas is located in Section 9.2.5.

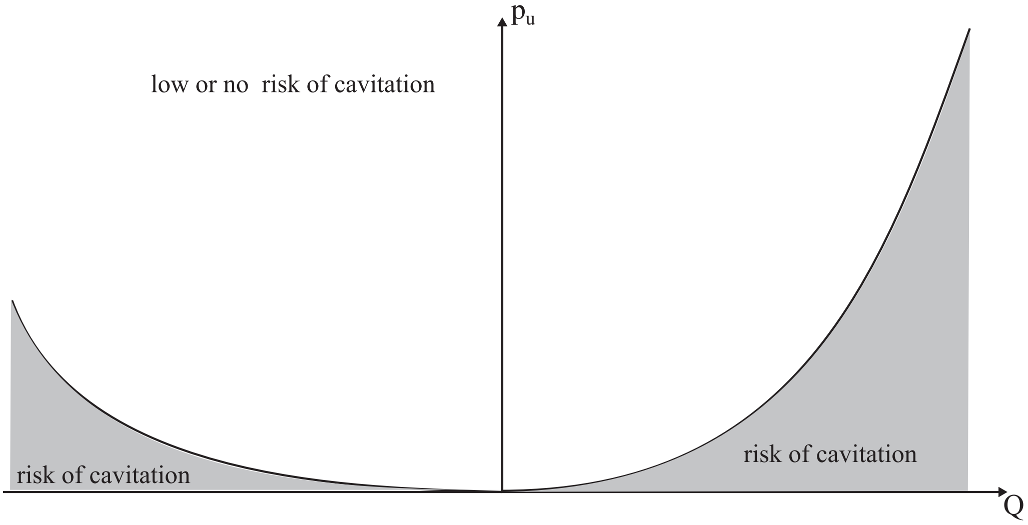

Figure 8.1 – Schematic view of a Q-p$_u$ plane for an orifice with the different areas of utilization with or without cavitation risk

8.2.3 Cavitation risk in surge tank throttles

During the design phase of an orifice throttle, the whole waterway is generally simulated with a 1D numerical model. The results are a temporal evolution of the discharge and water level in the surge tank. During mass oscillations, the water level and discharge are consistently changing.

The same approach from Section 8.2.2 can be applied to a surge tank with a throttle during mass oscillations (see Appendix F). It would be interesting to represent the main numerical results, i.e. the discharge flowing through the orifice and water level in the surge tank in a new (Q, H_{st}) plane. The water level in the surge tank is thus either the upstream section during the emptying of surge tank or the downstream section while the surge tank being filled. In this research study, the discharge is taken as positive during the filling (Eq.(8.5)) and negative during emptying (Eq.(8.4)).

$$H_{ST} = \sigma_i \cdot \frac{8\beta^4}{g\pi^2 d^4} k \cdot Q^2 - \sigma_i \cdot \kappa_Q Q^2 + p_{vg} \tag{8.4}$$

where $\kappa_Q = \frac{1}{2g} \cdot \left(\frac{1}{A_{ST}^2} - \frac{1}{A_{PT}^2}\right)$ is the correction owing to the effect of the difference of kinetic energy between the surge tank and the pressure tunnel.

$$H_{ST} = (\sigma_i - 1) \cdot \frac{8\beta^4}{g\pi^2 d^4} k \cdot Q^2 - (\sigma_i - 1) \cdot \kappa_Q Q^2 + p_{v.g.} \tag{8.5}$$

where $\kappa_Q = \frac{1}{2g} \cdot \left(\frac{1}{A_{PT}^2} - \frac{1}{A_{ST}^2} \right)$ is the correction based on the effect of the difference of kinetic energy between the surge tank and the pressure tunnel.

An application of these formulas is found in Section 9.2.5.

8.3 Results and analysis

8.3.1 Low pressure zones

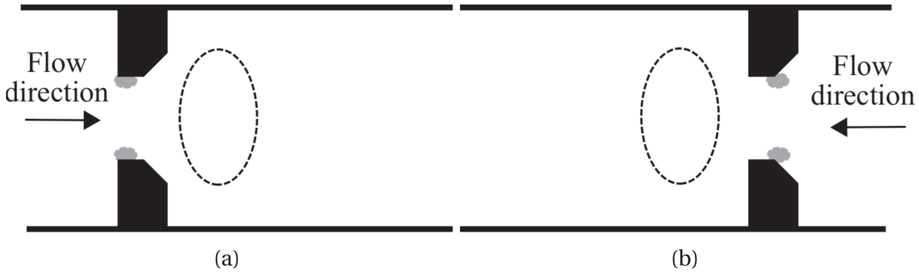

Figure 8.2 – Zones with expected low pressures: (a) gray zone where there are the lowest pressures; (b) white zone representing the *vena-contracta*

The location of the pressure drops can occur in two different zones as in Figure 8.2:

- close to the orifice walls (gray zones in Figure 8.2), where the water velocity locally increases because of the flow contraction. It produces the lowest pressure in the pipe and has different locations depending on flow direction, i.e. sharp or chamfer approach flow. This is the pressure considered for the evaluation of the incipient cavitation number, σ_i (defined in Figure 3.6); Eq.(8.6) defines the lowest pressure coefficient, k_{min}, analogous to the head loss coefficient, k; and

$$\frac{\Delta p_{min}}{\rho g} = k_{min} \cdot \frac{v_D^2}{2g} \tag{8.6}$$

- in the *vena-contracta* (white zones in Figure 8.2), where the velocities are the highest owing to contraction. The occurrence of cavitation is across the whole of the *vena-contracta* when the cavitation number is equivalent to the chocking cavitation number. Eq.(8.7) defines a *vena-contracta* pressure coefficient, k_{vc}, analogous to the head loss coefficient, k.

$$\frac{\Delta p_{vc}}{\rho g} = k_{vc} \cdot \frac{v_D^2}{2g} \tag{8.7}$$

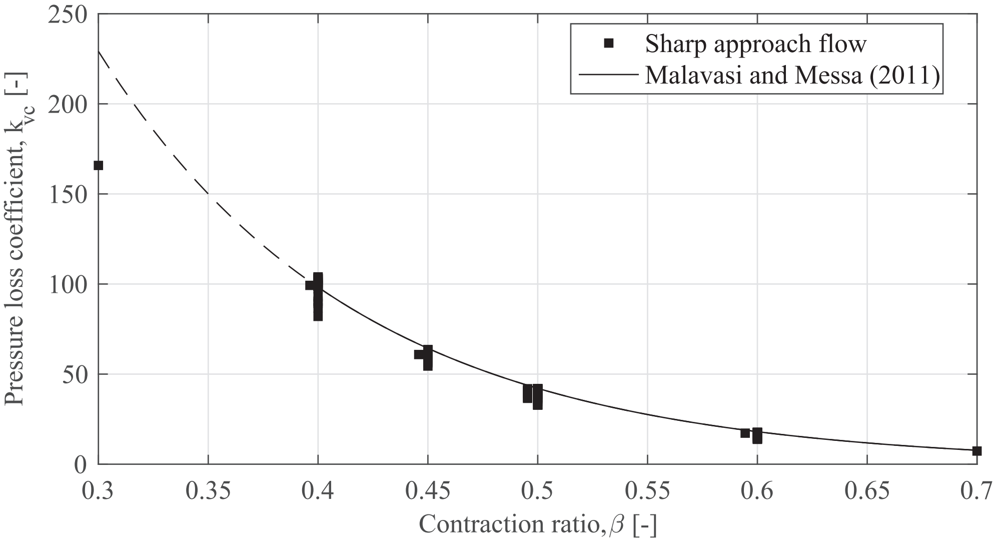

Figure 8.3 – Comparison of the numerical result of the pressure loss coefficient (between the upstream and *vena-contracta* pressure) and the experimental formula-obtained values of Malavasi and Messa (2011) valid for $\beta \in [0.39, 0.7]$ and $\alpha \in [0.25, 1.5]$

For the estimation of σ_i, the lowest value of pressure closest to the orifice walls must be used as was proposed by Ferrarese et al. (2015). The pressure in the *vena-contracta* characterizes the σ_{vc}.

Malavasi and Messa (2011) put forth an empirical expression of the *vena-contracta* pressure coefficient, k_{vc}, as shown in Eq.(8.8) valid for $\beta \in [0.39, 0.7]$ and $\beta \in [0.25, 1.5]$. The numerical results are in fairly strong agreement with Eq.(8.8) even if ones only considers the effect of the contraction ratio β. However, it can be seen that Eq.(8.8) should not be used outside its limitation ($\beta \in [0.39, 0.7]$ and $\alpha \in [0.25, 1.5]$) when taking into account its exponential term.

$$k_{vc} = 2908 \cdot e^{-8.47\beta} \tag{8.8}$$

8.3.2 Prediction of cavitation number

The incipient cavitation number, σ_i, is the limit between a flow with and without cavitation. While the *vena-contracta* does not cavitate, the flow producing head losses through the orifice is moderately sensitive to this phase whereas little cavitation produces only small bubbles (Malavasi et al., 2015). However, if the discharge (or the upstream pressure) continues to rise (or decreases), the flow reaches the critical cavitation, for which there is still no damage to the structures (Tullis, 1989). The *vena-contracta* cavitation number, σ_{vc}, is introduced to delve further into cavitation without damage versus the incipient cavitation number, σ_i, which is conservative (Tullis, 1989).

Figure 8.4 shows the incipient cavitation number, σ_i, and the *vena-contracta* cavitation number, σ_{vc}. Both incipient cavitation numbers tend to increase when β rises. However, the spreading of the σ_i for the chamfer approach flow is higher than for the others. The vena-contracta cavitation numbers, σ_{vc}, are more or less the same for the two flow approaches. The value of σ_i is, logically, always higher than the corresponding σ_{vc}.

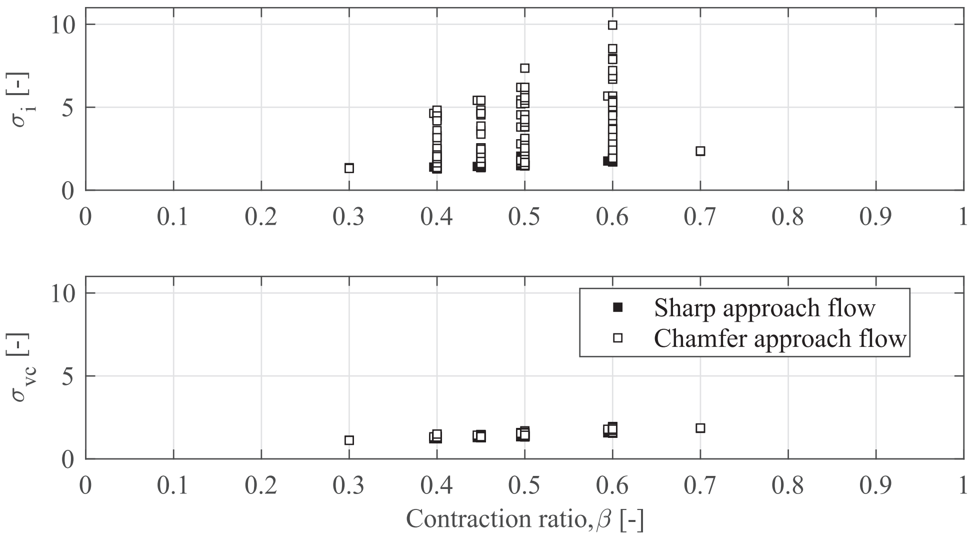

Figure 8.4 – Value of the incipient cavitation number, σ_i, and the vena contracta cavitation number, σ_{vc}, as a function of the contraction ratio, β

Analysis of incipient cavitation, σ_i

For the sharp approach flow, it can be seen in Figure 8.6 that σ_i increases when β and α_i rise. The chamfer angle θ does not have an influence on σ_i, except for $\theta = 0°$ (for which α_i increases). The variability of σ_i is low from 1.29 to 2.40 for the sharp approach flow. An empirical formula is proposed in Eq.(8.9) in order to predict σ_i. The fit is shown in Figure 8.9.

$$\sigma_i^{sharp} = 1 + 2.02 \cdot \beta^2 + 2.50 \cdot \alpha_i^{1.5} \tag{8.9}$$

For the chamfer approach flow, Figure 8.7 exhibits how the chamfer angle, θ, has a large-scale influence with a maximum incipient cavitation number, σ_i, between 30° and 45°. σ_i tends to increase with β and α_i as it does for the sharp approach flow. A conservative empirical formula is proposed in Eq.(8.10) while in Figure 8.5, the envelope curve for different β, α_i and

θ values is displayed.

$$\sigma_i^{chamfer} = \sigma_i^{sharp} \cdot \left[1 + 4.15 \cdot (\sin(2\theta))^2\right] \tag{8.10}$$

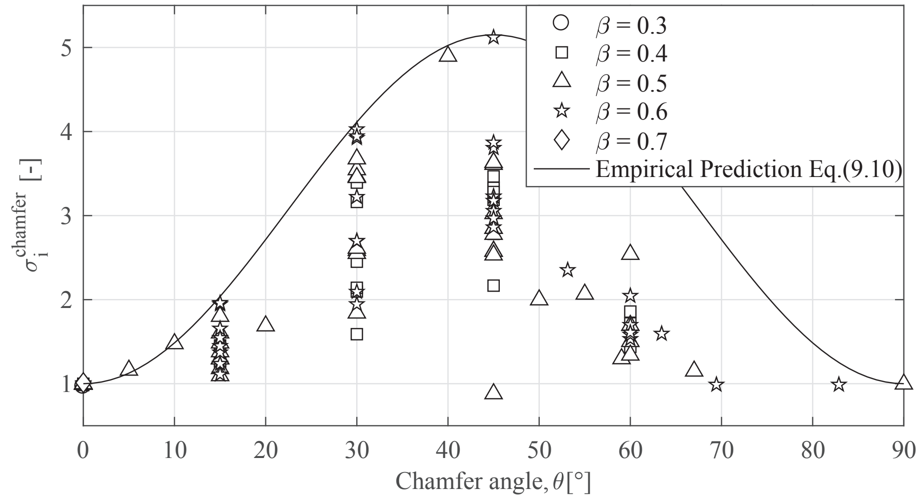

Figure 8.5 – Comparison of the numerical prediction and empirical prediction of the incipient cavitation number, σ_i, for the chamfer approach flow

Analysis of vena-contracta cavitation number, σ_{vc}

For the sharp and chamfer flow approaches, the variability of the *vena-contracta* cavitation number, σ_{vc}, is lower than the variability of the incipient cavitation number, σ_i.

For the sharp flow approach, the contraction ratio, β, and the thickness ratio, α_i, are the most impactful parameters. Another empirical formula (Eq.(8.11)) is also proposed with the same structure.

$$\sigma_{vc}^{sharp} = 1 + 1.47 \cdot \beta^2 + 0.45 \cdot \alpha_i^{1.5} \tag{8.11}$$

For the chamfer approach flow, the variability is also lower than for the incipient cavitation number, σ_i. However, as portrayed in Figure 8.8, there is no clear influence of the chamfer angle, θ, and a predicting formula similar to Eq.(8.11) can be fitted onto the numerical results.

$$\sigma_{vc}^{chamfer} = 1 + 2.01 \cdot \beta^2 + 0.23 \cdot \alpha_i^{1.5} \tag{8.12}$$

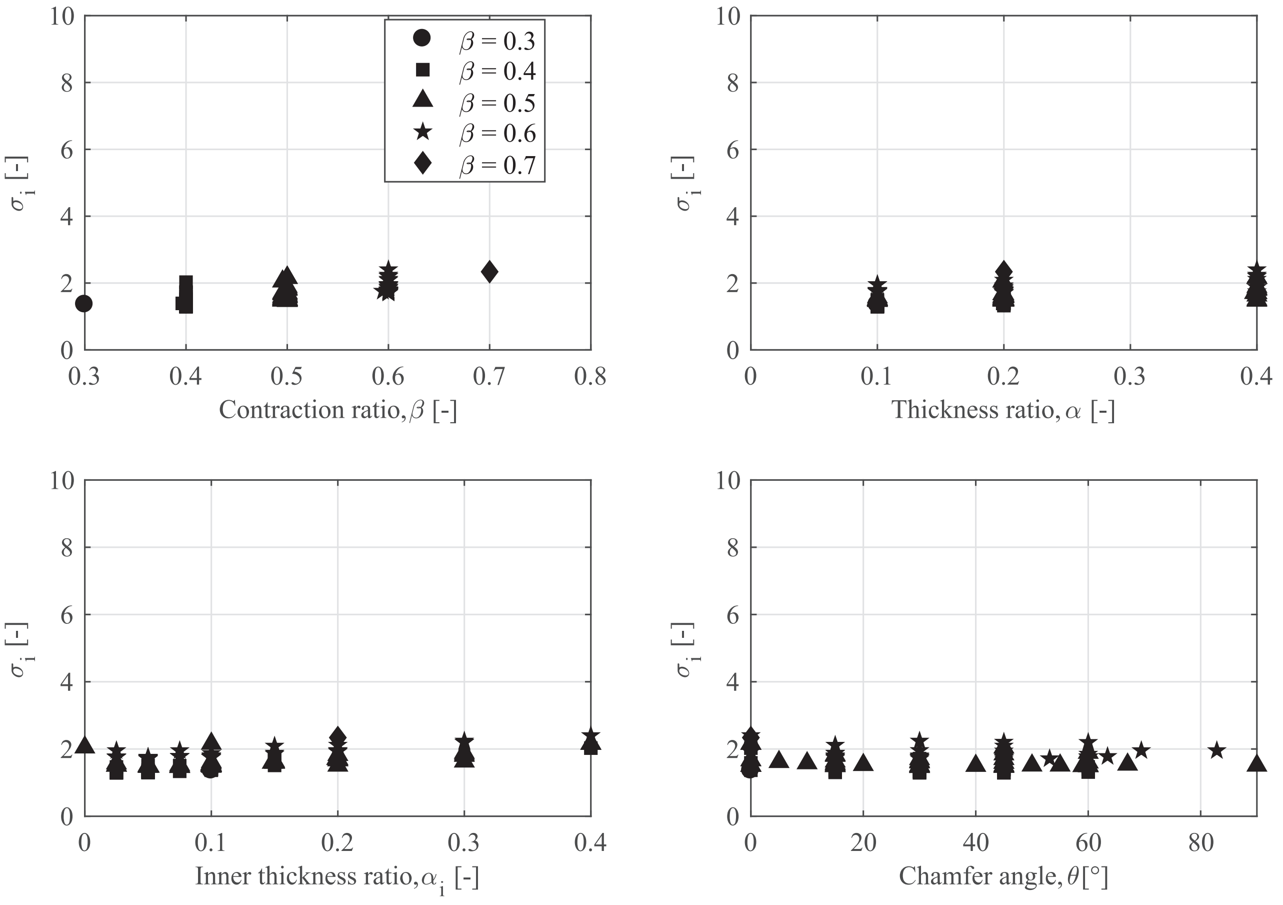

Figure 8.6 – Sharp approach flow - incipient cavitation number σ_i as a function of the contraction ratio, β, the thickness ratio α, the inner thickness ratio, α_i ,and the chamfer angle, θ

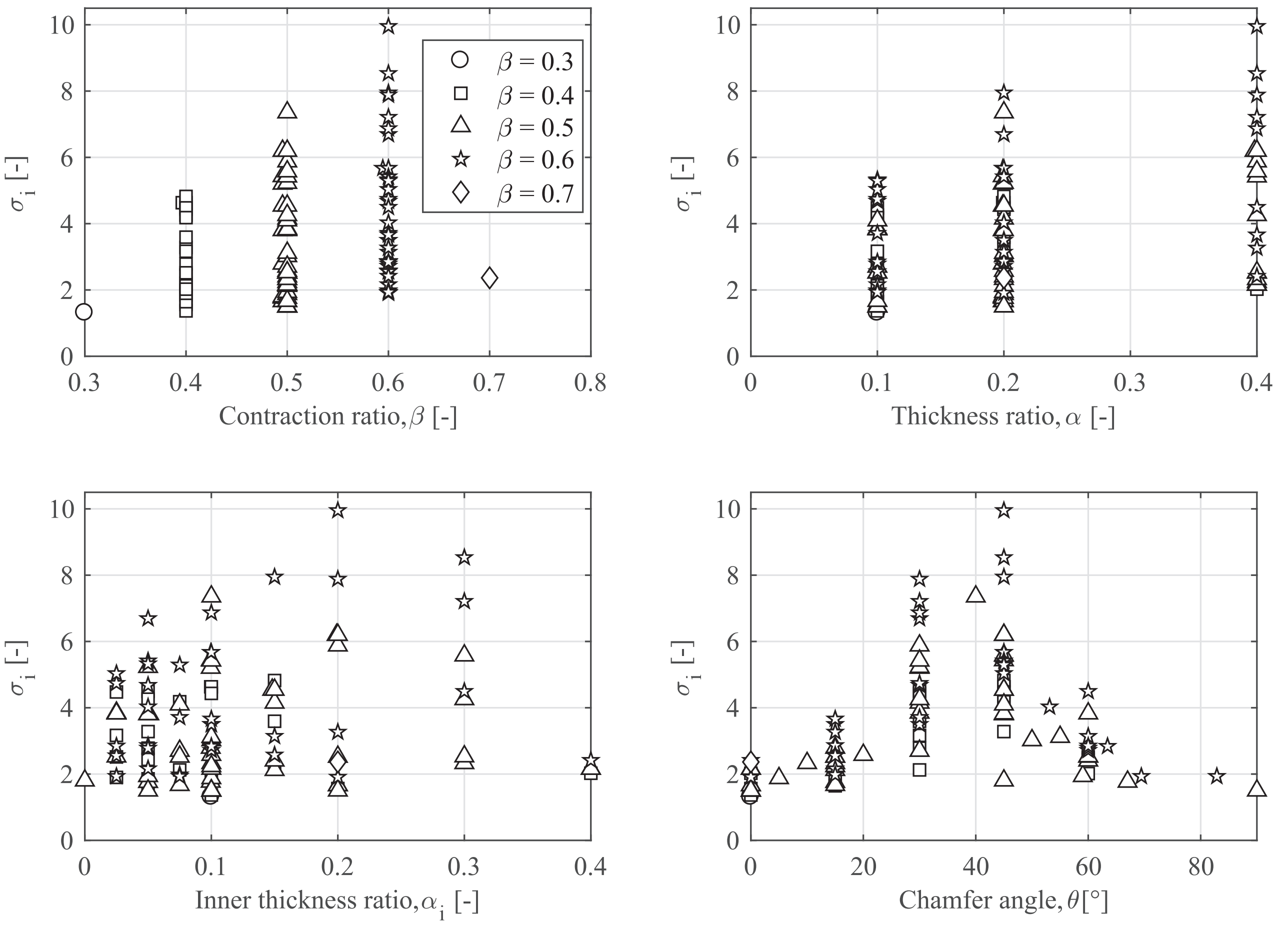

Figure 8.7 – Chamfer approach flow - incipient cavitation number, σ_i, as a function of the contraction ratio, β, the thickness ratio, α, the inner thickness ratio, α_i, and the chamfer angle, θ

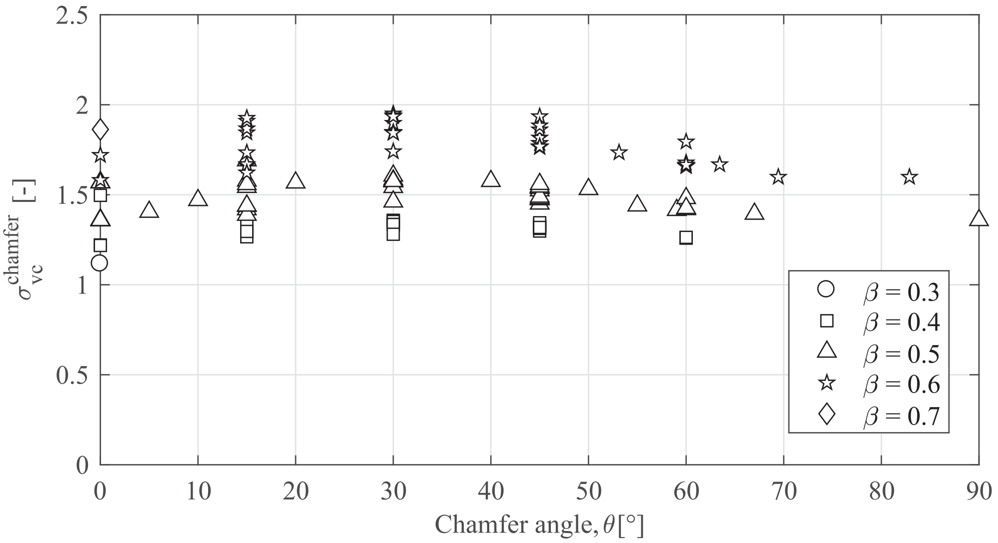

Figure 8.8 – The *vena-contracta* cavitation number as a function of the chamfer angle, θ, and the contraction β for the chamfer approach flow

8.4 Discussion

The incipient cavitation number, σ_i, does not vary significantly for the sharp approach flow and depends predominantly on the contraction ratio, β, and the inner thickness ratio α_i (see Figure 8.9 for the fit). With respect to the chamfer approach flow, σ_i, has greater variability. Chamfer angles between 30 and 50 degrees are characterized by the highest σ_i but the lowest head loss coefficients for the chamfer approach flow. As can be seen in Figures 5.25 and 5.26, the orifice walls gradually guide the flow to less flow contraction and, thus, less flow expansion. Yet, at the same time, the flow velocities locally increases because of the geometry changes that the water adheres to, thereby creating a pressure drop. For smaller angles (roughly 15 degrees), the change of direction is less stark for the same flow contraction leading to equivalent head losses. For the greatest and smallest angle ($\theta < 10°$ or $> 60°$), the flow streamlines do not follow the geometry and tend to exhibit the sharp behavior that results in highly contracted flow at the *vena-contracta* and to large head losses. In order to predict the chamfer incipient cavitation, a conservative empirical formula was fitted onto the numerical results (Eq.(8.10)). Figure 8.9 illustrates the conservative prediction.

For both approach flow directions, the *vena-contracta* cavitation number, σ_{vc}, varies across small ranges and also depends on β and α_i. Two predictive formulas (Eq.(8.11) and (8.12)) were suggested and corroborate the numerical results as seen in Figure 8.10. The almost constant value of σ_{vc} demonstrates that the head loss and the pressure loss coefficients vary with the same geometrical parameters and on the same order of magnitude.

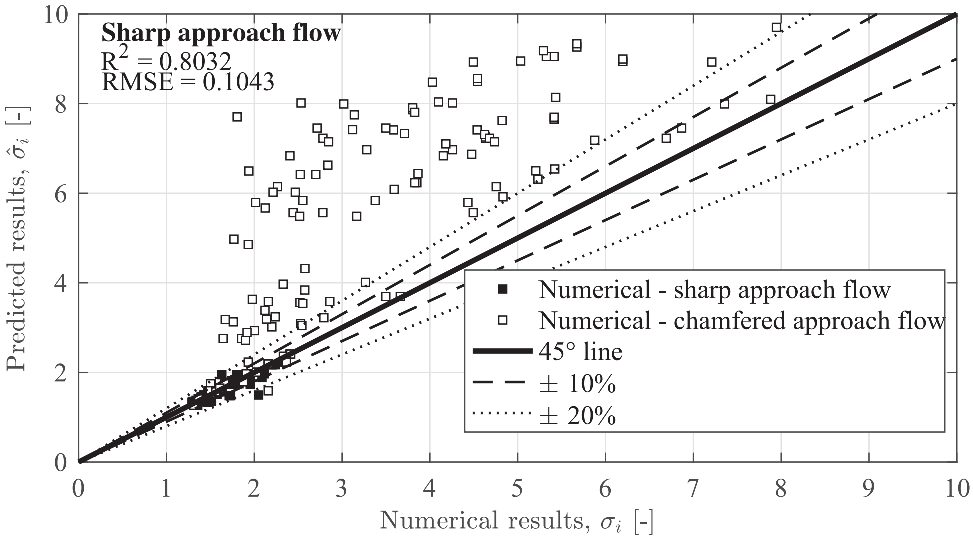

Figure 8.9 – Comparison of numerical prediction with the empirical prediction of the incipient cavitation number, σ_i, for the sharp and chamfer approach flows

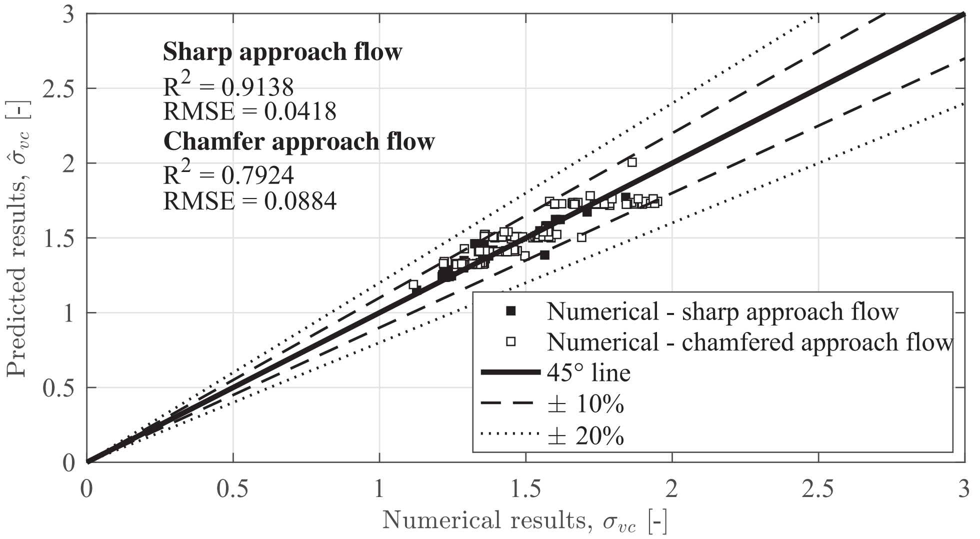

Figure 8.10 – Comparison of numerical prediction and empirical prediction of the *vena-contracta* cavitation number, σ_{vc}, for the sharp and chamfer approach flows

8.5 Conclusions

The cavitation numbers are based on either the local lower pressures appearing close to the orifice side because of the sudden constriction or on the low pressure in the *vena-contracta*. This numerically obtained low pressure is in solid agreement with a formula of Malavasi and

Messa (2011). However, this formula should not be used outside its validity range owing to the observations of large discrepancies for $\beta = 0.3$.

For the sharp approach flow, both incipient and *vena-contracta* cavitation numbers depend mainly on the contraction ratio, β, and on the inner thickness ratio, α_i. For the chamfer approach flow, the chamfer angle, θ, has more influence on the incipient cavitation number, σ_i, than on the *vena-contracta* cavitation number, σ_{vc}.

The incipient cavitation number, σ_i, can be predicted by the empirical formulas given by Eq.(9.9) for the sharp approach flow and Eq.(8.10) for the chamfer flow approach.

The *vena-contracta* cavitation number can be predicted by the empirical formulas given by Eq.(8.11) for the sharp approach flow and Eq.(8.12) for the chamfer flow approach.

Finally, the definition of the cavitation number was derived in order to be able to evaluate the risk of cavitation with the upstream pressure and discharge for the pipe along with the water level and the discharge for a surge tank. An application of the evaluation of this risk of cavitation is established in Chapter 9.2.

9 Design guidelines and case studies

9.1 Design guidelines

In this section, the term "orifice" is used but can be replaced by the generic term "throttle"

9.1.1 Introduction

Surge tank orifices can improve the behavior of a surge tank by limiting the maximum and minimum water levels during mass oscillations as well as in their duration. The introduction of an orifice take place during or after the construction of a surge tank. An orifice allows, during the design phase, to limit construction costs by diminishing the required volume of the surge tank. For upgrading projects with a change of the installed capacity of high-head power plants, orifices help avoid an extension of the surge tank.

9.1.2 Required basic data

The required inputs are the characteristics of the waterway and the high-head power plant. The features of the waterway are: geometrical parameters of the pressure tunnel and shaft, including diameter, roughness and length, different local head losses produced by the change of tunnel geometry, such as enlargement, contraction and changes of direction, but also the geometry and the position of the surge tank. The characteristics of the power plant are: design discharge, net head between the reservoir and turbine, opening or closure time of turbine and its operation curves.

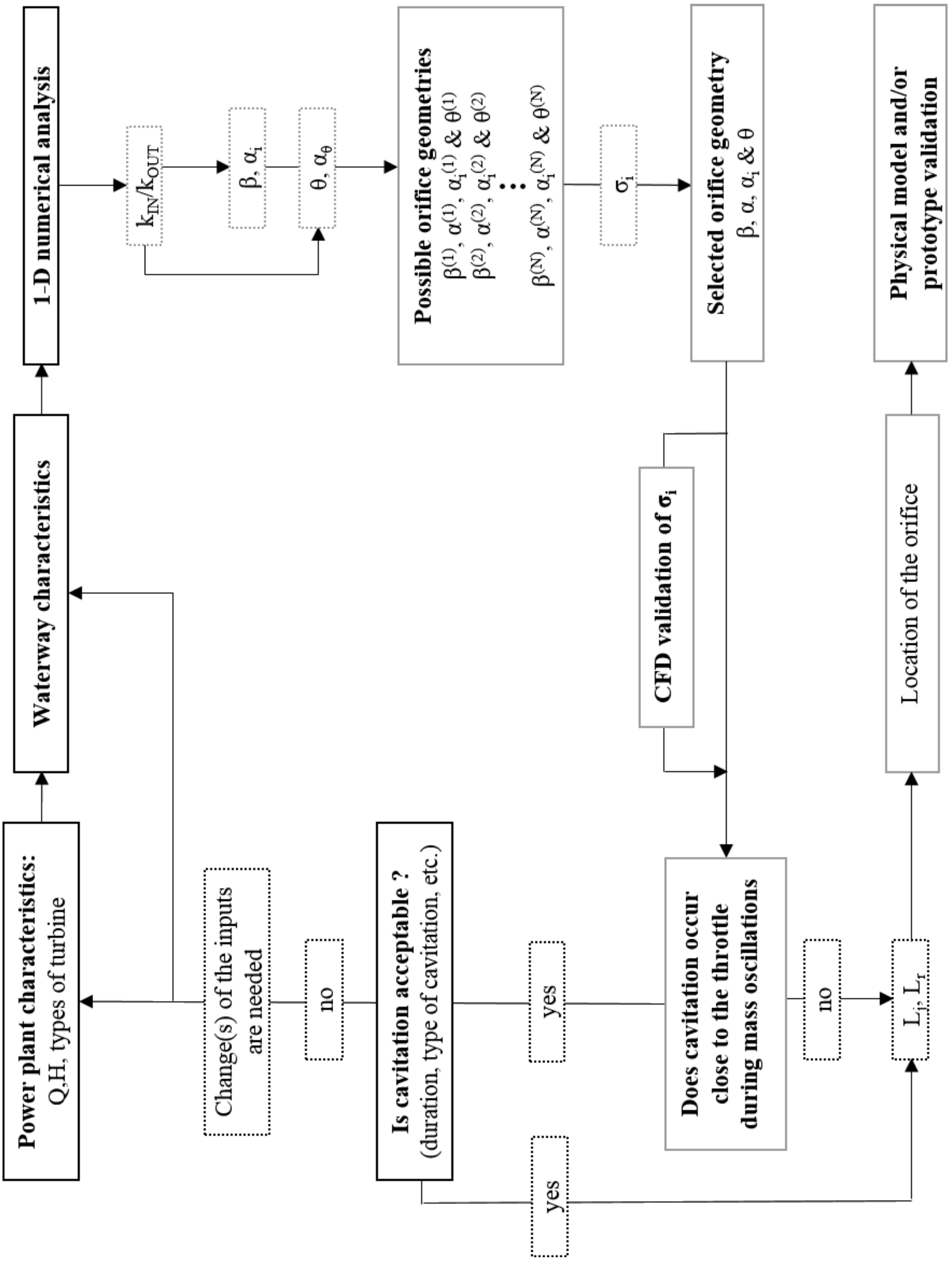
Power plant characteristics:
Q,H, types of turbine
Waterway characteristics
1-D numerical analysis
k_{IN}/k_{OUT}
β, α_i
θ, α_θ
Possible orifice geometries
$\beta^{(1)}, \alpha^{(1)}, \alpha_i^{(1)}$ & $\theta^{(1)}$
$\beta^{(2)}, \alpha^{(2)}, \alpha_i^{(2)}$ & $\theta^{(2)}$
$\beta^{(N)}, \alpha^{(N)}, \alpha_i^{(N)}$ & $\theta^{(N)}$
σ_i
Selected orifice geometry
β, α, α_i & θ
CFD validation of σ_i
Does cavitation occur close to the throttle during mass oscillations
no
yes
L_l, L_r
Location of the orifice
Physical model and/or prototype validation
Is cavitation acceptable ?
(duration, type of cavitation, etc.)
no
yes
Change(s) of the inputs are needed

Figure 9.1 – Schematic view of the proposed orifice design procedure

9.1.3 Numerical transient analysis

Once all the high-head power plant characteristics are known, a numerical analysis is carried out to determine the response of the plant to the different load cases (Adam et al., 2017):

- emergency shutdown of all the units;
- simultaneous loading of all units;
- loading followed by emergency shutdown at the worst moment for the upsurge in the surge tank;
- load rejection followed by a reloading while all units remain connected to the grid; and
- emergency shutdown as well as loading and emergency shutdown leading to the closure of injectors during penstock reflection time, i.e., the so-called Peak of Michaud (Nicolet et al., 2012).

The main output of these numerical simulations are the two required head losses characterizing the orifice at the entrance of the surge tank for inflow and outflow. In the case of upgrading projects, the structural resistance of the pressure tunnel lining must be verified regarding the increased pressure waves (water hammer), that are transmitted to the pressure tunnel.

9.1.4 Design of the orifice producing the required head losses

Hereafter, the head loss coefficient for the water flowing out of the surge tank, k_{OUT}, is considered higher than the head loss coefficient for the water flowing into it, k_{IN}. A catalog of the experimentally obtained head loss coefficients is located in Appendix B and can be used instead of the empirical relationships from this section. In addition, there is an expert sheet, which is described in Appendix G and on-line available (doi:10.5075/epfl-thesis-8090).

Determination of β and α_i for certain k_{OUT}

With Eq.(6.3) (defined in Chapter 5, Section 5.3.3) several pairs of contraction and inner thickness ratios (β, α_i), which produced the required head loss coefficient k_{OUT}, can be determined.

$$k_{sharp} = \Upsilon_{\alpha i} \cdot \frac{(1 + \tau\sqrt{(1-\beta^2)} - \beta^2)^2}{\beta^4} \tag{6.3}$$

where $\Upsilon_{\alpha i} = 1 - \kappa_{\alpha i} \cdot \alpha_i$, $\kappa_{\alpha i} = 0.9486$ and $\tau = 0.745$.
In Figure 9.2, the sharp head loss coefficient is represented as a function of the contraction ratio, β, and the inner thickness ratio, α_i. A certain k_{OUT} can thus lead to a line giving an infinite number of pairs (β, α_i).

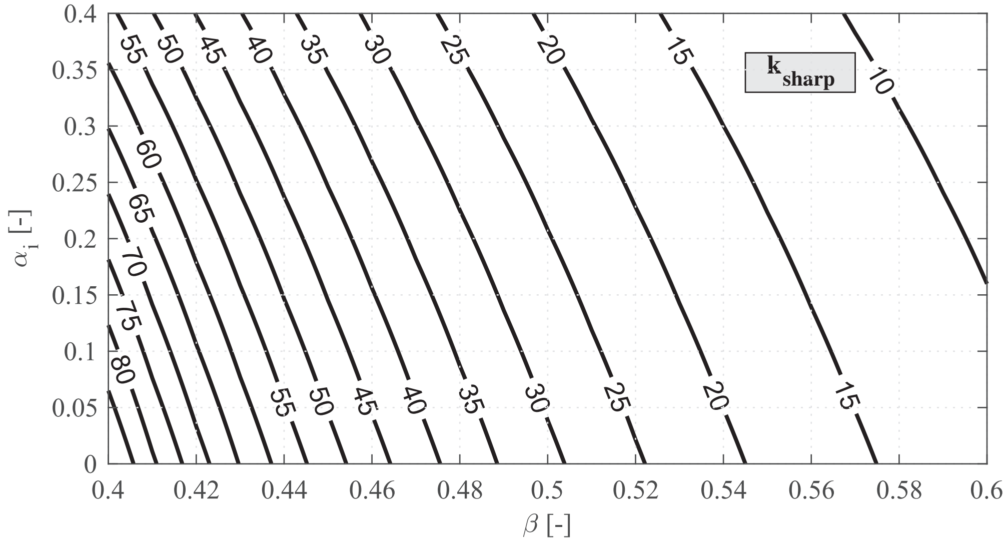

Figure 9.2 – Variation of sharp head loss coefficient for $\beta \in [0.4, 0.6]$ and $\alpha_i \in [0, 0.4]$

Determination of θ and α_θ

The contraction ratio, β, and the inner thickness ratio, α_i, were selected. Eqs.(6.10) and (6.11) (see Chapter 5) compute the head loss coefficient of the, respectively, chamfer and rounded approach flows. Chamfer orifices are preferred for asymmetry ratios, λ, between 0.35 and 1, while rounded orifices are best for smaller λ.

– *Chamfered orifices:*

$$k_{chamfer} = \lambda_\theta \cdot \Upsilon_{\alpha i} \cdot \frac{(1 + \tau\sqrt{(1-\beta^2)} - \beta^2)^2}{\beta^4} \tag{6.10}$$

where λ_θ is given by Eq.(6.7), $\Upsilon_{\alpha i}$ is given by Eq.(6.4) and $\tau = 0.745$.

$$\lambda_\theta = \frac{\lambda_\theta^0 \cdot \alpha_\theta + 0.0125}{\alpha_\theta + 0.0125} \tag{6.7}$$

where λ_θ^0 is given by Eq.(6.8)

$$\lambda_\theta^0(\theta) = 1.304\theta^4 - 5.97\theta^3 + 9.054\theta^2 - 4.55\theta + 1 \tag{6.8}$$

where θ is in radians

$$\Upsilon_{\alpha i} = 1 - \kappa_{\alpha i} \cdot \alpha_i \tag{6.4}$$

where $\kappa_{\alpha i}$ given by Eq.(6.9)

$$\kappa_{\alpha i}(\theta) = 3.18\theta^4 - 13.88\theta^3 + 18.60\theta^2 - 7.29\theta + 0.949 \tag{6.9}$$

where: θ is in radians

– *Rounded orifices*

$$k_{rounded} = \lambda_a \cdot \Upsilon_{\alpha i} \cdot \frac{(1 + \tau\sqrt{(1-\beta^2)} - \beta^2)^2}{\beta^4} \tag{6.11}$$

where λ_a is given by Eq.(6.12), , $\Upsilon_{\alpha i}$ is given by Eq.(6.4) with $\kappa_{\alpha i} = 0.071$ and $\tau = 0.745$.

$$\lambda_a = \frac{\lambda_a^0 \cdot \alpha_\theta + 0.0125}{\alpha_\theta + 0.0125} \tag{6.12}$$

where $\lambda_a^0 = 0.271$

– *Comments* In practice, the asymmetry ratio, λ, can be determined with Eq.(9.1). The easiest way is to assume that α_θ is greater than or equal to 0.1. Thereafter λ_θ (or λ_a) is independent of α_θ (or α_a). In Figure 9.4, it can be seen that λ is a function of θ and α_i for $\alpha_\theta \geq 0.1$.

$$\lambda = \lambda_\theta \cdot \frac{\Upsilon_{\alpha i}^{chamfer}}{\Upsilon_{\alpha i}^{sharp}} \tag{9.1}$$

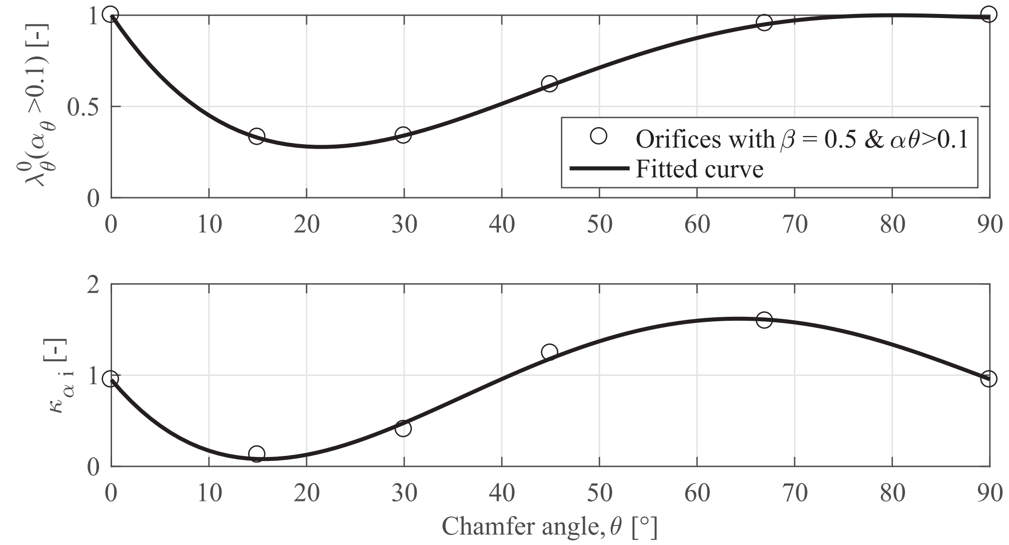

Figure 9.3 – Evolution of the coefficient λ^0_θ and $\kappa_{\alpha i}$ as a function of the chamfer angle θ

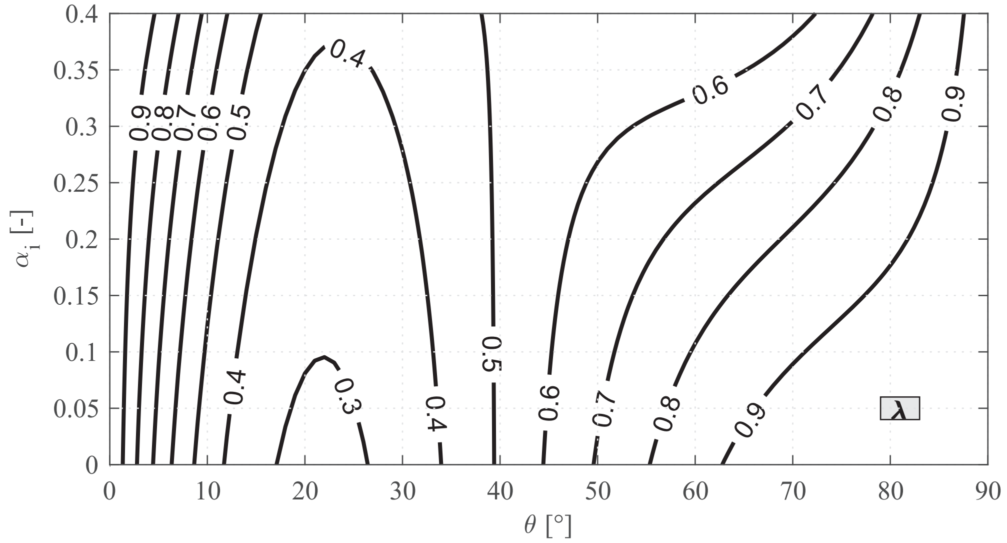

Figure 9.4 – Asymmetry ratio, λ, as a function of $\theta \in [0°, 90°]$ and $\alpha_i \in [0, 0.4]$ for $\alpha_\theta \geq 0.1$

Assessment of the incipient cavitation number σ_i

Several orifices depending on the four parameters, (β, α, α_i and θ) may be found with the same required head losses based on the incipient cavitation number, σ_i, which can be determined by the empirical relations of Eqs.(9.9) and (9.10) in Chapter 8. An orifice with a higher incipient cavitation number, σ_i, should be preferred for the same required head losses.

$$\sigma_i^{sharp} = 1 + 2.02 \cdot \beta^2 + 2.50 \cdot \alpha_i^{1.5} \tag{9.9}$$

$$\sigma_i^{chamfer} = \sigma_i^{sharp} \cdot \left[1 + 4.15 \cdot (\sin(2\theta))^2\right] \tag{9.10}$$

The incipient cavitation number, σ_i, can be predicted more accurately through employing the method developed by Ferrarese et al. (2015) via CFD simulations of single-phase flow. The risk of cavitation could be verified with graphical views (Chapter 8) and the results of the 1-D numerical simulations (see Section 9.2.5). If a risk of cavitation is identified, the design be further enhanced by assessing whether the cavitation characteristics, e.g. duration and severity, are acceptable. Figure 9.5 depicts a contour plot of the incipient capitation numbers for sharp approach flow with various pairs of contraction and inner thickness ratios, β and α_i, respectively.

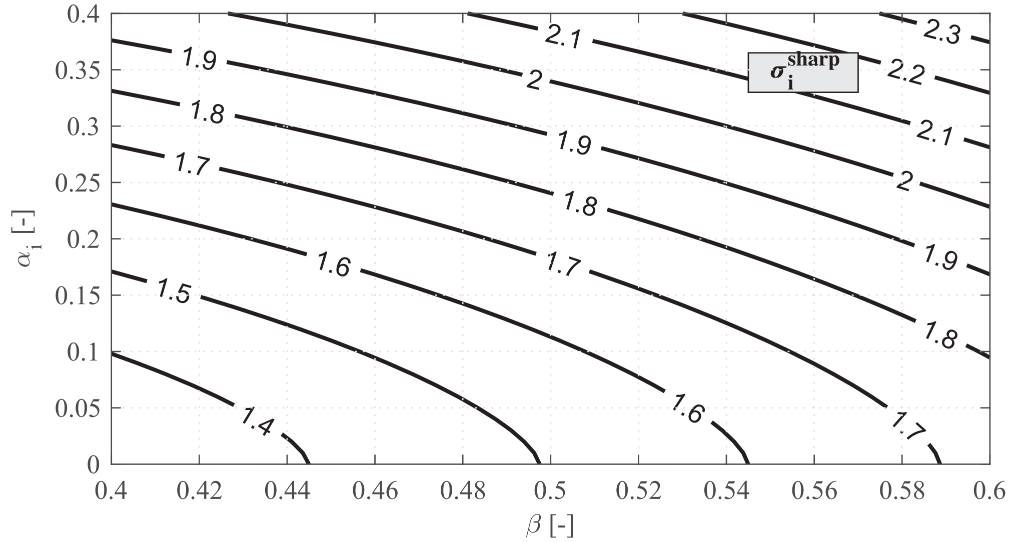

Figure 9.5 – Incipient cavitation number, σ_i, for the sharp approach flow as a function of $\beta \in [0.4, 0.6]$ and $\alpha_i \in [0, 0.4]$

Determination of the influence and reattachment length

– *Reattachment length* The reattachment length, L_r, is the length between the downstream orifice side and the pipe where the flow reattaches to the main pipe wall. L_r is independent of the presence of a chamfer and can be predicted with the empirical relation obtained through Eq.(7.10) from Chapter 6.

$$\begin{aligned} l_r &= a_{l,r}\cdot\gamma_o,\ if\,\beta \geq 0.5\,(\gamma_o \leq 0.25) \\ l_r &= b_{l,r}\cdot\gamma_o + c_{l,r},\ if\,\beta < 0.5\,(\gamma_o > 0.25) \end{aligned} \tag{7.10}$$

where: $\gamma_o = \frac{1-\beta}{2}$

$$\begin{aligned} a_{l,r} &= -5.46\cdot\alpha_i + 14.10 \\ b_{l,r} &= 3.95\cdot\alpha_i + 2.32 \\ c_{l,r} &= \frac{a_l - b_l}{4} \end{aligned} \tag{7.11}$$

Figure 9.6 presents a graphical estimation of the reattachment length, L_r, for different β and α_i values.

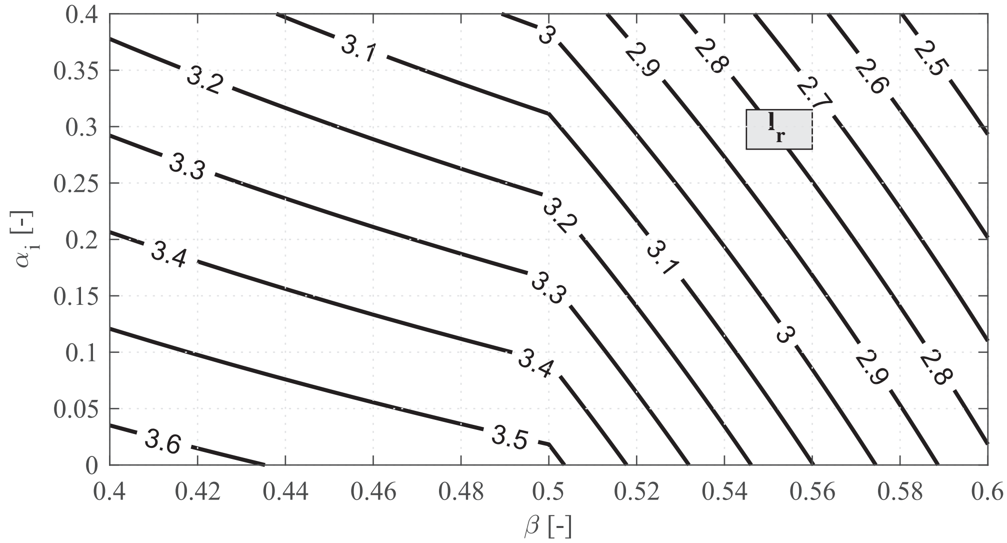

Figure 9.6 – Variation of the dimensionless reattachment length, l_r, for the sharp and chamfer approach flows with $\beta \in [0.4, 0.6]$ and $\alpha_i \in [0, 0.4]$

– *Influence length* The influence length, L_j, is the length between the upstream orifice side and the pipe cross-section, that is not influenced by the presence of the orifice. It can be estimated with the assistance of the two empirical relationships suggested in Chapter 6 and via Eq.(7.4) and (7.7).

$$l_{j,sharp} = 1.47 + 6.90 \cdot \beta + 0.77 \cdot \alpha_i \tag{7.4}$$

$$\begin{aligned} l_{j,chamfer} = \left(1.47 + 6.90 \cdot \beta + 0.77 \cdot \alpha_i\right) \cdot \left(1 + d_{l,j} \cdot \sin^2(2\theta)\right) \\ d_{l,j} = 0.97 \cdot \alpha_i + 0.14 \end{aligned} \tag{7.7}$$

Figure 9.7 presents a graphical estimation of the influence length, L_j, for the sharp approach flow with different β and α_i values.

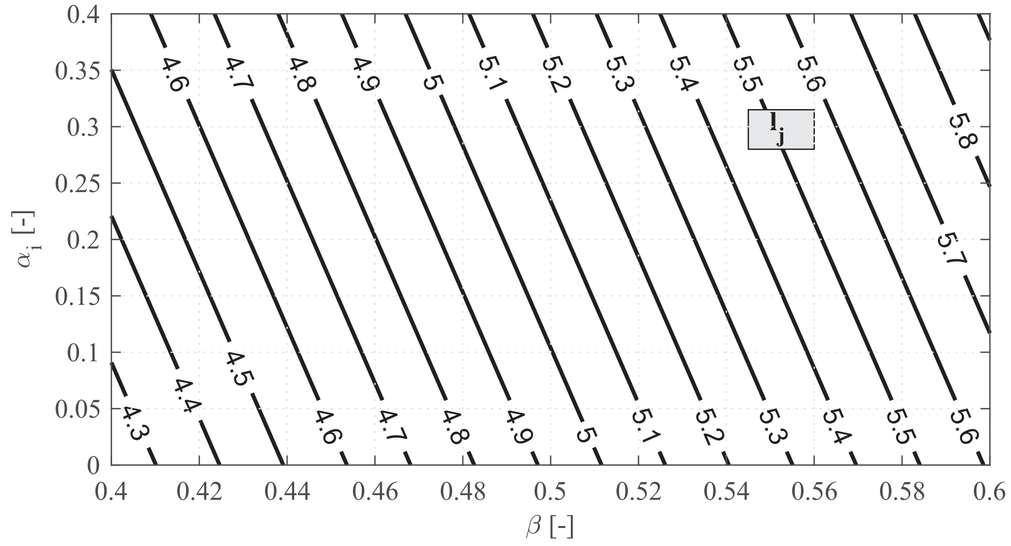

Figure 9.7 – Influence length of the orifice, l_j, for the sharp approach flow as a function of $\beta \in [0.4, 0.6]$ and $\alpha_i \in [0, 0.4]$

– *Uses* On one hand, the reattachment length, L_r, fosters evaluation of the needed downstream length to facilitate a reliable estimation of the produced head losses. If possible, there should not have a geometrical change, e.g. pipe expansion or T-junction, before the end of this length (refer to in Section 9.2.3). Furthermore, low pressures can take place within this pipe zone and can require a steel liner to protect the pipe from cavitation. On the other hand, the influence length allows for the assessment of the minimum length between two orifices if it is needed to generate the required head losses.

9.1.5 Validation by hydraulic model tests or prototype measurements

The aforementioned empirical design procedure can reduce the iterations needed to find the required orifice geometry. Nevertheless, the final geometry should be validated in a physical model, which would ultimately be more precise.

Finally, prototype measurements could confirm the design and reveal scale effects if there are any.

9.1.6 Conclusion

These design guides describe the different steps for the design of surge tank orifices. The empirical relationships suggested in this study are summarized to ease practical use. Certain results are graphically depicted as a function of the orifice geometrical parameters in order to arrive at first estimations without calculation.

9.2 Case Study

9.2.1 Effects of a throttle on the whole water way system

Numerical simulations of transient pressures and surge tank oscillations were performed with the Hydraulic System software described by Boillat and de Souza (2004) with the objective of exhibiting the effect of the throttle placement on the global transient behaviors of a high-head power plant. Only the contraction ratio, β, and thus head loss coefficients, vary. The orifice was modeled by local head losses and a short pipe. The diameter of this pipe was equal to the inner orifice diameter so as to model more reliability the wave transmission at the T-junction (Table 9.1) during the water hammer.

Simulations of the Cleuson-Dixence high-head power plant (Figure 9.8) consider how the surge tank is throttled with an orifice (Figure 2.2) in a connecting tunnel with a diameter of 3 m. Such simulations were performed for just a complete linear closure over 90 s and focused mainly on the first amplitude of the mass oscillation.

The plant characteristics as follows:

- total head, 1883 m;
- flow discharge, 75 m^3/s;
- installed capacity, 1269 MW (3 Pelton turbines);
- only linear closure is studied for a closure time of 90 s; and
- the surge tank had two expansions (Figure 9.9) and an orifice (Table 9.1) that together created head losses at its entrance. Considering the existing lateral chambers like cylin-

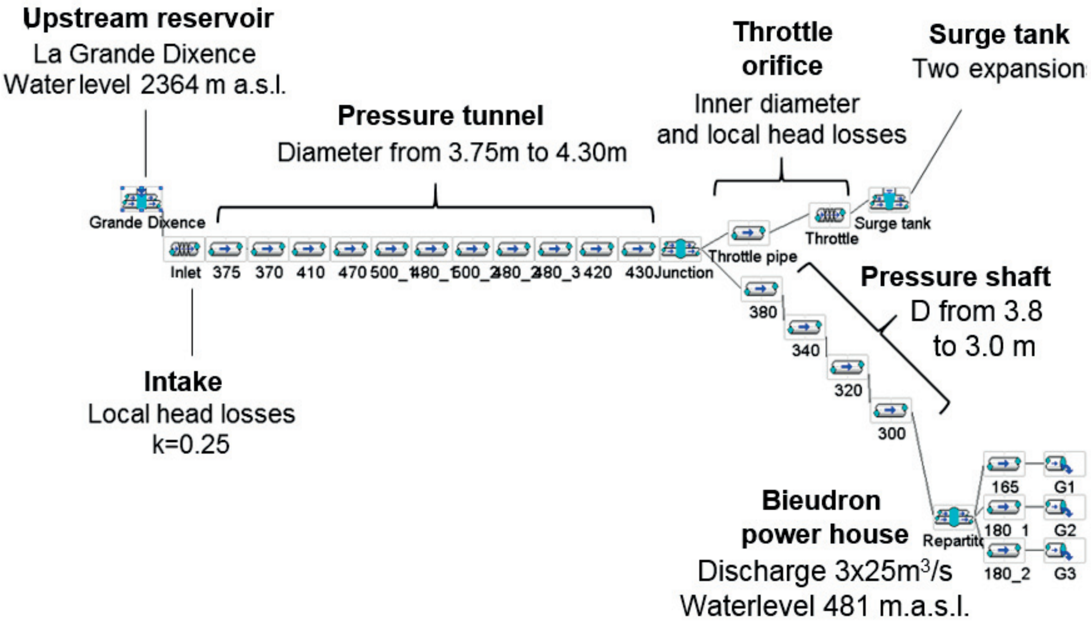
Upstream reservoir
La Grande Dixence
Water level 2364 m a.s.l.
Pressure tunnel
Diameter from 3.75m to 4.30m
Throttle orifice
Inner diameter and local head losses
Surge tank
Two expansion
Grande Dixence
Inlet
375
370
410
470
500_1
480_1
500_2
480_2
480_3
420
430
Junction
Throttle pipe
Throttle
Surge tank
Pressure shaft
D from 3.8 to 3.0 m
380
340
320
300
Intake
Local head losses
k=0.25
Bieudron power house
Discharge 3x25m³/s
Waterlevel 481 m.a.s.l.
Repartit
165
180_1
180_2
G1
G2
G3

Figure 9.8 – Hydraulic System model of the Bieudron power house of Grande-Dixene scheme

drical expansions: the diameter of the lower chamber was 23.17 m; of the intermediate shaft was 7.49 m; and the upper chamber had a diameter of 30.44 m. The head loss coefficients taking into account the connecting pipe were $(k_{IN}/k_{OUT}) = (14.70/28.66)$.

In order to render the analysis more generally applicable, thereby independent from the existing surge tank geometry (i.e., two expansions with an intermediate shaft), an equivalent diameter D_{Eq} was first determined for the existing surge tank and its throttle leading to the same maximum measured water level. Next, numerical simulations were conducted with D_{Eq} for all the different cases (Table 9.1) to evaluate the throttling effects. Finally, an optimized surge tank diameter D_{Opt} was establish for each contraction ratio, β (Table 9.1), where the higher head loss coefficients were obtained by Eq.(5.3) in Chapter 5. For cases 1 to 9, the head loss coefficients are given without the head losses produced by the small pipe enabling robust pressure wave transmission at the T-junction.

Simplified surge tank with equivalent diameter

Figure 9.10 (or Figure 9.11) depicts the temporal evolution of the water level in the surge tank (or the pressure in the pressure tunnel) for the given closure time and for the existing surge tank (real geometry) as well as the simplified surge tanks with the equivalent diameter, $D_{Eq} = 12.231\,m$. The following observations are relevant:

- the equivalent diameter D_{Eq} for the simplified surge tank was determined in order to

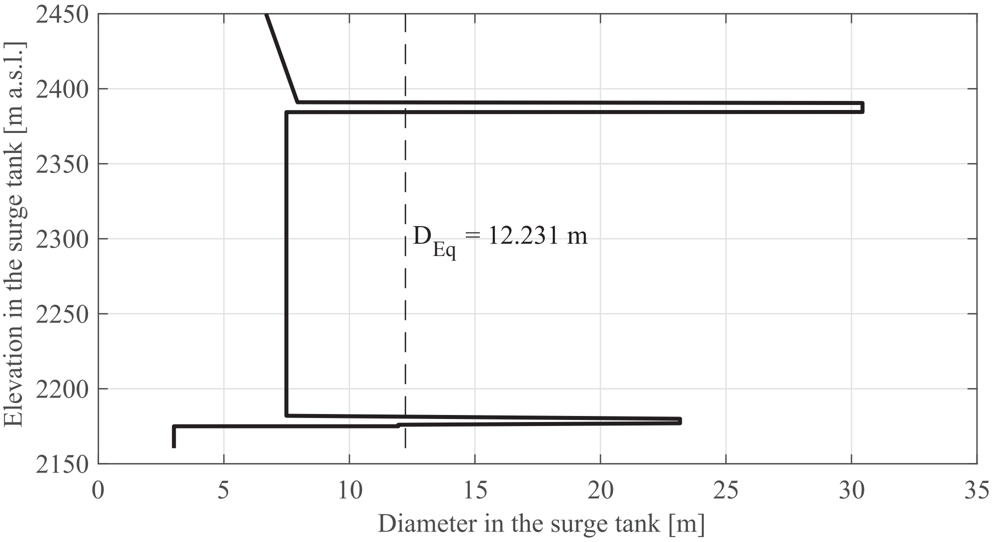

Figure 9.9 – The different equivalent diameters along the surge tank used for modeling with in Hydraulic System

reach the same maximum water level as the existing surge tank. However, the oscillation period increases and the maximum pressure in the pressure tunnel decreases;

- the smaller the contraction ratio, β, is (and thus, the greater the head losses are), the lower the maximum water level in the surge tank is;
- for lower values of β, the water level converges to the static water level without oscillations. No simulations were performed for contraction ratios below 0.2 (except for the case with no surge tank, $\beta = 0$);
- the behavior of the pressure fluctuations change at $\beta = 0.6$. For $\beta > 0.6$, the pressure was influenced by mass oscillations, whereas the maximum pressure results from the higher transmission of surge waves produced by the closure, for $\beta < 0.6$; and
- for the throttle existing real geometry ($\beta = 0.53$), the behavior was slightly different due to the combined effects of the throttling and expansions. The rise of pressure in the pressure tunnel was more important than without expansions as the rise of water level in the surge tank was more rapid.

Hence, throttling a surge tank decreases its maximum amplitude of water level oscillations (Figures 9.10 and 9.12) while the maximum pressure in the pressure tunnel rises (Figures 9.11 and 9.12). However, according to Figure 9.12, for a contraction ratio larger than $\beta > 0.6$, the maximum water level and pressure decreases. This behavior diverges for $\beta < 0.6$, whereby the maximum pressure in the pressure tunnel becomes the higher possible pressure without surge tank ($\beta = 0$). As shown in Figure 9.11, the reason for this difference is based on the higher

Table 9.1 – Simulation parameters - the contraction ratios β and two of the head loss coefficients

Case	β [-]	d [m]	Head loss coefficients [-]	
			Inflow	Outflow
Real geometry	0.53	1.6	14.7	28.66
1	1	3	4.8	5.47
2	0.9	2.7	4.98	5.87
3	0.8	2.4	5.48	7.06
4	0.7	2.1	6.74	10
5	0.6	1.8	9.85	17.29
6	0.5	1.5	18.13	36.69
7	0.4	1.2	43.55	96.26
8	0.3	0.9	188.5	330.42
9	0.2	0.6	768.15	1793.9
10	0 – No surge tank	/	/	/

surge wave transmitted in the pressure tunnel from the pressure shaft. For smaller β values, water levels tend directly to the upstream static water level.

To conclude, a throttle would be beneficial for $\beta > 0.6$ even during the design phase of a new surge tank. The maximum water level and the pressure were indeed lower than without throttling. Nevertheless, a throttle placement could limit future increases in installed capacity. Moreover, Figure 9.12 shows that a throttled surge tank with expansions seems to elevate the pressure transmitted within the pressure tunnel with respect to real geometry as it combines the effect of the throttle and intermediate shaft.

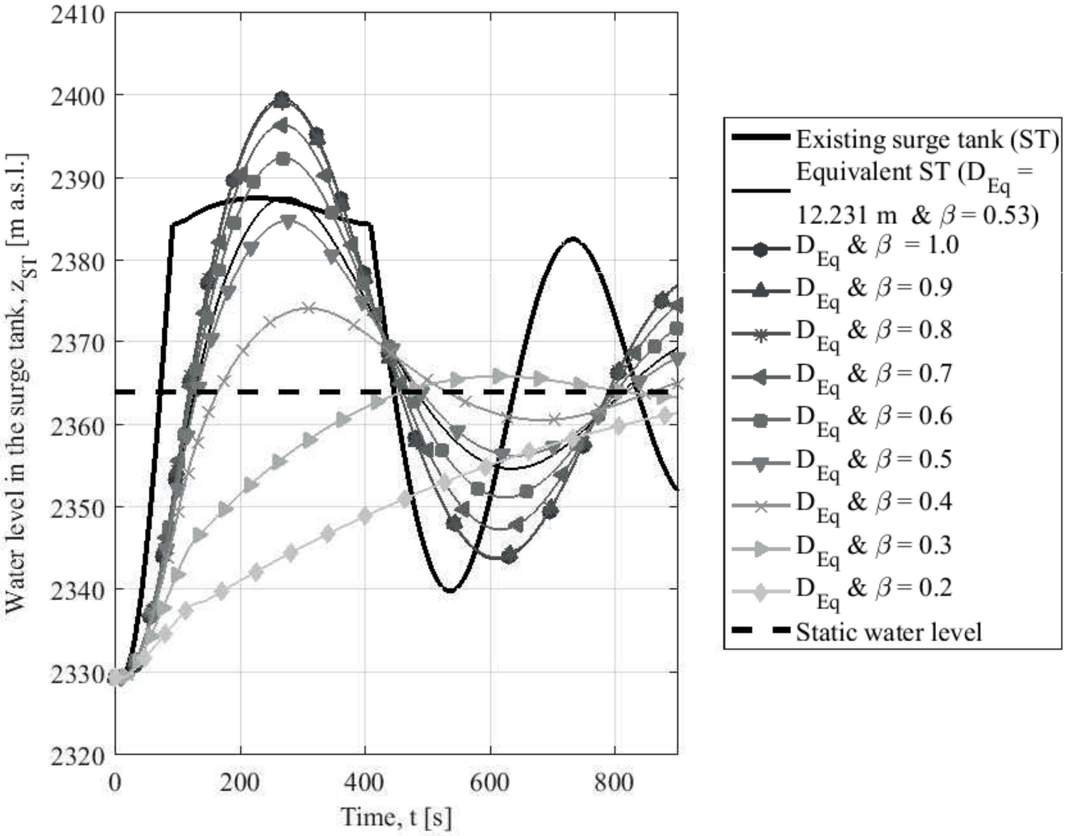

Figure 9.10 – Variation of the water level in the surge tank, z_{ST}, following a closure (duration 90s) for the existing surge tank and for the equivalent simple surge tank for different contraction ratios listed in Table 9.1

Simplified surge tank with optimized diameters

For each contraction ratio β, an optimized surge tank diameter, D_{Opt}, was determined in order to obtain the same maximum water level as in the existing surge tank. Figure 9.13 illustrates the optimized equivalent diameter, D_{Opt}, as a function of β. It is reduced when β decreases and seems to converge to 0 without a surge tank ($\beta = 0$). This reduction is almost linear for β between 0 and 0.6 ($D_{Opt}/\beta \approx 22.6$). D_{Opt} is slightly increasing for $\beta > 0.6$, however, D_{Opt} has to satisfy the required Thoma cross-section, A_{ST}^{T}, defined as ((Thoma, 1910) see Figure 9.13):

$$A_{ST}^{T} > \frac{L_{PT} \cdot A_{PT}}{2g \cdot k_{PT} \cdot H_n} \tag{9.2}$$

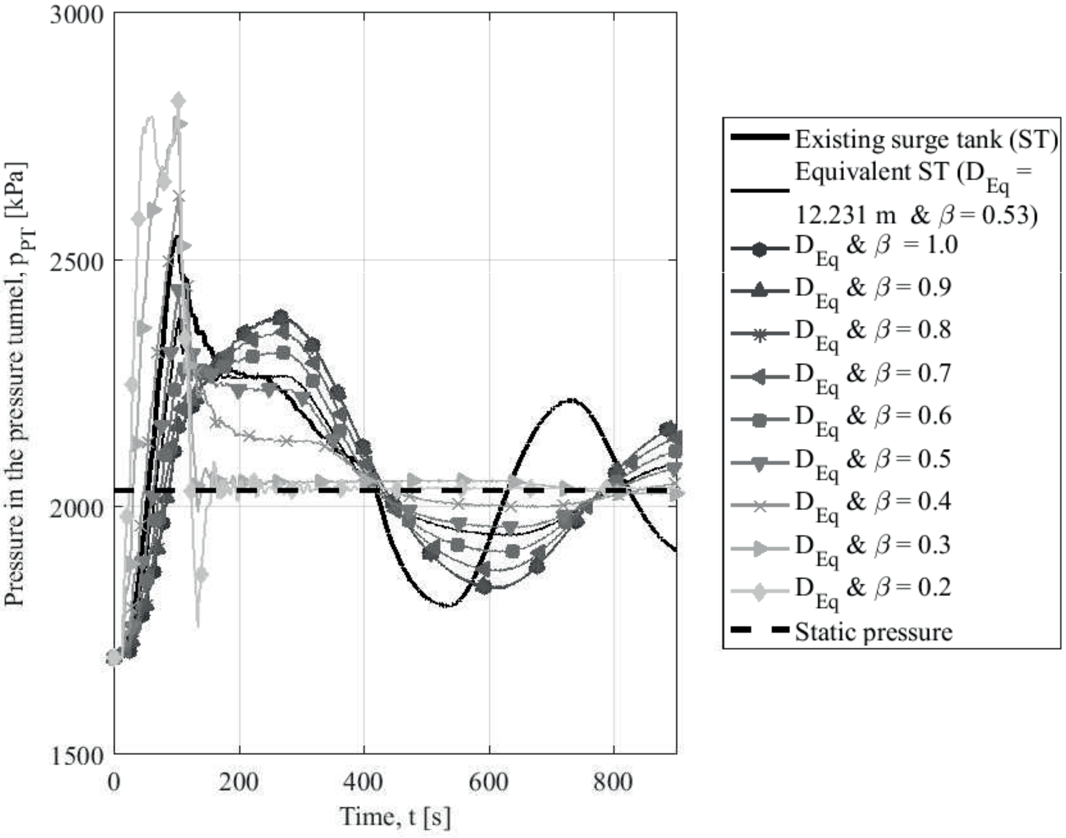

Figure 9.11 – Variation of the pressure in the pressure tunnel close to the surge tank, p_{PT}, following a closure (duration 90s) for the existing surge tank and for the equivalent simple surge tank for different contraction ratios listed in Table 9.1 (the static pressure is relative to an upstream water level of 2156.6 m a.s.l.)

and thus,

$$D_{ST}^{T} = 2\sqrt{\frac{A_{ST}^{T}}{\pi}} \tag{9.3}$$

where A_{PT} is the pressure tunnel cross-section, L_{PT}, the pressure tunnel length, k_{PT}, the head loss coefficient for both friction and local losses in the pressure tunnel related to cross-section of the pressure tunnel and H_n, the net head between the surge tank and the tail water.

Figure 9.13 shows that the diameter of the existing surge tank ($D_{min}^{Existing}$= 7.49) is much higher than the required Thoma diameter without considering a safety factor.

The decrease of D_{Opt} is significant for β = 0.6...0.7. Furthermore, for $\beta > 0.6$, the optimization

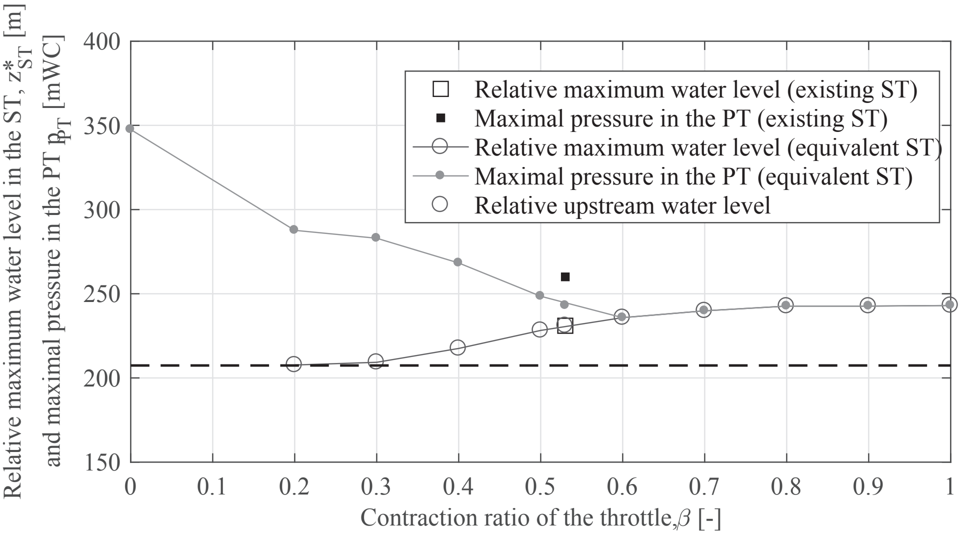

Figure 9.12 – Maximum water level in the surge tank and the maximum pressure in the pressure tunnel as a function of the contraction ratio β. The reference elevation is the altitude of the tunnel axis below the surge tank (2156.6 m a.s.l.)

of the surge tank diameter does not have a large influence on the maximal pressure in the pressure tunnel (Figure 9.14). The reduction of the surge tank diameter, however, results also in higher costs of construction.

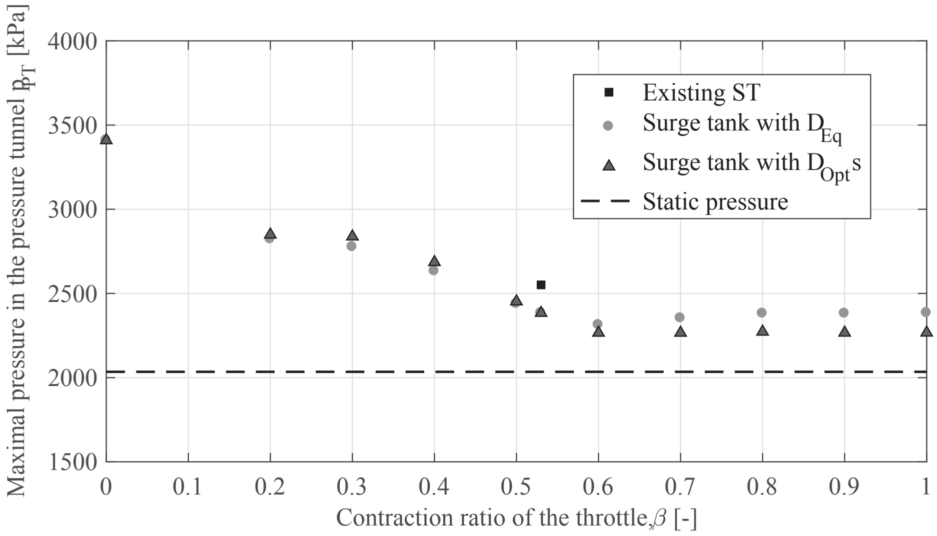

Figure 9.14 – Maximal pressure in the pressure tunnel as a function of the contraction ratio β resulting in a maximum water level equivalent to the existing surge tank (2187.6 m a.s.l.)

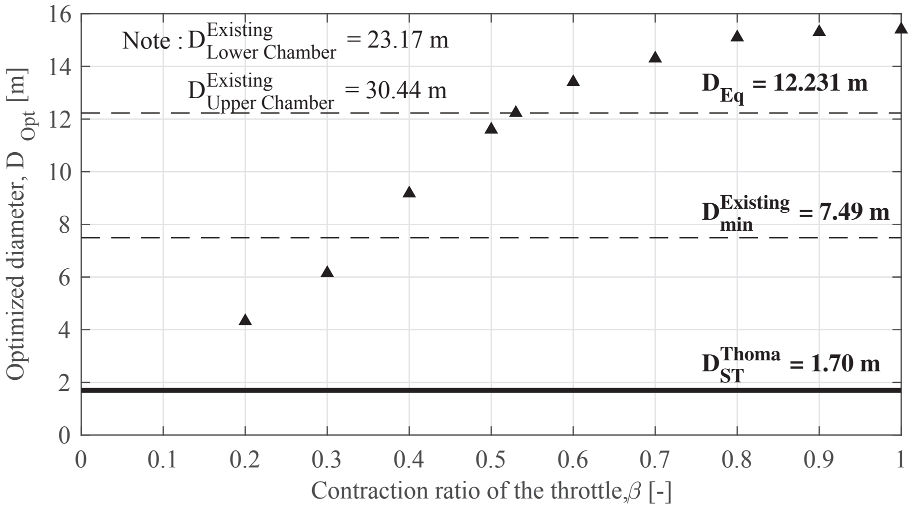

Figure 9.13 – Optimized equivalent diameter as a function of the contraction ratio β resulting in a maximum water level equivalent to the existing surge tank (2187.6 m a.s.l.). Also featured is a comparison of the required Thoma diameter (Eq.(9.3)), with the smallest diameter of the existing surge tank and the diameter of the existing lower and upper chambers

Conclusions

The analysis performed on the case study featuring the Bieudron power plant of the Grande-Dixence scheme demonstrated that throttles with contraction ratios of $\beta \geq 0.6$ are advantageous and can slightly diminish the cost of construction because of the reduction of the surge tank volume. The transmitted element of the surge waves increases in the pressure tunnel for $\beta < 0.6$. Furthermore, $\beta < 0.3$ should be avoided as the pressure amplitudes rise rapidly within the pressure tunnel. Finally, a throttled surge tank with expansions like the existing surge tank produces higher pressure in the pressure tunnel than a throttled surge tank without expansions for the same excavated volume.

9.2.2 Design of throttle geometry

Cleuson-Dixence

– *Existing orifice*

The orifice (see Figure 2.2 and Section 9.2.1) placed at the entrance of the Grande-Dixence surge tank produces head losses equal to (14.7 , 28.66). The asymmetry ratio is therefore 0.51.

– *Determination of orifice geometries*

The highest contraction ratio, β, can be found with Eq.(6.3) for a theoretical orifice with $\alpha = \alpha_i = 0$: $\beta_{max} = 0.5385$. The smallest contraction ratio, β, is obtained with the theoretical approximation of the minimum head loss coefficient according to Eq.(5.23): $\beta_{min} = 0.43$. Once β_{min} and β_{max} are known, different combination of (β, α_i) can be found as reported in Table 9.2. However, in order to stay within the tested range of this research project, α_i was limited to 0.4.

Table 9.2 – Preliminary design of the Grande-Dixence throttle

	$\beta[-]$	$\alpha_i[-]$	$k_{out}[-]$	$\sigma_{i,out}[-]$	$\alpha_\theta[-]$	$\theta[°]$	k_{in}	$\sigma_{i,in}[-]$
Existing	0.53	0.01	28.66		0.19	30	14.7	
Orifice 1	0.5385	0.0	28.66	1.56	0.1	39.91 or 8.4	14.7	7.61 or 2.08
Orifice 2	0.53	0.08	28.66	1.61	0.1	39.92 or 9.2	14.7	7.85 or 2.25
Orifice 2’	0.53	0.01	30.83	1.55	0.19	30	9.7	6.2
Orifice 3	0.50	0.33	28.66	2.00	0.1	40.04 or 13.25	14.7	9.76 or 3.59
Orifice 4	0.49	0.4	28.66	2.15	0.1	40.27 or 15.07	14.7	10.52 or 4.32

Assuming $\alpha_\theta \geq 0.1$, the chamfer angle, θ, becomes close to 40° or stays between 8° and 15°. Orifice 2 corresponds to the geometrical parameters producing the existing required head loss coefficients, while the head loss coefficients of orifice 2’ are obtained for the existing geometrical parameters. The predicted head loss coefficients for orifice 2’ are 7% higher for the sharp approach flow and 34% lower for the chamfer approach flow.

– *Comparison of incipient cavitation numbers* σ_i

For all the orifice geometries given in Table 9.2, the incipient cavitation number, σ_i, is predicted by Eqs.(9.9) and (9.10) and the results are found in Table 9.2. The following observations are relevant:

- for this orifice, the smaller α_i, the higher the predicted σ_i is. This confirms the existing design with a small inner thickness; and
- for each pair of β and α_i, there are two chamfer angles producing the same head losses. According to $\sigma_{i,in}$, the small angles are better with respect to the cavitation risk.

FMHL +

The experimental campaign that was executed at LCH of EPFL for the orifice placed at the entrance of the new surge tank of the FMHL pumped-storage power plant was summarized in Section 2.4.3. The orifice has a symmetrical geometry and is placed in a connecting tunnel (Figure 2.8). The symmetrical sharp head loss coefficient is 3.3 (Hachem et al., 2013).

The smallest contraction ratio, $\beta_{min} = 0.634$, was obtained by Eq.(5.13) for $k_{sharp} = 3.3$, while the highest contraction ratio $\beta_{max} = 0.764$ was obtained by Eq.(6.10). The existing thickness ratio α_i was equal to 0.04. This results in a predicted contraction ratio, β, equal to 0.760 while the existing orifice was 0.768.

Gondo

The experimental campaign executed at LCH of EPFL for the orifice placed at the entrance of the new surge tank of the FMHL pumped-storage power plant was summarized in Section 2.4.4. The throttle placed in the Gondo surge tank was not an orifice but a rack throttle (see Section 2.4.4). However, the empirical relationships were tested in order to evaluate the robustness of the method. The numerical simulations gave a pair of head loss coefficients (k_{OUT}, k_{IN}) equal to $(40,30)$. The smallest contraction $\beta_{min} = 0.402$ was obtained by Eq.(5.13) for $k_{sharp} = 40$, while the highest contraction ratio, $\beta_{max} = 0.504$ was yielded with Eq.(6.10).

The throttle of Gondo had an $\alpha_i = 0$. The predicted contraction ratio was equal to 0.504 while the existing $\beta_{eq} = 0.43$. It can be deduced that flow expansions at the throttle affect each other and have an influence on global head losses. The difference between the predicted and existing contraction ratio was 16%. As described in Section 2.4.4, α_θ was equal to 0.143, which means that the asymmetry ratio, λ, is independent of α_θ. Finally, for $\lambda = 0.75$, the chamfer angle should be 4° or 52°, while the existing angle was 12°.

Conclusions

The empirical relations and the method proposed in the practical guideline (Chapter 9.1) were tested on three different throttles, i.e. two orifices and one rack throttle. The method elicited satisfactory results for the two orifice design. However, for the rack throttle, there were quite large differences in the contraction ratio, β, and the chamfer angle θ. These differences could be explained by the varied geometry of the throttle (bar screen), an interaction between the distributed jets or by the complex connection at the entrance of the Gondo surge tank (Adam et al., 2017).

9.2.3 Influence and reattachment lengths[1]

Description Steady head losses were recorded on the physical model of FMHL + at the LCH of EPFL (see Figure 9.15; Section 2.4.3 and 9.2.2). The position, P_i, and the contraction ratio, β, of the existing orifice placed in the connecting tunnel were varied in order to evaluate the influence of the position, and thus the characterizing lengths, on the head loss coefficients. Hereafter, the head losses were evaluated between the surge tank B and the pressure control section S_6.

Two different orifice contraction ratios, $\beta = 0.70$ and 0.73, were tested with four positions from P_a to P_d. Table 9.3 gives the distance of the positions between the headrace tunnel and the surge tank. The reattachment and influence lengths (Table 9.4) for the two contraction ratios

---

[1] This subsection is based on a published conference paper: "Adam, N.J. & De Cesare,G. (2015). Diaphragm in pressure pipe: steady head loss evolution and transient phenomena. *5th IAHR International Junior Researcher and Engineer Workshop on Hydraulic Structures, Spa, Belgium.*". The experimental work presented hereafter is original and was performed by the author.

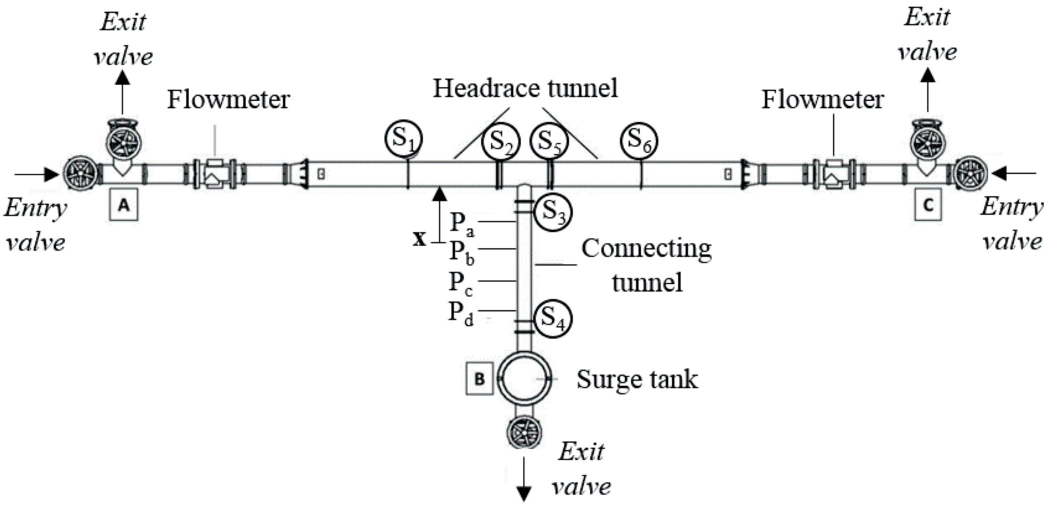
Exit valve
Exit valve
Flowmeter
Headrace tunnel
Flowmeter
S1
S2
S5
S6
Entry valve
A
C
Entry valve
S3
x
Pa
Pb
Pc
Pd
Connecting tunnel
S4
B
Surge tank
Exit valve

Figure 9.15 – Plan view of the new FMHL surge tank at LCH of EPFL with the different orifice positions

(β) were obtained through Eqs.(6.4) to (6.11) in Chapter 6.

Table 9.3 – The positions of the orifice relative to the headrace tunnel and surge tank B

	P_a	P_b	P_c	P_d
Position relative to the headrace tunnel	2.24D	4.97D	7.69D	9.96D
Position relative to the surge tank B	10.56D	7.83D	5.11D	2.84D

Table 9.4 – The influence and reattachment length, l_j and l_r, for $\beta = 0.70$ and $\beta = 0.73$ with a thickness ratio of $\alpha = 0.04$

Orifice	l_j	l_r
$\beta = 0.70$	6.33D	2.08D
$\beta = 0.73$	6.54D	1.87D

Results Figure 9.16 depicts the head loss coefficients in both flow directions for the four positions, P_i, and the two contraction ratios β. The following observations are pertinent:

- there was no influence of the orifice position on the head loss coefficient for $\beta = 0.73$ in both flow directions;
- for $\beta = 0.7$, particularly for the two position close to surge tank B (P_c and P_d), there is no influence of the position on the head loss coefficients; and
- for the smallest contraction ratio, $\beta = 0.7$, the head loss coefficient decreases when the water flows from the surge tank to the head-race tunnel.

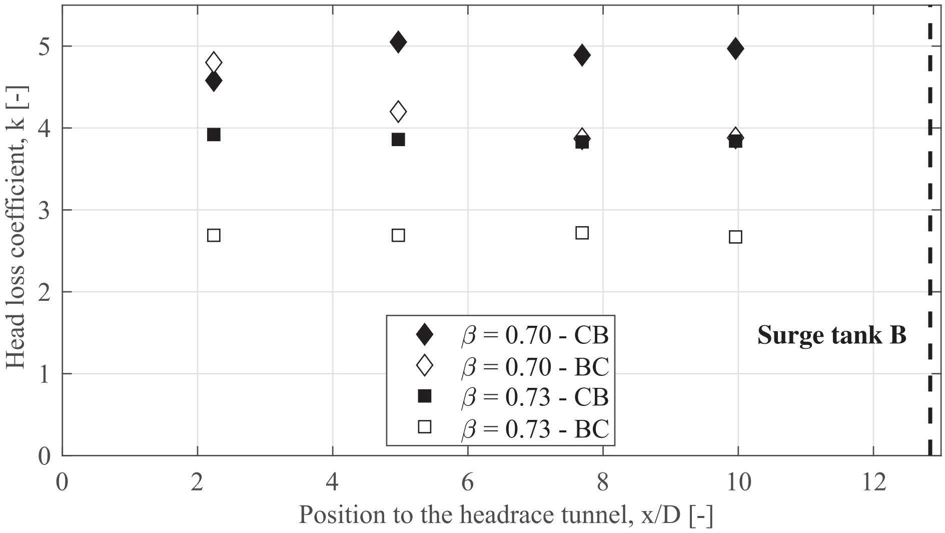

Figure 9.16 – Head loss coefficients characterizing the orifices as a function of the orifice position in the connecting tunnel (P_a to P_d in Figure 9.15)

Conclusions It can be stated that the influence length, l_j, does not have an influence on the head losses. However, for position P_a and $\beta = 0.7$, the reattachment zone should be in the T-junction, which seems to raise the head losses generated by the orifice for the BC flow direction (Figure 9.15).

9.2.4 Determination of the transient head losses for a down-surge (FMHL+)[2]

– *Description*

---

[2] This subsection is based on a published conference paper: "Adam, N.J. & De Cesare,G. (2015). Diaphragm in pressure pipe: steady head loss evolution and transient phenomena. *5th IAHR International Junior Researcher and Engineer Workshop on Hydraulic Structures, Spa, Belgium.*". The experimental work presented hereafter is original and was performed by the author.

Surge tank emptying was performed on the physical model of FMHL+ at the LCH of EPFL (see Figure 9.15; Sections 2.4.3 and 9.2.2). For the transient experiment, downstream valve C (Figure 9.15) was opened (over approximatively 10 seconds). The discharge and the pressure in the head race and connecting tunnel are recorded in order to evaluate the instantaneous head losses.

– *Results*

Figure 9.18 focuses on the time period $t \in [10s, 30s]$ because of the perturbation from the fast opening of the downstream valve. Throughout this period, the flow deceleration, dv_d/dt, was assumed constant and equal to $-0.14 m/s^2$. It can be seen in Figure 9.18 that the 0.1-second average head losses were always smaller than the steady head losses. After 25 s, the discharge and thus the head losses became small and on the same order as magnitude of the instrumentation errors (Appendix A).

– *Conclusions*

By comparing the steady head loss coefficient and transient effects, it is possible to evaluate the transient head loss coefficient k_t, which is in this case is equal to 3.64 with inertial effects. This value tends to confirm the results that were highlighted in Chapter 7.

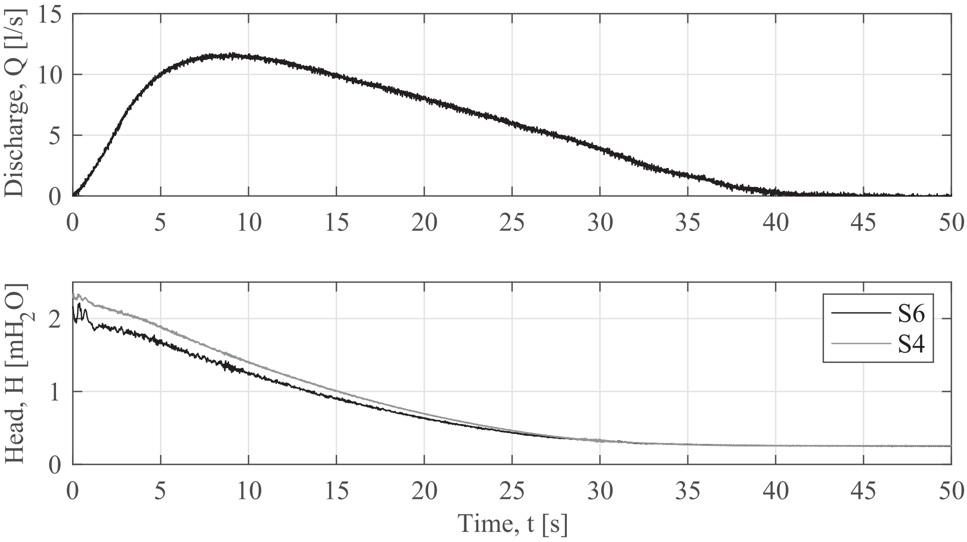

Figure 9.17 – Temporal evolution of the discharge and heads during the emptying of the new FMHL surge tank

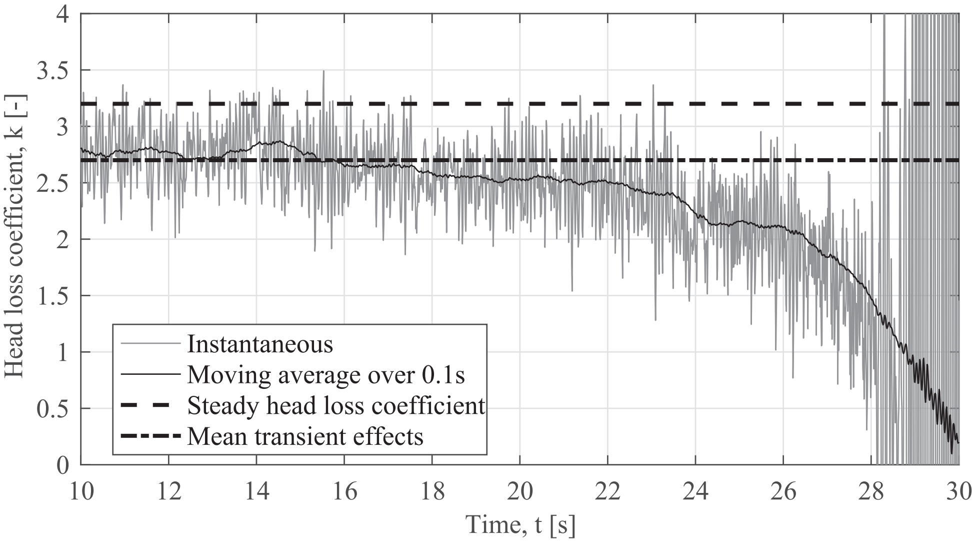

Figure 9.18 – Evolution of the head loss coefficient during emptying (0s after the end of the valve opening)

9.2.5 Estimation of the cavitation risk

Straight pipe

A method for the evaluation of the risk of cavitation is proposed in Section 8.2.2. Eq.(8.3) was applied to the following orifices: NUM_001 ($\beta = 0.5$), NUM_002 ($\beta = 0.4$), NUM_003 ($\beta = 0.45$) and NUM_004 ($\beta = 0.6$). Figure 9.19 portrays the limit of the incipient and *vena-contracta* cavitation. It can be seen that the incipient cavitation appears first for the chamfer approach flow for all the tested contraction ratios β, while the *vena-contracta* cavitates first for the sharp approach flow.

For experimental tests, it is possible to evaluate whether the flow would cavitate or not. For example, if the upstream pressure is equal to 4 mH_2O, the discharge should be respectively smaller than 27, 32 or 39 l/s for contraction ratios of 0.4, 0.45 or 0.5 in order to avoid incipient cavitation.

Surge tank - Gondo

A method for the evaluation of the risk of cavitation was proposed in Section 8.2.3. This limit of the risk of cavitation is graphically applied to the Gondo waterway system with throttle (Adam et al., 2017) (Sections 2.4.4 and 9.2.2).

Table 9.5 summarizes the main geometrical parameters of the Gondo throttle counted as an orifice. The characteristic cavitation numbers were predicted using the formulas developed in Section 8.3.2 and are summarized in Table 9.5.

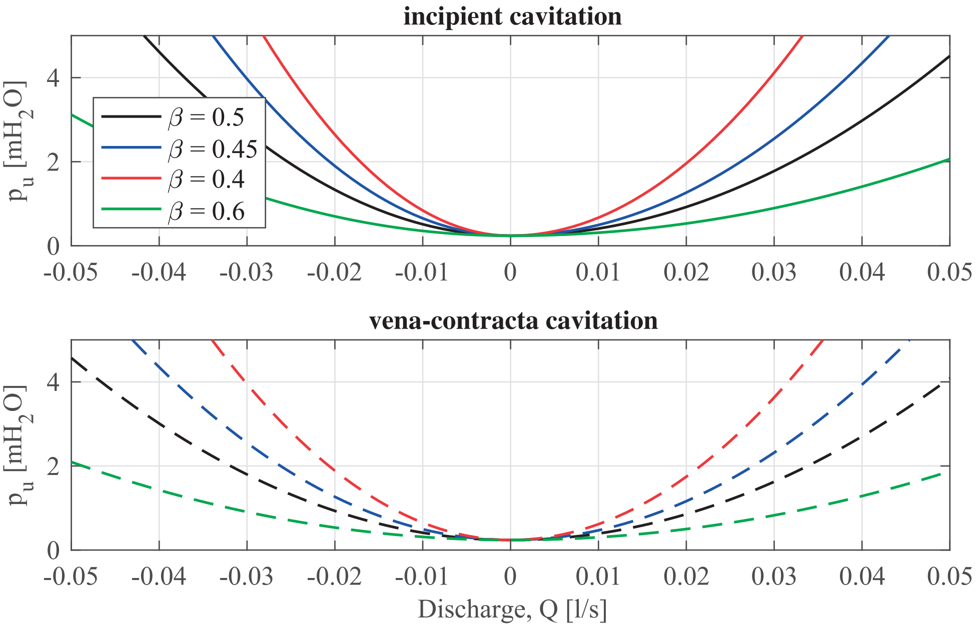
incipient cavitation

vena-contracta cavitation

Figure 9.19 – Graphical representation of the risk of cavitation (water at 20°C)for a straight pipe using either the incipient cavitation number, σ_i, or the *vena-contracta* cavitation number, σ_{vc}, for four different numerically tested orifices: NUM_001 ($\beta = 0.5$), NUM_002 ($\beta = 0.4$), NUM_003 ($\beta = 0.45$) and NUM_004 ($\beta = 0.6$). The discharge was taken as positive for the sharp approach flow.

Table 9.5 – Geometrical parameters of an equivalent orifice for the Gondo rack throttle

β	α	α_i	θ	σ_i^{sharp}	$\sigma_i^{chamfer}$	σ_{vc}^{sharp}	$\sigma_{vc}^{chamfer}$
0.43	0.143	0	12°	1.37	1.62	1.27	1.37

Figure 9.20 portrays the limit of the risk of cavitation for the Gondo throttled surge tank subjected to an emergency shutdown. It can be seen that there is a risk of cavitation for the first oscillation. Over the course of the first increase of the water level in the surge tank, only the incipient cavitation could appear (during almost 17 s). During the first decrease, the vena-contracta could cavitate (during almost 80 s).

Conclusions

The limit of the risk of cavitation was tested on a straight pipe and a throttled surge tank subjected to mass oscillations. It can be demonstrated for the Gondo throttled surge tank the usefulness of the graphical representation of the cavitation for a surge tank subjected to mass oscillations.

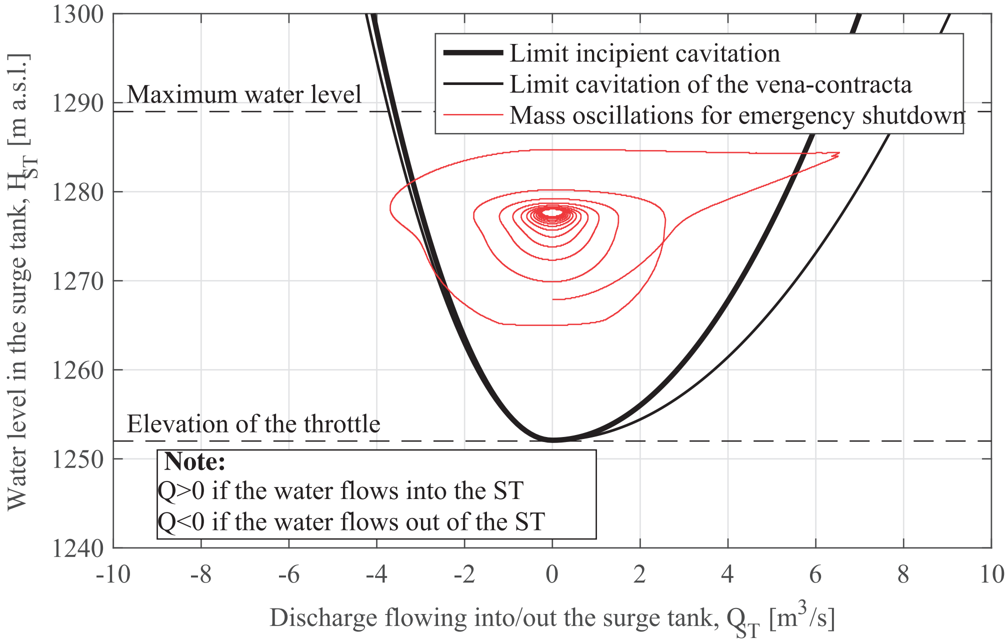

Figure 9.20 – The risk of cavitation (water at 5°C) for the Gondo surge tank subjected to a emergency shutdown leading to converging mass oscillations

10 Conclusions and outlook

10.1 Estimation of steady head loss coefficients for orifices

Based on novel systematic tests, it is possible to link geometry and head losses but also to find geometries producing target head loss coefficients. Three different orifice geometries were studied and compared in this research, i.e. orifices with a sharp, chamfered side or a rounded side along with orifices with two chamfered sides. The results indicated that the different geometrical parameters strongly influence the steady head loss coefficients in both flow directions. The main conclusions are listed subsequently:

- for the two approach flow directions and all orifice geometries, the most influential parameter was the contraction ratio, β. The head loss coefficients decreases with the fourth power of β. The lower the contraction ratio was, the higher the head loss coefficients were. Furthermore, the head loss coefficients decrease when the inner thickness ratio, α_i, rises. The lowest head loss coefficient was achieved when the flow reattached the orifice inner wall;

- for the sharp approach flow, the head loss coefficient depended only on β and the inner thickness ratio, α_i. The orifice thickness, α, did not play a primary role if the chamfer angle, θ, or the curvature of the orifice was high enough. Numerical simulations showed that a chamfer angle, θ, higher than 15° was sufficient;

  The sharp head loss coefficient can be obtained either by the empirical relationship Eq.(6.3), graphically in Figure 9.2 in the design guidelines (Chapter 9.1), by the catalog of the experimentally obtained head loss coefficients given in Appendix B or with the expert sheet (see Appendix G), which is available on-line with the thesis (doi:10.5075/epfl-thesis-8090);

- for the chamfer approach flow, the chamfer angle, θ, had a strong influence on the asymmetry ratio, λ, defined as the ratio between the chamfer and sharp head loss coefficients varying from 0.35 to 1. The lowest values of λ were obtained for the angle between 15° and 40°. The effect of the angle was reduced when the chamfer thickness ratio, α_θ, decreases. The asymmetry ratio, λ, was independent of α_θ if it was higher or equal to 0.1;

The chamfer head loss coefficient could be obtained via the empirical relationship of Eq.(6.10) or graphically with the asymmetry ratio, λ, in Figure 9.4 of the design guidelines (Chapter 9.1), by the catalog of the experimentally obtained head loss coefficients in Appendix B or with the expert sheet (see Appendix G), which is available on-line with the thesis (doi:10.5075/epfl-thesis-8090);

- for the two-chamfered orifices, the head loss coefficient relied upon the contraction ratio, β, the chamfer angles, θ_R and θ_L, and the inner thickness ratio, α_i. The second chamfer angle did not influence the head loss coefficient of the opposite approach flow. However, this type of geometry had a smaller theoretical range of asymmetry ratios as the highest head loss coefficient was produced for the sharp approach flow. Asymmetry can be easily achieved with a sharp side producing higher head losses. Using two-chamfer orifices decreases the value of the contraction ratio β, which is a key parameter in the transmission of the water-hammer within the pressure tunnel (Section 9.2.1).

  The head loss coefficients could be obtained through the empirical relationship of Eq.(6.10) for the chamfer approach flows; and

- for the rounded approach flow, the head loss coefficient did not vary significantly and was lower than for the chamfer orifices. The asymmetry ratio, λ, varied from 0.25 to 0.5.

  The head loss coefficient for the rounded approach flow could be obtained by the empirical relationship in Eq.(6.11) from the design guidelines (Chapter 9.1).

10.2 Determination of recirculation and influence lengths of the orifice

The influence and reattachment lengths were defined by systematic testing that allow the definition of the undisturbed flow conditions for use of the developed empirical formulas evaluating the head loss coefficients. The main findings can be summarized in what follows:

- the zone disturbed by the presence of the orifice was longer than the reattachment length of the jet. The chamfer increases the disturbed zone for the chamfer approach flow, while it did not affect the reattachment length;

- the influence length depended mainly on the contraction ratio β. For both approach flow directions, the influence length rose linearly with β in the tested range ($\beta \in [0.3, 0.7]$).

  For the sharp approach flow, the influence length could be estimated with the empirical relationship of Eq.(7.4) or graphically in Figure 9.7 of the design guidelines (Chapter 9.1). For the chamfer approach flow, the influence length depended on the chamfer angle, θ, and could be estimated with the empirical relationship of Eq.(7.7);

- the chamfer has very little influence on the reattachment length. This reattachment length increases firstly with β and then tends to be constant for $\beta < 0.4$.

  For both approach flow directions, the reattachment length could be obtained by the empirical relationship of Eq.(7.10) or graphically with Figure 9.6 from the design guidelines (Chapter 9.1); and

- the reattachment length seems to have a stronger influence on head losses than the influence length. A case study (see Section 9.2.3) revealed that a bifurcation in the reattachment length modified the value of the predicted head losses.

10.3 Transient head losses in orifices

Transient effects have been highlighted and can account for up to 20% of steady head losses. The following conclusions can be made:

- the head losses produced when the flow accelerates were higher than the steady head losses evaluated in Chapter 5. For decelerating flows, the transient head losses were smaller than the steady head losses. A case study focusing on a down-surge of a surge tank confirmed this behavior in Section 9.2.4;
- the transient component of the head losses was directly proportional to the flow acceleration and was higher than the inertial effects;
- the duration of a steady experimental test was almost two hours for each approach flow direction. The duration could be decreased, in the future, by a continuous range of discharge with a low flow acceleration. A flow acceleration of 0.05 m/s^2 was sufficient for evaluating the steady head loss coefficient without increasing uncertainty.

10.4 Estimation of the cavitation risk

A method, that predicts the incipient cavitation number, σ_i, was applied to the orifices tested numerically. The main conclusions are:

- for the two approach flow directions, the incipient cavitation number, σ_i, was higher than the *vena-contracta* cavitation number σ_{vc};
- for the sharp approach flow, the incipient cavitation number, σ_i, increases with the contraction ratio, β, and the inner thickness ratio, α_i. The chamfer angle, θ, and the thickness ratio, α, did not influence on σ_i for the sharp approach flow.

  The sharp incipient cavitation number could be predicted by the empirical relationship of Eq.(9.9) or graphically from Figure 9.5 in the design guidelines (Chapter 9.1);

- for the chamfer approach flow, the incipient cavitation number, σ_i, rose with the contraction ratio, β, and the inner thickness ratio, α_i, and is influenced as well by the chamfer angle, θ.

  The chamfer incipient cavitation number could be predicted by the conservative relationship in Eq.(9.10) from the design guidelines (Chapter 9.1);

- for the two approach flow directions, the *vena-contracta* cavitation number rose with the contraction ratio, β, and the inner thickness ratio, α_i.

  The *vena-contracta* cavitation was predicted by the numerically obtained empirical relationship in Eq.(8.9) for the sharp approach flow and Eq.(8.10) for the chamfer approach flow in Chapter 9; and

- a case study of the estimation of the cavitation risk was presented in Section 9.2.5. An application to a surge tank with mass-oscillations uncovered the relevance of a graphical estimation of this risk.

10.5 Practical recommendations

- the 1-D numerical analysis still appeared to be essential. It allowed for simulating the whole high-head power plants, their connection with the electrical network and the response of the surge tank to different loads. From a hydraulic point of view, the main results of this phase were the head losses the throttle should produce at the entrance of the surge tank;

- empirical formulas offered in Chapter 9.1 should be employed in order to improve design in the preliminary design of the orifice;

- 3-D numerical simulations are useful for determining the effect of each orifice's geometrical parameter at the local surge tank junction;

- the physical model should be used at the end of all work to confirm and assist selecting the final orifice design;

- it is possible to assess the risk of cavitation from the discharge flowing into or out of the surge tank with a characteristic cavitation number and the results of the 1D numerical analysis of the waterway system; and

- prototype tests with the throttle are quite valuable for feedback on all the previous steps.

10.6 Outlook and future work

This study has mainly focused on chamfered and rounded orifices. The following aspects should be studied for a better understanding of throttle behavior:

- other orifice shapes in order to enrich the developed catalog;
- the effect of the upstream and downstream flow conditions, e.g swirling upstream flows, asymmetric flows because of the T-junction or different downstream diameters should be assessed. Correction parameters would best be applied to the head loss coefficients so as to get closer to the existing surge tank junction; and
- an improved experimental set-up could be used to allow for a better understanding of the transient head losses during mass oscillations. Furthermore, the overall pressure within the waterway system depends on the time and opening or closure rate of the downstream valve (or turbine). In Figure 10.1, a future experimental set-up is proposed that could simulate a mass oscillations with different flow accelerations, amplitudes and pressures within the tank.

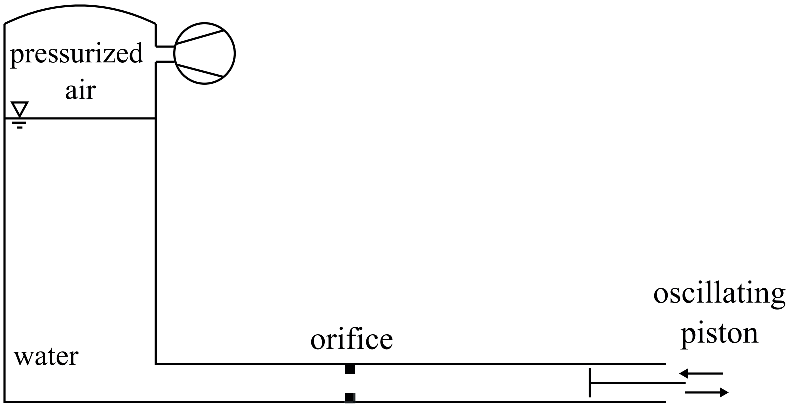

Figure 10.1 – Proposition of a new experimental testing setup for the assessment of the transient head losses during mass oscillations

A Instrumentation

This appendix presents the instrumentation, the calibration and the determination of the sampling parameters, e.g. frequency and sample number, for the physical recordings.

A.1 Presentation

A.1.1 Pressure transducers

This subsection is based on the supplier's information that the reader can find here: http://www.keller-druck.com/picts/pdf/engl/23e.pdf

During the experimental campaign, two different pressure transducers are used are shown in Figure A.1: G1/2" piezo-resistive transducers (KELLER - series 25, Figure A.1a) and G1/4" piezo-resistive transducers (KELLER - series 23, Figure A.1b).

For both types, the pressure range goes from $-0.2\,bar$ (-2 mH_2O) to $0.5\,bar$ (5 mH_2O) for a voltage range $0...10V$. According to the supplier, the typical error is ±0.2% of the full pressure range, while the maximum error is ±0.5%. In this experimental campaign, the typical and maximum errors for each pressure transmitter are respectively $\pm 0.0014 bar$ (± 0.014 mH_2O) and $\pm 0.0035 bar$ (± 0.035 mH_2O).

The pressure transmitters are connected to a National Instruments data acquisition card type NI USB-6259 series M, which records the pressure variations in volts.

A.1.2 Flow-meter

This subsection is based on the supplier's information that the reader can find here: https://www.endress.com/en/.

There is only one type of flow-meter used in this experimental campaign: ENDRESS+HAUSER PROMAG 50 W with a nominal diameter of 150 mm. As shown in Chapter 4.1, there are two

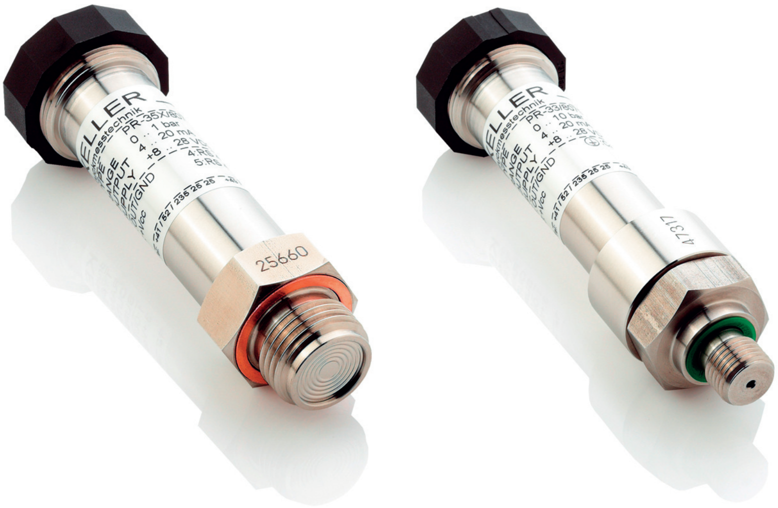
(a) G1/2" piezo-resistive transducers (b) G1/4" piezo-resitive transducers

Figure A.1 – Pressure transducers used in the experimental campaign

flow-meters on the laboratory supply pipes at each end of the main PVC pipe. Each flow-meter records only positive discharges even if they could theoretically record negative ones.

For both flow-meters, the discharge range goes from 0.0 l/s to 40.0 l/s while the maximum flowing discharge in the design of experiment is 30.0 l/s. According to the supplier, the maximum error is ±0.5% of the full discharge range. In this experimental campaign, the maximum errors is thus ±0.2 l/s.

The flowmeter are connected to a National Instruments data acquisition card type NI USB-6259 series M, through a $500-\Omega$ electrical resistance to obtain a full voltage range from 0 to $10V$.

Note: Two flow-meters are placed at each end of the main pipe recording only positive values. The utilization of two flow-meters recording a full discharges range (from -40 to +40 l/s) would theoretically produce a maximum error two times bigger. However, it would be possible to compare the value of the recorded discharge.

A.2 Calibration

A.2.1 Pressure transducers

The pressure transmitters are separately calibrated, either the G1/2"'s or the G1/4"'s. Fourteen different pressures are evaluated two times between 2 mH_2O (resp. 19.62 kPa) and 0.4 mH_2O (resp. 3.92 kPa) with a calibration stand developed by the LCH (Figure A.2).

For each pressure, the output signal is recorded during 15 seconds with a sampling frequency

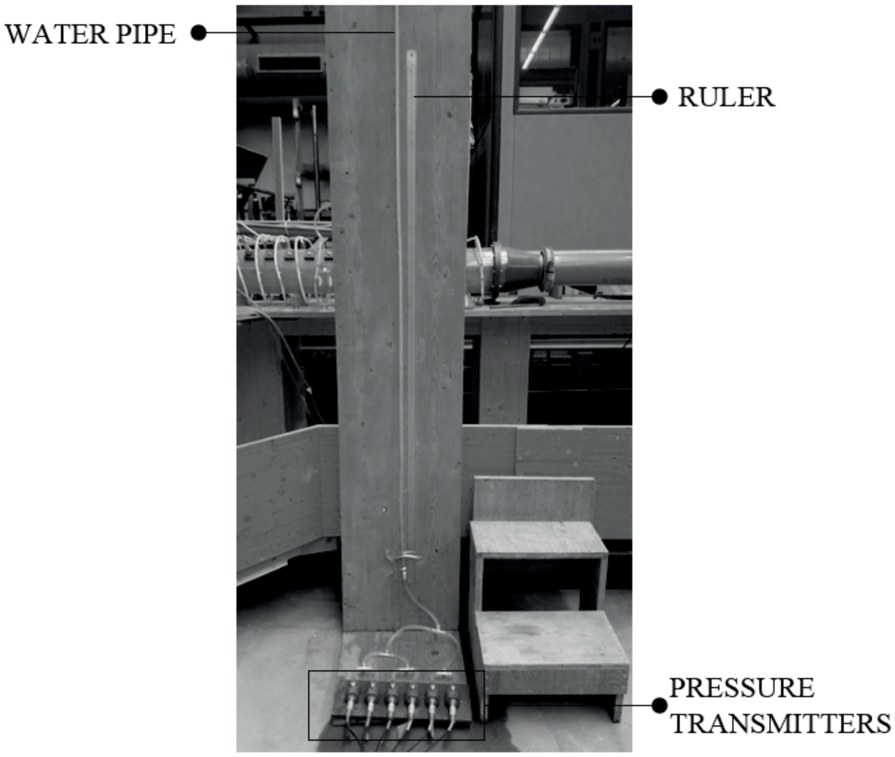

Figure A.2 – Calibration stand at LCH (EPFL)

of 100 Hz. According to the results and the manufacturer (Figure A.3 and A.4), there is a linear relation between the output signal in volt and the pressure. The parameter values of the linear regression are respectively given for G1/2" and G1/4" pressure transmitters in Table A.1 and A.2.

Table A.1 – Calibrations of the six G1/2" pressure transmitters: Mean values and 5% - 95 % confidence intervals (CI) of the calibration linear parameters a and b

Transmitter	$\bar{a}\,[mH_2O/V]$	$CI(a)\,[mH_2O/V]$	$b\,[mH_2O]$	$CI(b)\,[mH_2O]$
G1/2"(1)	0.50915	±0.00044	−0.69945	±0.00163
G1/2"(2)	0.50947	±0.00050	−0.81163	±0.00199
G1/2"(3)	0.50997	±0.00136	−0.84416	±0.00541
G1/2"(4)	0.50845	±0.00124	−0.75334	±0.00472
G1/2"(5)	0.50985	±0.00125	−0.79130	±0.00484
G1/2"(6)	0.51035	±0.00070	−0.71403	±0.00260

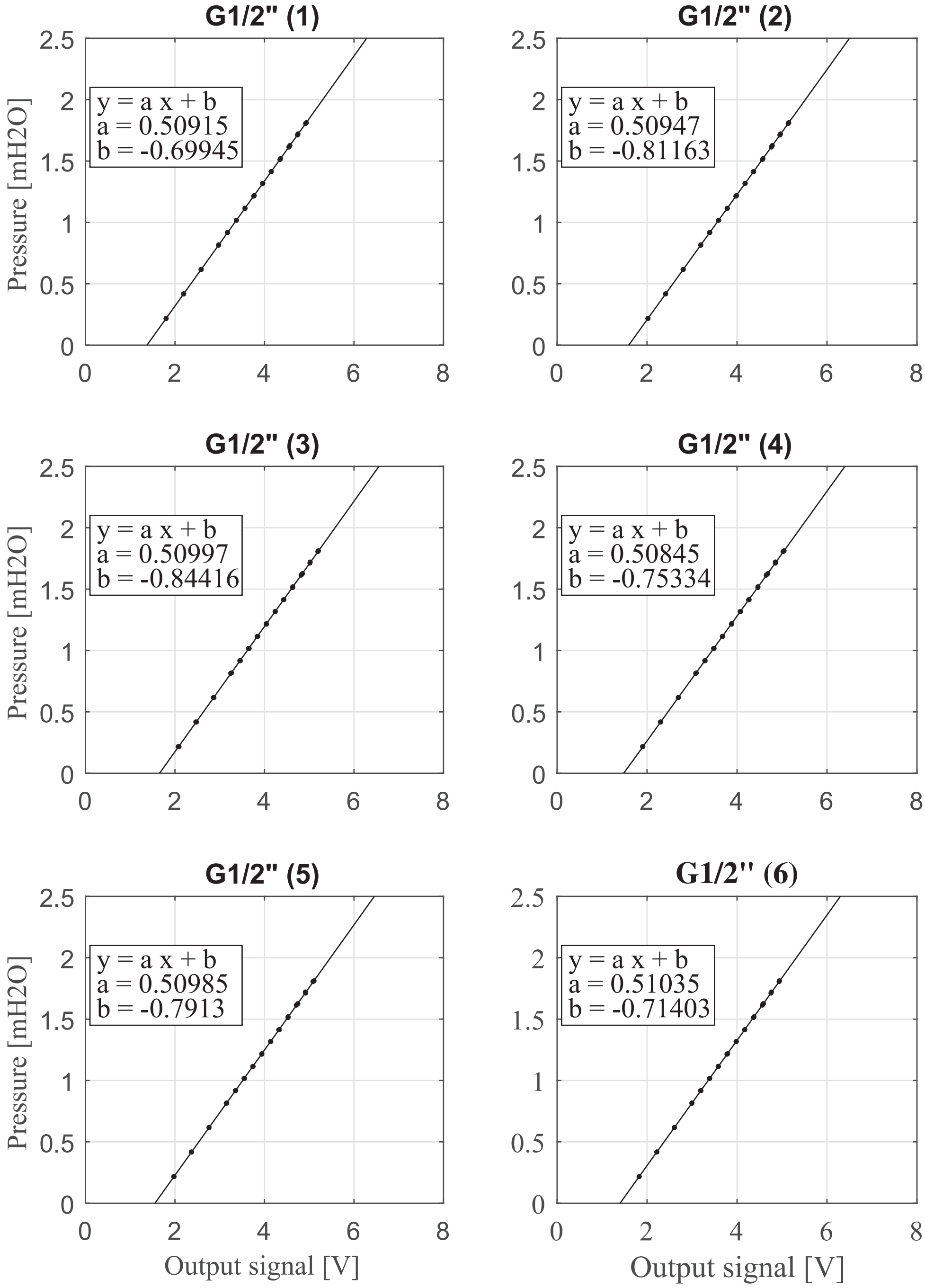

Figure A.3 – Calibrations for the six G1/2" pressure transmitters

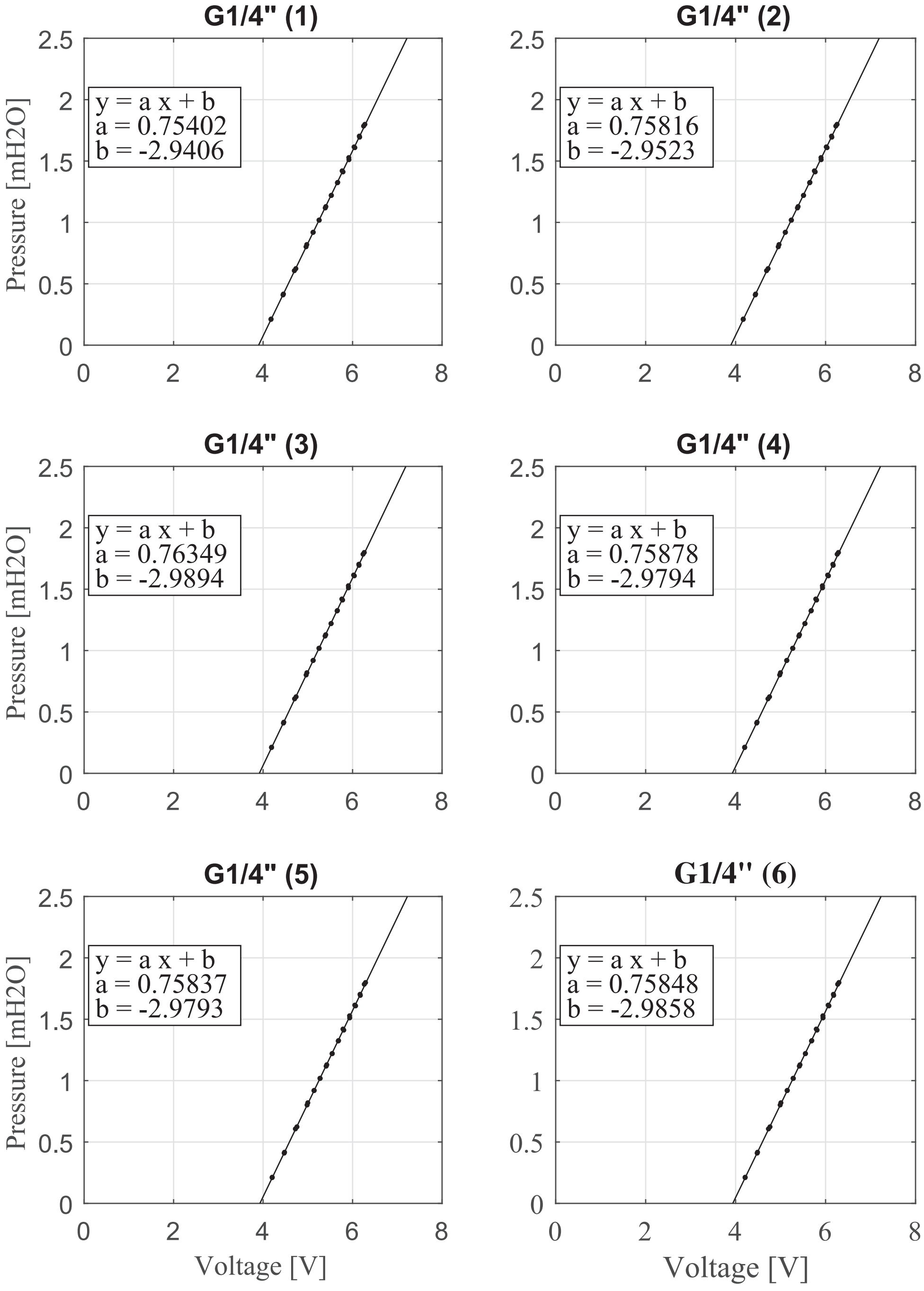

Figure A.4 – Calibrations for the six G1/4" pressure transmitters

Table A.2 – Calibrations of the six G1/4" pressure transmitters: Mean values and 5% - 95 % confidence intervals (CI) of the calibration linear parameters a and b

Transmitter	$\bar{a}\,[mH_2O/V]$	$CI(a)\,[mH_2O/V]$	$b\,[mH_2O]$	$CI(b)\,[mH_2O]$
G1/4"(1)	0.75402	±0.00456	−2.94060	±0.02470
G1/4"(2)	0.75816	±0.00454	−2.95230	±0.02450
G1/4"(3)	0.76349	±0.00453	−2.98940	±0.02400
G1/4"(4)	0.75878	±0.00455	−2.97940	±0.02480
G1/4"(5)	0.75837	±0.00457	−2.97930	±0.02480
G1/4"(6)	0.75848	±0.00455	−2.98580	±0.02480

A.2.2 FLow-meter

There are two electromagnetic flow-meters, ENDRESS+HAUSER PROMAG 50 W, on the experimental set-up. This type of flow-meter allows setting the maximum recorded flowing discharge for the maximum electric current (20mA). In this study, the maximum flowing discharge was set at 40 l/s. For the calibration, five different discharges between 9.5 and 40 l/s are used and directly read on the flow-meter screen during the recording.

For each pressure, the output signal is recorded during 60 seconds with a sampling frequency of 100 Hz. According to the results (Figure A.5), there is a linear relation between the output signal in volt and the pressure. The parameter values of the linear regression are respectively given for G1/2" and G1/4" pressure transmitters in Table A.3.

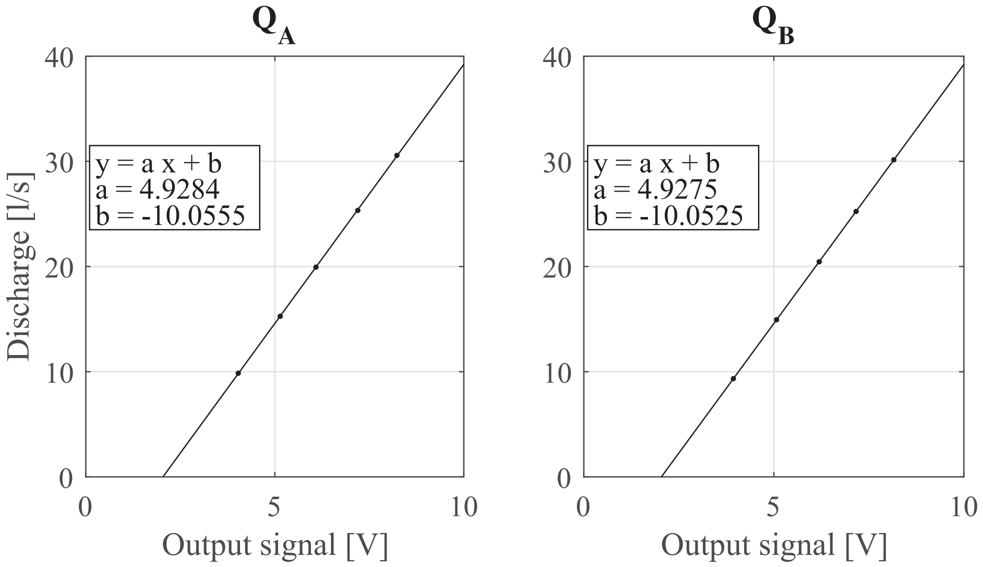

Figure A.5 – Calibrations for the two flow-meters

Table A.3 – Calibrations of the two flow-meters: Mean values and 5% - 95 % confidence intervals (CI) of the calibration linear parameters a and b

Transmitter	$\bar{a}\,[l/s/V]$	$CI(a)\,[mH_2O/V]$	$b\,[l/s]$	$CI(b)\,[mH_2O]$
Q_A	4.9284	±0.0555	−10.0555	±0.3496
Q_B	4.9275	±0.0117	−10.0525	±0.0731

A.3 Sampling parameters

As explained in the Section 4.1.4, there are 6 G1/2" pressure transmitters connected to 24 cross-sections through a dispatcher. In order to record a least one time each cross-sections, six recordings should be performed by discharge and by flow direction for a given orifice. It leads to 240 recordings per orifice. The recording time should be as small as possible to decrease the time spent for each orifice.

The pressure from both transmitters and the discharge were recorded during 900 s with a sampling frequency of 1 kHz for the maximum discharge of 30.0 l/s. The goal is to define the required sampling number, which leads to an good compromise between a statistically correct representation and acceptable duration.

Figure A.6 shows the results for pressure transmitters $G/2(1)$ (the other pressure transmitters gave same results). The duration of 30 seconds seems adequate as the maximum difference on the average value is 3% and the 95% confidence interval is below ± 1%.

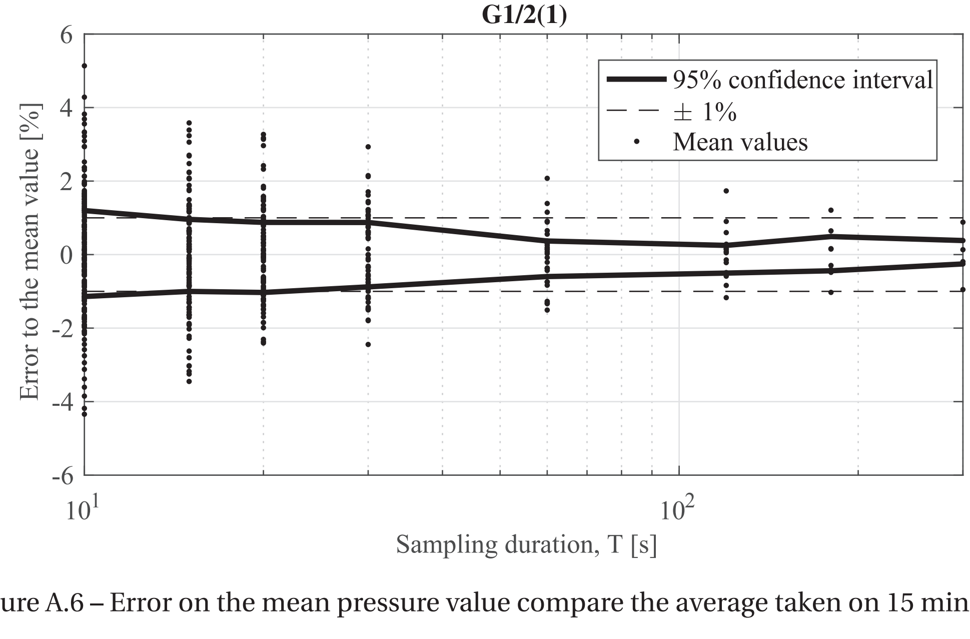

Figure A.6 – Error on the mean pressure value compare the average taken on 15 minutes

B Overview table of experiments and measured head losses

Table B.1 – Set of sharp orifices tested during the experimental work

Orifice name	Shape	Varying parameter	$\beta\,[-]$	$\alpha\,[-]$	$\alpha_i\,[-]$	$\theta\,[°]$	α_i/α
EXP_001	sharp	Reference	0.50	0.20	0.10	45	0.5
EXP_002	sharp	β	0.45	0.20	0.10	45	0.5
EXP_003	sharp	β	0.40	0.20	0.10	45	0.5
EXP_004	sharp	β	0.59	0.20	0.10	45	0.5
EXP_005	sharp	β	0.54	0.20	0.10	45	0.5
EXP_006	sharp	θ	0.50	0.20	0.20	0	1.0
EXP_007	sharp	θ	0.50	0.20	0.10	15	0.5
EXP_008	sharp	θ	0.50	0.20	0.10	30	0.5
EXP_009	sharp	θ	0.50	0.20	0.10	67	0.5
EXP_010	sharp	α_i	0.50	0.20	0.15	45	0.74
EXP_010.5	sharp	α_i	0.50	0.20	0.00	45	0.00
EXP_011	sharp	α_i	0.50	0.20	0.05	45	0.26
EXP_012	sharp	α	0.50	0.10	0.05	45	0.51
EXP_013	sharp	α	0.50	0.05	0.025	45	0.49
EXP_032	sharp	α	0.50	0.40	0.20	45	0.50
EXP_026	sharp	α, θ	0.50	0.40	0.40	0	1.0

Table B.2 – Set of rounded orifices tested during the experimental work

Orifice name	Shape	Varying parameter	$\beta\,[-]$	$\alpha\,[-]$	$\alpha_i\,[-]$	$\beta_b\,[-]$	α_i/α
EXP_014	rounded	Rounded shape	0.50	0.20	0.04	0.10	0.19
EXP_015	rounded	Shape, β	0.45	0.20	0.01	0.14	0.07
EXP_016	rounded	Shape, β	0.40	0.20	0.04	0.15	0.19
EXP_017	rounded	Shape, β	0.59	0.20	0.06	0.03	0.32
EXP_018	rounded	Shape, β	0.54	0.20	0.04	0.07	0.19
EXP_019	rounded	Shape, θ	0.50	0.20	0.04	0.21	0.20
EXP_020	rounded	Shape, θ	0.50	0.20	0.04	0.16	0.19
EXP_021	rounded	Shape, θ	0.50	0.20	0.05	-0.09	0.23
EXP_022	rounded	Shape, α_i	0.50	0.20	0.12	0.18	0.60
EXP_023	rounded	Shape, α_i	0.50	0.20	-0.04	0.02	-0.19
EXP_024	rounded	Shape, α	0.50	0.10	0.02	0.18	0.19
EXP_025	rounded	Shape, α	0.50	0.05	0.01	0.21	0.14
EXP_932	rounded	Shape, α	0.50	0.40	0.24	0.10	0.60

Table B.3 – Set of sharp orifices tested during the experimental work

Orifice name	Right	Left	β [−]	α [−]	α_i [−]	α_L [−]	θ_L [°]	α_R [−]	θ_R [°]
EXP_026	SHARP006	SHARP006	0.50	0.40	0.40	0.20	0	0.20	0
EXP_027	SHARP006	SHARP001	0.50	0.40	0.30	0.20	0	0.10	45
EXP_028	SHARP006	SHARP007	0.50	0.40	0.30	0.20	0	0.10	15
EXP_029	SHARP006	SHARP008	0.50	0.40	0.30	0.20	0	0.10	30
EXP_030	SHARP006	SHARP009	0.50	0.40	0.30	0.20	0	0.10	67
EXP_031	SHARP006	SHARP010	0.50	0.40	0.35	0.20	0	0.05	45
EXP_032	SHARP006	SHARP011	0.50	0.40	0.25	0.20	0	0.15	45
EXP_033	SHARP006	SHARP010.5	0.50	0.50	0.20	0.20	0	0.20	45
EXP_034	SHARP012	SHARP006	0.50	0.50	0.25	0.05	45	0.20	0
EXP_035	SHARP013	SHARP006	0.50	0.50	0.23	0.03	45	0.20	45
EXP_036	SHARP001	SHARP007	0.50	0.40	0.20	0.10	45	0.10	15
EXP_037	SHARP001	SHARP009	0.50	0.40	0.20	0.10	45	0.10	67
EXP_038	SHARP001	SHARP011	0.50	0.40	0.15	0.10	45	0.15	45
EXP_039	SHARP012	SHARP001	0.50	0.30	0.15	0.05	45	0.10	45
EXP_040	SHARP007	SHARP008	0.50	0.40	0.20	0.10	15	0.10	30
EXP_041	SHARP007	SHARP010	0.50	0.40	0.25	0.10	15	0.05	45
EXP_042	SHARP007	SHARP010.5	0.50	0.40	0.10	0.10	15	0.20	45
EXP_043	SHARP0013	SHARP007	0.50	0.40	0.20	0.10	45	0.10	15
EXP_044	SHARP008	SHARP009	0.50	0.40	0.20	0.10	30	0.10	67
EXP_045	SHARP008	SHARP011	0.50	0.40	0.15	0.10	30	0.15	45
EXP_046	SHARP012	SHARP008	0.50	0.30	0.15	0.05	45	0.10	45
EXP_047	SHARP009	SHARP010	0.50	0.40	0.25	0.10	67	0.05	45
EXP_048	SHARP009	SHARP010.5	0.50	0.40	0.10	0.10	67	0.20	45
EXP_049	SHARP012	SHARP009	0.50	0.30	0.15	0.05	45	0.10	67
EXP_050	SHARP010	SHARP011	0.50	0.40	0.20	0.05	45	0.15	45
EXP_051	SHARP012	SHARP010	0.50	0.30	0.20	0.05	45	0.05	45
EXP_052	SHARP011	SHARP010.5	0.50	0.40	0.05	0.15	45	0.20	45
EXP_053	SHARP013	SHARP011	0.50	0.25	0.08	0.03	45	0.15	45
EXP_054	SHARP012	SHARP010.5	0.50	0.30	0.05	0.05	45	0.20	45
EXP_055	SHARP013	SHARP012	0.50	0.15	0.08	0.03	45	0.05	45

Table B.4 – Overview table sorted with descending highest head loss coefficient

Orifice	Highest head loss coefficient	Lowest head loss coefficient
EXP016	92.4	29.6
EXP003	89.5	43.5
EXP015	46.7	21.3
EXP002	42.8	31.7
EXP010.5	32.9	18.5
EXP020	32.9	8.6
EXP021	32.7	9.1
EXP019	32.4	8.6
EXP014	31.9	9.0
EXP023	31.5	12.6
EXP011	31.5	18.2
EXP012	31.5	20.1
EXP025	31.3	16.4
EXP009	31.0	24.6
EXP022	30.8	8.0
EXP007	30.6	10.6
EXP008	30.6	10.5
EXP010	30.1	12.7
EXP024	30.0	13.0
EXP001	29.4	18.2
EXP013	29.0	20.5
EXP006	26.9	26.2
EXP048	26.4	16.8
EXP032	26.2	12.5
EXP049	23.9	18.6
EXP033	23.4	10.2
EXP035	22.9	14.6
EXP055	21.8	17.7
EXP053	21.8	17.4
EXP054	21.7	21.2
EXP030	21.2	15.0
EXP034	20.9	13.6
EXP037	20.4	13.7
EXP052	20.4	18.5
EXP044	19.5	11.8
EXP031	19.3	10.8
EXP027	18.9	12.3
EXP047	18.8	11.1
EXP026	18.2	17.2
EXP029	17.6	10.5
EXP005	17.4	12.7
EXP018	17.3	7.5
EXP028	16.6	11.1
EXP039	16.2	13.4

Orifice	Highest head loss coefficient	Lowest head loss coefficient
EXP038	14.9	13.1
EXP043	14.6	11.2
EXP046	14.1	9.4
EXP017	13.8	3.5
EXP051	13.7	11.0
EXP050	13.4	10.3
EXP045	12.3	11.5
EXP004	11.8	6.8
EXP036	10.7	10.4
EXP041	10.6	7.6
EXP040	10.6	9.6
EXP042	10.6	12.0

C Design of the numerical simulations

Name	β [–]	α [–]	α_i [–]	θ [°]
NUM_001	0.50	0.20	0.10	45
NUM_002	0.45	0.20	0.10	45
NUM_003	0.40	0.20	0.10	45
NUM_004	0.59	0.20	0.10	45
NUM_005	0.54	0.20	0.10	45
NUM_006	0.50	0.20	0.20	0
NUM_007	0.50	0.20	0.10	15
NUM_008	0.50	0.20	0.10	30
NUM_009	0.50	0.20	0.10	67
NUM_010	0.50	0.20	0.15	45
NUM_011	0.50	0.20	0	45
NUM_012	0.50	0.20	0.05	45
NUM_013	0.50	0.10	0.05	45
NUM_014	0.50	0.05	0.03	45
NUM_015	0.50	0.40	0.20	45
NUM_016	0.50	0.20	0.10	5
NUM_017	0.50	0.20	0.10	10
NUM_018	0.50	0.20	0.10	20
NUM_019	0.50	0.20	0.10	40
NUM_020	0.50	0.20	0.10	50
NUM_021	0.50	0.20	0.10	55
NUM_022	0.50	0.20	0.10	60
NUM_023	0.50	0.20	0.10	90
NUM_024	0.50	0.20	0.200	0
NUM_025	0.50	0.20	0.050	15
NUM_026	0.50	0.20	0.050	30
NUM_027	0.50	0.20	0.050	59.0
NUM_028	0.50	0.20	0.150	15
NUM_029	0.50	0.20	0.150	30
NUM_030	0.50	0.20	0.150	60
NUM_031	0.50	0.10	0.05	0
NUM_032	0.50	0.10	0.05	15
NUM_033	0.50	0.10	0.05	30
NUM_034	0.50	0.10	0.05	45
NUM_035	0.50	0.10	0.05	60
NUM_036	0.50	0.10	0.025	15
NUM_037	0.50	0.10	0.025	30
NUM_038	0.50	0.10	0.025	45
NUM_039	0.50	0.10	0.025	60
NUM_040	0.50	0.10	0.075	15
NUM_041	0.50	0.10	0.075	30
NUM_042	0.50	0.10	0.075	45
NUM_043	0.50	0.10	0.075	60
NUM_044	0.50	0.40	0.40	0
NUM_045	0.50	0.40	0.20	15
NUM_046	0.50	0.40	0.20	30
NUM_047	0.50	0.40	0.20	45
NUM_048	0.50	0.40	0.40	0
NUM_049	0.50	0.40	0.100	15
NUM_050	0.50	0.40	0.100	30
NUM_051	0.50	0.40	0.300	30
NUM_052	0.50	0.40	0.300	45
NUM_053	0.50	0.40	0.300	60

Name	β [–]	α [–]	α_i [–]	θ [°]
NUM_101	0.40	0.20	0.20	0
NUM_102	0.40	0.20	0.10	45
NUM_103	0.40	0.20	0.10	15
NUM_104	0.40	0.20	0.10	30
NUM_105	0.40	0.20	0.10	60
NUM_106	0.40	0.20	0.05	15
NUM_107	0.40	0.20	0.05	30
NUM_108	0.40	0.20	0.05	45
NUM_109	0.40	0.20	0.15	15
NUM_110	0.40	0.20	0.15	30
NUM_111	0.40	0.20	0.15	45
NUM_112	0.40	0.20	0.15	60
NUM_113	0.40	0.10	0.10	0
NUM_114	0.40	0.10	0.05	45
NUM_115	0.40	0.10	0.05	15
NUM_116	0.40	0.10	0.05	30
NUM_117	0.40	0.10	0.05	60
NUM_118	0.40	0.10	0.025	15
NUM_119	0.40	0.10	0.025	30
NUM_120	0.40	0.10	0.025	45
NUM_121	0.40	0.10	0.025	60
NUM_122	0.40	0.10	0.075	15
NUM_123	0.40	0.10	0.075	30
NUM_124	0.40	0.10	0.075	45
NUM_125	0.40	0.10	0.075	60
NUM_126	0.40	0.40	0.40	0

Name	β [–]	α [–]	α_i [–]	θ [°]
NUM_200	0.45	0.20	0.20	0
NUM_201	0.45	0.20	0.10	45
NUM_202	0.45	0.20	0.10	15
NUM_203	0.45	0.20	0.10	30
NUM_204	0.45	0.20	0.10	60
NUM_205	0.45	0.20	0.05	15
NUM_206	0.45	0.20	0.05	30
NUM_207	0.45	0.20	0.05	45
NUM_208	0.45	0.20	0.15	15
NUM_209	0.45	0.20	0.15	30
NUM_210	0.45	0.20	0.15	45
NUM_211	0.45	0.20	0.15	60
NUM_212	0.45	0.10	0.10	0
NUM_213	0.45	0.10	0.05	45
NUM_214	0.45	0.10	0.05	15
NUM_215	0.45	0.10	0.05	30
NUM_216	0.45	0.10	0.05	60
NUM_217	0.45	0.10	0.025	15
NUM_218	0.45	0.10	0.025	30
NUM_219	0.45	0.10	0.025	45
NUM_220	0.45	0.10	0.025	60
NUM_221	0.45	0.10	0.075	15
NUM_222	0.45	0.10	0.075	30
NUM_223	0.45	0.10	0.075	45
NUM_224	0.45	0.10	0.075	60
NUM_225	0.45	0.40	0.40	0

Name	β [–]	α [–]	α_i [–]	θ [°]
NUM_300	0.60	0.20	0.20	0
NUM_301	0.60	0.20	0.10	45
NUM_302	0.60	0.20	0.10	15
NUM_303	0.60	0.20	0.10	30
NUM_304	0.60	0.20	0.10	60
NUM_305	0.60	0.20	0.05	15
NUM_306	0.60	0.20	0.05	30
NUM_307	0.60	0.20	0.05	45
NUM_308	0.60	0.20	0.15	15
NUM_309	0.60	0.20	0.15	30
NUM_310	0.60	0.20	0.15	45
NUM_311	0.60	0.20	0.15	60
NUM_312	0.60	0.10	0.10	0
NUM_313	0.60	0.10	0.05	45
NUM_314	0.60	0.10	0.05	15
NUM_315	0.60	0.10	0.05	30
NUM_316	0.60	0.10	0.05	60
NUM_317	0.60	0.10	0.025	15
NUM_318	0.60	0.10	0.025	30
NUM_319	0.60	0.10	0.025	45
NUM_320	0.60	0.10	0.025	60
NUM_321	0.60	0.10	0.075	15
NUM_322	0.60	0.10	0.075	30
NUM_323	0.60	0.10	0.075	45
NUM_324	0.60	0.10	0.075	60
NUM_325	0.60	0.40	0.40	0
NUM_326	0.60	0.40	0.20	45
NUM_327	0.60	0.40	0.20	15
NUM_328	0.60	0.40	0.20	30
NUM_329	0.60	0.40	0.20	45.0
NUM_330	0.60	0.40	0.100	15
NUM_331	0.60	0.40	0.100	30
NUM_332	0.60	0.40	0.100	45
NUM_333	0.60	0.40	0.300	15
NUM_334	0.60	0.40	0.300	30
NUM_335	0.60	0.40	0.300	45
NUM_336	0.60	0.40	0.300	60

Name	β [–]	α [–]	α_i [–]	θ [°]
NUM_400	0.30	0.20	0.20	0
NUM_401	0.30	0.10	0.10	0
NUM_402	0.30	0.40	0.40	0

Name	β [–]	α [–]	α_i [–]	θ [°]
NUM500	0.70	0.20	0.20	0
NUM501	0.70	0.10	0.10	0
NUM502	0.70	0.40	0.40	0

D Example of test sheet

The test sheets of all experiments are available on-line (doi:10.5075/epfl-thesis-8090) with detailed experimental results for the chamfered, rounded and 2-chamfered orifices.

Orifice : **EXP_001**

Type : chamfered orifice

Head loss coefficients

k_{AB}	29.4 ±0.46
k_{BA}	18.2 ±0.16
λ	0.64

Jet length

$L_{j,AB}$	3.97
$L_{j,BA}$	4.47

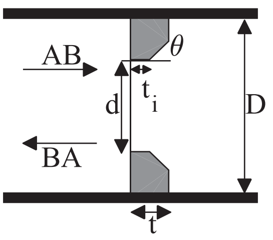

Geometrical parameters

d	107	[mm]	β	*0.495*	*[-]*
t	43.0	[mm]	α	*0.199*	*[-]*
t_i	21.5	[mm]	α_i	*0.099*	*[-]*
			θ	45	*[deg]*

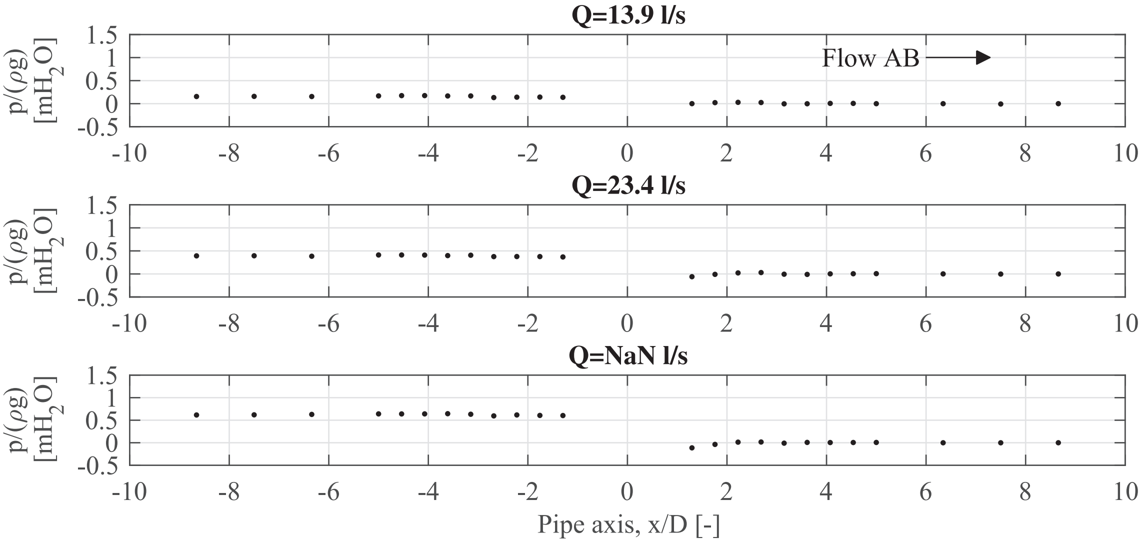

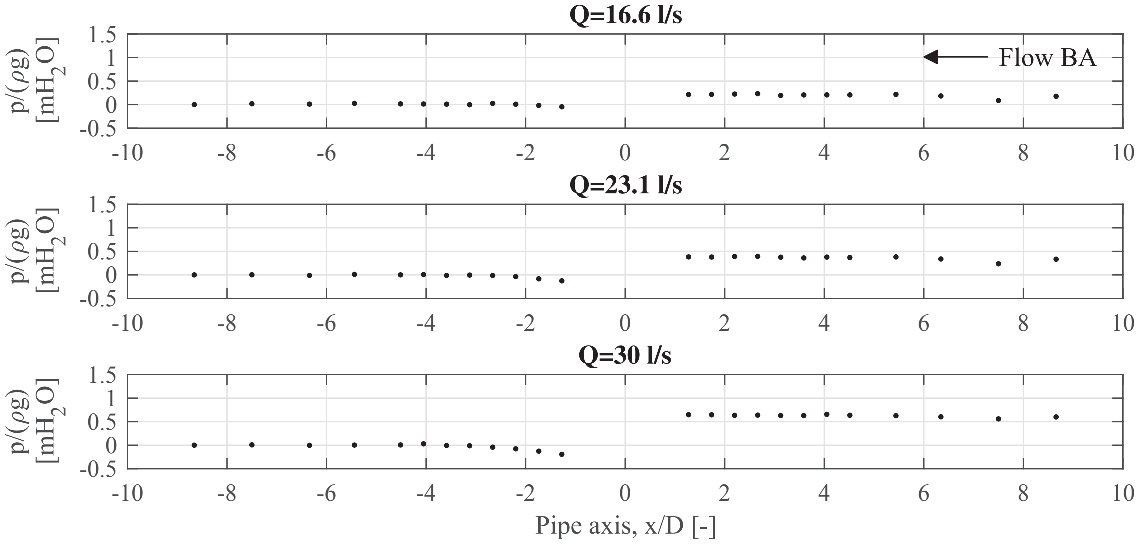

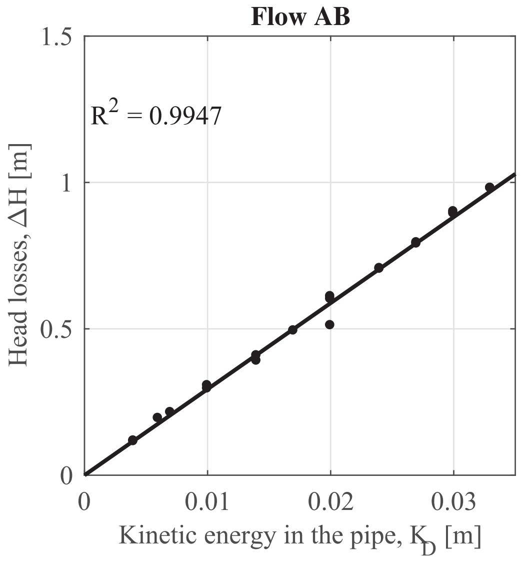

Q [l/s]	K_D [m]	ΔH [m]
9.8	0.004	0.117
9.8	0.004	0.115
13.0	0.006	0.194
13.4	0.007	0.214
16.1	0.010	0.295
16.3	0.010	0.306
18.9	0.014	0.390
18.9	0.014	0.408
20.9	0.017	0.493
22.7	0.020	0.511
23.1	0.020	0.601
23.1	0.020	0.610
24.9	0.024	0.706
25.1	0.024	0.704
26.5	0.027	0.790
26.6	0.027	0.794
28.2	0.030	0.900
28.3	0.030	0.893
29.6	0.033	0.980
29.6	0.033	0.980

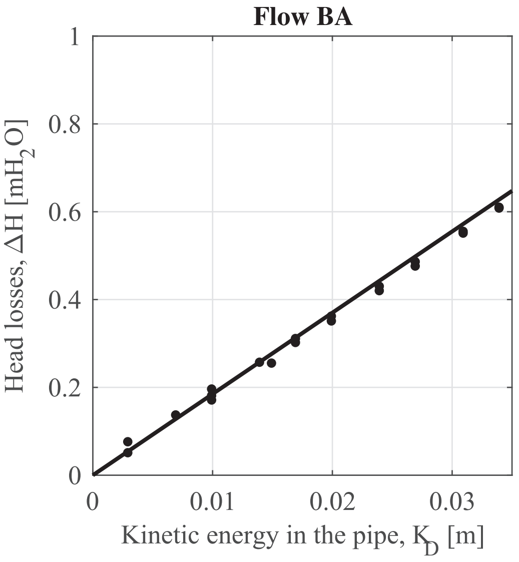

Q [l/s]	K_D [m]	ΔH [m]
9.4	0.003	0.049
9.4	0.003	0.064
13.3	0.007	0.128
16.3	0.010	0.171
16.3	0.010	0.189
16.6	0.010	0.183
19.1	0.014	0.239
19.7	0.015	0.259
21.1	0.017	0.312
21.4	0.017	0.308
22.8	0.020	0.363
23.1	0.020	0.359
25.0	0.024	0.431
25.1	0.024	0.428
26.7	0.027	0.490
26.7	0.027	0.498
28.5	0.031	0.567
28.7	0.031	0.564
30.0	0.034	0.623
30.0	0.034	0.624

E Transient experiments

Tables E.1 to E.5 show the main conditions of the transient experiments. The notation used in the Tables E.1 to E.5 are explained in Figure E.1 and below :

- $Q_{low,b}$: the steady discharge before the rising phase;
- Q_{high}: the steady discharge within the rising and falling phase;
- $Q_{low,e}$: the steady discharge after the falling phase;
- T_r (resp. T_f): the duration of the rising (resp. falling) phase;
- $\left(\frac{dv_d}{dt}\right)_{t,inc.}$ (resp. $\left(\frac{dv_d}{dt}\right)_{t,dec.}$): the average acceleration of the velocity in the orifice section.

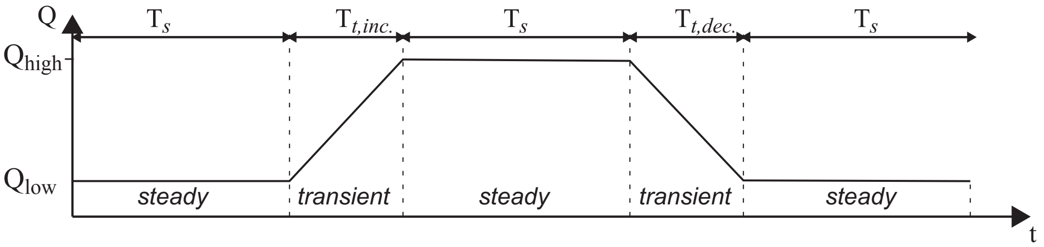
Q
Q$_{high}$
Q$_{low}$
T$_s$
T$_{t,inc.}$
T$_s$
T$_{t,dec.}$
T$_s$
steady
transient
steady
transient
steady
t

Figure E.1 – Procedure of the transient experiments

Table E.1 – Transient experiments performed on the orifice EXP_001

	$Q_{low,b}\,[l/s]$	$Q_{high}\,[l/s]$	$Q_{low,e}\,[l/s]$	$T_{t,inc.}\,[s]$	$\left(\frac{dv_d}{dt}\right)_{t,inc.}\,[m/s^2]$	$T_{t,dec.}\,[s]$	$\left(\frac{dv_d}{dt}\right)_{t,dec.}\,[m/s^2]$
TRANS_001_05(1)	19.27	28.58	19.39	3.48	0.292	3.25	-0.309
TRANS_001_05(2)	19.35	28.57	19.21	5.05	0.199	3.18	-0.321
TRANS_001_05(3)	19.25	28.46	19.35	3.88	0.259	3.14	-0.316
TRANS_001_10(1)	19.20	28.56	19.61	4.55	0.225	9.43	-0.104
TRANS_001_10(2)	19.60	28.59	19.42	9.73	0.101	9.41	-0.106
TRANS_001_10(3)	19.57	28.58	19.26	9.49	0.104	9.64	-0.106
TRANS_001_20(1)	19.31	29.24	19.16	14.81	0.073	17.84	-0.062
TRANS_001_20(2)	19.40	28.44	19.59	17.47	0.057	18.86	-0.051
TRANS_001_20(3)	19.44	28.55	19.33	16.38	0.061	16.83	-0.060
TRANS_001_30(1)	19.06	28.24	19	33	0.030	23.76	-0.042
TRANS_001_30(2)	19.54	28.49	19.29	21.77	0.045	19.31	-0.052
TRANS_001_30(3)	19.28	28.50	19.32	21.53	0.047	23.44	-0.043

Table E.2 – Transient experiments performed on the orifice EXP_002

	$Q_{low,b}\,[l/s]$	$Q_{high}\,[l/s]$	$Q_{low,e}\,[l/s]$	$T_{t,inc.}\,[s]$	$\left(\frac{dv_d}{dt}\right)_{t,inc.}\,[m/s^2]$	$T_{t,dec.}\,[s]$	$\left(\frac{dv_d}{dt}\right)_{t,dec.}\,[m/s^2]$
TRANS_002_05(1)	18.97	28.13	19.06	4.37	0.282	3.63	-0.337
TRANS_002_05(2)	19.08	28.12	19.07	3.99	0.306	3.13	-0.389
TRANS_002_05(3)	19.10	28.31	18.94	3.82	0.325	5.14	-0.245
TRANS_002_10(1)	19.09	28.16	18.95	7	0.175	8.228	-0.150
TRANS_002_10(2)	18.95	28.21	19.01	7.13	0.175	10.28	-0.121
TRANS_002_10(3)	18.98	28.21	18.96	6.71	0.185	6.39	-0.195
TRANS_002_20(1)	18.92	28.21	19.17	14.86	0.084	20.51	-0.059
TRANS_002_20(2)	19.17	28.18	19.10	18.91	0.064	23.80	-0.051
TRANS_002_20(3)	19.13	28.08	19.07	20.07	0.060	17.42	-0.070
TRANS_002_30(1)	19.14	28.12	19.04	29.40	0.041	27.08	-0.045
TRANS_002_30(2)	19.03	28.14	19.03	27.18	0.045	25.57	-0.048
TRANS_002_30(3)	19.01	28.07	18.91	28.19	0.043	33.69	-0.037

Table E.3 – Transient experiments performed on the orifice EXP_004

	$Q_{low,b}\,[l/s]$	$Q_{high}\,[l/s]$	$Q_{low,e}\,[l/s]$	$T_{t,inc.}\,[s]$	$\left(\frac{dv_d}{dt}\right)_{t,inc.}\,[m/s^2]$	$T_{t,dec.}\,[s]$	$\left(\frac{dv_d}{dt}\right)_{t,dec.}\,[m/s^2]$
TRANS_004_05(1)	19.05	28.98	19.18	4.93	0.153	4.30	-0.173
TRANS_004_05(2)	19.30	28.42	19.40	2.88	0.240	2.26	-0.302
TRANS_004_05(3)	19.36	28.50	19	4.93	0.141	3.23	-0.223
TRANS_004_10(1)	19.50	28.46	19.42	7.57	0.090	7.44	-0.092
TRANS_004_10(2)	19.29	28.30	19.29	6.41	0.107	7.43	-0.092
TRANS_004_20(1)	19.14	27.96	18.87	14.91	0.045	16.13	-0.043
TRANS_004_20(2)	18.86	27.99	19.55	13.31	0.052	15.87	-0.040
TRANS_004_20(3)	19.54	28.42	19.36	14.55	0.046	21.39	-0.032
TRANS_004_30(1)	19.16	28.32	18.81	21.67	0.032	19.95	-0.036
TRANS_004_30(2)	19.09	28.11	18.99	21.48	0.032	27.73	-0.025
TRANS_004_30(3)	19.37	28.10	19.61	27.99	0.024	25.98	-0.025

Table E.4 – Transient experiments performed on the orifice EXP_012

	$Q_{low,b}\,[l/s]$	$Q_{high}\,[l/s]$	$Q_{low,e}\,[l/s]$	$T_{t,inc.}\,[s]$	$\left(\frac{dv_d}{dt}\right)_{t,inc.}\,[m/s^2]$	$T_{t,dec.}\,[s]$	$\left(\frac{dv_d}{dt}\right)_{t,dec.}\,[m/s^2]$
TRANS_012_05(1)	19.19	28.44	19.26	5.68	0.178	5.70	-0.176
TRANS_012_05(2)	19.23	28.50	19.22	4.83	0.210	3.23	-0.314
TRANS_012_05(3)	19.22	28.41	19.12	3.45	0.291	3.47	-0.293
TRANS_012_10(1)	19.06	28.49	19.02	6.72	0.153	11.20	-0.092
TRANS_012_10(2)	19.01	28.53	19.27	12.66	0.082	10.53	-0.096
TRANS_012_10(3)	19.28	28.44	19.21	10.53	0.095	10.21	-0.099
TRANS_012_20(1)	19.37	28.49	19.10	18.33	0.054	22.65	-0.045
TRANS_012_20(2)	19.11	28.54	18.96	23.10	0.045	20.37	-0.051
TRANS_012_20(3)	18.95	28.49	19.03	23.84	0.044	23.53	-0.044
TRANS_012_30(1)	19.25	28.22	19.45	21.18	0.046	24.65	-0.039
TRANS_012_30(2)	19.29	28.47	19.14	20.79	0.048	30.36	-0.034
TRANS_012_30(3)	19.07	28.43	19.39	27.16	0.038	11.60	-0.085

Table E.5 – Transient experiments performed on the orifice EXP_032

	$Q_{low,b}\,[l/s]$	$Q_{high}\,[l/s]$	$Q_{low,e}\,[l/s]$	$T_{t,inc.}\,[s]$	$\left(\frac{dv_d}{dt}\right)_{t,inc.}\,[m/s^2]$	$T_{t,dec.}\,[s]$	$\left(\frac{dv_d}{dt}\right)_{t,dec.}\,[m/s^2]$
TRANS_032_05(1)	19.18	28.45	19.23	4.77	0.212	3.78	-0.266
TRANS_032_05(2)	19.22	28.43	19.31	4.19	0.240	2.75	-0.362
TRANS_032_05(3)	19.11	28.40	19.65	3.82	0.265	2.77	-0.344
TRANS_032_05(4)	19.30	25.17	19.40	5.28	0.121	5.53	-0.114
TRANS_032_05(5)	19.19	25.23	19.63	4.54	0.145	4.21	-0.145
TRANS_032_05(6)	19.41	25.26	19.13	4.76	0.134	3.95	-0.169
TRANS_032_10(1)	19.07	28.25	19.24	8.55	0.117	9.20	-0.107
TRANS_032_10(2)	19.28	28.17	19.26	9.19	0.106	8.65	-0.112
TRANS_032_10(3)	18.77	28.21	18.88	8.15	0.126	8.55	-0.119
TRANS_032_20(1)	19.45	28	19.45	20.01	0.047	14.67	-0.064
TRANS_032_20(2)	19.06	28.04	19.29	16.11	0.061	15.96	-0.060
TRANS_032_20(3)	19.14	25.07	19.23	19	0.034	15.41	-0.041
TRANS_032_20(4)	19.02	25.17	19.46	18.03	0.037	22.27	-0.028
TRANS_032_20(5)	19.28	25.11	18.90	17.59	0.036	19.30	-0.035
TRANS_032_30(1)	19.25	28.01	19.46	29.37	0.033	29.78	-0.031
TRANS_032_30(2)	19.41	28.09	19	28.61	0.033	25.15	-0.039
TRANS_032_30(3)	18.99	27.92	19.41	28	0.035	26.41	-0.035

F Theoretical bases for the cavitation limit

F.1 Straight pipe

Figure F.1 shows a schematic draw of the streamlines and of the pressure line when water flows through an orifice. The goal of this appendix is evaluating the cavitation risk of orifice by knowing the upstream pressure p_u, the discharge Q and the incipient cavitation number σ_i.

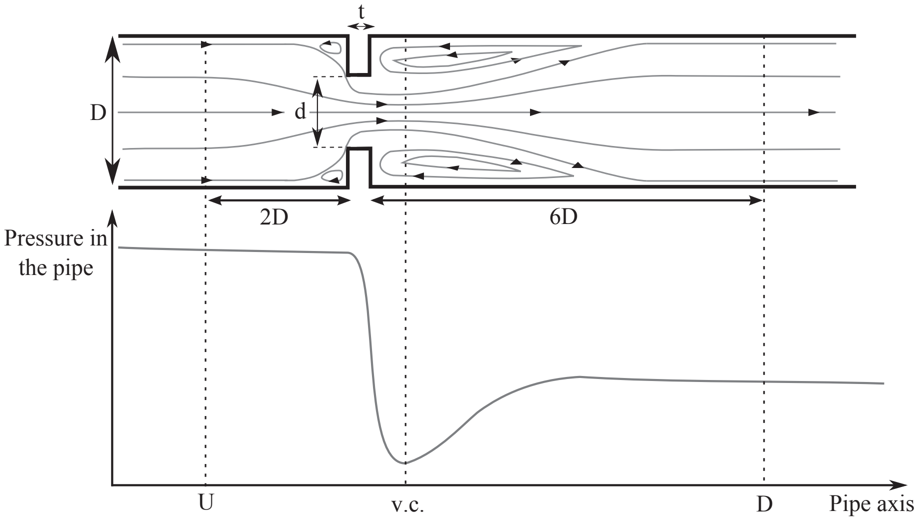

Figure F.1 – Flow through an orifice and localization of the different section used in the evaluation of σ_i and $\sigma_{v.c.}$

Eq.(F.1) reminds the definition of σ_i in this research project with p_u the upstream pressure, p_d the downstream pressure and $p_{v.g.}$ the vapour pressure.

$$\sigma_i = \frac{p_u - p_{v.g.}}{p_u - p_d} \tag{F.1}$$

The difference between the upstream and downstream pressure, $p_u - p_d$, is equivalent to the local head losses in the straight pipe by assuming the linear friction losses are negligible. Here, two relation can be found by highlighting the orifice diameter d (Section F.1.1) or the pipe diameter D (Section F.1.2).

F.1.1 Reference diameter - orifice diameter d

$$p_u = \sigma_i \cdot \Delta H + p_{v.g.} \tag{F.2}$$

$\leftrightarrow p_u = \sigma_i \cdot k_d \frac{v_d^2}{2g} + p_{v.g.}$

$\leftrightarrow p_u = \sigma_i \cdot \frac{k_d}{(\pi(d/2)^2)^2} \frac{Q^2}{2g} + p_{v.g.}$

$\leftrightarrow p_u = \sigma_i \cdot \frac{8}{g\pi^2 d^4} k_d \cdot Q^2 + p_{v.g.}$

However, generally, the head loss coefficient k, relative to the pipe diameter D, is generally used and k_d relative to the orifice diameter d (Eq.(F.3)).

$$\Delta H = k_d \cdot \frac{v_d^2}{2g} = k \cdot \frac{v_D^2}{2g} \leftrightarrow k_d = k \cdot \beta^4 \tag{F.3}$$

where β is the contraction ratio, $\beta = \frac{d}{D}$.

Finally, Eq.(F.2) becomes Eq.(F.4).

$$\leftrightarrow p_u = \sigma_i \cdot \frac{8\beta^4}{g\pi^2 d^4} k \cdot Q^2 + p_{v.g.} \tag{F.4}$$

F.1.2 Reference diameter - pipe diameter D

From Eq.(F.4) with $\beta = d/D$, the E.(F.5) gives the relation depending only on D.

$$\leftrightarrow p_u = \sigma_i \cdot \frac{8}{g\pi^2 D^4} k \cdot Q^2 + p_{v.g.} \tag{F.5}$$

F.2 Surge tank orifices

Figure F.2 shows the schematic view of the situation during the filling or the emptying of the surge tank during the mass oscillations. Comparing to the case with a straight pipe, the pressure and discharge are transient and depend on the time. The construction of the cavitation limit criteria is assumed time independent for the purpose of simplification. Thus, the quasi-steady Bernoulli's law is applied for the head losses without the inertial term.

The discharge is taken positive when the water flows in the surge tank.

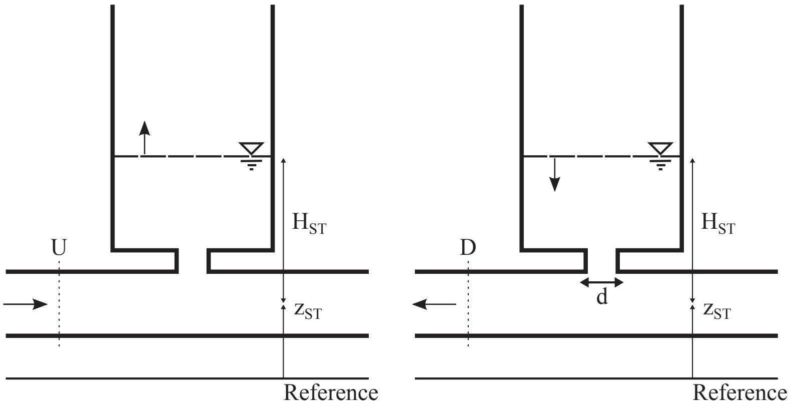

(a) Surge tank filling (b) Surge tank emptying

Figure F.2 – View of the idealized surge tank during when water flows in (a) or out (b) the surge tank

F.2.1 Surge tank emptying

In this case, the cross-section of the upstream (Surge tank) and downstream pipe (pressure tunnel) are different and, then, the difference of pressure are not equal to the head losses (Eq.(F.6)).

$$\Delta H = (p_u - p_d) + \left(\frac{v_u^2}{2g} - \frac{v_d^2}{2g}\right) \leftrightarrow (p_u - p_d) = \Delta H - \left(\frac{v_u^2}{2g} - \frac{v_d^2}{2g}\right) = \Delta H - \frac{Q^2}{2g} \cdot \left(\frac{1}{A_u^2} - \frac{1}{A_d^2}\right) \quad \text{(F.6)}$$

The same relation between the water level in the surge tank, H_{ST}, and the discharge can now be found:

$$H_{ST} = \sigma_i \cdot \frac{8\beta^4}{g\pi^2 d^4} k \cdot Q^2 - \sigma_i \cdot \kappa_Q Q^2 + p_{v.g.} \quad \text{(F.7)}$$

where $\kappa_Q = \frac{1}{2g} \cdot \left(\frac{1}{A_{ST}^2} - \frac{1}{A_{PT}^2} \right)$ is the correction due to the effect of the difference of kinetic energy between the surge tank and the pressure tunnel.

F.2.2 Surge tank filling

For the filling, H_{ST} is equivalent to the downstream pressure, p_d. The definition of the downstream cavitation number σ_d is thus used as shown in Eq.(F.8). The relation between the water level in the surge tank and the upstream pressure is consequently reported in Eq.(F.9).

$$\sigma_i^d = \frac{p_d - p_{v.g.}}{p_u - p_d} = \sigma_i - 1 \tag{F.8}$$

$$H_{ST} = (\sigma_i - 1) \cdot \frac{8\beta^4}{g\pi^2 d^4} k \cdot Q^2 - (\sigma_i - 1) \cdot \kappa_Q Q^2 + p_{v.g.} \tag{F.9}$$

where $\kappa_Q = \frac{1}{2g} \cdot \left(\frac{1}{A_{PT}^2} - \frac{1}{A_{ST}^2} \right)$ is the correction due to the effect of the difference of kinetic energy between the surge tank and the pressure tunnel.

F.3 Conclusions

Cavitation limits have been derived from the definition of the incipient cavitation number σ_i for a straight pipe and a throttled surge tank. For the throttled surge tank, the water level is function of the discharge going into or out of the surge tank and σ_i. This allows to depict the limit of cavitation in a plan (H_{ST}, Q) in order to compare with the mass oscillations.

G Expert sheet for orifice design

An expert sheet (see Figure G.1) is available on-line (doi:10.5075/epfl-thesis-8090), which summarizes the experimental and numerical results of the orifices. For wished target head loss coefficients, this expert sheet allows to find the closest tested orifices.

A given range with the target head loss coefficients can be defined. Then, as shown in Figure G.1, the cells corresponding to experimental or numerical results within the defined range are highlighted.

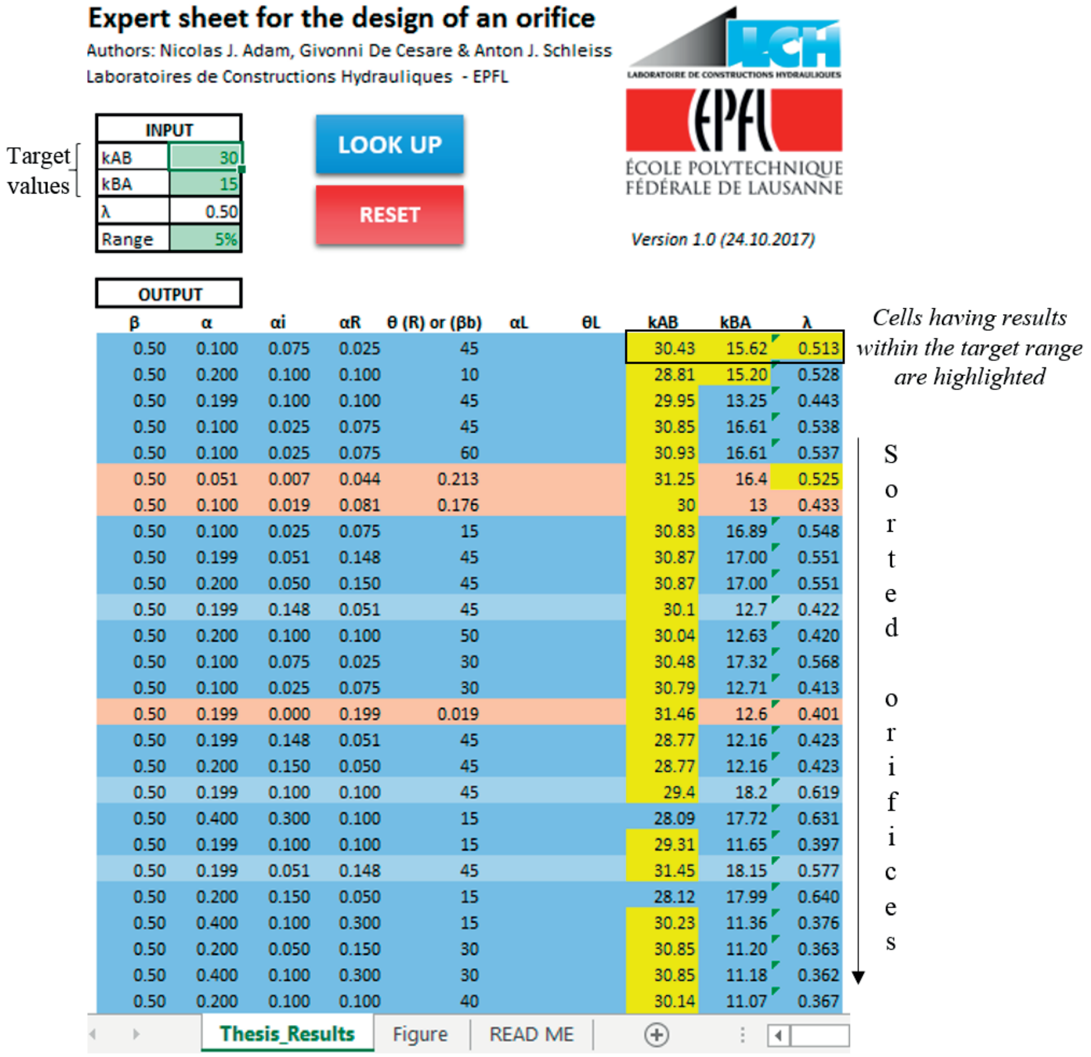

Expert sheet for the design of an orifice
Authors: Nicolas J. Adam, Givonni De Cesare & Anton J. Schleiss
Laboratoires de Constructions Hydrauliques - EPFL

Version 1.0 (24.10.2017)

INPUT	
kAB	30
kBA	15
λ	0.50
Range	5%

OUTPUT

β	α	αi	αR	θ (R) or (βb)	αL	θL	kAB	kBA	λ
0.50	0.100	0.075	0.025	45			30.43	15.62	0.513
0.50	0.200	0.100	0.100	10			28.81	15.20	0.528
0.50	0.199	0.100	0.100	45			29.95	13.25	0.443
0.50	0.100	0.025	0.075	45			30.85	16.61	0.538
0.50	0.100	0.025	0.075	60			30.93	16.61	0.537
0.50	0.051	0.007	0.044	0.213			31.25	16.4	0.525
0.50	0.100	0.019	0.081	0.176			30	13	0.433
0.50	0.100	0.025	0.075	15			30.83	16.89	0.548
0.50	0.199	0.051	0.148	45			30.87	17.00	0.551
0.50	0.200	0.050	0.150	45			30.87	17.00	0.551
0.50	0.199	0.148	0.051	45			30.1	12.7	0.422
0.50	0.200	0.100	0.100	50			30.04	12.63	0.420
0.50	0.100	0.075	0.025	30			30.48	17.32	0.568
0.50	0.100	0.025	0.075	30			30.79	12.71	0.413
0.50	0.199	0.000	0.199	0.019			31.46	12.6	0.401
0.50	0.199	0.148	0.051	45			28.77	12.16	0.423
0.50	0.200	0.150	0.050	45			28.77	12.16	0.423
0.50	0.199	0.100	0.100	45			29.4	18.2	0.619
0.50	0.400	0.300	0.100	15			28.09	17.72	0.631
0.50	0.199	0.100	0.100	15			29.31	11.65	0.397
0.50	0.199	0.051	0.148	45			31.45	18.15	0.577
0.50	0.200	0.150	0.050	15			28.12	17.99	0.640
0.50	0.400	0.100	0.300	15			30.23	11.36	0.376
0.50	0.200	0.050	0.150	30			30.85	11.20	0.363
0.50	0.400	0.100	0.300	30			30.85	11.18	0.362
0.50	0.200	0.100	0.100	40			30.14	11.07	0.367

Target values
LOOK UP
RESET
LABORATOIRE DE CONSTRUCTIONS HYDRAULIQUES
ÉCOLE POLYTECHNIQUE FÉDÉRALE DE LAUSANNE
Cells having results within the target range are highlighted
Sorted orifices
Thesis_Results
Figure
READ ME

Figure G.1 – Print-screen of the expert-sheet, which is on-line available with the thesis (doi: 10.5075/epfl-thesis-8090)

Bibliography

ABSI, R. (2006). A roughness and time dependent mixing length equation. *Doboku Gakkai Ronbunshuu B*, 62(4):437–446.

Adam, N. J., De Cesare, G., Nicolet, C., Billeter, P., Angermayr, A., Valluy, B., and Schleiss, A. J. (2017*). Design of a throttled surge tank for refurbishment by increase of installed capacity at a high-head power plant (in publication process). *Journal of Hydraulic Engineering*. Accepted for publication.

Adam, N. J., De Cesare, G., and Schleiss, A. J. (2016). Surge tank throttles for safe and flexible operation of storage plants. In *Hydro Conference 2016*, Montreux, Switzerland.

Adamkowski, A. (2012). Discharge measurement techniques in hydropower systems with emphasis on the pressure-time method. In *Hydropower-practice and application*. InTech.

Allievi, L. (1913). Théorie du coup de bélier (in french, translated by r. neeser). *Bulletin technique de Suisse romande*, 39(11):121–124.

Alligne, S., Rodic, P., Arpe, J., Mlacnik, J., and Nicolet, C. (2012). Détermination des Pertes de Charge dún Diaphragme de Cheminée déquilibre par Simulations Numériques. In *SimHydro 2012: Nouvelles frontières de la simulation*.

Alligne, S., Rodic, P., Arpe, J., Mlacnik, J., and Nicolet, C. (2014). Determination of Surge Tank Diaphragm Head Losses by CFD Simulations. In *Advances in Hydroinformatics*, pages 325–336. Springer.

An, J. F., Zhang, J., and Cheng, S. (2013a). Coefficients of local head losses in steady-state flow of throttled surge tanks with standpipe by cfd. In *Advanced Materials Research*, volume 677, pages 290–295. Trans Tech Publ.

An, J.-f., Zhang, J., Yu, X.-d., and Chen, S. (2013b). Influence of flow field on stability of throttled surge tanks with standpipe. *Journal of Hydrodynamics, Ser. B*, 25(2):294–299.

Anderson, A. (1984). Surge shaft stability with pumped-storage schemes. *Journal of Hydraulic Engineering*, 110(6):687–706.

ANSYS (2016a). Ansys icem cfd user's manual , release 17.1. ansys. onlime.

ANSYS (2016b). Cfx documentation, cfx-pre user's guide, release 17.1. ansys inc.

ANSYS (2016c). Cfx documentation, cfx-solver modeling guide, release 17.1. ansys inc.

ANSYS (2016d). Cfx documentation, cfx-solver theory guide , release 17.1. ansys inc.

Bergant, A., Ross Simpson, A., and Vìtkovsk, J. (2001). Developments in unsteady pipe flow friction modelling. *Journal of Hydraulic Research*, 39(3):249–257.

Bergeron, L. (1950). *Du coup de bélier en hydraulique au coup de foudre en électricité.* Dunod.

Billeter, P., Portner, C., Blötz, A., and Hager, H. (1996). Coupled numerical and physical simulation of te surge tank dynamics for the refurbishment of a high head power plant. In *Modelling, Testing and Monitoring for Hydro Powerplants - II*, Lausanne (Switzerland). The International Journal on Hydropower & Dams.

Blevins, R. D. (1984). Applied Fluid Dynamics Handbook. *New York, Van Nostrand Reinhold Co.*

Boillat, J.-L. and de Souza, P. (2004). *Hydraulic System - Modélisation des systèmes hydrauliques à écoulements transitoires en charge.* Communiation LCH 16. Ed. Anton Schleiss, Ecole polytechnique fédérale de Lausanne.

Brown, G. O. (2002). The history of the Darcy-Weisbach equation for pipe flow resistance. *Environmental and Water Resources History*, 38(7):34–43.

Buckingham, E. (1915). The principle of similitude. *Nature*, 96:396–397.

Cao, H., Zheng, C., Luo, F., and Guo, L. (2013). The Effect of Surge Tanks in the Process of the Protection towards Water Hammer Fluctuation in Long-Distance Pipelines. In *ICPTT 2013: Trenchless Technology*, pages 249–261. American Society of Civil Engineers.

Chaudhry, M. H. (2011). Modeling of One-Dimensional, Unsteady, Free-Surface, and Pressurized Flows. *Journal of Hydraulic Engineering*, 137(2):148–157.

Chaudhry, M. H. (2014). *Applied Hydraulic Transients.* Springer New York, New York, NY.

Craft, T., Launder, B., and Suga, K. (1996). Development and application of a cubic eddy-viscosity model of turbulence. *International Journal of Heat and Fluid Flow*, 17(2):108–115.

Daily, J., Hankey Jr, W., Olive, R., and Jordaan Jr, J. (1955). Resistance coefficients for accelerated and decelerated flows through smooth tubes and orifices. Technical report, DTIC Document.

De Cesare, G., Adam, N. J., Nicolet, C., Billeter, P., Angermayr, A., and Valluy, B. (2015). Surge tank geometry modification for power increase. In *Hydro Conference 2015*, Bordeaux, France.

De Martino, G. and Fontana, N. (2012). Simplified Approach for the Optimal Sizing of Throttled Air Chambers. *Journal of Hydraulic Engineering*, 138(12):1101–1109.

Erdal, A. and Andersson, H. (1997). Numerical aspects of flow computation through orifices. *Flow Measurement and Instrumentation*, 8(1):27–37.

Ferrarese, G., Messa, G. V., Rossi, M. M., and Malavasi, S. (2015). New method for predicting the incipient cavitation index by means of single-phase computational fluid dynamics model. *Advances in Mechanical Engineering*, 7(3):1687814015575974.

Ferràs Segura, D. (2016). *Fluid-structure interaction during hydraulic transients in pressurized pipes: experimental and numerical analyses (Thesis 7099)*. PhD thesis, Ecole Polytechnique Fédérale de Lausanne.

Fossa, M. and Guglielmini, G. (2002). Pressure drop and void fraction profiles during horizontal flow through thin and thick orifices. *Experimental Thermal and Fluid Science*, 26(5):513–523.

Fratino, U. and Pagano, A. (2011). Head loss coefficient of orifice plate energy dissipator. *Journal of Hydraulic Research*, 49(6):830–831.

Gabl, R. (2012). *Numerische und physikalische Untersuchung des Verlustbeiwertes einer asymmetrischen Düse im Wasserschloss*. PhD thesis, Innsbruck university, Innsbruck.

Gabl, R., Achleitner, S., Neuner, J., Götsch, H., and Aufleger, M. (2011). 3d-Numerical Optimisation of an Asymmetric Orifice in the Surge Tank of a High-head Power Plant. In *Proceedings of the 34th World Congress of the International Association for Hydro-Environment Research and Engineering: 33rd Hydrology and Water Resources Symposium and 10th Conference on Hydraulics in Water Engineering*, page 2428. Engineers Australia.

Gabl, R., Gems, B., Plörer, M., Klar, R., Gschnitzer, T., Achleitner, S., and Aufleger, M. (2014). Numerical Simulations in Hydraulic Engineering. In *Computational Engineering*, pages 195–224. Springer.

Gan, G. and Riffat, S. B. (1997). Pressure loss characteristics of orifice and perforated plates. *Experimental Thermal and Fluid Science*, 14(2):160–165.

Gardel, A. (1956). *Chambres d" équilibre - Analyse de quelques hypothèses usuelles: Méthodes de calcul rapide*. PhD thesis, Ecole Polytechinque de l'Université de Lausanne.

Giesecke, J., Heimerl, S., and Mosonyi, E. (2014). *Wasserkraftanlagen: Planung, Bau und Betrieb*. Springer-Verlag.

Gomsrud, D. (2015). Design of a surge tank throttle for tonstad hydropower plant. Master's thesis, NTNU.

Goodall, D., Kjorholt, H., Tekle, T., and Broch, E. (1988). Air cushion surge chambers for underground power plants. *International water power & dam construction*, 40(11):29–34.

Haakh, D.-I. F. (2003). Vortex chamber diodes as throttle devices in pipe systems. computation of transient flow. *Journal of Hydraulic Research*, 41(1):53–59.

Hachem, F., Nicolet, C., Duarte, R., De Cesare, G., and Micoulet, G. (2013). Hydraulic Design of the Diaphragm s Orifice at the Entrance of the Surge Shaft of FMHL Pumped-storage Power Plant. *Proceedings of 35th IAHR World Congress*.

Hasmatuchi, V., Bosioc, A., and Münch-Alligné, C. (2016). On the dynamic measurements of hydraulic characteristics. In *IOP Conference Series: Earth and Environmental Science*, volume 49, page 062001. IOP Publishing.

Hobbs, J. M. and Humphreys, J. S. (1990). The effect of orifice plate geometry upon discharge coefficient. *Flow Measurement and Instrumentation*, 1(3):133–140.

Huber, B. (2010). Physikalischer Modelversuch und CFD-Simulation einer asymmetrischen Drossel in einem T-Abzweigstück. *Österreichische Wasser-und Abfallwirtschaft*, 62(3-4):58–61.

Hydropower and Dams (2016). *World Atlas and Industry Guide 2016*. Alison Bartle.

Idel'cik, I. (1969). Mémento des pertes de charges singulières et de pertes de charges par frottement [Handbook of singular and friction head losses]. *Eyrolles, Paris*.

Instrument Society of America (1995). *Considerations for evaluating control valve cavitation*. Instrument Society of America, Research Triangle Park, N.C. OCLC: 59391765.

ISO (2003). Measurement of fluid flow by means of pressure differential devices inserted in circular cross-section conduits running full – part2: Orifices plates. In *ISO 5167-2:2003*, Geneva.

Jaeger, C. (1933). *Théorie générale du coup de bélier: application au calcul des conduites à caractéristiques multiples et des chambres d'équilibre (in french)*. Dunod.

Jaeger, C. (1943). De la stabilité des chambres d'équilibre et des systèmes de chambres d'équilibre (in french). *Schweizerische Bauzeitung*, 122(21):255–257.

Jaeger, C. (1960). A review of surge-tank stability criteria. *Journal of Basic Engineering*, 82(4):765–775.

Jaeger, C. (1977). *Fluid transients in hydro-electric engineering practice*. Blackie.

Jianhua, W., Wanzheng, A., and Qi, Z. (2010). Head loss coefficient of orifice plate energy dissipator. *Journal of Hydraulic Research*, 48(4):526–530.

Kendir, T. E. and Ozdamar, A. (2013). Numerical and experimental investigation of optimum surge tank forms in hydroelectric power plants. *Renewable Energy*, 60:323–331.

Kim, S.-H. (2010). Design of surge tank for water supply systems using the impulse response method with the ga algorithm. *Journal of Mechanical Science and Technology*, 24(2):629–636.

Klasinc, R. and Bilus, I. (2009). Experimental and Numerical Approach to Surge Tank Improvements. In *International Symposium on Water Management and Hydraulic Engineering*.

Kuroda, M., Fukuda, T., and Cho, T. (1978). Hydraulic experiments on pressure dissipation with orifices in conduit pressure dissipation in closed conduit used in irrigation system (i). *Transactions of The Japanese Society of Irrigation, Drainage and Reclamation Engineering*, 1978(78):57–64.

Lancial, N., Arenas, M., Gamel, H., Thibert, E., Dessachy, N., and Veau, J. (2016). Discharge coefficient prediction through an orifice plate in a round pipe: experimental and numerical investigation. In *17th International Flow Measurement Conference, Sydney, 26-29 September 2016*.

Landry, C. (2015). *Hydroacoustic modeling of a cavitation Vortex rope for a Francis turbine (Thesis 6547)*. PhD thesis, Ecole Polytechnique Fédérale de Lausanne.

Leknes, E. (2016). Comparison of the svee and thoma stability criteria for mass oscillations in surge tanks. Master's thesis, NTNU.

Li, X., Hou, J., Wu, X., and Li, X. (2012). Parameter optimization on asymmetry orifice in a differential surge chamber. *Energy Procedia*, 16:730–736.

Malavasi, S., Messa, G., Fratino, U., and Pagano, A. (2012). On the pressure losses through perforated plates. *Flow measurement and instrumentation*, 28:57–66.

Malavasi, S. and Messa, G. V. (2011). Dissipation and Cavitation Characteristics of Single-Hole Orifices. *Journal of Fluids Engineering*, 133(5):051302.

Malavasi, S., Messa, G. V., Fratino, U., and Pagano, A. (2015). On cavitation occurrence in perforated plates. *Flow Measurement and Instrumentation*, 41:129–139.

Massonet, C. and Cescotto, S. (1994). *Mécanique des matériaux*. De Boeck Supérieur.

Maynes, D., Holt, G. J., and Blotter, J. (2013). Cavitation Inception and Head Loss Due to Liquid Flow Through Perforated Plates of Varying Thickness. *Journal of Fluids Engineering*, 135(3):031302.

Meusburger, P. (2015). Study of different surge tank design for obervermuntwerk ii. *WASSERWIRTSCHAFT*, 105(1):53–57.

Montes, J. (1980). Damping and stability of orifice plate surge tanks by approximate analytical technique. In *7th Australasian Conference on Hydraulics and Fluid Mechanics 1980: Preprints of Papers*, page 360. Institution of Engineers, Australia.

Montes, J. and Delphin, P. (1983). Surge tanks with horizontal galleries. In *8th Australasian Fluid Mecanichs Conference, University of Newcastle, N.S.W., 28 November-2December 1893*, University of Newcastle.

Morrison, G., DeOtte, R., Moen, M., Hall, K., and Holste, J. (1990). Beta ratio, swirl and reynolds number dependence of wall pressure in orifice flowmeters. *Flow measurement and instrumentation*, 1(5):269–277.

Morrison, G. L., Hauglie, J., and DeOtte Jr, R. E. (1995). Beta ratio, axisymmetric flow distortion and swirl effects upon orifice flow meters. *Flow Measurement and Instrumentation*, 6(3):207–216.

Nabi, G., Kashif, M., Tariq, M., et al. (2016). Hydraulic transient analysis of surge tanks: Case study of satpara and golen gol hydropower projects in pakistan. *Pakistan Journal of Engineering and Applied Sciences*.

Nicolet, C. (2007). *Hydroacoustic modelling and numerical simulation of unsteady operation of hydroelectric systems (Thesis 3751)*. PhD thesis, Ecole Polytechnique Fédérale de Lausanne.

Nicolet, C., Vullioud, G., Weiss, E., Bocherens, E., Dayer, J.-D., and Chéne, O. (2012). Transient analysis of Cleuson-Dixence power plant and injector closure in the reflection time. In *Proceeding of 11th International Conference on Pressure Surges*, pages 27–41, Lisbon (Portugal). BHR Group.

Numachi, F., Yamabe, M., and Oba, R. (1960). Cavitation effect on the discharge coefficient of the sharp-edged orifice plate. *Journal of Basic Engineering*, 82(1)(1):1–6.

Nygård, F. and Andersson, H. (2013). Numerical simulation of turbulent pipe flow through an abrupt axisymmetric constriction. *Flow, turbulence and combustion*, 91(1):1–18.

Piccolier, G. (1966). *Etude de la stabilité des chambres d'équilibre*. PhD thesis, Université Joseph-Fourier-Grenoble I.

Popescu, M., Arsenie, D., and Vlase, P. (2003). *Applied Hydraulic Transients: For Hydropower Plants and Pumping Stations*. CRC Press.

Qing, M., Jinghui, Z., Yushan, L., Haijun, W., and Quan, D. (2006). Experimental studies of orifice-induced wall pressure fluctuations and pipe vibration. *International journal of pressure vessels and piping*, 83(7):505–511.

Reader-Harris, M. (2015). *Orifice Plates and Venturi Tubes*. Springer.

Reader-Harris, M. J., Sattary, J. A., and Spearman, E. P. (1995). The orifice plate discharge coefficient equation—further work. *Flow measurement and instrumentation*, 6(2):101–114.

Richter, W., Dobler, W., and Knoblauch, H. (2012). Hydraulic and numerical modelling of an asymmetric orifice within a surge tank. In *4th IAHR International Symposium on Hydraulic Structures. Porto, Portugal.*

Richter, W., Zenz, G., Schneider, J., and Knoblauch, H. (2015). Surge tanks for high head hydropower plants–hydraulic layout–new developments/wasserschlösser für hochdruckwasserkraftanlagen–hydraulische auslegung–neue entwicklungen. *Geomechanics and Tunnelling*, 8(1):60–73.

Roul, M. K. and Dash, S. K. (2012). Single-phase and two-phase flow through thin and thick orifices in horizontal pipes. *Journal of Fluids Engineering*, 134(9):091301.

Şahin, B. (1989). Pressure losses in an isolated perforated plate and jets emerging from the perforated plate. *International Journal of Mechanical Sciences*, 31(1):51–61.

Sánchez, R., Juana, L., Laguna, F. V., and Rodríguez-Sinobas, L. (2008). Estimation of cavitation limits from local head loss coefficient. *Journal of Fluids Engineering*, 130(10):101302.

Schleiss, A. (2002). Chambres d'équilibre, Polycopié du cycle postgrade en aménagements hydrauliques, LCH-EPFL.

Schleiss, A. (2007). L'hydraulique suisse: Un grand potentiel de croissance par l'augmentation de la puissance. *Bulletin SEV/AES*, (num. 2):24–29.

Schleiss, A. (2012). Talsperrenerhöhungen in der Schweiz: energiewirtschaftliche Bedeutung und Randbedingungen. *Wasser Energie Luft*, 104:199–203.

Schneider, J., Richter, W., Knoblauch, H., and Zenz, G. (2014). Physikalische und numerische untersuchungen von wasserschlössern im rahmen der neuerrichtung von pumpspeicherkraftwerken. In *37. Dresdner Wasserbaukolloquium 2014 - "Simulationsverfahren und Modelle für Wasserbau und Wasserwirtschaft, Institut für Wasserbau und Techische Hydromechanik, Dresden, Germany*.

Schönfeld, J. (1949). Resistance and inertia of the flow of liquids in a tube or open canal. *Applied Scientific Research*, 1(1):169–197.

SFOE (2015a). Prognosis 2050 for replacement of nuclear energy.

SFOE (2015b). Statistique suisse de l'électricité 2015. Technical report, Swiss Federal Office of Energy.

Shah, M. S., Joshi, J. B., Kalsi, A. S., Prasad, C., and Shukla, D. S. (2012). Analysis of flow through an orifice meter: Cfd simulation. *Chemical engineering science*, 71:300–309.

Singh, S., Seshadri, V., Singh, R., and Gawhade, R. (2006). Effect of upstream flow disturbances on the performance characteristics of a v-cone flowmeter. *Flow Measurement and Instrumentation*, 17(5):291–297.

Smith, A. and Cebeci, T. (1967). Numerical solution of the turbulent-boundary-layer equations. Technical report, DOUGLAS AIRCRAFT CO LONG BEACH CA AIRCRAFT DIV.

Spalart, P. R., Allmaras, S. R., et al. (1994). A one equation turbulence model for aerodynamic flows. *RECHERCHE AEROSPATIALE-FRENCH EDITION-*, pages 5–5.

Steyrer, P. (1999). Economic surge tank design by sophisticated hydraulic throttling. In *Proceedings of the 28th IAHR congress, Graz, Austria*.

Stucky, M. A. (1950). *Chambres d'equilibre: cours d'amenagement des chutes d'eau.* Ecole Polytechnique de l'Universite de Lausanne.

Thoma, D. (1910). *Zur Theorie des Wasserschlosses bei selbsttatig geregelten Turbinenanlagen.* PhD thesis, Oldenbourg.

Tian, Z., Xu, W.-L., Wang, W., and Liu, S.-J. (2009). Hydraulic characteristics of plug energy dissipater in flood discharge tunnel. *Journal of Hydrodynamics, Ser. B*, 21(6):799–806.

Tullis, J. P. (1989). *Hydraulics of pipelines: Pumps, valves, cavitation, transients.* John Wiley & Sons.

Urner, G. (1997). Pressure loss of orifice plates according to ISO 5167-1. *Flow Measurement and Instrumentation*, 8(1):39–41.

Vereide, K., Lia, L., and Nielsen, T. K. (2015a). Hydraulic scale modelling and thermodynamics of mass oscillations in closed surge tanks. *Journal of Hydraulic Research*, 53(4):519–524.

Vereide, K., Richter, W., Zenz, G., and Lia, L. (2015b). Surge tank research in austria and norway. *WASSERWIRTSCHAFT*, 105(1):58–62.

Vereide, K., Svingen, B., Nielsen, T. K., and Lia, L. (2017). The effect of surge tank throttling on governor stability, power control, and hydraulic transients in hydropower plants. *IEEE Transactions on Energy Conversion*, 32(1):91–98.

Vereide, K. V. (2016). *Hydraulics and Thermodynamics of Closed Surge Tanks for Hydropower Plants.* PhD thesis, Norwegian University of Science and Technology (NTNU).

Wójtowicz, P. and Kotowski, A. (2009). Influence of design parameters on throttling efficiency of cylindrical and conical vortex valves. *Journal of Hydraulic Research*, 47(5):559–565.

Wu, J.-H. and Ai, W.-Z. (2010). Flows through energy dissipaters with sudden reduction and sudden enlargement forms. *Journal of Hydrodynamics, Ser. B*, 22(3):360–365.

Yamaguchi, A. (1976). Non-Steady Characteristics of Orifices. *Bulletin of JSME*, 19(131):505–512.

Yan, Y. and Thorpe, R. B. (1990). Flow regime transitions due to cavitation in the flow through an orifice. *International journal of multiphase flow*, 16(6):1023–1045.

Zeghloul, A., Azzi, A., Saidj, F., Messilem, A., and Azzopardi, B. J. (2017). Pressure drop through orifices for single-and two-phase vertically upward flow - implication for metering. *Journal of Fluids Engineering*, 139(3):031302.

Zhang, Z. and Cai, J. (1999). Compromise orifice geometry to minimize pressure drop. *Journal of Hydraulic Engineering*, 125(11):1150–1153.

Zicman, B. (1953). Méthodes nouvelles pour le calcul des cheminées d'équilibre. *La Houille Blanche*, (5):580–598.

Acknowledgements

This thesis was elaborated during four years of research at the Laboratory of Hydraulic Constructions of the Swiss Federal Institute of Technology in Lausanne (EPFL). It is part of the Chopin S2C project and supported by the "The Ark - The foundation for innovation in Valais" and the Swiss Federal Office of Energy (SFOE), Hydropower research program.

First, I would like to thank and express my gratitude to my supervisor Prof. Anton J. Schleiss, who gave me the opportunity to perform this research, participate in several engineering projects and provided excellent conditions for the achievement of my PhD thesis.

Secondly, I sincerely thank my co-supervisor Dr Giovanni De Cesare for his (almost) daily availability and for his active encouragements along these four years. The share of his expertise in the field of hydraulics while working on engineering projects or hydraulic theory were highly appreciated.

I wish to thank Prof. Leif Lia, Dr. Mohamed Farhat and Dr. Roman Gabl for being part of the thesis jury and Prof. Dimitrios Lignos for being the president of the jury-.

The Chopin S2C Project involves the LCH and the research group on hydroelectricity at the HES-SO Valais headed by Prof. Cecile Muench-Alligne. Special thanks to Sylvain Richard for his support while doing numerical simulations in CFD.

A special thank goes to the PLTE Workshop, especially Michel, Laurent, Armin, David and Kosta, who helped me to solve all the issues related with the experimental setup. Thanks to Panpam and Cédric for their technical support in the laboratory.

Thanks to all the LCH team from those who finished their thesis four years ago to the current ones for the good atmosphere at LCH. I would like to personally thank Michael Pfister and Pedro Manso for sharing their research and practical experiences. Special thanks to Alain and Severin, my office mates, for all the distracting discussions during these years.

Furthermore, I also would like to thank the group Hydraulics in Environmental and Civil Engineering at the University of Liege headed by Prof. Michel Pirotton for giving me the opportunity to take a first step in the field of hydraulics. A special thank goes to Prof. Benjamin Dewals, who gave me the chance to work with him during my master’s project.

J'aimerais terminer en remerciant tous ceux qui ont contribué de près ou de loin à cette thèse, présents en Suisse, en Belgique, dans les Hautes-Alpes ou ailleurs. Merci à André de m'avoir accueilli dans sa famille et permis d'échapper le temps de week-ends à la pression du Doctorat. Merci à ma famille et particulièrement à mes parents, ma soeur et mon frère qui malgré la distance m'ont toujours laissé faire les études et choix que j'ai voulu.

Enfin, si la thèse est un voyage, je ne l'ai pas fait seul. Je finirais, donc, par remercier la personne avec qui je partage ma vie depuis neuf ans, celle qui me fait rire et m'a permis de tenir bon tout au long de cette thèse. Chaque moment passé à tes côtés ont été mes bouffées d'oxygène. Tu m'es vraiment spéciale et je suis heureux d'être à tes côtés sur le chemin de la vie. Je t'aime.

Lausanne, 18 Août 2017 N. A.

ADAM Nicolas Jean François Pascal Ghislain

Nationality Belgian

Date of birth October 27th 1990

Contact nicolas.adam@protonmail.ch

Education

September 2013 – December 2017	PhD in Civil Engineering at Laboratory of Hydraulic Constructions [Ecole Polytechnique Fédérale de Lausanne, EPFL] *PhD thesis: Characterization of hydraulic behavior of orifices in conduits*
2011 - 2013	Master's degree in Civil Engineering. [University of Liège, ULg, Belgium] *Master thesis: Management of sediments in large reservoirs*
2008 - 2011	Bachelor's degree in engineering science [ULg]
June 2008	Certificat d'Etudes Secondaires Supérieures [Athénée Royal de Spa, Belgium]

Awards

October 2013	Award SOFICO of the best master project in civil engineering given by the AILg (Association des Ingénieurs diplômés de l'Université de Liège)
June 2008	Award Dexia of the best student in Science at Athénée Royal de Spa

Work Experiences

September 2013 – December 2017	Civil engineer at Laboratory of Hydraulic Constructions [EPFL] - On-site measuring campaign in a fish farm (Valperca SA) - Experimental design of a throttle placed at the bottom of an existing surge tank (Energie Electrique du Simplon SA) - Numerical simulation of 4th turbine draft tube of the old Hagneck hydroelectric power plant (BKW AG) - Assessment of extreme loading for an existing water intake (Hydro Exploitation SA)

September 2013 – December 2017	Research and teaching assistant at Laboratory of Hydraulic Constructions [EPFL] - Hydraulic and hydroelectric structures and schemes - Hydraulic network - Semester projects of Dam design and for SolarDecathlon - Master projects learning the feasibility and/or the design of different hydropower plants (Mauvoisin – Corbassière, Bief Rouge, Gletsch-Oberwald)
January – June 2012 & 2013	Student assistant in Geotechnics at University of Liège
September 2012 – June 2013	Student assistant in Structural Mechanics II: Dynamics, plate theory at University of Liège
July - August 2012	Trainee engineer at Bureau d'études Greisch (Angleur , Belgium) Construction phasing stages of a cable-stayed bridge in prestressed concrete (Calculation of the longitudinal counter jib)

Languages & Computer Skills

Languages	French (Native speaker), English (B2) & German (A2-B1)
Hydraulic modelling	ANSYS CFX & Fluent, Hydraulic System, Flow 3D, SIMSEN & WOLF 2D
Computational tools	Matlab, AutoCAD, Inventor
General	Microsoft Office, OPENOFFICE and LATEX
Others	Programming in finite elements and volumes + utilization of FE software for structural design (FineLg)

Journal and conference publications

Adam, N., Erpicum, S., Archambeau, P., Pirotton, M., & Dewals, B. (2015). Stochastic modelling of reservoir sedimentation in a semi-arid watershed. *Water Resources Management*, *29*(3), 785-800.

Adam, N.J., De Cesare, G., Nicolet, C., Billeter, P., Angermayr, A., Valluy, B. & Schleiss, A.J. (accepted for publication). Design of a throttled surge tank for the refurbishment by power increase of a high head power plant. *Journal of Hydraulic Engineering.*

Adam, N.J., De Cesare, G. & Schleiss, A.J. (under revision). Influence of geometrical parameters on the head losses of standard orifice. Submitted to *Journal of Hydraulic Research*.

Adam, N. J., De Cesare, G., & Schleiss, A. (under revision). Throttles in surge tank to reduce mass oscillations. Submitted to *Canadian Journal of Civil Engineering*.

Adam, N. J., De Cesare, G., & Schleiss, A. (2017). Head losses and influence length of sharp-edged and rounded orifices under steady flow conditions. *In Proc. of the 37th IAHR World Congress, Kuala Lumpur, Malaysia.*

Adam, N. J., De Cesare, G., & Schleiss, A. (2016). Surge tank throttles for safe and flexible operation of storage plants. In *HYDRO 2016, Montreux, Switzerland.*

Adam, N. J., De Cesare, G., & Schleiss, A. J. (2016). Non-intrusive flow velocity measurements in pressurized pipe with orifice. In *Proc. of the 10th International Symposium on Ultrasonic Doppler Methods for Fluid Mechanics and Fluid Engineering*, Tokyo, Japan.

Adam, N. J., De Cesare, G., Schleiss, A. J., Richard, S., & Muench-Alligné, C. (2016). Head loss coefficient through sharp-edged orifices. *In IOP Conference Series: Earth and Environmental Science (Vol. 49, No. 6, p. 062009). IOP Publishing.*

Adam, N. J., De Cesare, G., & Schleiss, A. (2016). Experimental assessment of head losses through elliptical and sharp-edged orifices. *In Proc. of the 4th IAHR Europe Congress, Liège, Belgium.*

Adam, N. J., & De Cesare, G. (2015). Diaphragm in pressure pipe: Steady state head loss evolution and transient phenomena. *In 5th IAHR International Junior Researcher and Engineer Workshop on Hydraulic Structures, Spa, Belgium.*

De Cesare, G., **Adam, N. J.**, Nicolet, C., Billeter, P., Angermayr, A., & Valluy, B. (2015). *Surge tank geometry modification for power increase*. In *HYDRO 2015*, Bordeaux, France.